

**AIR-COOLED CONDENSERS FOR THERMOELECTRIC POWER
GENERATION**

A Thesis
Presented to
The Academic Faculty

by

Jennifer Lin

In Partial Fulfillment
of the Requirements for the Degree
Master of Science in the
School of Mechanical Engineering

Georgia Institute of Technology
August 2016

COPYRIGHT© 2016 BY JENNIFER LIN

AIR-COOLED CONDENSERS FOR THERMOELECTRIC POWER GENERATION

Approved by:

Dr. Srinivas Garimella, Advisor
School of Mechanical Engineering
Georgia Institute of Technology

Dr. S. Mostafa Ghiaasiaan
School of Mechanical Engineering
Georgia Institute of Technology

Dr. Sheldon M. Jeter
School of Mechanical Engineering
Georgia Institute of Technology

Date Approved: July 25, 2016

ACKNOWLEDGEMENTS

First, I would like to thank my advisor, Dr. Garimella, for giving me the opportunity to work on this challenging project. I am grateful for the valuable technical and personal development advice that he has given me, and I look forward to applying those skills in future endeavors. I would also like to thank the members of the Sustainable Thermal Systems Laboratory for all of their technical guidance, feedback, and friendship, especially Dr. Alex Rattner, Allison Mahvi, Taylor Kunke, Khoudor Keniar, Girish Kini, Darshan Pahinkar, Bachir El Fil, Subhrajit Chakraborty, and Daniel Boman. It has truly been an honor and privilege to work with such bright, hard working, and motivated individuals during my graduate school career. Finally, I would like to thank my family and friends, without whose support I would not be here.

TABLE OF CONTENTS

ACKNOWLEDGEMENTS	iii
LIST OF TABLES	vii
LIST OF FIGURES	x
LIST OF SYMBOLS AND ABBREVIATIONS	xiv
SUMMARY	xvii
CHAPTER 1: INTRODUCTION	1
1.1 Thermoelectric Power Plants.....	1
1.1 Condenser Technologies	4
1.2 Air-Cooled Condenser Challenges.....	6
1.3 Scope of Present Work.....	9
1.4 Thesis Organization.....	9
CHAPTER 2: LITERATURE REVIEW	11
2.1 Tube-Side Modeling.....	11
2.1.1 Condensation.....	11
2.1.2 Two-Phase Pressure Drop	19
2.2 Air-Side Heat Transfer Enhancement Techniques	27
2.2.1 Fins	28
2.2.2 Vortex Generation	36
2.3 Summary	40
CHAPTER 3: MODELING	43
3.1 Segmented Condenser Model.....	43
3.1.1 Tube-side Modeling	43

3.1.2	Air-side Modeling	56
3.1.3	Determining the number of nodes	70
3.2	Baseline Power Plant Cycle Model	71
3.2.1	Coal-Fired Rankine Cycle	71
3.2.2	Combined Cycle	73
CHAPTER 4:	RESULTS AND DISCUSSION	79
4.1	Stand-Alone Condenser Model	79
4.1.1	Base-Case Model	80
4.1.2	Air-Side Parametric Studies	90
4.2	Power Plant Cycle Model	116
4.2.1	Rankine Cycle Model	116
4.2.2	Combined Cycle Model	132
CHAPTER 5:	CONCLUSIONS AND RECOMMENDATIONS	147
5.1	Conclusions	147
5.2	Recommendations for future work	155
APPENDIX A:	Segmented Heat Transfer Model Sample Calculations	157
APPENDIX B:	Air-Side Minor Loss Calculations	169
APPENDIX C:	Louvered and Wavy Fin Sample Calculations	173
C.1	Wavy fin calculations	173
C.2	Louvered fin calculations	176
APPENDIX D:	Cycle Model Sample Calculations	178
D.1	Rankine cycle sample calculations	178
D.2	Combined cycle sample calculations	181

REFERENCES..... 190

LIST OF TABLES

Table 1.1 Dry cooling system shares thermoelectric generation technologies worldwide as predicted by Davies <i>et al.</i> (2013).....	5
Table 2.1 Summary of Two-Phase Condensation Studies	17
Table 2.2 Summary of Some Available Frictional Pressure Drop Studies	26
Table 2.3 List of various enhancement techniques grouped by classification	27
Table 3.1 Summary of baseline geometry dimensions	44
Table 3.2 Summary of operating conditions	44
Table 3.3 Summary of C values for Chisholm (1967).....	54
Table 3.4 Parameters associated with the jetting and outlet loss coefficient	62
Table 3.5 Constants for j and f factors for the correlation of Park and Jacobi (2009)	68
Table 3.6 Comparison of Carbon Steel and Aluminum Fin Performance	69
Table 3.7 Sensitivity Analysis	70
Table 4.1 Summary of baseline geometry dimensions	80
Table 4.2 Summary of operating conditions	80
Table 4.3 Summary of baseline geometric parameters	81
Table 4.4 Predicted Colburn and friction factors as a function of wave amplitude.....	102
Table 4.5 Comparison between ITD and pressure drop predictions using two sets of wavy fin correlations	106
Table 4.6 Summary of dimension combinations for wavy fins to reach an ITD of 27 K using the Ismail <i>et al.</i> (2008) correlation	108
Table 4.7 Performance predictions as a function of louver pitch	111
Table 4.8 Predicted Colburn j and friction factor values as a function of louver length	112

Table 4.9 Summary of ITD, air side pressure drop, and amount of heat rejected from each individual ACC for different fin types	115
Table 4.10 Summary of property values at the different state points and key values to consider for plain fins with a fin height of 25.4 mm and fin thickness of 0.254 mm	117
Table 4.11 Rankine Cycle performance results as a function of fin height	120
Table 4.12 Representative values for wavy fins in the Rankine Cycle that occur from a change in wave amplitude	122
Table 4.13 Representative values for wavy fins in the Rankine Cycle that occur from a change in wavelength	123
Table 4.14 Representative values for louvered fins in the Rankine Cycle as a function of louver pitch	126
Table 4.15 Change in turbine, fan, and pump work in the Rankine Cycle for a change in louver length from 12.7 mm to 24.13 mm	128
Table 4.16 Dimensions and efficiencies of the optimized plain, louvered, and wavy fins for the Rankine Cycle	130
Table 4.17 Summary of cycle efficiencies and work and heat loads for the different fin types in the Rankine Cycle.....	131
Table 4.18 Summary of property values at the different state points and key parameters and results	133
Table 4.19 Representative values for wavy fins in the Combined Cycle that occur from a change in wave amplitude.....	136

Table 4.20 Representative values for wavy fins in the Combined Cycle for a change in wavelength	138
Table 4.21 Representative values for louvered fins in the Combined Cycle that occur for a change in louver pitch	140
Table 4.22 Change in turbine, fan, and pump work in the Combined Cycle for a change in louver length from 12.7 mm to 24.13 mm	142
Table 4.23 Dimensions of the optimized plain, louvered, and wavy fins for the Combined Cycle	144
Table 4.24 Summary of cycle efficiencies and work and heat loads for the different fin types in the Combined Cycle	145
Table 5.1 Summary of cycle efficiencies and work and heat loads for the different fin types in the Rankine Cycle.....	153
Table 5.2 Summary of cycle efficiencies and work and heat loads for the different fin types in the Combined Cycle	155
Table A.1 Baseline inputs	157
Table C.1 Wavy Fin Inputs.....	173
Table C.2 Louvered fin inputs	176
Table D.1 Baseline inputs	178
Table D.2 Cycle inputs.....	178
Table D.3 Summary of cycle properties	180
Table D.4 Baseline inputs	181
Table D.5 Cycle inputs.....	181
Table D.6 Summary of cycle properties	189

LIST OF FIGURES

Figure 1.1 Schematic of (a) a basic Rankine Cycle and (b) a Combined Cycle	3
Figure 1.2 A typical A-Frame ACC (source: (SPX, 2015)).....	6
Figure 2.1 Triangular rounded corner, sinusoidal, and triangular wavy fin profiles	31
Figure 2.2 Common wing and winglet designs for vortex generation.....	36
Figure 3.1 Top view and key dimensions of the steam tube and attached fins.....	43
Figure 3.2 View of a single tube assuming air flow into the page.....	46
Figure 3.3 Schematic of the segmented model (100 nodes)	50
Figure 3.4 Schematic showing thermal resistances analyzed in the model	51
Figure 3.5 Schematic of individual condenser segment.....	52
Figure 3.6 Location of minor losses on an A-Frame Air Cooled Condenser	56
Figure 3.7 Minor Losses upstream of the fan (Source: Stewart (2014)).....	57
Figure 3.8 Minor Losses downstream of the fan (Source: Accessories (-)).....	58
Figure 3.9 Air flow path from upstream of the fan through the air channels.....	59
Figure 3.10 Jetting loss of the air located between adjacent ACC cells	61
Figure 3.11 Outlet loss of the air located between adjacent ACC cells.....	62
Figure 3.12 Pressure drop due to temperature difference	63
Figure 3.13 Illustrations of the plain (left), wavy (center), and louvered (right) fins investigated	64
Figure 3.14 Schematic of the Rankine Cycle with representative values	71
Figure 3.15 Schematic of the Combined cycle with representative values.....	73
Figure 3.16 Temperature versus Heat Transferred graph in a HRSG.....	77
Figure 3.17 Flow of steam into and out of the steam drum	78

Figure 4.1 Plot of steam-side quality and void fraction with respect to relative axial tube position.....	82
Figure 4.2 Segmental Heat Duty and corresponding change in quality as a function of relative axial tube position	83
Figure 4.3 Thermal resistances as a function of position along tube	84
Figure 4.4 Plot of the steam side heat transfer coefficient calculated using the Akhavan- Behabadi <i>et al.</i> (2007) correlation as a function of tube position	84
Figure 4.5 UA as a function of location along the tube	86
Figure 4.6 Frictional, gravitational, and total steam-side pressure drop.....	88
Figure 4.7 Plot of outlet air from the condenser versus location along the tube.....	88
Figure 4.8 Summary of pressure drops at baseline operating conditions	90
Figure 4.9 Impact of varying fin spacing on the ITD and Air-Side Pressure Drop	92
Figure 4.10 Impact of varying fin thickness on the ITD and Air-Side Pressure Drop.....	93
Figure 4.11 Impact of varying fin height on the ITD and Air-Side Pressure Drop	95
Figure 4.12 Single tube and total effective area versus fin height	96
Figure 4.13 Example of plot used to visually eliminate poor performing fin geometry combinations	97
Figure 4.14 Enlargement of plot used to visually eliminate poor performing fin geometry combinations	98
Figure 4.15 Comparison of ITD and air-side pressure drop of the baseline and optimized configurations.....	100
Figure 4.16 Schematics of wavy fin specific geometry	101
Figure 4.17 Impact of wavelength on Colburn j and friction factors.....	103

Figure 4.18 Effects of varying fin height on two wavy fin performance prediction models	104
Figure 4.19 Effects of varying fin spacing on two wavy fin performance prediction models.....	104
Figure 4.20 Cross-sectional view of louver fin.....	108
Figure 4.21 Colburn j and friction factors as a function of louver angle correct Colburn to Colburn j in the axis label also.....	110
Figure 4.22 Test section used for the reed experiments (Crittenden and Glezer, 2015).	113
Figure 4.23 A “H” (left) and rectangular (right) that will be inserted into the channels (Crittenden and Glezer, 2015).....	114
Figure 4.24 ITD and air-side pressure drop comparison for the different fin configurations in the stand-alone condenser.....	115
Figure 4.25 State points of the Rankine Cycle.....	117
Figure 4.26 Rankine Cycle efficiency as a function of fin height and fin spacing.....	119
Figure 4.27 Rankine Cycle efficiency as a function of wave amplitude and fin spacing	121
Figure 4.28 Rankine Cycle efficiency as a function of wavelength and fin spacing.....	123
Figure 4.29 Rankine Cycle efficiency as a function of louver pitch for fin spacings of 1.27, 1.91, and 2.54 mm.....	125
Figure 4.30 Rankine Cycle efficiency as a function of louver length for a fin height of 25.4 mm.....	127
Figure 4.31 Comparison of the highest Rankine cycle efficiency for each fin type and the corresponding compressor, turbine, pump, and fan work.....	130
Figure 4.32 Labeled picture of the states in the Combined Cycle.....	132

Figure 4.33 Combined Cycle efficiency as a function of fin height and fin spacing.....	134
Figure 4.34 Combined Cycle efficiency as a function of wave amplitude and fin spacing assuming a constant fin height, fin thickness, and wavelength.....	135
Figure 4.35 Combined cycle efficiency as a function of wavelength and fin spacing....	137
Figure 4.36 Combined Cycle efficiency as a function of louver pitch for fin spacings of 1.27, 1.91, and 2.54 mm.....	139
Figure 4.37 Combined Cycle efficiency as a function of louver length and fin spacing	141
Figure 4.38 Comparison of the highest efficiency for each fin type and the corresponding compressor, turbine, pump, and fan work.....	143
Figure 4.39 Optimal Combined Cycle efficiency and fan and pump work for different fin configurations.....	144
Figure 5.1 ITD and resulting fan power comparison for the standalone ACC with different fin types	150
Figure 5.2 Comparison of Rankine Cycle efficiency and net cycle work for the different fin types.....	152
Figure 5.3 Comparison of Combined Cycle efficiency and net cycle work for the different fin types.....	154
Figure A.1 Condenser, fin, and tube geometry schematic (Source: (SPX, 2015))	157
Figure C.1 Wavy fin and tube schematic	173
Figure C.2 Louvered fin and tube schematic	176
Figure D.1 Rankine cycle schematic.....	178
Figure D.2 Combined cycle schematic	181

LIST OF SYMBOLS AND ABBREVIATIONS

Symbols

<i>A</i>	Area, m ²
<i>D</i>	Diameter, m
<i>f</i>	Friction factor
<i>F</i>	Fin
<i>g</i>	Gravity, m s ⁻²
<i>G</i>	Mass flux, kg m ⁻² s ⁻¹
<i>H</i>	Heat transfer coefficient, W m ⁻² K ⁻¹
<i>H</i>	Enthalpy, kJ kg ⁻¹
<i>j</i>	Colburn <i>j</i> factor
<i>k</i>	Thermal conductivity, W m ⁻¹ K ⁻¹
<i>K</i>	Loss coefficient
<i>L</i>	Louver
<i>M</i>	Wave amplitude, m
<i>MM</i>	Molar mass, kg kmole ⁻¹
<i>Nu</i>	Nusselt number
<i>num</i>	Number
<i>P</i>	Pressure, kPa
<i>Per</i>	Perimeter, m
<i>Pr</i>	Prandtl number
<i>Q̇</i>	Heat duty, kW
<i>Re</i>	Reynolds number
<i>SP</i>	Section percent
<i>T</i>	Temperature, °C
<i>TPP</i>	Two phase percent
<i>Tube</i>	Tube
<i>U</i>	Velocity, m s ⁻¹
<i>Ẇ</i>	Work, kW
<i>x</i>	Vapor quality
<i>X_{tt}</i>	Two-phase Martinelli parameter

Abbreviations

<i>ACC</i>	Air-cooled condenser
<i>AFR</i>	Auto-flutter reed
<i>EA</i>	Excess Air
<i>EES</i>	Engineering Equation Solver
<i>HRSG</i>	Heat Recovery Steam Generator
<i>ITD</i>	Initial temperature difference, K
<i>LHV</i>	Lower Heating Value, kJ kg ⁻¹
<i>LMTD</i>	Log mean temperature difference
<i>NTU</i>	Number of transfer units

Greek Symbols

α	Void fraction
α^*	Aspect ratio
β	Volumetric quality, inclination angle
ρ	Density, kg m ⁻³
η	Efficiency
Δ	Differential
λ	Wavelength, m
μ	Viscosity, kg m ⁻¹ s ⁻¹
φ	Relative humidity
Φ	Two-phase multiplier
σ	Contraction ratio
θ	Angle
ε	Roughness
ω	Humidity ratio

Subscripts

airside	Airside
avg	Average
bare	Bare
Boiler	Boiler
ci	Contraction inlet
cs	Cross section
cycle	Cycle
d	Depth
dec	Deceleration
eff	Effective
ff	Free flow
fin	Fin
fr	Frontal
fric	Frictional component
g	Gas
grav	Gravitational component
h	Height
hy	Hydraulic
i	Inside
in	Inlet
j	Node number
l	Liquid
LB	Louver banks
os	Outside surface
out	Outlet
p	Pitch

per	Perimeter
r	Reduced
rat	Ratio
sat	Saturation
seg	Segmental
steam	Steam
t	Thickness, m
total	Total
TP	Two phase
tube	Tube
v	Vapor
w	Width

SUMMARY

Thermoelectric power generation accounts for a significant portion of the worldwide fresh water demand, with the major portion of the water being used for steam condensation. Currently, many thermoelectric power plants use wet-cooled condenser technology, which lead to evaporation losses or thermal pollution of the water such that it is unfit to return to its source. An alternate method for steam condensation is to use dry-cooled technologies with air as the cooling fluid. These air-cooled systems are beneficial where water is unavailable or uneconomical. However, dry-cooled systems require large surface areas and footprints, lead to lower power plant efficiencies, and are therefore not as economical as wet-cooled systems.

The present study investigates the application of an A-frame air-cooled condenser (ACC) with different air-side enhanced surfaces to increase dry-cooled plant performance to levels approaching wet-cooled plants. A segmented condenser model was developed to predict the condenser performance with these different surfaces as a standalone heat exchanger. Applicable two phase heat transfer and pressure drop correlations for inclined flows were used to predict the performance of the condensing steam inside each individual tube in the condenser. Minor pressure drop losses associated with the path of the air from upstream of the condenser fan, through the ACC, to downstream of the ACC array were also accounted for. Parametric studies were conducted to identify the optimal geometries of plain smooth, wavy, and louvered fins for these condensers. Data from a novel autofluttering reed technology designed to improve heat transfer within the air channels was also implemented into the model. While both wavy and louvered fins do provide enhancements in heat transfer, the large number of geometry related variables and the large

discrepancies in the predictions of different correlations for such geometries in the literature made it difficult to predict performance results.

The segmented condenser model was also integrated into cycle models representative of either a 500 MW Rankine coal fired or a combined cycle plant to determine the impact of condenser fin geometries on overall cycle performance. Decreases in required initial temperature differences for the condenser due to improved geometries and tradeoffs associated with cooling fan and pump power requirements were considered to assess changes in the net plant power production and plant efficiency. From this analysis, it was found that a reduction in fin spacing of the plain fins can result in a ~1% increase in the overall cycle efficiency. While the ACCs with wavy fins, louvered fins, or plain fins with AFRs increased the cycle efficiency from that of the baseline plain fin case, adjusting the dimensions of the plain fins was found to be the most optimal choice to increase overall cycle efficiency for the range of operating conditions and parameters considered in this study.

CHAPTER 1: INTRODUCTION

Fresh water is a renewable resource whose replenishment through the water cycle is being increasingly compromised due to climate change, and increased demand for residential, commercial, agricultural, and power generation activities. Thermoelectric power generation accounted for 38% of total United States freshwater withdrawals in 2010, with the major portion consumed by steam condensation (Maupin *et al.*, 2014). One alternative method to using water to condense the steam is by using air, which has been reportedly considered since the early 1930s in the United Kingdom, Sweden, and Germany (Miliaras, 1974).

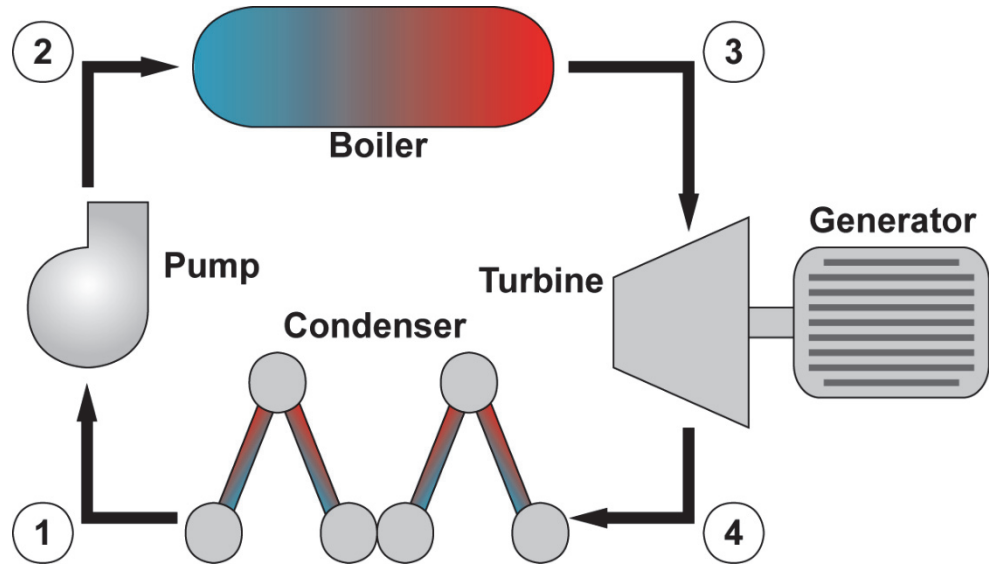
1.1 Thermoelectric Power Plants

The Rankine cycle is the most widely used cycle for electric-power plant generation (El-Wakil, 1984). In the simple ideal case, the cycle consists of four major components: the boiler, turbine, condenser, and pump. Vapor exits the turbine at a low pressure and enters the condenser, where heat is rejected. The fluid, exiting the condenser as a slightly subcooled liquid, is then pumped to a higher pressure before it enters the boiler, where heat is added to increase its temperature and boil it. Thermal energy for this process can be supplied by the firing of coal, waste heat recovered from another process, solar energy, and others. The heated and pressurized fluid enters the turbine that is used for power generation.

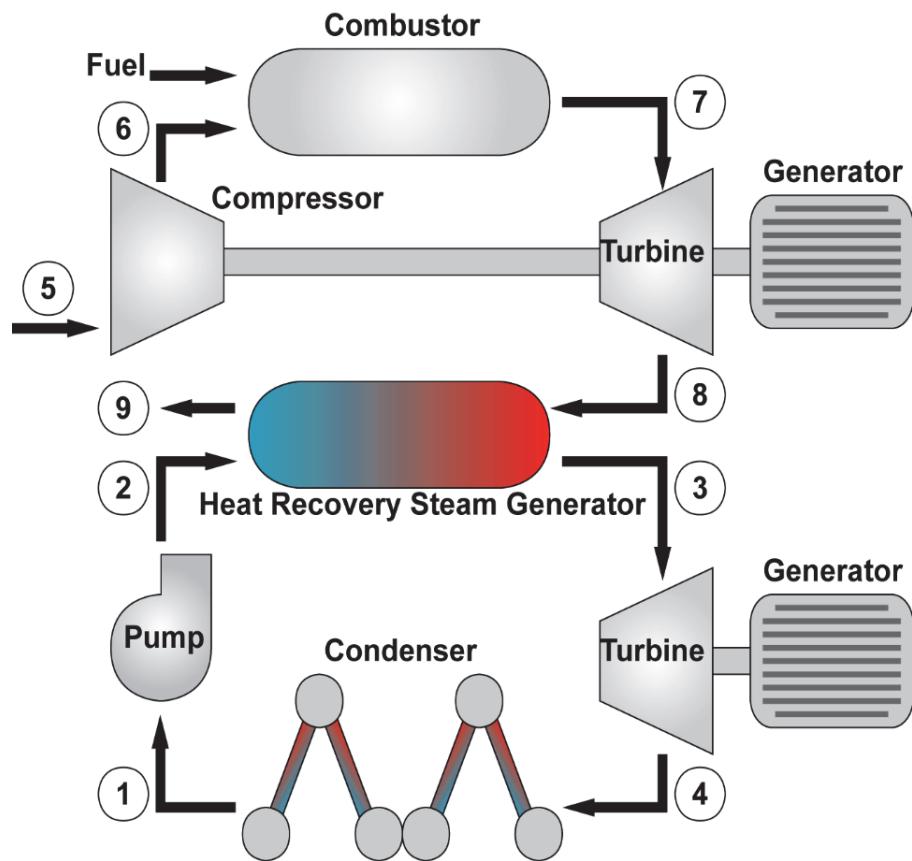
Rankine Cycles implemented in power plants are more advanced versions of this simple cycle to achieve higher thermal efficiencies, defined as the ratio of net work output to heat input of the cycle or power plant. Superheating and reheat strategies are typically employed in power plants. Superheating improves thermal efficiency by allowing for heat addition past the saturation temperature, increasing the average temperature at which the

heat is added. An additional advantage of superheating is drier steam flowing through the turbine, resulting in a more efficient turbine and less turbine blade damage (El-Wakil, 1984). In a reheat cycle, vapor exiting from the boiler expands part-way in a high pressure turbine section, after which it returns to the boiler. The vapor is then ideally heated at a constant pressure to a higher temperature before expanding in the low pressure turbine section to the pre-condenser pressure. Similar to superheating, reheat results in drier steam. Many modern power plants employ superheat and one or two stages of reheat. In situations with more than two stages of reheat, cycle complications and additional capital costs typically offset any additional increase in cycle efficiency (El-Wakil, 1984).

Combined cycle power plants refer to combining multiple thermodynamic cycles with gas and steam turbines to increase the overall cycle thermal efficiency, which can reach as high as 60% (Boyce, 2002). The Brayton cycle is commonly used as the topping cycle in conjunction with a steam or water Rankine bottoming cycle. In the Brayton cycle, air is compressed and combusted with a fuel, reaching a high temperature and pressure prior to entering the turbine to produce work. The net work for this cycle is the difference between the turbine work output and the work necessary for the compressor. Air exiting the turbine then enters a heat recovery steam generator, which captures waste heat from the gas turbine in the topping cycle and transfers it to the water in the bottoming Rankine cycle to power a steam turbine that generates additional electric power. In addition to the high thermal efficiency, advantages of the combined cycle include a rapid cold start-up time, and low initial capital costs of \$550 to \$800 kW⁻¹ depending on the size of the plant (Kehlhofer *et al.*, 2009). Schematics of a simple Rankine Cycle and a Combined Cycle are shown in Figure 1.1.



(a) Rankine Cycle



(b) Combined Cycle

Figure 1.1 Schematic of (a) a basic Rankine Cycle and (b) a Combined Cycle

1.1 Condenser Technologies

Steam condensation typically occurs in thermoelectric power plants in one of three ways: once-through, wet-recirculating, or dry. Once-through systems, accounting for 42.7% of cooling technology in United States power plants, withdraw relatively large amounts of water from a water source, lose a small portion of it to evaporation during the condensation of steam, and discharge the rest back to the original source (DOE and NETL, 2010). Due to the large amount of heat removed during the condensation process, the discharged water is at a high enough temperature that it can thermally pollute the water source and harm marine life (EPRI, 2013). Wet-recirculating systems are similar to once-through systems, but do not withdraw as much water and lose most of it to evaporation as the water is circulated through either a cooling tower or discharged to a cooling pond. Cooling towers, implemented in 41.9% of United States power plants, use ambient air flowing through the tower to cool the heated air (DOE and NETL, 2010). Spray nozzles, splash bars, or film fill can be used to facilitate the interaction of the water and the air (Kröger, 1998). There are two main designs for cooling towers, based on the method of moving the air through the towers. Mechanical draft cooling towers use fans to force air through the tower while natural draft cooling towers rely on the density difference between the humid and heated air inside the tower to the ambient air outside the tower. Cooling ponds, 14.5% of the U.S. cooling technology fleet, operate in a manner similar to cooling towers (DOE and NETL, 2010). These man-made ponds take heated water and dissipate it through evaporation.

Dry systems, accounting for 0.9% of United States power plants in 2010, eliminate the need for water as the cooling fluid by forcing air over heat exchangers to condense the steam (DOE and NETL, 2010). Davies *et al.* (2013) derived percentages of cooling systems

from all GCAM (Global Change Assessment Model) regions and thermoelectric generation technologies in 2005 based on data on cooling system shares in the literature for the United States, Australia, and China, and estimates for other regions. A summary of the predicted dry cooled system shares used in thermoelectric generation technologies in 2005 by region is shown in Table 1.1.

Table 1.1 Dry cooling system shares thermoelectric generation technologies worldwide as predicted by Davies *et al.* (2013)

Region	Dry Cooling Share			
	Coal	Other fossil/bio	Combined Cycle	Nuclear
USA	0.2	0	10	0
Canada	0	0	0	0
Western Europe	3	2.7	2.7	0
Japan	3.5	3.5	3.5	0
Australia and New Zealand	6.9	0	0	0
Former Soviet Union	0	0	0	0
China	8.1	8.1	8.1	0
Middle East	1.8	1.8	1.8	0
Africa	12	12	12	0
Latin America	4.1	4.1	4.1	0
Southeast Asia	3.5	3.5	3.5	0
Eastern Europe	0	0	0	0
Korea	3.5	3.5	3.5	0
India	3.5	3.5	3.5	0

Dry-cooling systems can be further divided into two categories depending on the heat rejection method: direct or indirect. Direct systems refer to systems where steam from the turbine is directly ducted to air-cooled heat exchangers, allowing for heat from the steam to be rejected directly to the air. Indirect dry cooling refers to systems where heat is rejected indirectly to the air, usually through a shell-and-tube condenser. Because of the additional thermal resistance of the shell-and-tube condenser, the condensation temperature of indirect systems is typically higher than the condensation temperature in a direct system, resulting in a decrease in overall system efficiency.

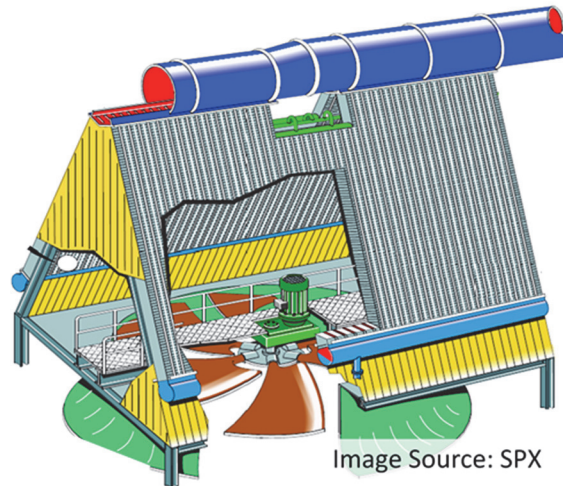


Figure 1.2 A typical A-Frame ACC (source: (SPX, 2015))

Air-cooled condensers, or ACCs, arranged in an A-Frame design like the one seen in Figure 1.2, are a common example of a direct dry cooling system (SPX, 2015). The A-frame consists of finned tube bundles sloped at an angle with respect to the horizontal to reduce plot area. Axial flow fans located under the A-frames force ambient air across the finned tube bundles, causing the steam ducted to the apex of the frame to condense as it flows down the inclined tubes. Care has to be taken to minimize the length of the steam condensation tubes to reduce possible steam-side pressure drop. The A-Frame Condenser design is the subject of the present study.

1.2 Air-Cooled Condenser Challenges

Although no water is consumed in dry-cooled power plants, there are still several key challenges to be addressed. One possible problem in air-cooled condensers is the presence of non-condensables, atmospheric gases and chemicals, in the system. Non-condensables enter the system through leaks, and can be trapped inside the tubes between inlet steam from the turbine exhaust and “backflow” steam at the tube outlet (Larinoff *et*

al., 1978). The presence of the trapped non-condensables restricts the flow of the steam, resulting in cold segments along the length of the metal tube where the condensate will freeze as it flows downwards due to gravity. In addition to potentially freezing the condensate, non-condensables can impair heat-transfered in the summer, or get absorbed by the condensate and result in material corrosion if not properly purged. Possible approaches to vent out the non-condensables include dephlegmators, vent tubes, and steam-jet air-ejector systems.

Dry-cooled technologies have not been as main stream in the United States as their wet-cooled technology counterparts due to the tradeoff between water consumption reduction, cost, and performance. Capital and operating costs include labor, equipment, and plant elements such as fans or water supply associated with the cooling system choice. Assuming comparable cycle capacities, air-cooled systems have higher capital costs than wet-cooling tower systems because of their larger size and correspondingly larger support structures and footprint (Putman and Jaresch, 2002). Zhai and Rubin (2010) conducted a study to compare the cost of wet and dry cooling systems of a plant with a 550 MW net output. Using the cost categories and models designated by Institute *et al.* (1993), the authors found that 12% of the total plant capital for the base design accounted for the dry cooling system compared to only 5% for the wet cooling system. This corresponded to capital requirements of \$224 per kW for dry cooling versus \$90 per kW for wet cooling, respectively. Depending on the plant site location and operating environment, the annual cost of dry cooling systems can be on average three times more than its wet cooling counterpart (EPRI, 2004).

As previously mentioned, dry cooling technologies do not perform as effectively as wet cooling technologies, a problem that is only exacerbated at higher ambient temperatures. Air has poor thermal transport properties when compared to those of water. Assuming atmospheric pressure, water has a specific heat capacity over four times greater than that of air, with corresponding values of $4.18 \text{ kJ kg}^{-1} \text{ K}^{-1}$ and $1.01 \text{ kJ kg}^{-1} \text{ K}^{-1}$, respectively. Therefore, a substantially greater flow rate of air than water is needed to remove similar heat duties from the condenser, increasing parasitic fan power consumption. The air-cooled heat exchanger can be constructed with a larger surface area to increase the heat transfer rate to compensate for its thermal transport properties, but doing so increases cost and required land area.

The performance of air-cooled heat exchangers is influenced by operating conditions such as the ambient temperature, humidity, wind, rain, snow, hail, and solar radiation (Kröger, 1998). An increase in ambient temperature corresponds to an increase in the turbine backpressure, decreasing plant output and therefore plant performance. This is further penalized by the energy demand, which peaks during times of high ambient temperature. The decrease in power plant performance can be compensated by increasing the overall size of the air-cooled condenser, but this also results in an increase in capital cost. Assuming an ambient temperature change from 15 to 25°C, Zhai and Rubin (2010) found that the size of the dry cooling system would have to increase approximately 40% over the base size, increasing the capital and levelized cost of the system by over 35%. Snow and rain typically have minimal effects on performance, but rain can reduce dry bulb temperatures to wet bulb temperatures (Kröger, 1998).

Wind can negatively impact forced draught air-cooled heat exchanger performance as a result of reduced fan performance and increased hot plume air recirculation (Duvenhage and Kröger, 1996). To reduce the possibility of hot air recirculation and wind effects, wind walls can be used to surround the cells (EPRI, 2005). Other methods to mitigate the negative effect of wind are to raise the fan platform height or add a walkway. Raising the fan platform height increases the size of the flow passage, decreases the flow separation up-wind of the air cooled heat exchanger, and therefore improves overall performance (Duvenhage and Kröger, 1996). Adding a walkway skirt around the periphery of the fans on the platform minimizes the separation or distortion around the inlet of the edge fan (Salta and Kröger, 1995; Bredell *et al.*, 2006).

1.3 Scope of Present Work

The present research focuses on the development of an optimized air-cooled A-frame condenser that will lead to an improvement in the efficiency of a thermo-electric power plant. A detailed, segmented model is developed to predict the performance of air-cooled condensers with varying air-side heat transfer enhancement methods.

1.4 Thesis Organization

This thesis is organized into the following chapters:

Chapter Two presents a review of literature on predicting performance based on the tube-side and fin-side geometries, condensing tube-side and the air-side thermal resistances, and the respective pressure drops.

Chapter Three presents a description of the developed segmented air-cooled condenser, Rankine Cycle model, and Combined Cycle model used to predict overall cycle performance.

Chapter Four presents an analysis and discussion of the predicted results from the developed segmented model, parametric studies, and the two cycle models.

Chapter Five summarizes the present study and suggests recommendations for further research.

CHAPTER 2: LITERATURE REVIEW

A review of the literature relevant to the modeling of condensers for power plants is summarized here. The reviewed literature includes heat transfer and pressure drop models and correlations for condensing flows on the tube-side, and also for the finned geometries on the air-side.

2.1 Tube-Side Modeling

Heat transfer and pressure drop models and correlations have been developed for vertical and horizontal flows. For the A-frame ACC configuration under consideration, steam flows downward through inclined finned tubes, for which there are relatively fewer studies. Vertical downwards or inclined flow models are better suited for the present study on ACCs.

2.1.1 Condensation

Several investigators have studied in-tube condensation and developed models and predictive tools for heat transfer and pressure drop. Traviss *et al.* (1973) applied the von Karman universal velocity distribution and momentum and heat transfer analogy to an annular flow model to describe the liquid film. The local heat transfer coefficient was calculated by using an order of magnitude and non-dimensional analysis to derive the final model, resulting in accurate predictions of their data. Akers *et al.* (1958) developed an “equivalent Reynolds number” model, where the all-liquid flow rate is assumed to provide the same heat transfer coefficient as an annular condensing flow. The “equivalent Reynolds number” was used in a single-phase, turbulent flow equation to predict the condensation coefficient and a Nusselt number. The resulting Nusselt number would be equal to the condensing flow Nusselt number. Moser *et al.* (1998) built on the “equivalent Reynolds

number” approach of Akers *et al.* (1958) by integrating the heat-momentum analogy to incorporate the relationship between the heat transfer and wall shear stress, with an appropriate correction factor. The model predictions were compared with 558 local and 639 average heat transfer data points from 18 sources and found to be as accurate as or better than the predictions of the Shah (1979) correlation.

Shah (1979) analyzed 474 data points from 21 experimental studies to empirically develop a commonly used dimensionless correlation. The studies considered included a wide range of fluids condensing in horizontal, vertical, and inclined pipes with diameters between 7 to 40 mm, as well as a wide range of heat fluxes, mass fluxes, vapor velocities, and pressures. Although his correlation had a mean deviation of 15.4% from the data and is commonly used, it is not suitable for flows with high vapor qualities and low liquid Reynolds numbers. Shah (2009) updated this correlation by expanding the database to include 39 sources that consist of 1189 data points for 22 pure fluids, azeotropic mixtures, and near-azeotropic mixtures. To reduce the numerical burden on correlation due to the large database, Shah (2009) took data at larger intervals than those included in the publications. For instance, if the quality varied from 0 to 1.0 at intervals of 0.1, Shah (2009) took data at larger intervals, such as 0.2. Shah (2009) reasoned that analyzing the data in this manner would be sufficient for correlation development. The updated correlation was found to have a mean deviation of 13.8%, and has been found to be in good agreement for a reduced pressure range of 0.0008 to 0.9, and for all flow rates for vertical tubes. However, further research is needed to validate and extend it for horizontal and slightly inclined tubes at vapor-only Reynolds numbers less than 16,000.

Some investigators have also studied vertical downward condensing flow, which is more relevant to ACC operation of interest in the present study. Kim and No (2000) experimentally investigated high pressure steam condensation in a single 46 mm diameter, single vertical tube to analytically develop a turbulent annular film condensation model. Their correlation shows better agreement with large diameter tube data from the literature than the predictions from the Shah (1979) model. Park *et al.* (2013) investigated vertical, downward flows inside a stainless-steel tube with inner diameter of 11.89 mm for slightly superheated FC-72 at flow rates ranging from 184.5 to 458.0 kg m⁻²s⁻¹. Their control-volume-based model incorporates an eddy diffusivity profile that accounts for interfacial damping and showed good accuracy in predicting the experimental data, as evidenced by the 12.5% mean absolute error.

Some researchers have argued that the heat transfer coefficient is heavily dependent on the flow pattern during condensation in addition to its dependence on fluid properties, mass flux, vapor quality, and inclination angle. Therefore, efforts have been made to develop flow regime dependent models.

Dobson and Chato (1998) experimentally studied two-phase condensation of various refrigerants in horizontal tubes of diameters ranging from 3.14 mm to 7.04 mm to develop heat transfer models based on condensation flow regimes, including stratified, wavy, wavy annular, annular mist, and slug flows. They classified these regimes into gravity or shear dominated flows and developed different correlations for annular and wavy flow regimes to account for the different underlying flow mechanisms.

Cavallini *et al.* (2002) proposed a model for smooth pipes based on flow patterns (annular, stratifying, wavy, slug) for condensation of halogenated refrigerants over the

whole vapor quality range in a horizontal, 8-mm diameter plain tube for saturation temperatures between 30 and 50°C and mass velocities between 100 to 750 kg m² s⁻¹. Their model was based on 600 data points from their own experiments, and was compared to 2,164 points for other refrigerants taken by several other laboratories.

Thome *et al.* (2003) evaluated a database consisting of fifteen fluids from nine different research laboratories to propose a heat transfer model for condensation inside horizontal, plain tubes with as few empirical constants and exponents as possible. The model assumes two types of heat transfer mechanisms in the tube, convective condensation and film condensation. They defined convective condensation as the axial flow when there is condensate flow along the channel due to the imposed pressure gradient, and film condensation as the flow of condensate from the top to the bottom of the tube due to gravity. Thome *et al.* (2003) divided the flow into six flow regimes: annular flow, stratified-wavy flow, fully stratified flow, intermittent flow, mist flow, and bubbly flow. The final model was found to predict 85% of the refrigerant database within 20%, and 75% of the refrigerant and hydrocarbon heat transfer coefficients in the database to within 20%.

Heat transfer performance for inclined flows has also been investigated. Akhavan-Behabadi *et al.* (2007) tested condensation of R-134a vapor in an inclined microfin tube at three different mass fluxes. They compared found that their experimental results were within 20% of the predictions from four different models (Cavallini *et al.*, 1995; Shikazono *et al.*, 1998; Yu and Koyama, 1998; Kedzierski and Goncalves, 1999). From their investigation, Akhavan-Behabadi *et al.* (2007) developed a heat transfer correlation and concluded that an inclination angle of +30°, or upward flow at an angle of 30° above the

horizon, provided an increase in heat transfer coefficient compared to other inclination angles.

Because the distribution of vapor and liquid within the tube is dependent on the shear stress between the liquid-vapor interface and other gravitational forces, Mohseni *et al.* (2013) conducted an experimental investigation to determine the flow pattern and its impact on condensation heat transfer performance in a smooth, inclined tube with an 8.38 mm inner diameter. Inclination angles ranged from -90 to $+90^\circ$ for six different mass fluxes ranging from 53 to $212 \text{ kg m}^{-2} \text{ s}^{-1}$. As the tube inclination was varied, they observed eight different flow regimes, noticeable differences in vapor and liquid distribution, and different condensation heat transfer coefficients. An empirical correlation was developed from this investigation to predict condensation heat transfer for different inclination angles.

Lips and Meyer (2012a) conducted an experimental condensation study of R-134a condensing in an inclined 8.38-mm inner diameter smooth tube at different mass fluxes. Flows were identified as stratified-wavy, annular-wavy, annular, intermittent and churn flow patterns based on the classifications of Kim and Ghajar (2002). They found that the flow pattern is strongly dependent on the inclination angle at low mass and vapor fluxes, and thus influences the heat transfer coefficient. Contributing factors for the condensation heat transfer coefficient include the perimeter occupied by the condensate film and the thickness. By depicting the inclination effect on heat transfer on the flow regime map of El Hajal *et al.* (2003), it was possible to determine an optimized inclination angle of -15° that results in a maximum increase of 20% in heat transfer. Gravitational forces in slightly downward flows result in an increase in liquid velocity and void fraction, leading to a stratified flow. The higher heat transfer coefficient is due to the thin liquid film that forms

at the top of the tube. Beyond the optimized angle, the heat transfer coefficient will decrease because of a decrease in the perimeter of the thin film at the top of the tube. Flow pattern transitions from this experiment were not accurately predicted by other flow pattern transition models, highlighting the need to develop better predictive tools for flow regimes and heat transfer. A summary of the heat transfer models and correlations discussed above is shown in Table 2.1.

Table 2.1 Summary of Two-Phase Condensation Studies

Author(s) (Year)	Approach	Working Fluids	Tube Orientation	D_i (mm)	Range of Applicability
Akhavan- Behabadi <i>et al.</i> (2007)	Experimental and empirical	R-134a	Horizontal, Vertical, Inclined	8.92	$54 < G < 107 \text{ kg m}^{-2} \text{ s}^{-1}$ $0.2 < x < 0.8$ $26 < T_{\text{sat}} < 32^\circ\text{C}$
Cavallini <i>et al.</i> (2002)	Empirical	R-22, R-134a, R-125, R- 32, R-236ea, R-407C, R- 410A	Horizontal	3 to 21	$100 < G < 750 \text{ kg m}^{-2} \text{ s}^{-1}$ $0 < x < 1$ $30 < T_{\text{sat}} < 50^\circ\text{C}$ $P_r < 0.75$
Dobson and Chato (1998)	Experimental , adiabatic	R-134a, R-22, 60/40 and 50/50 blends of R-32 and R-125	Horizontal	3.14, 4.57, 7.04	$25 < G < 800 \text{ kg m}^{-2} \text{ s}^{-1}$ $0.1 < x < 0.9$ $5 < q'' < 15 \text{ kW m}^{-2}$ $35 < T_{\text{sat}} < 60^\circ\text{C}$ $0.21 < P_r < 0.57$
Kim and No (2000)	Experimental	Steam	Vertical	7.4 to 50	$0.35 < P < 7.2 \text{ MPa}$ $0.84 < Pr < 1.27$ $2,400 < Re_l < 18,000$
Lips and Meyer (2012a)	Experimental	R-134a	Inclined	8.38	$200 < G < 600 \text{ kg m}^{-2} \text{ s}^{-1}$ $0.1 < x < 0.9$ $T_{\text{sat}} = 40^\circ\text{C}$
Park <i>et al.</i> (2013)	Experimental	FC-72	Vertical	11.89	$184.45 < G < 457.97 \text{ kg m}^{-2} \text{ s}^{-1}$ $1.04 < x < 1.08$ $63.43 < T_{\text{in}} < 86.58^\circ\text{C}$ $108.57 < P_{\text{in}} < 209.88^\circ\text{C}$
Mohseni <i>et al.</i> (2013)	Experimental	R-134a	Horizontal, Vertical, Inclined	8.38	$53 < G < 212 \text{ kg m}^{-2} \text{ s}^{-1}$ $T_{\text{sat}} = 35^\circ\text{C}$

Table 2.1 Summary of Two-Phase Condensation Studies continued

Author(s) (Year)	Modeling Approach	Working Fluids	Tube Orientation	D_i (mm)	Range of Applicability
Shah (1979)	Empirical	R-11, R-12, R-22, R-113, benzene, ethanol, methanol, toluene, trichloroethylene, water	Horizontal, Vertical, Inclined	7 to 40	$10.8 < G < 210.6 \text{ kg m}^{-2} \text{ s}^{-1}$ $0 < x < 1$ $21 < T_{\text{sat}} < 310^\circ\text{C}$ $0.002 < P_r < 0.44$
Shah (2009)	Empirical	R-11, R-12, R-22, R-32, R-113, R-123, R-125, R-134a, R-142b, R-404A, R-410A, R-502, R-507, propylene, isobutene, propane, benzene, Dowtherm 209, ethanol, toluene, methanol, water	Horizontal, Vertical, Inclined	2 to 49	$4 < G < 820 \text{ kg m}^{-2} \text{ s}^{-1}$ $0 < x < 1$ $0.0008 < P_r < 0.9$
Thome <i>et al.</i> (2003)	Empirical	R-11, R-12, r-22, R-32, R-113, R-125, R-134a, R-236ea, a R-32/R-125 near azeotrope, R-404A, R-410A, propane, <i>n</i> -butane, iso-butane and propylene	Horizontal	3.1 to 21.4	$24 < G < 1022 \text{ kg m}^{-2} \text{ s}^{-1}$ $0.03 < x < 0.97$ $0.02 < P_r < 0.8$
Traviss <i>et al.</i> (1973)	Isothermal	R-12, R-22	Horizontal	8	$161 < G < 1,532 \text{ kg m}^{-2} \text{ s}^{-1}$ $0.1 < x < 0.96$ $21 < T_{\text{sat}} < 56^\circ\text{C}$

2.1.2 Two-Phase Pressure Drop

Despite the low mass fluxes in ACC condensers, the low saturation pressures at the typical operating conditions imply that small changes in pressure drop can significantly affect operating temperatures and heat rejection, and therefore overall plant efficiencies.

Assuming a cross-section averaged, steady state two-phase mixture in a one-dimensional flow system, pressure drop during condensation in inclined tubes can be attributed to frictional, gravitational, and acceleration or deceleration components.

$$\left(-\frac{dP}{dz}\right) = \left(-\frac{dP}{dz}\right)_{fric} + \left(-\frac{dP}{dz}\right)_{grav} + \left(-\frac{dP}{dz}\right)_{dec} \quad (2.1)$$

Equation (2.1) can be rewritten to explicitly account for the momentum change term as follows:

$$\left(-\frac{dP}{dz}\right) = \left(-\frac{dP}{dz}\right)_{fric} + \left(\frac{1}{2}[(1-\alpha)\rho_l + \alpha\rho_v]g \sin \beta\right) + \left(\frac{d}{dz} \left[\frac{G^2 x^2}{\alpha\rho_v} - \frac{G^2 (1-x)^2}{(1-\alpha)\rho_l} \right]\right) \quad (2.2)$$

Two-phase frictional pressure drop is commonly modeled using either the homogeneous or separated flow approach. The homogeneous flow model assumes that the two phases are well mixed and move with identical velocities everywhere, essentially modeling the flow as a compressible single-phase fluid with variable properties (Ghiaasiaan, 2007). Estimates for two-phase properties such as density and viscosity are needed to predict two-phase flow. Cicchitti *et al.* (1959), Dukler *et al.* (1964), and McAdams *et al.* (1942) have all provided expressions to predict the viscosity of a homogeneous gas-liquid two-phase mixture based on the flow quality or volumetric quality, and liquid and vapor viscosities. These expressions are shown in Equations (2.3) to (2.5), respectively.

$$\mu_{TP} = x\mu_G + (1-x)\mu_L \quad (2.3)$$

$$\mu_{TP} = \beta\mu_G + (1-\beta)\mu_L \quad (2.4)$$

$$\mu_{TP} = \left(\frac{x}{\mu_G} + \frac{1-x}{\mu_L} \right)^{-1} \quad (2.5)$$

Chen *et al.* (2002) collected experimental two-phase frictional pressure drop data from the literature for three studies with air-water mixtures and eight refrigerants in tubes with a diameter less than 10 mm. They found that the Chisholm (1967) correlation did not accurately predict the datasets for smaller diameters, the correlation of Friedel (1979) predicted the refrigerant data fairly well, and the homogeneous model yielded reasonable predictions of the refrigerant and air-water data with a mean deviation of 34.7%. By adding the Bond and Weber numbers as well as other dimensionless parameters to the original homogeneous model, the model developed by Chen *et al.* (2002) is able to better predict the refrigerant and air-water data than the aforementioned correlations and the homogeneous model, improving the mean deviation from the data points to 19.1%.

Many empirical correlations based on the separated flow model incorporate two-phase flow multipliers, an idea introduced by Lockhart and Martinelli (1949). To develop the correlation, Lockhart and Martinelli (1949) grouped flows from an isothermal experiment into four different categories depending on if whether the flows of the individual phases were viscous or turbulent. The data were correlated using X , the Martinelli parameter, a two-phase parameter equal to the square root of the ratio of liquid only pressure drop in the pipe to gas only pressure drop in the pipe, and is seen in Equation (2.6).

$$X^2 = \frac{\left(-\frac{dP}{dz}\right)_{f,L}}{\left(-\frac{dP}{dz}\right)_{f,G}} \quad (2.6)$$

The Martinelli parameter takes into account the flow quality as well as phasic properties, and can be approximated using different expressions, exponents, and constants depending on the flow type. Chisholm (1967) curve fit the data of Lockhart and Martinelli (1949) and to develop simplified equations, shown in Equation (2.7), that accounted for interfacial shear force between the phases.

$$\Phi_G^2 = 1 + CX + X^2 \quad , \quad \Phi_L^2 = 1 + \frac{C}{X} + \frac{1}{X^2} \quad (2.7)$$

Two-phase multipliers dependent on flow inclination have also been developed (Friedel, 1979; Storek and Brauer, 1980). The multipliers for the correlation of Friedel (1979) are dependent on the Weber number, the Froude number, single-phase friction factors, and liquid- and vapor- only Reynolds numbers. Predictions from this model are often used as points of comparison for experimental and other empirical correlations (Cavallini *et al.*, 2001; Cavallini *et al.*, 2002). Prediction models of both Friedel (1979) and Storek and Brauer (1980) have been widely used, but the result of a study by Müller-Steinhagen and Heck (1986) suggest that the models have poor accuracy at lower flow qualities or higher mass flow rates and flow qualities, respectively.

To fill gaps in the literature, a simple, two-phase frictional pressure drop correlation was developed by Müller-Steinhagen and Heck (1986), and compared with fourteen other correlations against a database containing over 9,300 frictional pressure drop data points representing various flow conditions, fluids, and pipe diameters. Their correlation was built by superimposing, or otherwise combining, observations of single-phase pressure drop and

the influence of flow quality less than 0.7 on pressure drop to cover the full range of flow qualities between zero and one. Even though the correlation is simple to implement, the major portion of the database used by Müller-Steinhagen and Heck (1986) to develop their model is for horizontal or vertically upward flow, with only ~ 1% of the data pertaining to vertically downward flow.

The impact of inclination angle, which is more relevant to predicting ACC behavior, on pressure drops has also been investigated. Spedding *et al.* (1982) presented data for angle of inclination from vertical upward to vertical downward co-current air-water flow in a 45.5 mm diameter pipe and classified flow regimes as suggested by Spedding and Nguyen (1980). Results were presented in the form of frictional velocity, $\sqrt{\left(\left(\Delta P/\Delta l\right)_f (D/4\rho_l)\right)}$, versus the total velocity. Presenting the data in this manner does not explicitly display the effect of diameter and liquid density on frictional pressure drop, and highlights the influence of liquid viscosity. Comparisons of the work done by Spedding *et al.* (1982) showed some agreement with databases of vertical (Isbin *et al.*, 1957; Brown *et al.*, 1960; Hewitt *et al.*, 1961; Beggs, 1972; Harrison, 1975) and horizontal (Govier and Omer, 1962; Eaton, 1966; Andrews *et al.*, 1967; Chisholm, 1967; Beggs, 1972) flows. However, the majority of the empirical and semi-theoretical correlations failed to predict their data. Therefore, Spedding *et al.* (1982) concluded that it will be extremely difficult to develop a general purpose two-phase frictional pressure loss model because of its heavy dependence on prevailing flow regime.

Mukherjee and Brill (1985) developed pressure drop correlations for inclined two-phase flow by analyzing data for an inverted, 38-mm inner diameter U-shaped steel pipe, the closed end of which could be raised or lowered to any angle from zero to 90 degrees

from horizontal. Kerosene and lube oil were the fluids used for the liquid phase in the experiments at temperatures between -7.8 and 55.6°C . The type of flow and flow pattern present influenced the frictional pressure gradient. The friction factor from the Moody diagram for bubble and slug flow was adequate for the frictional pressure drop, while a momentum balance assuming a smooth gas-liquid interface was more effective for downhill stratified flow. For annular-mist flow, the friction factor was found to be a function of the holdup ratio, otherwise known as the ratio between the volume fraction and liquid holdup, and the no-slip Moody friction factor.

Lips and Meyer (2012) more recently studied the effect of inclination angle on pressure drops under the same operating conditions as their heat transfer experiments. Void fraction was also studied to predict momentum and gravitational pressure drops. An increase in inclination angle resulted in an increase in gravitational pressure drop, an outcome more apparent at lower vapor qualities. The experimental pressure drops resulting from downward, slightly inclined flows were successfully predicted by the model of Taitel and Dukler (1976), but only for stratified flows.

Empirical models are common because of the ease of application and accurate results. However, these models are designed for specific ranges, restricting their applicability. A phenomenological approach is sometimes taken to account for interfacial characteristics, allowing for the possibility of general models to be developed. Unfortunately, most phenomenological models are applicable only for individual flow patterns or structures (Quiben and Thome, 2007). Therefore, a reliable flow pattern map that can successfully predict flow regime transitions is essential to implement a phenomenological model.

A two-phase frictional phenomenological model for pressure drop in horizontal flows that took into account the interfacial characteristics between the phases was developed by Quiben and Thome (2007) based on 1,745 data points. The experiment consisted of flows at mass fluxes between 150 and 600 kg m⁻² s⁻¹ in 8.0- and 13.8-mm diameter pipes for heat fluxes ranging from 7.5 to 57.5 kW m⁻². Although this correlation was developed for evaporating flows, the flow regimes studied are similar to those expected in ACCs.

Müller-Steinhagen and Heck (1986) compiled a data bank consisting of 9,313 measurements of frictional pressure drop, with about two thirds of the points from the data bank of Dukler (1962) and the rest from a data bank assembled by the Institut für Thermische Verfahrenstechnik (TVT). The data bank covers data for horizontal, vertically upwards and downwards flow in tubes between 5 and 392 mm and working fluids air-water, hydrocarbons, air-oil, steam-water, argon-water, R11-R11, R12-R12, R22-R22, neon-neon, and air-water-CMC systems. The predictions of fifteen frictional pressure drop correlations, including the one developed by Müller-Steinhagen and Heck (1986), were compared with the compiled data banks. From this comparison with other models, Müller-Steinhagen and Heck (1986) concluded that the phenomenological correlation developed by Bandel (1973) had the best agreement and their own convenient model performed next best, with average relative errors of 32.6% and 41.9%, respectively. The correlation of Bandel (1973) proposes calculating flow transition pressure drop by interpolating between stratified and annular flow, a complicated process that requires the prediction of critical mass fluxes. However, Müller-Steinhagen and Heck (1986) point out that predictions are far from

satisfactory, with the correlation of Bandel (1973) only able to predict 59.9% of the frictional pressure drop values within 30%.

The pressure drop prediction methods described above are summarized in Table 2.2.

Table 2.2 Summary of Some Available Frictional Pressure Drop Studies

Author(s) (Year)	Approach	Working Fluids	Tube Orientation	D_i (mm)	Range of Applicability
Bandel (1973)	Phenomenological	R-11, R-12, R-22	Horizontal	14	$-10 < T_{\text{sat}} < 10^\circ\text{C}$
Cavallini <i>et al.</i> (2001)	Empirical, adiabatic	R-134a, R-125, R-236ea, R-32, R-410A, HCFC-22	Horizontal	8	$0.07 < P_r < 0.75$
Cavallini <i>et al.</i> (2002)	Empirical, adiabatic	R-22, R-134a, R-125, R-32, R-236ea, R-407C, R-410A	Horizontal	3 to 21	$100 < G < 750 \text{ kg m}^{-2} \text{ s}^{-1}$ $0 < x < 1$ $30 < T_{\text{sat}} < 50^\circ\text{C}$ $P_r < 0.75$
Chen <i>et al.</i> (2002)	Empirical	Ammonia, R-22, R-12, R-134a, R-404, R-407C, R410A, R-125, Air-water	Horizontal	1 to 10	$45 < G < 3,279 \text{ kg m}^{-2} \text{ s}^{-1}$ $0.0006 < x < 0.93$ $97.6 < P < 3,300 \text{ kPa}$
Chisholm (1967)	Empirical, adiabatic	Air-benzene, air-kerosene, air-water, air-oil	Horizontal	1.48 to 25.83	Annular or wavy flow
Friedel (1979)	Empirical, adiabatic	Air-water, air-oil, steam, R-11, R-12, R-22, R-113, N ₂ , NH ₃ , Ne, Na	Horizontal, Vertical	3 to 200	Annular flow
Lips and Meyer (2012)	Empirical, condensing	R-134a	Horizontal, Vertical, Inclined	8.38	$200 < G < 600 \text{ kg m}^{-2} \text{ s}^{-1}$ $0.1 < x < 0.9$ $T_{\text{sat}} = 50^\circ\text{C}$
Lockhart and Martinelli (1949)	Experimental, isothermal	Benzene, kerosene, water, oils	Horizontal	1.49 to 25.83	Annular or wavy flow
Mukherjee and Brill (1985)	Empirical, adiabatic	Kerosene, lube oil	Horizontal, Vertical, Inclined	38	$-7.8 < T_{\text{sat}} < 55.6^\circ\text{C}$
Müller-Steinhagen and Heck (1986)	Empirical	Air-water, hydrocarbons, air-oil, steam-water, argon-water, argon	Horizontal, Vertical	14.0 to 24.3	$50 < G < 2,490 \text{ kg m}^{-2} \text{ s}^{-1}$ $0.01 < x < 0.91$ $\text{Re}_{10} > 100$
Quiben and Thome (2007)	Phenomenological, evaporating	R-22, R-134a, R-410A	Horizontal	8, 13.8	$50 < G < 2,490 \text{ kg m}^{-2} \text{ s}^{-1}$

2.2 Air-Side Heat Transfer Enhancement Techniques

Heat transfer enhancement techniques are commonly applied to improve convective heat transfer, and are generally grouped into two categories: active or passive. Combinations of the two techniques are possible, referred to as a compound heat transfer augmentation. Active techniques require external power, and sometimes involve complex designs that make it difficult to provide power (Dewan *et al.*, 2004). Passive techniques, on the other hand, require no direct application of an external power source (Bergles, 2002). These techniques aim to increase the heat transfer area or heat transfer coefficient by mixing the flow, reducing boundary layer thickness, creating a secondary flow, or raising the turbulence intensity (Guo *et al.*, 1998). A listing of different available techniques for the two classifications is included in Table 2.3 (Bergles, 2002; Dewan *et al.*, 2004).

Table 2.3 List of various enhancement techniques grouped by classification

Active techniques	Passive techniques
Surface or fluid Vibration Electrostatic Fields Flow pulsation Variable roughness structures Jet impingement	Surface Roughness Flow disruption and swirl flow Channel curvature Re-entrant obstructions Secondary flows Fluid additives Extended surfaces

Although augmentation of heat transfer improves performance, this does not immediately translate into increased power plant efficiency due to a corresponding increase in air-side pressure drop. Care has to be taken to select the heat transfer augmentation technique that maximizes enhancement with minimal increases in pressure losses. Two of the more prominent enhancement techniques are discussed here: fins and vortex generating techniques, with a focus on vortex generating techniques for the development of auto-fluttering reeds, or AFRs.

2.2.1 Fins

Finned surfaces are one common method to improve air-side heat transfer performance by increasing the overall heat transfer surface area and reducing the air-side thermal resistance. Tubes that the fins are a part of or attached to can be round, elliptical, flattened, or otherwise adjusted to minimize air-side flow resistance (Kröger, 1998). Round tubes are commonly used for industrial air-cooled systems because of their ease of manufacture and low cost (Kröger, 2004). Using elliptical or oval tubes instead of round tubes results in reduced air-side drag force as well as an increased tube-surface area for the same cross-sectional area. This results in higher compactness which leads to a reduced material cost, and a lower required fan power (Park and Jacobi, 2009). Even though circular tubes are stronger and can withstand higher pressures, ACCs operate at low enough pressures for oval tubes to be considered (Sohal and O'Brien, 2001). The history of using oval tubes for condensation can be traced back to the 1930s, when GEA Luftkuhler Gesellschaft in Germany produced an oval, air cooled fin design (Kröger, 2004).

Many combinations of tube and fin shape are possible depending on the industry and application. For example, GEA Group, a leading provider of ACCs, manufactures various fin tube bundle designs including flat steel tubes with brazed aluminum fins, round steel tubes with helical fins, and elliptical steel tubes with galvanized rectangular steel fins (GEA, 2012). Commonly used fins designs for air-cooled industrial heat exchangers include grooved– in or tightly wound aluminum fins, plate fins, louvered fins, dimpled fins, perforated plate fins, and others (Schulenberg, 1966; Kröger, 1998).

Finned tube heat exchangers are almost all made with various grades of carbon steel or aluminum. Due to severe corrosion between the fin and fin collar at a plant in Rugeley,

United Kingdom, there have been some concerns about aluminum tubes and fins. Bimetallic combinations of bonding aluminum to carbon steel have also resulted in problems, primarily in the process industry, but also at a power plant in Ibbenbüren, Germany, where the carbon steel tubes had expanded upon insertion into aluminum plates (Miliaras, 1974). Surveys and lab experiments conducted by Wheeler *et al.* (1982) on aluminum fins bonded with various tube materials show that corrosion was generally minimal at rural-arid, rural-humid, and industrial-arid conditions. They also noted that corrosion became a larger issue in industrial-humid locations where contaminants from coal dust could contribute to corrosion, as was the case in Ibbenbüren. Even though there may be some lingering concerns regarding corrosion, many power plants have chosen to construct ACCs out of flattened steel tubes with aluminum fins (Rathje and Pflaumbaum, 1996).

A majority of the heat transfer and pressure drop prediction models for wavy and louvered fins in the literature are presented in terms of j , the Colburn factor, and f , the friction factor. The Colburn factor, defined in Equation (2.8), is used to calculate the heat transfer coefficient. Pressure drops through the fins are calculated using the friction factor, f , and possibly other loss coefficients as specified by the investigators.

$$j = \frac{h}{\rho U C_p} Pr^{2/3} \quad (2.8)$$

Wavy, or herringbone, fin surfaces are a popular fin choice because of the increase in overall airflow length and heat transfer mixing as a result of interruptions in the boundary layer. Surface corrugations on the wavy fins consist of simple-to-manufacture patterns such as triangles, sinusoids, or trapezoids. Many studies predicting the performance of wavy fins on round tubes are based on the database created by Beecher and Fagan (1987). They

used a single-fin passage model to experimentally investigate the effects of varying heat exchanger geometry, fin patterns, and air velocity on the air-side thermal performance of plate finned tube heat exchangers. This database provides the general trends, and can be used to derive enhancement factors that can be applied to account for different types of fin patterns.

Kim *et al.* (1997) used a multiple regression technique on a database of 41 wavy fins, which included the data of Beecher and Fagan (1987), to develop correlations for staggered and in-line arrays of circular tubes. The correlation developed for the staggered layout was able to predict 92 percent of the heat transfer data within 10 percent and 91 percent of the friction factor data within 15 percent. Wavy aluminum fins bonded to flattened aluminum clad steel tubes can also be used. This design, found to have good performance characteristics, may replace two or more rows of elliptical or round tubes (Nagel, 1994). Correlations to predict heat transfer and pressure drop performance of the wavy fins have been developed experimentally as well as through numerical or computational fluid dynamics simulations for all of the different wavy fin profiles.

Dong *et al.* (2010) experimentally and numerically investigated three different profiles (triangular, sinusoidal, and triangular rounded corner) of wavy fin and flat tube heat exchangers to optimize design. The three different profiles can be seen in Figure 2.1.

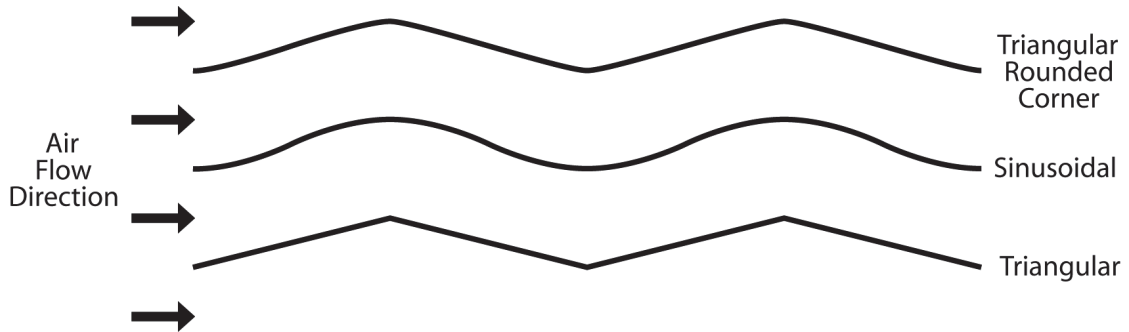


Figure 2.1 Triangular rounded corner, sinusoidal, and triangular wavy fin profiles

From their investigations, they found that although an increase in wave amplitude, the half distance between the highest and lowest points on the wave and denoted as M , resulted in an increase in heat transfer, waves with smaller amplitudes ($2M = 1.0 - 1.5 \text{ mm}$) at a constant Reynolds number result in a higher j to f ratio. While the triangular wavy fin has the highest friction factor when compared to the other two profiles at the same Reynolds number, the wavy profile had little impact on the j factor.

Many authors have investigated wavy fin heat exchanger performance through computational fluid dynamic (CFD) calculations. While 2D CFD simulations are valid when fin height is much larger than fin pitch, it is an idealization due to the neglect of span wise swirl flows (Khoshvaght Aliabadi *et al.*, 2014). Many CFD simulation studies on wavy channels have been conducted assuming 2D geometry (Yang *et al.*, 1997; Ničeno and Nobile, 2001; Comini *et al.*, 2003; Bahaidarah *et al.*, 2005), but some researchers have conducted 3D CFD simulations to predict wavy fin performance. Ismail *et al.* (2008) used “FLUENT” to simulate the impact of fin thickness, wavelength, curvature radius, amplitude, fin spacing, and fin height on the performance of 18 different wavy fin geometries to develop Colburn and friction factor correlations. From their studies, Ismail *et al.* (2008) found that the friction and Colburn factors decreased at higher Reynolds

numbers due to a decrease in the number of recirculation zones. To validate the results, j and f values from their correlation were compared with values from Kays and London (1984) and Ghosh (2004) and were found to vary by about 8 to 35% due to differences in the wavy fin curvature radius.

Khoshvaght Aliabadi *et al.* (2014) developed heat transfer and pressure drop correlations for three cooling fluids (air, water, and ethylene glycol) in wavy plate-fin heat exchangers. The fin pitch, wave length, fin thickness, wave amplitude, and fin length were all varied to yield 25 different models and 250 simulated data points to develop the correlation. The model predicted approximately 95% of the experimental data points obtained by Junqi *et al.* (2007) within 12%.

Louvered surfaces, in use since the 1950s and simple to manufacture, are used to interrupt the flow and break up the thermal boundary layer to enhance heat transfer (Chang and Wang, 1997). Heat exchangers with flat tubes and multilouver fins are common in air-cooling applications due to compactness, and the reduced material and required fan power (Park and Jacobi, 2009). Flow through the louvered fins can be categorized as “duct” flow at lower flow rates due to the thicker boundary layers that develop, which restrict the flow within the louver gaps. As flow velocity increases, boundary layers thin, allowing the flow to follow the louver paths. Typical flat-tube multilouver heat exchangers have many air-side and tube-side geometric parameters that can influence performance, therefore large databanks are necessary to develop accurate air-side performance correlations.

Kays and London (1984) were among the first to report heat transfer and pressure drop data for louvered fins, but the dimensions and designs of these fins do not cover several of those in use by industry today. Achaichia and Cowell (1988) and Davenport

(1983) investigated flow behavior in louvered heat exchangers and presented j and f in terms of Reynolds number. Aoki *et al.* (1989) developed sensing devices consisting of base metal, insulator, and nickel film, to measure the heat transfer coefficients of individual louvers in multilouver fin arrays with different louver angles, and louver and fin pitches. Locally averaged heat transfer coefficients for each individually heated louver were determined based on the power input into film and the temperature difference between the air and the element. Using this method, Aoki *et al.* (1989) clearly showed for the first time the differences in heat transfer coefficient upstream and downstream of the deflection louver at various fin pitches. Another advantage of using this measurement method is that only a few fins are needed to investigate the performance of the fins, instead of full-size heat exchangers. Webb and Trauger (1991) varied multiple geometric parameters and used a dye injection technique to visually determine their impact on flow structure for Reynolds numbers between 400 and 4,000. Data from this flow visualization study was presented in terms of flow efficiency, a relationship between the duct or boundary layer flow and the louver angle, versus the Reynolds number.

Analytical models have also been developed and further built upon to predict air-side louver fin performance. Sahnoun and Webb (1992) developed an analytical model based on boundary layer and channel flow equations that takes into account the flow efficiency, as defined by Webb and Trauger (1991). All parameters, including the louver depth, width, length, and angle, can be independently specified. Similarly, Dillen and Webb (1994) developed a semi-analytical correlation based on the different heat transfer and friction factor mechanisms at different regions along the fin surface. Results from the two analytical models were validated with the database of Davenport (1983)

Chang and Wang (1997) compiled a database that consisted of 91 samples of louvered fin heat exchangers from different researchers with different geometrical parameters such as louver angle, length, pitch, fin length and pitch to propose correlations for the Colburn factor and Fanning friction factor. While the heat transfer correlation was able to predict 89.3% of the louver fin data within $\pm 15\%$, a friction factor correlation was not presented due to an over 300% variation of the friction factors versus Reynolds number. Chang *et al.* (2000) continued the work from the previous study to develop a generalized friction factor correlation that it is able to predict 83.14% of the database within $\pm 15\%$. The friction factor correlation uses different expressions depending on the Reynolds number. However, at a Reynolds number of 150 (when the expressions switch from one to another), inconsistencies can occur. Improvements to this correlation were attempted by splitting the data into three regions ($Re \leq 130$, $130 < Re < 230$, $Re \geq 230$) instead of the previously proposed two. The amended correlation predicted 83.14% of the frictional data within $\pm 15\%$. Despite this predictive capability, the database of Chang and Wang (1997) does not include some current designs, limiting its range of applicability.

Some of the more recent investigations into the thermal-hydraulic performances of different louvered fins attempt to develop generalized correlations for the j and f factors. Dong *et al.* (2007) experimentally investigated 20 types of multilouver fin heat exchangers for air Reynolds numbers of 200-2,500. A total of 336 data points from tests, which included variations in geometric parameters such as fin pitch, height, length, thickness, and louver angle, were collected. The impact of each geometric parameter on heat transfer and pressure drop performances as a function of frontal air velocities, air-side Reynolds numbers based on louver pitch, and fan power, were compared. In general, changes to

either geometric parameter resulted in changes in the predicted Colburn and friction factors, where slight increases in both j and f are possible at a constant louver pitch Reynolds number with either a decrease in fin pitch or an increase in fin height. However, the changes in j and f were most noticeable for different fin lengths as functions of louver pitch Reynolds numbers and fan power. Based on these data, they developed generalized Colburn and friction factor correlations, which correlated 95% of the data within 10%.

Many of the heat transfer and friction factor correlations for louvered fins accurately predict the data that are from the respective investigations (Davenport, 1983; Achaichia and Cowell, 1988; Sahnoun and Webb, 1992; Chang and Wang, 1997; Kim and Bullard, 2002). However, some fail to predict data obtained from other labs for the same operating and geometric conditions (Park and Jacobi, 2009). To validate many of the empirical correlations currently available in literature, Park and Jacobi (2009) compiled any experimental data found in open literature into one database that can be used for the correlations. Comparisons of the j and f factors were made in two ways. The first was by calculating the percentage of the database the models predicted within a prescribed root mean square tolerance to assess the generality of each correlation, while the second was to calculate root mean square and mean errors of each correlation within subsets of the database and the composite database. In general, available correlations in literature failed to correlate data from other data sets, with biases possibly occurring due to narrow Reynolds- number ranges.

2.2.2 Vortex Generation

Vortex generation is a passive technique that enhances heat transfer without a significant increase in pressure drop. Wings and winglets, seen in Figure 2.2, as well as other vortex generators, are often placed in the flow path to interrupt the flow and generate vortices in addition to the naturally occurring vortices from flow and tube interaction (Jacobi and Shah, 1995).

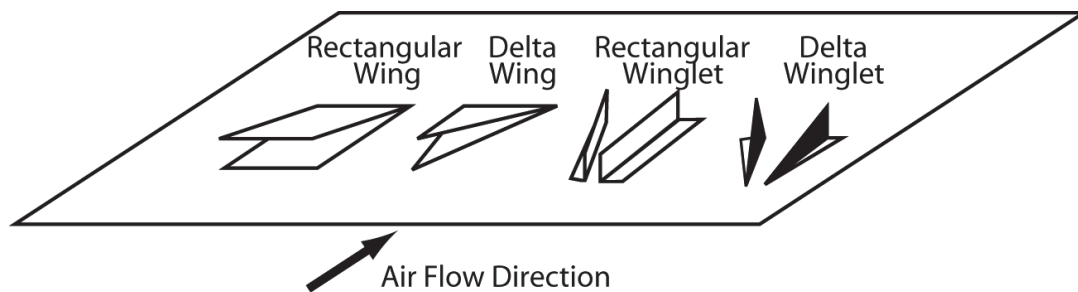


Figure 2.2 Common wing and winglet designs for vortex generation

Triangular (delta) or rectangular plates can be mounted onto the fins, or punched or bent from the fins, to project into the flow at some attack angle (Fiebig *et al.*, 1991). Vortex characteristics are influenced by the shape, size, and position of the generators relative to the condensation tubes. Many experimental studies that compare the performance of different shapes of wings and winglets in flat plate and channel flows have been conducted.

Depending on the winglet placement and the tube layout, studies have shown that it is possible to increase the heat transfer coefficient by 10 to 60%, with increases in friction factor of only 10 to 20% (Fiebig *et al.*, 1991; Mitra and Fiebig, 1994; Sohal and O'Brien, 2001; Pesteei *et al.*, 2005). Modifications in the winglet pair combined with different tube configurations can also lead to heat transfer enhancements of up to 30% with reductions in pressure drop of -15 to -8% (Torii *et al.*, 2002).

Many modern heat sinks are compact with high aspect ratio fin channels. Heat transfer in these heat sinks is limited by the temperature gradient in the thermal boundary layer and by the mixing of the heated air with the core flow. Common methods of overcoming those limitations are increasing the fin density to increase the surface area or increasing the flow Reynolds number, which consequently lead to increases in pressure drop and required fan power.

Synthetic jets, formed by vertical structure pairs that result from periodic suction and ejection of the ambient fluid out of an orifice, are jets that do not introduce mass into the system, and can be used to direct airflow across heated surfaces (Smith and Glezer, 1998). Mahalingam and Glezer (2005) designed a synthetic jet ejector heat sink that entrains cool, ambient air from a high momentum synthetic jet, created by pressure variations induced by electromagnetic actuators, to drive a secondary jet through the channels between the fins. A comparison between the thermal performances of the synthetic jets and fan flow through the channels showed that the synthetic jets were able to dissipate 20-40% more power than the fan for flows between 3 and 5 CFM. Similarly, the heat transfer coefficients for the case with the synthetic jets were found to be about 2.5 times (about $60 \text{ W m}^{-2} \text{ K}^{-1}$ versus $25 \text{ W m}^{-2} \text{ K}^{-1}$) higher than those achieved from a steady flow for the same Reynolds number due to the small-scale vortices and unsteadiness induced by the jets. These results showed that synthetic jets are a viable option for enhanced heat dissipation at low flow rates.

Gerty (2008) investigated flow patterns in forced convection heat transfer for steady and cantilevered, piezoelectric reed-augmented flows in channels. He found that steady flows, i.e., flow of bulk air through the channel without any reeds, had a steady increase in

surface thermal resistance and resulted in a not as uniform temperature distribution at the exit of the channel than the reed-augmented flow, suggesting that the reed-augmented flow induced mixing of the heated air with the core flow. On the other hand, he found that reed-augmented flows, i.e., bulk air flow with reeds in the channel, disrupted the thermal boundary layer that limits the heat transfer at the surface, resulting in up to a 30% higher exhaust air temperature and up to a 43% decrease in the surface thermal resistance when compared to that of the steady flow, depending on the air flow rate.

Hidalgo *et al.* (2010) investigated enhanced heat transfer and fluid mechanics associated with small-scale motions induced by 19 mm by 25 mm, cantilevered piezoelectric vibrating reeds. The cooling performance of the reeds was quantified based on two sets of measurements conducted in a high-power heat sink with an integrated blower. The first set involved maintaining a constant power to the sidewalls and comparing the wall temperature with the reed to the case without the reed to determine the local heat transfer enhancement. The second set was to quantify the increment in heat dissipation with the reed by adjusting the flow rate of the case without the reed to match the power dissipated when the reed was present. Assuming the same total fluid power (defined as the product of the fluid flow rate and the pressure drop), Hidalgo *et al.* (2010) found that the actuated flow from the reeds resulted in a 42% increase in the heat transfer coefficient over the baseline flow (without reeds) at half the flow rate. Additionally, the total power invested into the flow had to increase nearly 2.9 times for the case without the reed to match the heat transfer coefficient from the actuated flow case. From these results, it was concluded that the fluttering reeds could enhance the efficiency of high-power heat sinks without increases in the fluid flow rate or fin density.

While both synthetic jet actuators and piezoelectric vibrating reeds can enhance heat transfer in channels, these methods require device power consumption. Additionally, the reeds attached to the piezoelectric drivers have a wide profile, leading to increased pressure drops. Herrault *et al.* (2012) developed MEMs fabricated reed actuators that are flow powered and self-oscillating; thus, no power input or circuitry is needed. Flowing air forces the reeds to vibrate, inducing a flag-like motion and vortex shedding that interrupts the thermal boundary layers and enhances mixing with the core flow. A MEMs fabricated heat transfer channel was also designed such that the conductive and convective heat transfer performances could be decoupled and the reed performance could be identified. Pressure drop and heat transfer measurements were taken for flows with and without the reeds. While the presence of reeds increased the pressure drop, they found that the pressure drop due to the self-oscillating reeds was approximately two times lower than that for the piezoelectric vibrating reeds (Hidalgo *et al.*, 2010). Heat transfer was also enhanced by 60% using the self-oscillating reeds, showing the potential of this technology for application in air-cooled heat exchangers.

Self-oscillating fluttering reeds driven by air-flow, or aeroelastically fluttering reeds, were investigated by Hidalgo and Glezer (2015) in a single channel where the length could be varied between 62 and 186 mm and also in a 23 channel heat sink. The 24.4 mm long by 9 mm wide reeds were fabricated from 25 and 38 μm thick polyester sheets and positioned in the channels such that the longer side aligned with the cooling air, and the flow Reynolds number was varied from 2,000 to 5,100. Experimental results show that the flow rate of the air in the single channel with no reed has to be 2.1 greater than the flow rate when the reed is present to match some given power dissipation and fin surface

temperature, increasing the pressure drop by nearly 2.9 times. This behavior was similarly observed in the 23 channel heat sink, with results varying slightly because of differences in the way the reeds were installed in the channels.

Additional investigations of aeroelastically fluttering reeds in a single channel test bed and a five channel heat sink were conducted by Hidalgo *et al.* (2015). The heat flux into the single channel was set such that the maximum temperature difference between the inlet air and the wall was 60°C for any flow rate ($2,000 < Re < 10,000$). Measurements from this experiment indicate that the rate of increase of the Nusselt number versus Reynolds number is significantly higher for the situation when reeds are present, suggesting that the small vortices induced by the reeds enhances the heat transfer between the reed and the flow. Measurements showed that the Nusselt numbers with the reeds are 178, 182, and 181 percent greater than the values for channels without the reeds for Reynolds numbers of 2000, 4000, and 6000, respectively. A similar investigation with a maximum fin wall temperature (80°C) over a range of Reynolds numbers was conducted on reeds in a five channel heat sink. Results show that the Nusselt number enhancement due to the reeds ranged from 53% to 69% for Reynolds numbers of 4,000 and 1,600, respectively.

Investigations of this oscillating reed technology are ongoing, and data obtained from experimental work involving the AFRs are implemented into the model developed in this study to predict the resulting air-side enhancement, and therefore any potential improvement in plant performance.

2.3 Summary

The above discussion of the literature focuses on phenomena related to the prediction of the performance of an ACC for power generation. Many two-phase heat

transfer and pressure drop performance prediction models are available, for a range of inclination angles, mass fluxes, fluids, saturation temperatures and pressures, and channel sizes. For the purposes of the present study, models developed for vertical or inclined flows are better suited to predict performance than models for horizontal flows. However, the channels of interest for the present study generally have larger hydraulic diameters and fluid flow at lower mass fluxes than the range of applicability of geometric parameters for the majority of the correlations discussed above. Therefore, despite the large number of studies on heat transfer and pressure drop performance in inclined and vertical flows, the reliability of the resulting correlations in predicting condensation at these much lower mass fluxes and larger diameter channels is not expected to be very high.

One drawback to the installation of ACCs is the high air-side thermal resistance. Passive air-side enhancement techniques such as fins and vortex generating devices have been investigated in the literature for the reduction of air-side resistance. Finned tube material choice also affects heat transfer performance, with common choices being steel or aluminum. Wavy and louvered fin prediction models for many combinations of fin dimensions are available in literature for the flow rates expected in the present study ($Re \sim 1,000$), with some developed for rectangular tubes of interest in the present study. Even though the fin height, spacing, and thickness used in the present study were included in databases used to develop the air-side correlations discussed above, the tube or channel depth for the ACC in the present study is about 3 to 4 times greater (about 165 mm compared to 40-60 mm) than the depths investigated in the literature. The flow length in the present investigation leads to further development of the flow, resulting in lower average heat transfer coefficients. While there are many models that can be used to predict

the air-side performance, there are many fin dimensions that have to be considered, making it difficult to have reliable, general use correlations.

Another aspect in the modeling of air-cooled condensers in power plants is the flow direction of the air entering the fin channels. Air in the ACC investigated here exits the fan and turns to enter the fin channels at an angle, leading to maldistribution and non-uniform entry of the air into the fin bank, which will affect the heat transfer and pressure drop. Modeling of possible enhancements from the AFRs in the present study might also not be as accurate as desired because of the lower baseline air flow rate ($Re \sim 1,000$) in this study than that needed to induce oscillation of the reeds to generate the vortices.

Steam and air-side performance prediction correlations used for the ACC models in the present study are discussed in Chapter 3.

CHAPTER 3: MODELING

To develop the air-cooled steam condensers for the power plant application under consideration here, a segmented air-cooled condenser model, as well as cycle models comparing coal-fired and combined power plant configurations were developed on the Engineering Equation Solver software (Klein, 2015) platform.

3.1 Segmented Condenser Model

The baseline condenser geometry modeled here is representative of A-frame condensers used in dry-cooled power plants. Each condenser unit has a width of 12.2 m and carbon steel tubes of length 10.67 m to form an A-frame shape with an apex angle of 60 degrees.

3.1.1 Tube-side Modeling

Each tube has an elongated, rounded rectangular $190.5 \text{ mm} \times 25.4 \text{ mm}$ cross-section and a wall thickness of 1.27 mm (Acharya *et al.*, 2013). A cross-sectional view of a single tube with attached fins is shown in Figure 3.1.

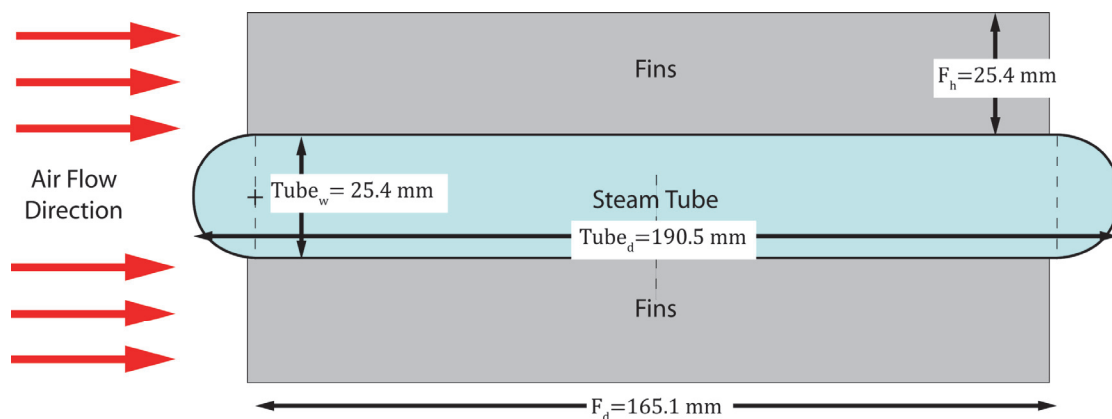


Figure 3.1 Top view and key dimensions of the steam tube and attached fins

The relevant baseline geometry parameters and operating conditions are summarized in Table 3.1 and 3.2.

Table 3.1 Summary of baseline geometry dimensions

Condenser		Tube		Fin			
ACC_w	12.2 m	$Tube_d$	190.5 mm	F_h	25.4 mm	F_t	0.254 mm
ACC_h	10.67 m	$Tube_w$	25.4 mm	F_s	2.54 mm	F_d	165.1 mm
β	60°	$Tube_t$	1.27 mm				

Table 3.2 Summary of operating conditions

Operating Conditions	
\dot{m}_{steam} (per ACC)	7 kg s ⁻¹
\dot{m}_{air} (per fan)	645 kg s ⁻¹
$P_{air,in}$	101.3 kPa
$T_{air,in}$	30°C
$\phi_{ambient}$	0.25

The tube pitch, a function of the fin channel height and tube width, influences the total number of tubes in the condenser, and therefore the total outside surface area. Equations (3.1) to (3.4) were used to compute the tube pitch, number of tubes, and the surface area inside the tube.

$$Tube_p = 2 \times F_h + Tube_w \quad (3.1)$$

With a fin height of 25.4 mm and a tube width of 25.4 mm, this yields a tube pitch of 76.2 mm. The tube pitch calculated using Equation (3.2) was used to calculate the total number of tubes in the ACC, taking into account the two faces through which the cooling air flows by multiplying the ACC width by two.

$$Num_{tube} = \frac{2 \times ACC_w}{Tube_p} \quad (3.2)$$

With an ACC width of 12.2 m and the calculated tube pitch of 76.2 mm, the total number of tubes that make up the two ACC faces is 320. The cross sectional area of each

elongated, rectangular tube is calculated using the tube depth, tube thickness, and tube width.

$$A_{tube,cs} = \frac{\pi}{4}(Tube_w - 2Tube_t)^2 + (Tube_d - Tube_w)(Tube_w - 2Tube_t) \quad (3.3)$$

Values of 190.5 mm, 1.27 mm, and 25.4 mm for the tube depth, thickness, and width, respectively, result in a cross sectional tube area of 4,185 mm² for a single tube. The inner surface area is calculated based on the ACC height, tube depth, width, and thickness.

$$A_{tube,in} = ACC_h \times [2 \times (Tube_d - Tube_w) + \pi(Tube_w - 2Tube_t)] \quad (3.4)$$

A 12.2 m ACC height, 190.5 mm tube depth, 25.4 mm tube width, and 1.27 mm tube thickness yields an internal tube surface area of 4.289 m².

The mass flow rate per tube was calculated by dividing the total steam mass flow rate per condenser module by the total number of tubes. To implement performance prediction correlations and to compute the necessary Reynolds numbers, the steam tube hydraulic diameter is defined by Equation (3.5).

$$D_{hy,tube} = \frac{4 \times A_{tube,cs}}{2 \times (Tube_d - Tube_w) + \pi(Tube_w - 2Tube_t)} \quad (3.5)$$

The 190.5 mm tube depth, 25.4 mm tube width, 1.27 mm tube thickness, and 4,185 mm² tube cross sectional area results in a tube hydraulic diameter of 41.64 mm.

Figure 3.2 shows a section of a single tube with steam assumed to flow downward and air assumed to be flowing into the page. Each flattened tube consists of a set of fins on each side. To simplify the area calculations, the fins were assumed to be rectangular. The number of fins, which can be calculated using the fin pitch, and other fin area calculations are shown in Equations (3.6) to (3.11).

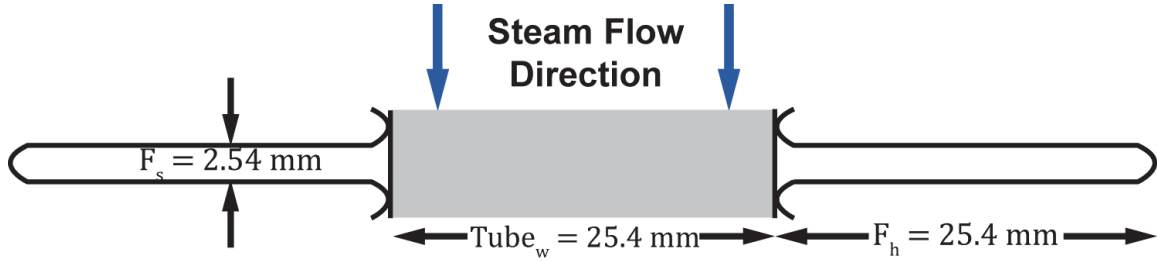


Figure 3.2 View of a single tube assuming air flow into the page

The fin pitch is calculated based on the fin thickness and fin spacing, as shown in Equation (3.6).

$$F_p = 2 \times F_t + F_s \quad (3.6)$$

A fin thickness of 0.254 mm and a fin spacing of 2.54 mm results in a fin pitch of 2.794 mm. The fin pitch is then used to calculate the number of fins on one side of each tube, as expressed in Equation (3.7).

$$Num_{fin} = \frac{ACC_h}{F_p} \quad (3.7)$$

The fin pitch of 2.794 mm and tube height, equivalent to the ACC height of 10.67 m, yields 3,818 fins per one side of a tube. The surface area of each fin exposed to the air is based on the fin height, fin depth, and fin thickness and calculated using the following equation.

$$A_{fin} = (2 \times F_h \times F_d) + (2 \times F_h \times F_t) \quad (3.8)$$

With a fin height of 25.4 mm, fin depth of 165.1 mm, and a fin thickness of 0.254 mm, the resulting fin area is 8,400 mm². The cross sectional area of a single fin in contact with the tube surface is calculated using Equation (3.9).

$$A_{fin,cs} = F_d \times F_t \quad (3.9)$$

A fin depth of 165.1 mm and fin thickness of 0.254 mm yields a cross sectional area of 41.94 mm² for a single fin. The fin cross sectional area in contact with the tube is calculated by doubling the total number of fins on a single side of the tube and multiplying the corresponding value by the single fin cross sectional area from Equation (3.9).

$$A_{fin,base,tube} = 2 \times Num_{fin} \times A_{fin,cs} \quad (3.10)$$

With 3,818 fins per side of the tube and an individual fin cross sectional area of 41.94 mm², the resulting total contact area between the fins and the tube is 0.3202 m². The total fin surface area per tube is calculated in a manner similar to the calculation of the total cross sectional fin area, but based on the single fin surface area instead.

$$A_{fin,tube} = 2 \times Num_{fin} \times A_{fin} \quad (3.11)$$

With 3,818 fins per side of the tube and a single fin surface area of 8,400 mm², the resulting total fin surface area on a single tube is 64.14 m². Other calculated areas, such as the frontal area, tube bare area, and overall outer surface area, are defined in Equations (3.12) to (3.15). The total frontal area of the ACC is based on the height and width of the two faces through which the air flows.

$$A_{fr} = 2 \times ACC_h \times ACC_w \quad (3.12)$$

With an ACC height and width of 10.67 m and 12.2 m, respectively, the total frontal area of the ACC is 260.3 m². The area of each tube that is not covered by fins, dependent on the ACC height, tube depth, tube width, and the total area of the tube in contact with the tube, is calculated according to Equation (3.13).

$$A_{tube,bare} = ACC_h \times [2 \times (Tube_d - Tube_w) + \pi(Tube_w)] - A_{fin,base,tube} \quad (3.13)$$

With an ACC height of 10.67 m, tube depth of 190.5 mm, tube width of 25.4 mm, and 0.3202 m² of the tube covered by fins, the total area of a tube that is not covered by

fins is 4.05 m². The outside surface area of each tube is calculated by summing the bare tube area with the total fin surface area per tube.

$$A_{os,tube} = A_{tube,bare} + A_{fin,tube} \quad (3.14)$$

The sum of the 4.05 m² bare tube area with the 64.14 m² fin outer surface area results in an overall outer surface area of 68.2 m² per finned tube. The total outer surface area of the finned tubes in the ACC is then determined by multiplying the result from Equation (3.14) with the total number of tubes in the ACC.

$$A_{os,total} = A_{os,tube} \times Num_{tube} \quad (3.15)$$

With an outer surface area of 68.2 m² per finned tube and a total of 320 tubes, the total outer surface area for the ACC is 21,823 m². Fin efficiency, as well as the overall surface efficiency, were computed using Equations (3.16) to (3.19). The fin efficiency was also used to calculate the effective heat transfer area of a tube and the associated fins. Variables used to calculate the fin efficiency include the fin perimeter, air-side heat transfer coefficient, thermal conductivity of the wall, and the fin cross sectional area.

$$m_{fin} = \sqrt{\frac{F_{per} h_{air}}{k_{wall} A_{cs,fin}}} \quad (3.16)$$

A fin perimeter of 0.3307 m, wall thermal conductivity of 60 W m⁻¹ K⁻¹, fin cross sectional area of 41.94 mm² for a single fin, and a calculated air-side heat transfer coefficient of 38.36 W m⁻² K⁻¹ for the baseline smooth fin configuration, and fin height of 25.4 mm yields $m = 40.99 \text{ m}^{-1}$. This is in turn used to compute the fin efficiency as follows.

$$\eta_{fin} = \frac{\tanh(m_{fin} F_h)}{(m_{fin} F_h)} \quad (3.17)$$

With $m = 40.99 \text{ m}^{-1}$ and a fin height of 25.4 mm, the resulting fin efficiency is 0.75. The fin efficiency, in conjunction with the fin area, overall finned tube surface area, and total number of fins, is used to calculate the overall surface efficiency.

$$\eta_{overall} = 1 - \frac{(2 \times Num_{fin}) A_{fin} (1 - \eta_{fin})}{A_{os,tube}} \quad (3.18)$$

The overall surface efficiency, with 3,818 fins per tube side, a fin area of 8,400 mm^2 , an overall outer surface area of 68.2 m^2 per finned tube, and fin efficiency of 0.75 is calculated to be 0.7625. The effective area for a single tube is the sum of the base tube area and the product of the fin area per tube and fin efficiency.

$$A_{eff} = A_{tube,bare} + \eta_{fin} \times A_{fin,tube} \quad (3.19)$$

A bare tube area of 4.05 m^2 , fin efficiency of 0.75, and total fin area on a single tube of 64.14 m^2 , yields an effective single tube surface area of 52 m^2 .

The total free flow area is calculated using Equation (3.21) by determining the total number of channels, or gaps between the fins, and multiplying it by the area of an individual channel.

$$Num_{channel} = 2 \times \left(\frac{ACC_h}{F_s} \right) \times \left(\frac{2 \times ACC_w}{2F_h + Tube_w} \right) \quad (3.20)$$

The total number of channels for this ACC, calculated in the previous equation assuming an ACC height of 10.67 m, ACC width of 12.2 m, fin spacing of 2.54 mm, and fin height and tube width of 25.4 mm, is 2.44×10^6 .

$$A_{ff} = Num_{channel} \times F_s \times F_h \quad (3.21)$$

Therefore, the free flow area of this ACC configuration with the 2.44×10^6 air channels with a fin spacing of 2.54 mm and fin height of 25.4 mm is 157.65 m².

A segmented approach was used to predict local performance along the length of an individual condenser tube. The number of nodes used for calculations is set, with the first and the final nodes corresponding to the inlet and outlet of the tube, respectively, resulting in one less heat transfer segment than the total number of nodes. This is shown schematically in Figure 3.3. In this view, the top and bottom green arrows correspond to the steam entering and exiting the ACC, respectively, and air flows from the left to right as indicated by the red arrow.

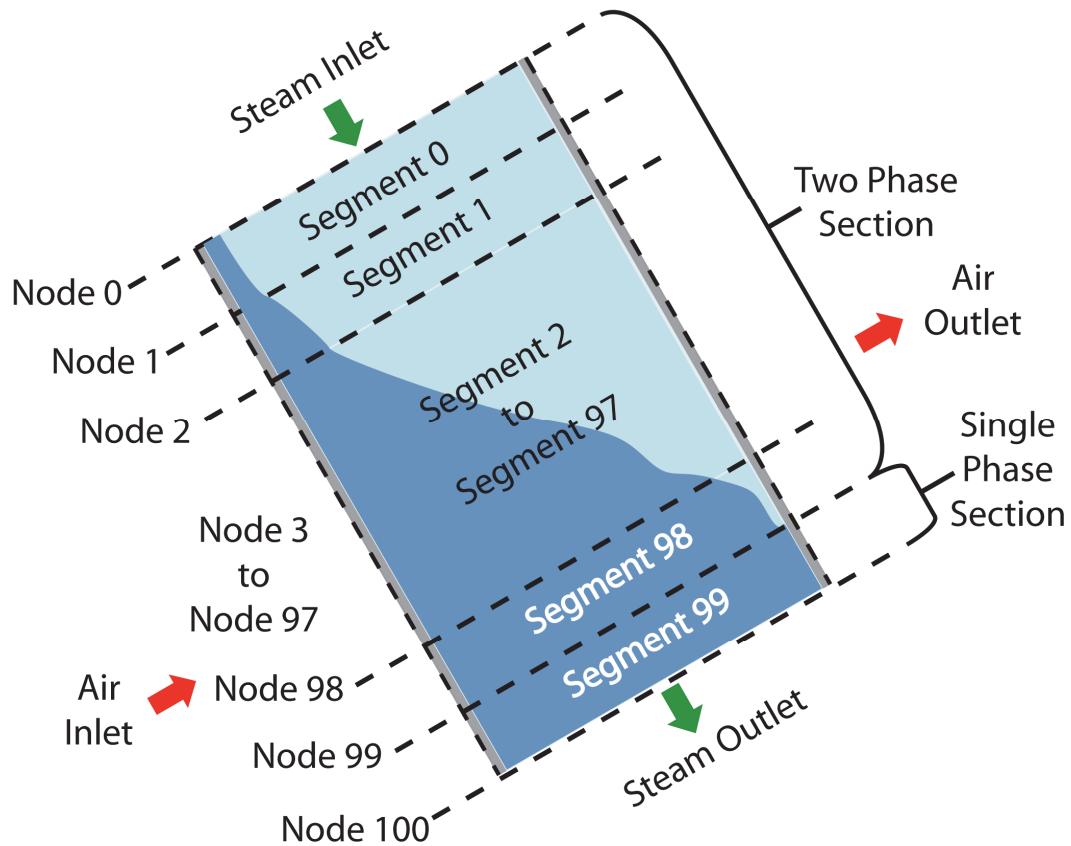


Figure 3.3 Schematic of the segmented model (100 nodes)

The first through the second-to-last segments are all equal in length and represent the portion of the condenser tube with two-phase flow. For the representative 100 node case in Figure 3.3, segments 0 to 98 correspond to the section of the condenser tube with two-phase flow. A term, denoted SP for section percent, reflects the ratio of each, individual two-phase segment (any segment from segment 0 to 98) length compared to the overall tube length. Another term, TPP for two-phase percent, represents the total fraction of the tube length that is two-phase. The final segment, segment 99 in this example, represents the section of the tube with subcooled liquid and differs in length from the preceding segments.

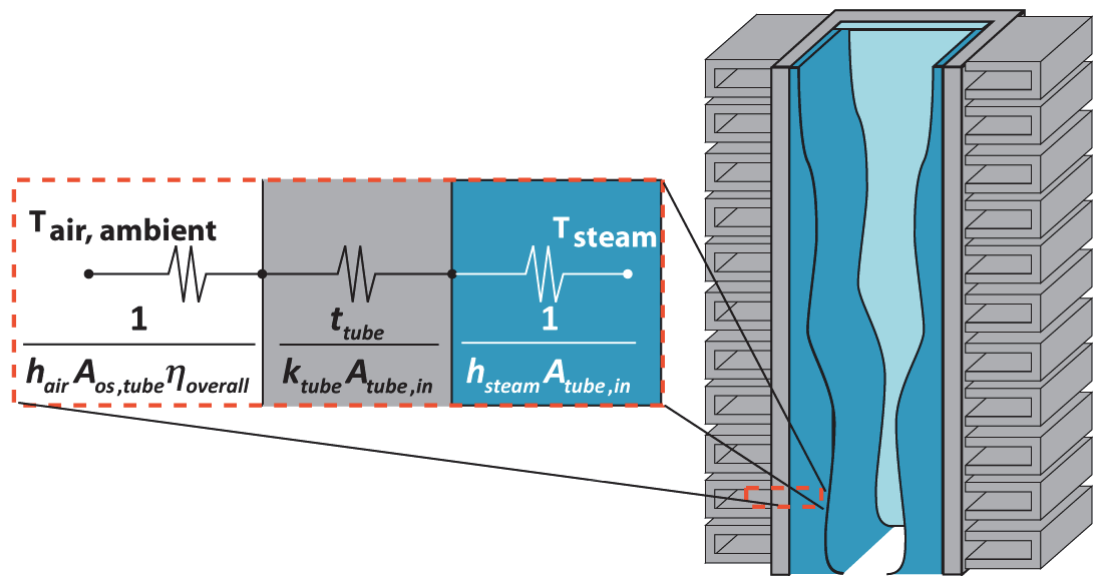


Figure 3.4 Schematic showing thermal resistances analyzed in the model

Fluid properties of the steam, assumed constant across individual segments, were calculated using the inlet steam pressure and quality and determined based on the database in EES. The UA-LMTD method was used to calculate the amount of heat transferred in each individual segment. The thermal resistances include convection on the air-side, conduction through the tube, and convection in the tube. The overall UA per segment,

which takes into account the overall surface efficiency, is shown in Equation (3.22), with the calculations of the heat transfer coefficients for the steam and air sides discussed in a subsequent section of this chapter. Equations (3.23) and (3.24) define the LMTD and the heat duty calculation per segment.

$$\frac{1}{UA_{seg}} = \frac{1}{h_{steam} A_{tube,in,total} SP} + \frac{Tube_t}{k_{tube} A_{tube,in,total} SP} + \frac{1}{h_{air} A_{os,total} \eta_{overall} SP} \quad (3.22)$$

$$LMTD_{seg} = \frac{(T_{steam,in} - T_{air,out}) - (T_{steam,out} - T_{air,in})}{\ln\left(\frac{T_{steam,in} - T_{air,out}}{T_{steam,out} - T_{air,in}}\right)} \quad (3.23)$$

$$Q_{seg} = UA_{seg} LMTD_{seg} \quad (3.24)$$

The indexing of key parameters in the model is shown in Figure 3.5.

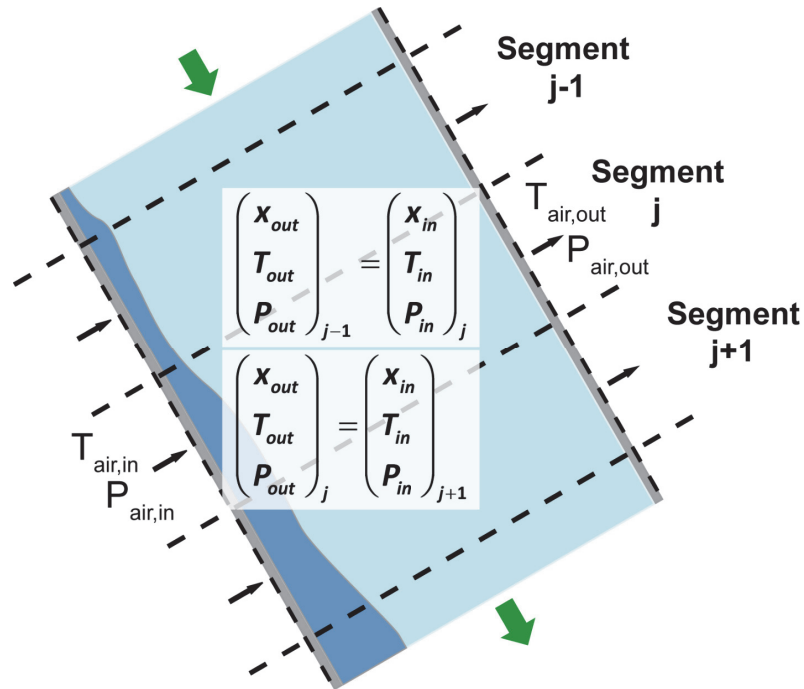


Figure 3.5 Schematic of individual condenser segment

Conservation of energy was applied to each segment, and the EES thermophysical property database was referenced to determine the outlet enthalpy of each segment.

Pressure losses in each segment were predicted using a trapezoidal integration method, described at a later point in this section. With both the enthalpy and pressure at the segment known, the segment outlet conditions are fully defined. These conditions are then used as the inlet conditions of the following segment, with the equation solver simultaneously solving all governing equations until all of the nodal conditions are determined. Energy balance equations over the segments are listed in Equations (3.25) and (3.26).

$$H_{air} \dot{m}_{air,seg} = H_{air,out,j} \dot{m}_{air,seg} - Q_j \quad (3.25)$$

$$H_{steam,j} \dot{m}_{steam,seg} = H_{steam,j+1} \dot{m}_{air,seg} + Q_j \quad (3.26)$$

Many correlations for predicting two phase heat transfer and pressure drop are available in literature, as evidenced by the discussion of this subject in Chapter 2. However, the majority of these studies were developed for flow orientations, tube diameters, and mass fluxes different from those typically seen in ACC operation. Local two-phase heat transfer performance in the steam tubes was predicted using the correlation of Akhavan-Behabadi *et al.* (2007) for inclined flows, which is dependent on the two-phase Martinelli parameter from Jung *et al.* (2003) and a model specific parameter, F_β .

$$X_{tt} = \left(\frac{1-x}{x} \right)^{0.90} \left(\frac{\rho_v}{\rho_l} \right)^{0.50} \left(\frac{\mu_l}{\mu_v} \right)^{0.10} \quad (3.27)$$

$$F_\beta = \frac{\left(1 + (1-x)^{0.2} \times \cos(\beta - 10^\circ) \right)}{x^{0.4}} \quad (3.28)$$

$$Nu = 1.09 Re_l^{0.45} F_\beta^{0.3} \sqrt{\frac{Pr_l}{X_{tt}}} \quad (3.29)$$

A trapezoidal integration approach was used to calculate steam-side pressure drop. The Blasius correlation was used to predict single-phase vapor friction factor and the void

fraction was calculated using a correlation developed by Lockhart and Martinelli (1949).

The Martinelli parameter was used to calculate the two-phase multiplier, Φ_L^2 , proposed by Chisholm (1967), where the values of coefficient C are listed in Table 3.3.

$$\alpha = \left[1 + 0.28 \left(\frac{1-x}{x} \right)^{0.64} \left(\frac{\rho_v}{\rho_l} \right)^{0.36} \left(\frac{\mu_l}{\mu_v} \right)^{0.07} \right]^{-1} \quad (3.30)$$

$$X_{tt} = \left(\frac{\rho_v}{\rho_l} \right)^{0.5} \left(\frac{\mu_l}{\mu_v} \right)^{0.125} \left(\frac{1-x}{x} \right)^{0.875} \quad (3.31)$$

$$\Phi_L^2 = 1 + \frac{C}{X_{tt}} + \frac{C}{X_{tt}^2} \quad (3.32)$$

Table 3.3 Summary of C values for Chisholm (1967)

Condition		C
$Re_L > 2,000$	$Re_v > 2,000$	20
$Re_L > 2,000$	$Re_v < 2,000$	10
$Re_L < 2,000$	$Re_v > 2,000$	12
$Re_L < 2,000$	$Re_v < 2,000$	5

The trapezoidal integration method was used to calculate the total pressure drop, where the nodes at each end of an individual segment were used as the endpoints of the integration and two multipliers, I_z and J_z , are needed to calculate the frictional and gravitational pressure drop components, respectively.

$$I_z = \frac{1}{2} \left[(f_v x_{out}^2 \Phi_v^2) + (f_v x_{in}^2 \Phi_v^2) \right] L_{seg} \quad (3.33)$$

$$J_z = \frac{1}{2} \left\{ ([1 - \alpha_{out}] \rho_l + \alpha_{out} \rho_v) + ([1 - \alpha_{in}] \rho_l + \alpha_{in} \rho_v) \right\} L_{seg} \quad (3.34)$$

The computed pressure drop for each segment is the sum of the terms shown in Equations (3.35), (3.36), and (3.37).

$$\Delta P_{fric} = \frac{2G^2}{\rho D} I_z \quad (3.35)$$

$$\Delta P_{grav} = g \sin(\gamma) J_z \quad (3.36)$$

$$\Delta P_{dec} = G^2 \left[\frac{x_{out}^2}{\rho_v \alpha_{out}} - \frac{(1-x_{out})^2}{\rho_l (1-\alpha_{out})} \right] - G^2 \left[\frac{x_{in}^2}{\rho_v \alpha_{in}} - \frac{(1-x_{in})^2}{\rho_l (1-\alpha_{in})} \right] \quad (3.37)$$

Excessive subcooling of the condensate is undesirable for plant efficiency, because it indicates excessive heat removal from the cycle without commensurate power generation (Putman *et al.*, 2000). The model developed here specifies a subcooling of 2°C. Calculations for the final, subcooled segment are conducted in a manner similar to that of each of the preceding two-phase segments, where the energy balance and thermal resistance equations are the same but with the subcooled segment length instead of the two-phase length. Also, the tube-side heat transfer and pressure drop were calculated using single-phase correlations instead of two-phase correlations, and the heat duty was determined using the epsilon-NTU method for two unmixed fluids in cross-flow (Equation (3.38)). Heat capacities for the ambient air as well as the water were found using EES, and their ratio, C_{rat} , was used to compute the number of transfer units, or NTU, as follows.

$$\varepsilon = 1 - \exp \left[\left(\frac{1}{C_{rat}} \right) (NTU)^{0.22} \left\{ \exp \left[-C_{rat} (NTU)^{0.78} \right] - 1 \right\} \right] \quad (3.38)$$

The relevant ACC module inputs for these calculations include the inlet air temperature, pressure, humidity, and overall flow rate of the air supplied by the fan. For the baseline operating condition of this study, steam at the condenser unit inlet was assumed to have a vapor quality of 0.95 and a flow rate of 7 kg s⁻¹, divided equally among all the tubes in the condenser.

3.1.2 Air-side Modeling

The condenser under consideration is equipped with an array of fins on each side of the tube, with different fin geometries considered to achieve optimal heat transfer configurations. The fins, which run the length of the tube, essentially form channels through which the air flows. These channels are idealized as rectangular ducts for the calculation of the fin perimeter and associated areas. Plain fins with a height of 25.4 mm, depth of 0.1651 m, thickness of 0.0254 mm, and pitch of 2.794 mm were used as a baseline for the initial analysis (Acharya *et al.*, 2013). Figure 3.6, based on a figure by Kröger (1998), and other figures similar to it discussed later in the chapter show the locations of minor losses associated with the A-frame ACC.

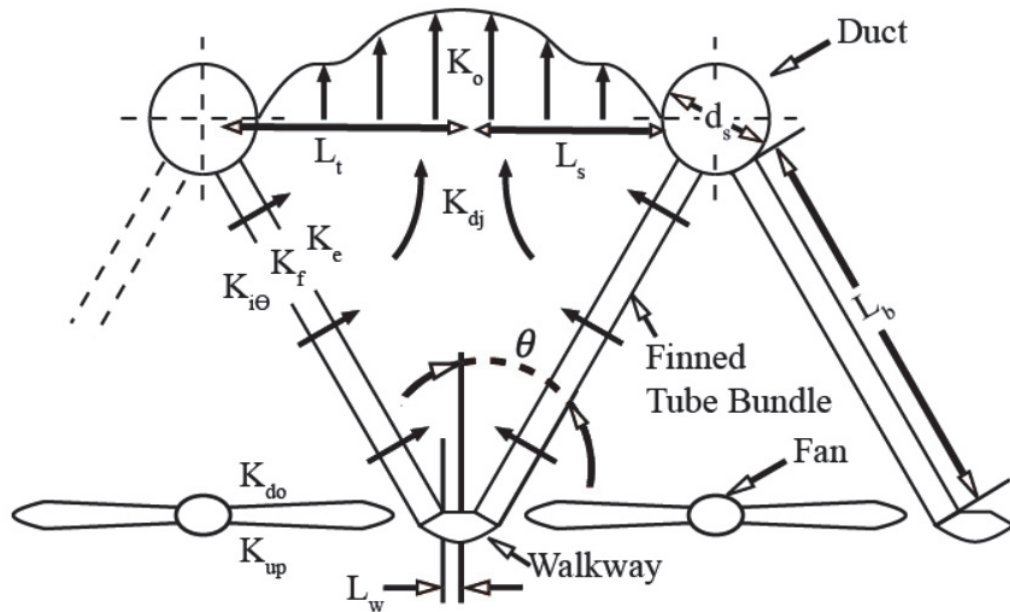


Figure 3.6 Location of minor losses on an A-Frame Air Cooled Condenser

The approach of Kröger (1998) was used to calculate the minor pressure losses that contribute to the total air-side pressure drop across the ACC. This approach accounts for resistances from upstream and downstream supports and screens, the fan velocity profile,

flow stream jetting downstream of the condenser, turning of the air flow at the inlet and outlet of the heat exchanger tubes, and pressure change due to temperature increase of the flow across the ACC module. The following discussion summarizes the minor loss calculations, and a more detailed analysis is provided in Appendix B.

The upstream loss coefficient, K_{up} , is the sum of the losses in the fan safety screen (si), and fan safety screen support beams (bi). Calculation of this loss is a function of the distance of each flow resistance element from the fan, fan casing diameter, projected blockage area by each obstruction, and the cross-sectional area of the fan inlet.

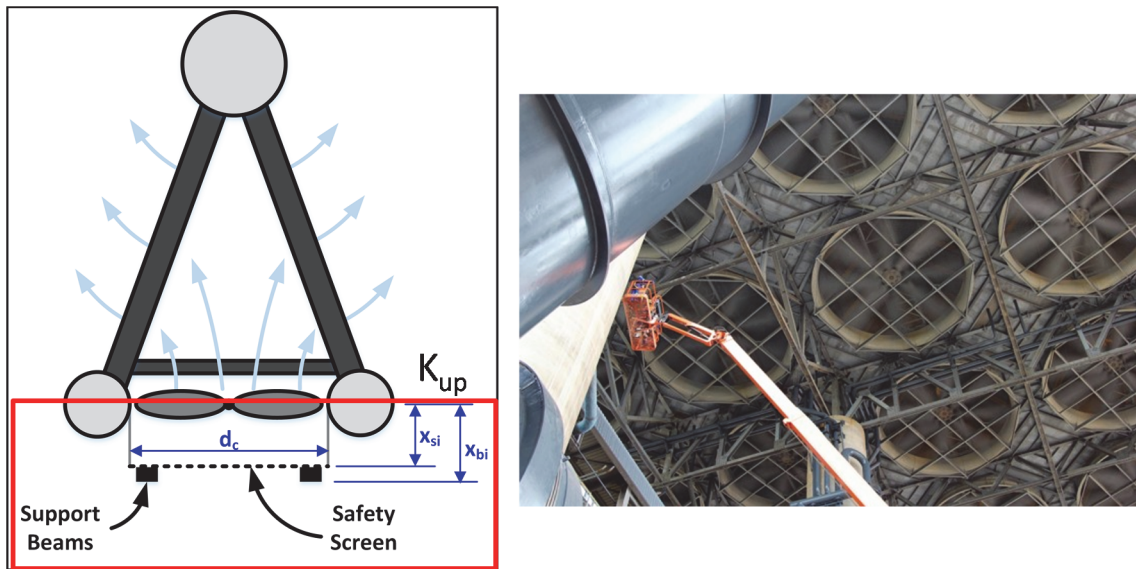


Figure 3.7 Minor losses upstream of the fan (Source: Stewart (2014))

To calculate the loss coefficients of each of the loss elements upstream of the fan, Kröger (1998) presented a plot that can be used given the ratio of the loss element size to the channel area, and the ratio of the distance of the loss element from the fan to the diameter of the fan. Losses from the fan safety screen (si) and fan safety screen support beams (bi), assumed to be 1.30 and 1.34 m away from the fan, respectively, were taken

into account. The interpretation of the plot presented by Kröger (1998) using the assumed loss element ratios, is shown in Appendix B.

The downstream loss coefficient consists of losses due to the walkway (s_o) and downstream support beams (b_o). Similar to the calculation of the upstream loss coefficient, calculation of the downstream loss coefficient is a function of the distance of each loss element from the fan, fan casing diameter, projected blockage area of each loss element, and the cross-sectional area of the fan.

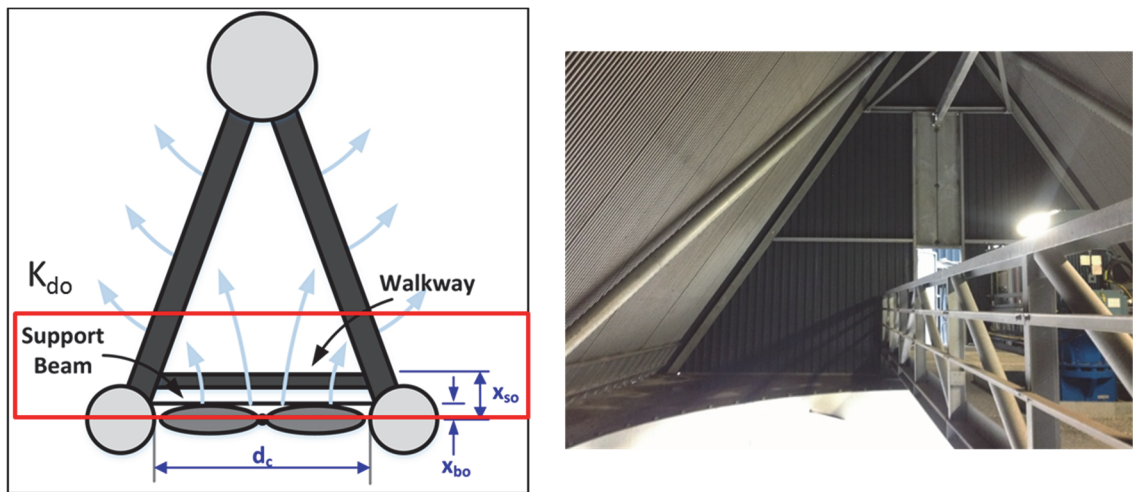


Figure 3.8 Minor losses downstream of the fan (Source: Accessories (-))

Another plot presented by Kröger (1998), shown in Appendix B, is used to determine the downstream loss coefficient. This plot is formatted similarly to the one for the upstream loss coefficient, where the loss coefficient is a function of the ratio between the loss element and fan casing areas, and the ratio of the distance from the fan to the fan casing diameter.

The air flow then experiences contraction losses and an angled flow pattern upstream and downstream of the air channels of the ACC.

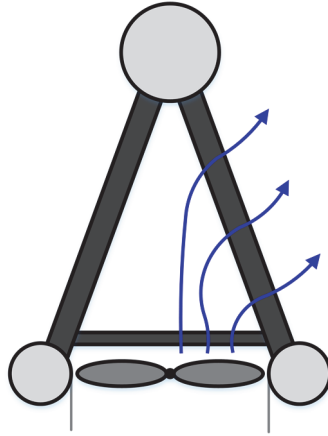


Figure 3.9 Air flow path from upstream of the fan through the air channels

Two different contraction ratios are needed to calculate the contraction loss coefficient, K_{ci} , which is needed in the computation of the angled inlet and outlet loss coefficients. The contraction ratio, σ , is a function of the total frontal area and the channel free flow area.

$$\sigma = \frac{A_{ff}}{A_{fr}} \quad (3.39)$$

With a baseline total ACC frontal area of 260.3 m² and a free flow area of 157.65 m², the contraction ratio is 0.606. The jetting contraction ratio, σ_c , is a function of σ and refers to the contraction of the air to the point of the vena contracta (where the diameter of the air stream is the least) inside the channel, as shown below.

$$\sigma_c = 0.61 + 0.05\sigma - 0.34\sigma^2 + 0.41\sigma^3 + 2.67\sigma^4 - 5.96\sigma^5 + 3.56\sigma^6 \quad (3.40)$$

The resulting jetting contraction ratio for this baseline case is 0.659. The inlet contraction loss coefficient, K_{ci} , is then found to be 0.733, based on the two calculated contraction ratio values, as shown in Equation (3.41).

$$K_{ci} = \left[\frac{1 - \frac{1}{\sigma_c}}{\sigma} \right]^2 \quad (3.41)$$

Angled inlet and outlet losses are also a function of the mean incidence angle, θ_m , which is typically less than the steam tube angle due to flow disturbances. An expression to calculate the mean incidence angle was presented by Kröger (1998) and is shown in Equation (3.42).

$$\theta_m = 0.0019\theta^2 + 0.913\theta - 3.156 \quad (3.42)$$

With a steam tube angle, θ , of 30° , the resulting mean incidence angle is 25.95° . The angled inlet and outlet loss coefficient, $K_{i,\theta,e}$, is a function of the air inlet and outlet density, mean incidence angle, contraction ratio and loss coefficient, tube pitch, and the tube height.

$$K_{i,\theta,e} = \frac{2}{\sigma^2} \left(\frac{\rho_{in} - \rho_{out}}{\rho_{in} + \rho_{out}} \right) + 2 \cdot \frac{\rho_{out}}{\rho_{in} + \rho_{out}} \cdot \left(\frac{1}{\sin(\theta_m)} - 1 \right) \cdot \left(\left(\frac{1}{\sin(\theta_m)} - 1 \right) + 2 \cdot K_{ci}^{0.5} \right) \cdot \left(\frac{Tube_p}{Tube_p - Tube_w} \right)^2 \quad (3.43)$$

With an inlet air density of 1.162 kg m^{-3} , outlet air density (determined based on calculations of the outlet air temperature of each segment) of 1.078 kg m^{-3} , contraction ratio of 0.6056, mean incidence angle of 25.95° , inlet contraction loss coefficient of 0.7329, tube pitch of 76.2 mm, and tube width of 25.4 mm, the resulting angled inlet and outlet loss coefficient is 8.545.

Upon exiting the bundle, the air experiences jetting losses, represented by the loss coefficient K_{dj} and labeled in Figure 3.10, due to turbulent decay of the jet near the air stream centerline and mixing of air streams from adjacent ACCs.

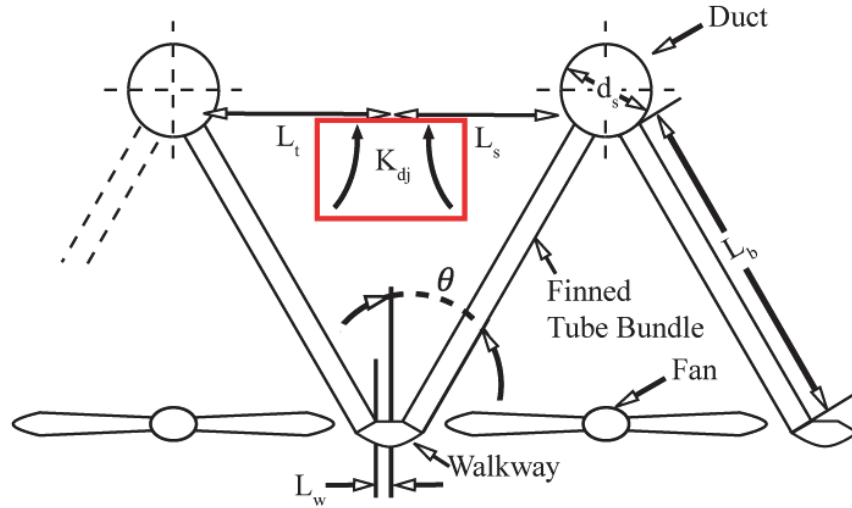


Figure 3.10 Jetting loss of the air located between adjacent ACC cells

The jetting loss, shown in Equation (3.44), is a function of the walkway width L_w , steam tube length L_b , half the distance between the condensate removal tube edges L_s , half the distance between condensate tube edges L_t , the length of the tube and walkway bend L_r , and the steam tube angle θ .

$$K_{dj} = \left[\left(-2.89 \left[\frac{L_w}{L_b} \right] + 2.93 \left[\frac{L_w}{L_b} \right]^2 \right) \left[\frac{L_b}{L_s} \right] \left[\frac{L_t}{L_s} \right] \left[\frac{28}{\theta} \right]^{0.4} \right]^2 + \left(e^{2.370+0.0586\theta-0.0034\theta^2} \left[\frac{L_s}{L_t} \right] \right)^{0.5} \left[\frac{L_b}{L_r} \right] \quad (3.44)$$

Values for the parameters necessary to calculate the jetting loss coefficient are shown in Table 3.4.

Table 3.4 Parameters associated with the jetting and outlet loss coefficient

Term	Definition	Value
L_w	Walkway Width	0.6096 m
L_b	Steam Tube Length	10.67 m
L_s	Half distance between condensate removal tube edges	5.004 m
L_t	Half distance between condensate tube edges	5.334 m
L_r	Length of tube and walkway bend	10.67 m
d_s	Inlet steam tube diameter	0.1524 m
θ	Steam tube angle	30°

The dimensions shown in Table 3.4, with Equation (3.44), result in a jetting loss coefficient of 1.75. The outlet loss coefficient, K_o , reflects the losses due to the velocity profile at the outlet of adjacent ACC cells.

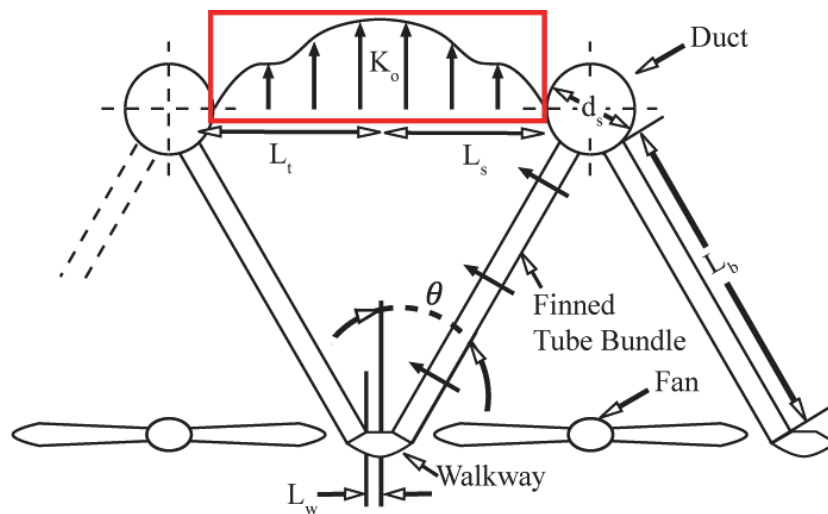


Figure 3.11 Outlet loss of the air located between adjacent ACC cells

The outlet loss coefficient, independent of the semi-apex angle, is a function of the walkway width L_w , steam tube length L_b , half the distance between condensate removal tube edges L_s , half the distance between condensate tube edges L_t , and the diameter of the

inlet steam tube d_s . The equation used to calculate K_o is shown in Equation (3.45) with the values for the dimensions also presented in Table 3.4.

$$K_o = \left[\left(-2.89 \left[\frac{L_w}{L_b} \right] + 2.93 \left[\frac{L_w}{L_b} \right]^2 \right) \left[\frac{L_s}{L_t} \right]^3 + 1.99 \right] \left[\frac{L_b}{L_s} \right]^2 - 3.03 \left[\frac{d_s}{2L_t} \right] + 2.02 \left[\frac{d_s}{2L_t} \right]^2 \quad (3.45)$$

Based on the dimensions in Table 3.4, the outlet loss coefficient for this ACC is 8.255.

The final minor pressure loss accounted for is the impact of the change in temperature. Air in the region between ACC cells is warmer than its ambient surroundings. The density difference between the warm air and ambient air can be interpreted as a buoyancy force in the heated air region. The height used in this calculation represents the average height of the volume of the heated air downstream of the condensation tube.

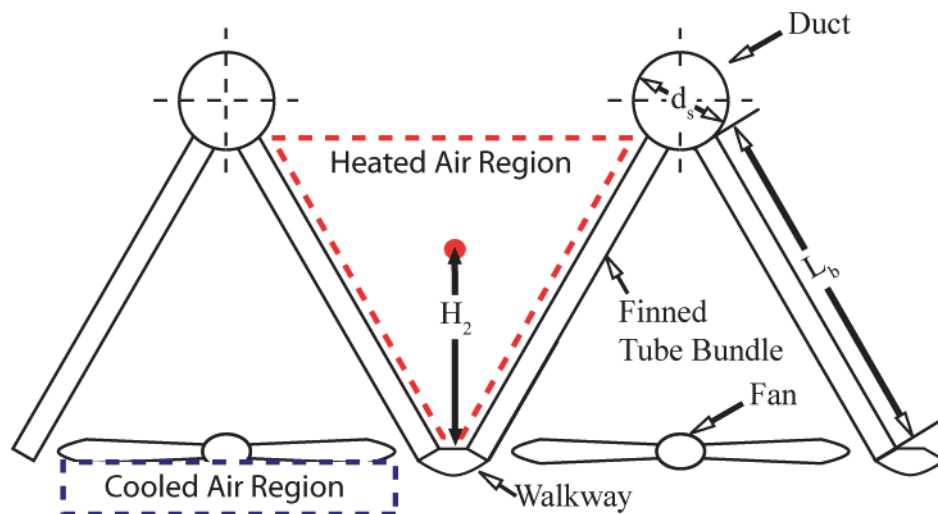


Figure 3.12 Pressure drop due to temperature difference

Each of the loss coefficients was calculated individually, and the appropriate density and velocity were used to compute the pressure drop. Total air-side pressure drop consists of all of the minor losses as well as the frictional pressure drop in the air channels.

The overall air-side pressure drop is directly proportional to the total parasitic fan power required for the cycle; therefore, minimizing the total air-side pressure drop is desirable. Heat transfer performance for the plain fins is predicted using single phase heat transfer data provided by Kakaç *et al.* (1987), as implemented in Engineering Equation Solver software.

The effect of the use of wavy and louvered fins on condenser performance was also investigated using different heat transfer and pressure drop prediction models.

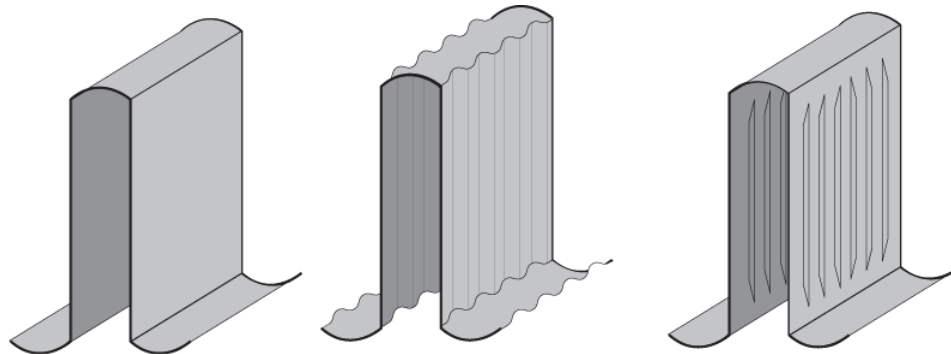


Figure 3.13 Illustrations of the plain (left), wavy (center), and louvered (right) fins investigated

Wavy fin performance was computed using the correlation of Junqi *et al.* (2007), who experimentally studied eleven cross-flow heat exchangers with wavy fins and flat tubes, similar to the configuration under consideration here for the ACC, inside an insulated wind-tunnel with a 270×270 mm cross section. They varied the air-side Reynolds number, fin pitch, fin length, and fin height while maintaining a constant tube-side hot water flow rate of $2.5 \text{ m}^3 \text{ h}^{-1}$. Air-side heat transfer and pressure drop correlations were developed in terms of j and f factors, respectively, that predicted 95% of their data within $\pm 10\%$. These

heat transfer coefficient and Fanning friction factor correlations are shown in Equations (3.46) and (3.47)

$$j = 0.0836Re^{-0.2309} \left(\frac{F_p}{F_h} \right)^{0.1284} \left(\frac{F_p}{2M} \right)^{-0.153} \left(\frac{F_d}{\lambda} \right)^{-0.326} \quad (3.46)$$

$$f = 1.16Re^{-0.309} \left(\frac{F_p}{F_h} \right)^{0.3703} \left(\frac{F_p}{2M} \right)^{-0.25} \left(\frac{F_d}{\lambda} \right)^{-0.1152} \quad (3.47)$$

However, the correlations of Junqi *et al.* (2007) were developed using constant values of wave amplitude and wave length; therefore, it is possible that they are not valid for different values for those parameters (Khoshvaght Aliabadi *et al.*, 2014). The correlations of Ismail *et al.* (2008), as shown in Equations (3.48) to (3.51) as power law expressions for both laminar and turbulent flows, were also used to predict heat transfer and friction factor.

Laminar Range ($100 \leq Re \leq 800$)

$$j = 2.348Re^{-0.786} \left(\frac{F_h}{F_s} \right)^{0.312} \left(\frac{2M}{F_s} \right)^{-0.192} \left(\frac{\lambda}{2M} \right)^{-0.432} \quad (3.48)$$

$$f = 9.827Re^{-0.705} \left(\frac{F_h}{F_s} \right)^{0.322} \left(\frac{2M}{F_s} \right)^{-0.394} \left(\frac{\lambda}{2M} \right)^{-0.603} \quad (3.49)$$

Turbulent Range ($1000 \leq Re \leq 15000$)

$$j = 0.242Re^{-0.375} \left(\frac{F_h}{F_s} \right)^{0.235} \left(\frac{2M}{F_s} \right)^{-0.288} \left(\frac{\lambda}{2M} \right)^{-0.553} \quad (3.50)$$

$$f = 10.628Re^{-0.359} \left(\frac{F_h}{F_s} \right)^{0.264} \left(\frac{2M}{F_s} \right)^{-0.848} \left(\frac{\lambda}{2M} \right)^{-0.1931} \quad (3.51)$$

Khoshvaght Aliabadi *et al.* (2014) used computational fluid dynamics to test multiple models of wavy plate fin heat exchangers and develop general heat transfer and pressure drop correlations for three different working fluids, air, water, and ethylene glycol. These general prediction models were obtained from 250 simulated data points. Evaluated parameters include the fin pitch, fin height, wavelength, fin thickness, wave amplitude, and fin length. Similar to the prediction models proposed by Ismail *et al.* (2008), their models are subdivided based on the Reynolds number.

Laminar Range ($Re < 1,900$)

$$j = 0.295 Re^{-0.191} \left(\frac{F_p}{D_h}\right)^{0.736} \left(\frac{F_h}{D_h}\right)^{0.138} \left(\frac{\lambda}{D_h}\right)^{-0.317} \left(\frac{F_t}{D_h}\right)^{0.049} \left(\frac{2M}{D_h}\right)^{0.247} \left(\frac{L_d}{D_h}\right)^{-0.498} \quad (3.52)$$

$$f = 38.8 Re^{-0.384} \left(\frac{F_p}{D_h}\right)^{-1.48} \left(\frac{F_h}{D_h}\right)^{-0.370} \left(\frac{\lambda}{D_h}\right)^{-1.45} \left(\frac{F_t}{D_h}\right)^{0.102} \left(\frac{2M}{D_h}\right)^{1.09} \left(\frac{L_d}{D_h}\right)^{-0.155} \quad (3.53)$$

Turbulent Range ($1,900 \leq Re$)

$$j = 0.729 Re^{-0.364} \left(\frac{F_p}{D_h}\right)^{0.797} \left(\frac{F_h}{D_h}\right)^{0.240} \left(\frac{\lambda}{D_h}\right)^{-0.498} \left(\frac{F_t}{D_h}\right)^{0.040} \left(\frac{2M}{D_h}\right)^{0.201} \left(\frac{L_d}{D_h}\right)^{-0.303} \quad (3.54)$$

$$f = 52.2 Re^{-0.352} \left(\frac{F_p}{D_h}\right)^{-1.63} \left(\frac{F_h}{D_h}\right)^{-0.353} \left(\frac{\lambda}{D_h}\right)^{-1.75} \left(\frac{F_t}{D_h}\right)^{0.103} \left(\frac{2M}{D_h}\right)^{1.23} \left(\frac{L_d}{D_h}\right)^{-0.237} \quad (3.55)$$

Louvered fin performance was predicted using the models of Kim and Bullard (2002), and Park and Jacobi (2009). Kim and Bullard (2002) tested 45 flat tubes with louver angles between 15 and 29°, fin pitches between 1.0 and 1.4 mm, flow depths of 16 to 24 mm, and air-side Reynolds numbers between 100 and 600 at a constant water flow rate. The resulting Colburn j factor and friction f factor correlations, Equations (3.56) and (3.57), were derived from 225 test data points.

$$j = Re^{-0.487} \left(\frac{L_\alpha}{90} \right)^{0.257} \left(\frac{F_p}{L_p} \right)^{-0.13} \left(\frac{F_h}{L_p} \right)^{-0.29} \times \left(\frac{F_d}{L_p} \right)^{-0.235} \left(\frac{L_l}{L_p} \right)^{0.68} \left(\frac{Tube_p}{L_p} \right)^{-0.279} \left(\frac{t_{fin}}{L_p} \right)^{-0.05} \quad (3.56)$$

$$f = Re^{-0.781} \left(\frac{L_\alpha}{90} \right)^{0.444} \left(\frac{F_p}{L_p} \right)^{-1.682} \left(\frac{F_h}{L_p} \right)^{-1.22} \left(\frac{F_d}{L_p} \right)^{-0.818} \left(\frac{L_l}{L_p} \right)^{1.97} \quad (3.57)$$

Park and Jacobi (2009) applied curve fits to a database of 1,030 heat transfer and 1,270 pressure drop measurements from nine independent laboratories to develop j and f correlations. Their correlations were formulated to account for parametric effects not captured by other correlations, thus improving the predictive performance and general applicability. The constants to be used with Equations (3.58) to (3.63) are shown in Table 3.5.

$$j = C_1 j_{Re} j_{low} j_{louver} \alpha^{C_2} N_{LB}^{C_3} \left(\frac{F_l}{L_p} \right)^{C_4} \left(\frac{F_d}{F_p} \right)^{C_5} \left(\frac{L_l}{F_l} \right)^{C_6} \left(\frac{F_l}{T_p} \right)^{C_7} \times \left(1 - \frac{F_t}{L_p} \right)^{C_8} \left(\frac{L_p}{F_p} \right)^{C_9} \quad (3.58)$$

$$j_{Re} = Re^{\left[C_{10} + C_{11} \cosh \left(\frac{F_p}{L_p} - 1 \right) \right]} \quad (3.59)$$

$$j_{low} = 1 - \sin \left(\frac{L_p}{F_p} \alpha \right) \left[\cosh \left(C_{12} Re - C_{13} \frac{F_d}{N_{LB} F_p} \right) \right]^{-1} \quad (3.60)$$

$$j_{louver} = 1 - C_{14} \tan(\alpha) \left(\frac{F_d}{N_{LB} F_p} \right) \cos \left[2\pi \left(\frac{F_p}{L_p \tan(\alpha)} - 1.8 \right) \right] \quad (3.61)$$

$$f_{cor} = D_1 f_{Re} N_{LB}^{D_2} \left(\frac{F_p}{L_p} \right)^{D_3} \sin(\alpha + D_4) \left(1 - \frac{F_l}{T_p} \right)^{D_5} \times \left(\frac{L_l}{F_l} \right)^{D_6} \left(\frac{F_l}{L_p} \right)^{D_7} \left(\frac{F_l}{F_p} \right)^{D_8} \quad (3.62)$$

$$f_{Re} = \left(Re \frac{F_p}{L_p} \right)^{D_9} + D_{10} Re^{\left[D_{11} \left(\frac{F_l}{F_p} \right) \right]} \quad (3.63)$$

Table 3.5 Constants for j and f factors for the correlation of Park and Jacobi (2009)

Colburn j factor		Fanning f factor	
Constant	Value	Constant	Value
C_1	0.872	D_1	3.69
C_2	0.219	D_2	-0.256
C_3	-0.0881	D_3	0.904
C_4	0.149	D_4	0.200
C_5	-0.259	D_5	0.733
C_6	0.540	D_6	0.648
C_7	-0.902	D_7	-0.647
C_8	2.62	D_8	0.799
C_9	0.301	D_9	-0.845
C_{10}	-0.458	D_{10}	0.00130
C_{11}	-0.00874	D_{11}	1.26
C_{12}	0.0490		
C_{13}	0.142		
C_{14}	-0.0065		

The area and perimeter for the louvered fins were calculated in the same manner as for the plain fins because of the negligible loss of material from the flat fins for these louvered geometries. For the baseline condition of this study, air was set to a relative humidity of 0.25, temperature of 30°C, pressure of 101.3 kPa, and a mass flow rate of 645 kg s⁻¹ through the cell. The inlet and outlet air humidity ratios were assumed to be equal because no water is added during the condensation process.

Material choice can have a large impact on performance due to differences in thermal conductivity. As mentioned previously, two common material choices for fins are carbon steel and aluminum, with thermal conductivities of around 60 and 180 W m⁻¹ K⁻¹, respectively. Assuming plain fins with baseline dimensions and operating conditions, the model was run to investigate the impact of fin thermal conductivity on overall ACC performance. Results from this analysis are shown in Table 3.6.

Table 3.6 Comparison of Carbon Steel and Aluminum Fin Performance

Key Variable	Carbon Steel Plain Fin	Aluminum Plain Fin
k	60	180
ITD	50.88	42.12
$\Delta P_{airside}$	143.63	143.59
η_{fin}	0.525	0.748
$h_{avg,steam}$	2,475	2,681

Aluminum has a thermal conductivity about three times larger than that of carbon steel, resulting in a higher fin efficiency of 0.748, compared to 0.525 of the carbon steel fins. Because of the higher fin efficiency and the lower ITD, aluminum was chosen as the fin material choice for further analyses.

One of the primary goals of this study is to predict the impact of a new, fluttering reed technology on the condenser and cycle performance and efficiency. In a companion study by collaborators to the present work, heat sinks with fin thicknesses similar to those found in the baseline configuration under consideration here were machined and inserted into a test section that consists of a nylon base, insulation, base heater, and guard heaters on the side of the test sections. The air flow rate and the heater voltage input into the section were controlled. Other measured values include the inlet air temperature and pressure, temperatures of the fin at six locations along the heat sink, outlet air pressure and the temperature profile along the width of the exit. A weighted outlet temperature was calculated based on the temperature profile of the air at the exit of the channel. Measurements were taken for cases with and without the AFRs, and analyzed to obtain the Nusselt number and friction factor. These data are curve fit as a function of the Reynolds number and implemented into the ACC module and full cycle codes. The ratio of the heat transfer and pressure drop for cases with is computed and integrated into the cycle model to predict the possible overall performance enhancement.

3.1.3 Determining the number of nodes

A sensitivity study was conducted to determine the minimum number of nodes necessary for the computational ACC model to provide accurate predictions. An increase in the number of nodes results in a finer grid and generally a more accurate solution. However, the increase in the number of nodes corresponds to an increase in computation time. The minimum number of nodes that can be used without compromising total condenser heat duty accuracy was determined by parametrically investigating node numbers ranging 40 to 140.

Table 3.7 Sensitivity Analysis

Number of Nodes	$\dot{Q}_{total,condenser}$ [MW]	$\dot{Q}_{total,condenser}$ % change
40	15.069	N/A
60	15.209	0.929
80	15.277	0.447
100	15.318	0.268
120	15.346	0.183
140	15.362	0.104

Table 3.7 summarizes the total condenser heat duty as a function of the number of nodes, as well as the percent change in the heat duty between runs. The percent change between 40 and 60 nodes was less than one percent, converging towards zero as the number of nodes monotonically increases. Based on these results, 100 nodes were chosen to discretize the geometries investigated in this study.

3.2 Baseline Power Plant Cycle Model

3.2.1 Coal-Fired Rankine Cycle

The condensers analyzed in the present study were used in models developed for representative power plant cycles to investigate the effects of condenser geometry on system level performance. The first cycle analyzed was the coal-fired Rankine cycle, shown in Figure 3.14 with representative values assuming smooth fins.

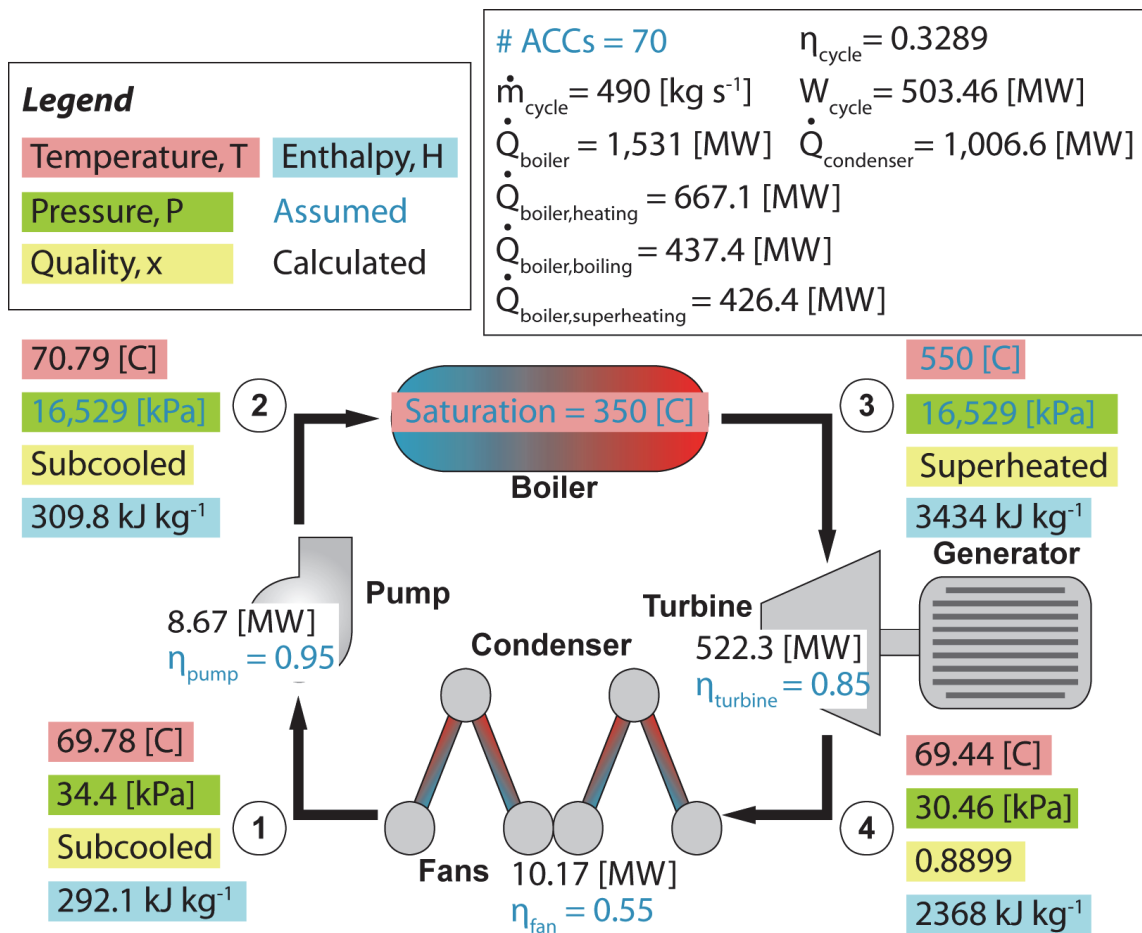


Figure 3.14 Schematic of the Rankine Cycle with representative values

The mass flow rate of steam through each individual ACC was assumed to be 7 kg s^{-1} , and the total number of ACCs was set to 70 such that the work output from the cycle was at least 500 MW. From the literature, it was found that steam turbine blades can

continuously withstand temperatures ranging from 500°C to as high as 650°C (Li and Pridov, 1985; Boyce, 2002; Klein, 2012) and pressures ranging from 9 to 31 MPa (Masuyama, 2001; Klein, 2012). Assuming no pressure losses in the boiler, the steam pressure at the turbine inlet (point 3) was set to a pressure of 16.5 MPa, which corresponds to a saturation temperature of 350°C. The turbine inlet temperature was set to 550°C to ensure that it is below the maximum allowable temperature for the steam turbine blades. With an assumed isentropic turbine efficiency of 0.85, an energy balance was used to calculate the turbine work and outlet enthalpy (Srinivas *et al.*, 2008).

Steam enters the ACCs downstream of the turbine at point 4. Assuming subcooling of 2°C at the outlet of the ACC (point 1), the saturation pressure at the ACC inlet and turbine outlet as well as the ACC outlet temperature and pressure can be calculated. The efficiency of the fan and flow rate of the fan were assumed to be 0.55 and 645 kg s⁻¹, respectively (Bredell *et al.*, 2006). The subcooled steam exiting the ACCs (point 1) then enters a pump with an assumed efficiency of 0.95 and with a high side pressure (point 2) of 16.5 MPa (Aljundi, 2009). An energy balance was used to calculate the required pump work and outlet enthalpy. Net cycle work, defined as the turbine work output less required pump and fan power, is shown in Equation (3.64), with the overall cycle efficiency shown in Equation (3.65).

$$\dot{W}_{Rankine} = \dot{W}_{turbine} - \dot{W}_{fan} - \dot{W}_{pump} \quad (3.64)$$

$$\eta_{Rankine} = \frac{\dot{W}_{Rankine}}{\dot{Q}_{boiler}} \quad (3.65)$$

With representative turbine, fan, and pump work of 522.3 MW, 10.17 MW, and 8.67 MW, respectively, the net work from this cycle is 503.46 MW.

3.2.2 Combined Cycle

Considering the fact that most new power plants use the combined cycle, a Rankine Bottoming Cycle topped by a Brayton Gas Turbine Cycle was also analyzed. A heat recovery steam generator connects the two cycles, which are shown with sample values in Figure 3.15.

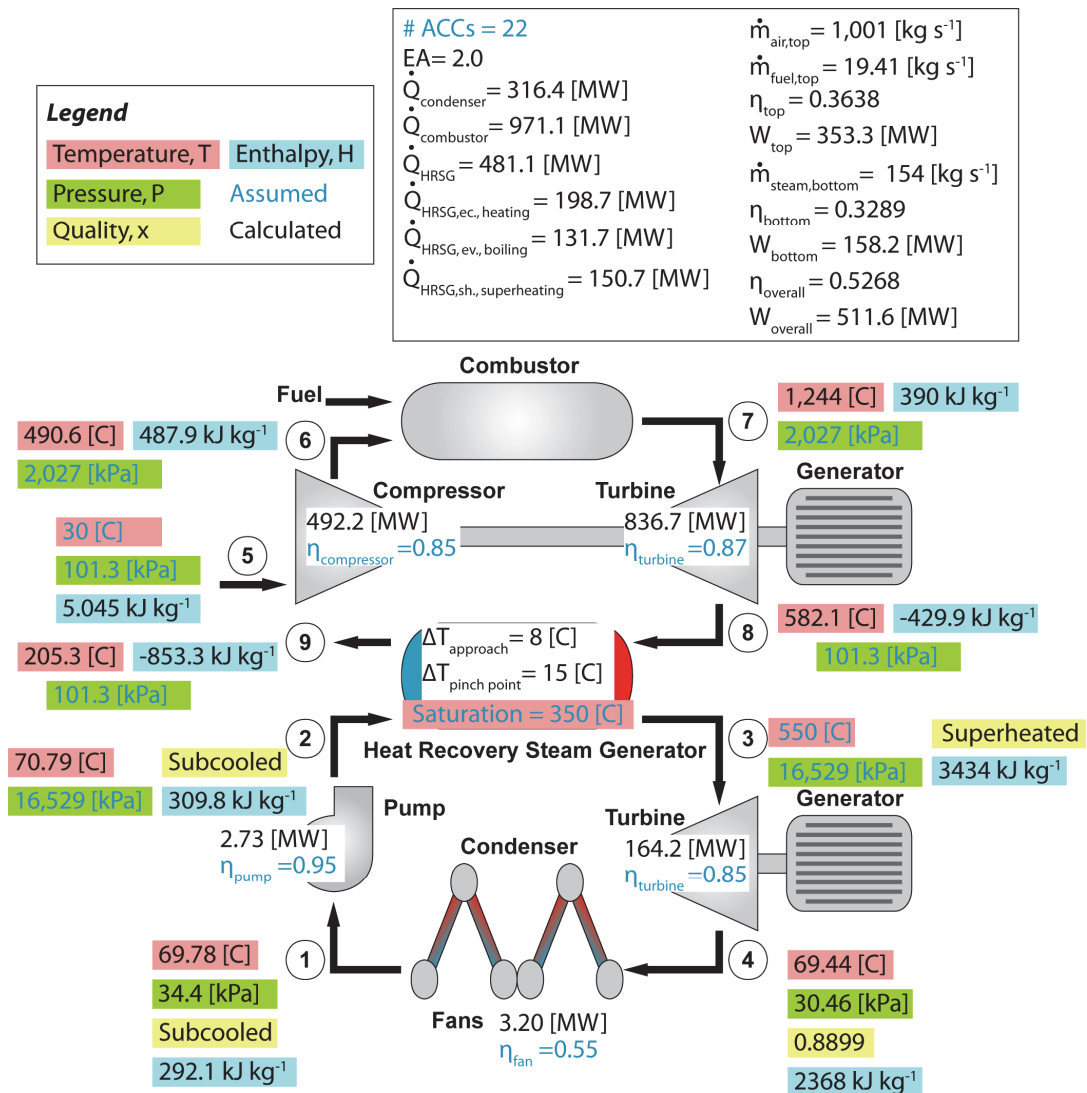
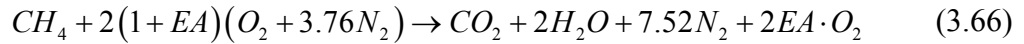


Figure 3.15 Schematic of the Combined Cycle with representative values

An analysis of this coupling heat exchanger was used to compute the air and fuel mass flow rates and gas exit temperature in the topping cycle. Reactants entering the

combustor include air exiting the compressor (point 6), as well as fuel that enters at ambient temperature, where the resulting chemical equilibrium is shown in Equation (3.66).



The stoichiometric Air to Fuel Ratio, AF, was calculated based on the balanced chemical equilibrium equation. Assuming an excess air of 200%, the actual AF ratio was found to be 51.57 and is used to calculate the air and fuel mass flow rates (Mahto and Pal, 2013).

The feedwater pump high side pressure and turbine inlet conditions used for the Rankine Cycle Model described in Chapter 3.2.1 were also used here for the bottoming Rankine cycle, shown as points 1 to 4 in the previous figure. The number of ACCs in the system is adjusted such that the net work of the cycle remains nominally 500 MW. Air idealized as 21% O₂ and 79% N₂ at an ambient temperature of 30°C and ambient pressure of 101.3 kPa with 200% excess air enters a compressor (point 5) with an isentropic efficiency of 0.85 and a pressure ratio of 20 (Valdés *et al.*, 2003).

The enthalpy, H_{air} , and entropy, S_{air} , of the compressor inlet (point 5) and outlet (point 6) air as functions of temperature were computed using Equations (3.67) and (3.68), where T and P represent the temperature and pressure at the state. The calculation of the overall air enthalpy and entropy at points 5 and 6 are also function of the number of moles of N₂ and O₂ in Equation (3.66), and their respective molar masses and enthalpy or entropy. Similar to the calculations done in the Rankine cycle, the entropy is necessary to calculate the isentropic enthalpy needed for the energy balance. For these calculations, however, the entropy is calculated based on the temperature and partial pressure of N₂ (79% of P) and O₂ (21% of P).

$$H_{air} = \frac{2MM_{N_2}(1+EA)3.76H_{N_2}(T) + 2MM_{O_2}(1+EA)H_{O_2}(T)}{MM_{air}} \quad (3.67)$$

$$S_{air} = \frac{2MM_{N_2}(1+EA)3.76S_{N_2}(T, 0.79P) + 2MM_{O_2}(1+EA)S_{O_2}(T, 0.21P)}{MM_{air}} \quad (3.68)$$

$$MM_{air} = 2(1+EA)(MM_{O_2} + 3.76MM_{N_2}) \quad (3.69)$$

With 200% excess air and molar masses of 28.01 kg kmol⁻¹ for N₂ and 32 kg kmol⁻¹ for O₂, the overall molar mass is calculated to be 824 kg kmol⁻¹.

Compressor outlet (point 6) pressure was calculated with the pressure ratio of 20, and the compressor work and outlet temperature were calculated using an energy balance and the iterative solving ability of EES.

Assuming no heat loss and negligible pressure drop in the combustor, an enthalpy balance between the reactants at point 6 (Equation (3.70)) and the products at point 7 (Equation (3.71)), expressed in Equation (3.72), was used to obtain the combustor outlet temperature.

$$H_{reactants} = H(CH_4, T_{fuel})MM_{CH_4} + 2(1+EA)H(O_2, T_{air})MM_{O_2} + 3.76(2+2EA)H(N_2, T_{air})MM_{N_2} \quad (3.70)$$

$$H_{products} = H(CO_2, T_{out}) \cdot MM_{CO_2} + 2H(H_2O, T_{out}) \cdot MM_{H_2O} + 2(1+EA)3.76 \cdot H(N_2, T_{out}) \cdot MM_{N_2} + 2EA \cdot H(O_2, T_{out}) \cdot MM_{O_2} \quad (3.71)$$

$$H_{reactants} = H_{products} \quad (3.72)$$

The corresponding heat input into the combustor is the product of the mass flow rate of the fuel and the calculated lower heating value. The lower heating value, defined as the amount of heat released by combusting a certain amount of fuel, was computed assuming that the reactants entered at and the products left the combustor at the fuel

temperature, T_{fuel} , of 30°C. Enthalpies of the reactants and the products necessary to calculate the lower heating value are expressed in Equations (3.73) and (3.74).

$$H_{reactants,LHV} = H(CH_4, T_{fuel}) \cdot MM_{CH_4} + 2(1+EA) \cdot H(O_2, T_{fuel}) \cdot MM_{O_2} + 3.76 \cdot (2+2EA) \cdot H(O_2, T_{fuel}) \cdot MM_{N_2} \quad (3.73)$$

$$H_{products,LHV} = H(CO_2, T_{fuel}) \cdot MM_{CO_2} + 2 \cdot H(H_2O, T_{fuel}) \cdot MM_{H_2O} + 2 \cdot (1+EA) \cdot 3.76 \cdot H(N_2, T_{fuel}) \cdot MM_{N_2} + 2 \cdot EA \cdot H(O_2, T_{fuel}) \cdot MM_{O_2} \quad (3.74)$$

$$LHV = \frac{H_{reactants,LHV} - H_{products,LHV}}{MM_{fuel}} \quad (3.75)$$

With the fuel temperature of 30°C, fuel molar mass of 16.04 kg kmol⁻¹ and reactant and product enthalpies of -70,258 kJ kmol⁻¹ and -871,722 kJ kmol⁻¹, respectively, the calculated lower heating value, LHV, is 50,020 kJ kg⁻¹.

The gas turbine inlet conditions (point 7) were calculated from the combustor analysis. Assuming an isentropic efficiency of 0.87 and no pressure drop through the heat recovery steam generator, the turbine work and outlet enthalpy were calculated using an energy balance (Polyzakis *et al.*, 2008).

Turbine exhaust gas (point 8) enters the heat recovery steam generator, HRSG, and superheats the steam in the bottoming Rankine Cycle. The HRSG consists of three heat exchanging components: the economizer, evaporator, and superheater, represented schematically in Figure 3.16.

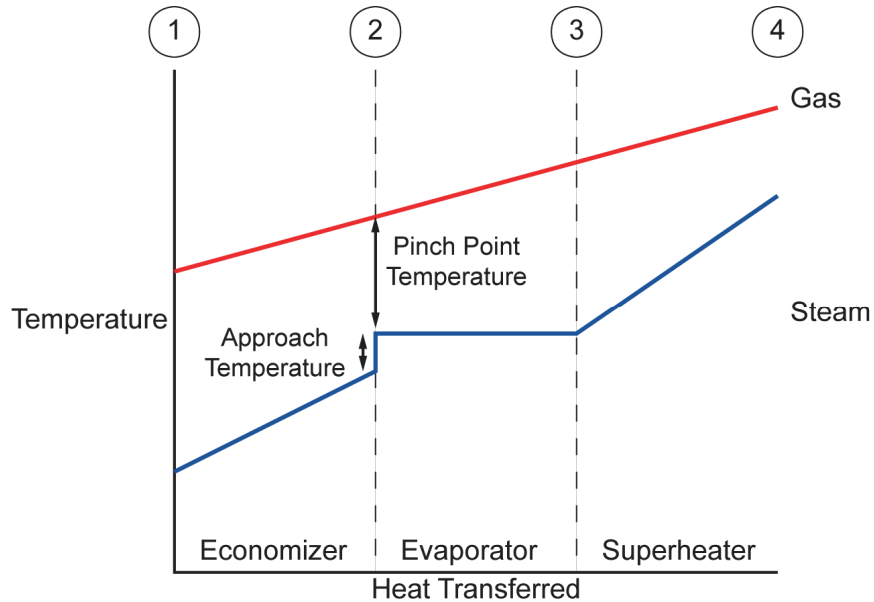


Figure 3.16 Temperature versus heat transferred graph in a HRSG

Subcooled steam enters the economizer (point 1), where it is heated to a temperature slightly lower than saturation temperature. The difference between the economizer steam exit temperature and the saturation temperature is known as the approach temperature. This temperature difference, commonly between 5 to 12°C, was assumed to be 8°C for this analysis (Boyce, 2002). Another important design parameter is the pinch point temperature, defined as the difference between the gas entering the economizer (point 2) and the steam saturation temperature. The pinch point temperature, which typically ranges from 8 to 22°C, is assumed to be 15°C (Boyce, 2002).

The temperature jump in the steam line between the economizer exit and the evaporator inlet is attributed to mixing of the steam in an adiabatic steam drum. Subcooled steam exiting the economizer enters the steam drum, from which saturated steam exits and enters the evaporator. Heat is transferred from the gas to the steam such that the steam returns to the steam drum at some higher quality. The amount of heat needed to increase

the economizer steam exit temperature to the saturation temperature is due to the higher quality evaporator exit steam mixing with the subcooled steam. Therefore, steam at a slightly lower quality than the evaporator outlet steam enters the superheater, where it is superheated to the maximum steam turbine inlet temperature. The location of the steam drum is depicted in Figure 3.17, where the numbered points correspond to the numbered labels in Figure 3.16

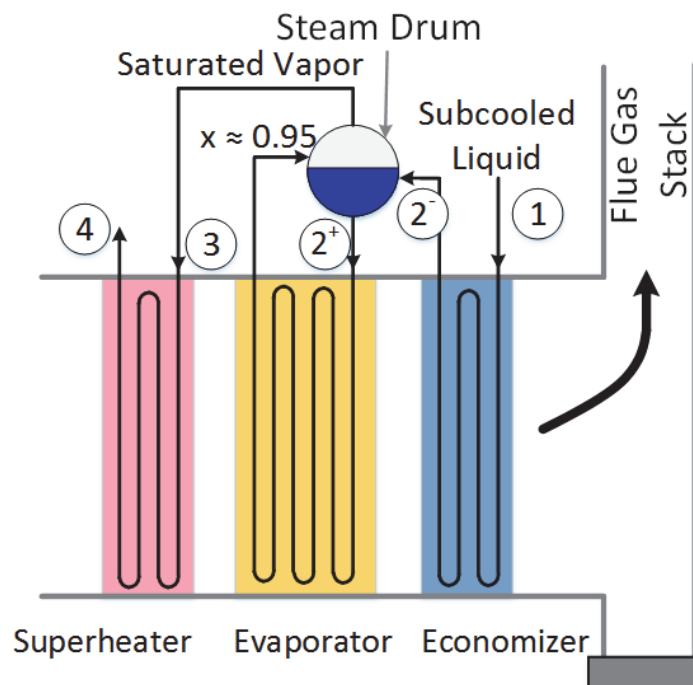


Figure 3.17 Flow of steam into and out of the steam drum

Net combined cycle work, the sum of the work from both turbines less required pump, fan, and compressor work, and the amount of heat added during the combustion process were used to compute the overall combined cycle efficiency. A net combined cycle work of 511.6 MW and combustion heat of 971.1 MW yielded an overall combined cycle efficiency of 52.68%.

CHAPTER 4: RESULTS AND DISCUSSION

The results from the analyses described in the previous chapter are discussed here, both on the basis of condenser performance, as well as system level performance. When analyzing the performance of condensers, one useful metric is the initial temperature difference, or ITD. The ITD is defined as the difference between the steam condensation and ambient air temperatures. A lower ITD leads to a lower turbine backpressure, resulting in a larger power output and a higher overall plant efficiency. However, a decrease in ITD usually requires an increase in the heat transfer coefficient, particularly of the air-side, that occurs from surface enhancements or some other features that also simultaneously increase the air-side pressure drop. In the case of ACCs, a higher air-side pressure drop results in a higher fan power consumption, which detracts from the net delivered power. In the present study, the condenser design was first optimized through progressive changes in geometric features. Once an optimal configuration was obtained, it was then analyzed in a system-level model to predict power plant performance, and further optimized based on plant-level performance predictions. To optimize the stand-alone condenser model, parametric studies were conducted on the dimensions of plain, wavy, and louvered fins to predict the resulting ITD and air-side pressure drop. The air-side pressure drop was then plotted versus the ITD, which assisted in determining the lowest possible air-side pressure drop to achieve a desired ITD.

4.1 Stand-Alone Condenser Model

This section discusses the results obtained for the stand-alone condenser model, where performance of components other than the ACC is not taken into account.

4.1.1 Base-Case Model

Prior to the parametric optimization study, the segmented model developed here was used to determine the baseline performance of the plain fin geometries. The baseline plain fin results were analyzed to ensure the model would provide reasonable results. Geometric dimensions and operating conditions for the baseline performance model are shown in Table 4.1 and Table 4.2.

Table 4.1 Summary of baseline geometry dimensions

<i>Condenser</i>		<i>Tube</i>		<i>Fin</i>			
ACC_w	12.2 m	$Tube_d$	190.5 mm	F_h	25.4 mm	F_t	0.254 mm
ACC_h	10.67 m	$Tube_w$	25.4 mm	F_s	2.54 mm	F_d	165.1 mm
β	60°	$Tube_t$	1.27 mm				

Table 4.2 Summary of operating conditions

<i>Operating Conditions</i>	
\dot{m}_{steam} (per ACC)	7 kg s ⁻¹
\dot{m}_{air} per fan	645 kg s ⁻¹
$P_{air,in}$	101.3 kPa
$T_{air,in}$	30°C
$\phi_{ambient}$	0.25

For the initial predictions of plain fin performance, the air-side heat transfer coefficient was calculated using an expression from Shah and London (1978b), which approximates the Nusselt number results from a finite difference method analysis by Miles and Shih (1967) within $\pm 0.1\%$, and is applicable for fully developed, laminar flow in a constant wall temperature, rectangular duct. The friction factor was also calculated using an equation developed by Shah and London (1978b), which approximated friction factors calculated by Shah and London (1971) from a closed-form friction factor equation. With the baseline fin geometry of fin height of 25.4 mm, fin spacing of 2.54 mm, and fin

thickness of 0.254 mm, the resulting air-side heat transfer coefficient and friction factor are 38.36 W m⁻² K⁻¹ and 0.1122, respectively.

For the dimensions shown in the previous tables, areas and efficiencies associated with the finned tube can be calculated as discussed in Chapter 3. With the baseline dimensions described in Table 4.1, areas and other geometry dependent variables associated with the finned tube are summarized in Table 4.3.

Table 4.3 Summary of baseline geometric parameters

Number of fins	2,444,000	Frontal area, A_f	260.3 m ²
Number of tubes	320	Single fin area, A_{fin}	0.0084 m ²
Fin efficiency, η_{fin}	0.7475	Total area of fins per tube, $A_{fin,tube}$	64.14 m ²
Overall surface efficiency, $\eta_{overall}$	0.7625	Internal steam tube area per finned tube	4.289 m ²
Effective area per tube	52 m ²	Outer surface area per finned tube	68.2 m ²
Total condenser effective area	16,641 m ²	Total outer surface area	21,823 m ²
Tube cross sectional area, $A_{tube,cs}$	4,185 mm ²		

Figure 4.1 shows the steam quality and void fraction as a function of the relative tube position, where z (some length of the tube), was normalized against the overall length of the tube, L , of 10.67 m.

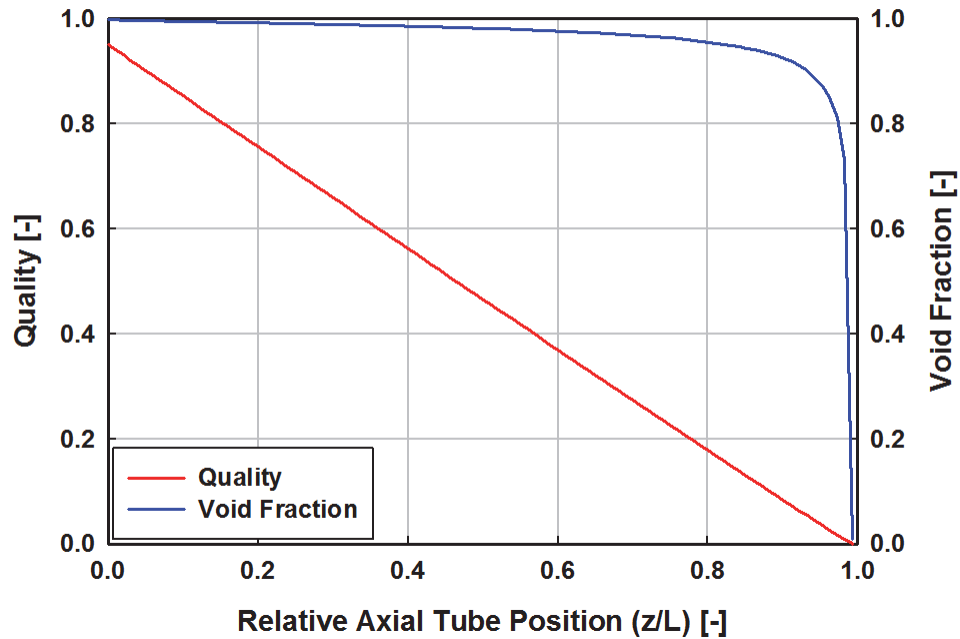


Figure 4.1 Plot of steam-side quality and void fraction with respect to relative axial tube position

Steam has a critical pressure of 22,064 kPa; therefore, a steam saturation pressure of 34 kPa represents a reduced pressure of about 0.0016. The quality decreases as the flow makes its way through the tube, condensing from the vapor to liquid phase. While the decrease in quality is generally linear through the bulk of the condenser, the rate decreases slightly as it approaches the end of the tube, as evidenced in Figure 4.2. For example, the change in quality in the first segment is -0.0097, while in the last two-phase segment, it is -0.0087, i.e., a difference of about 10%.

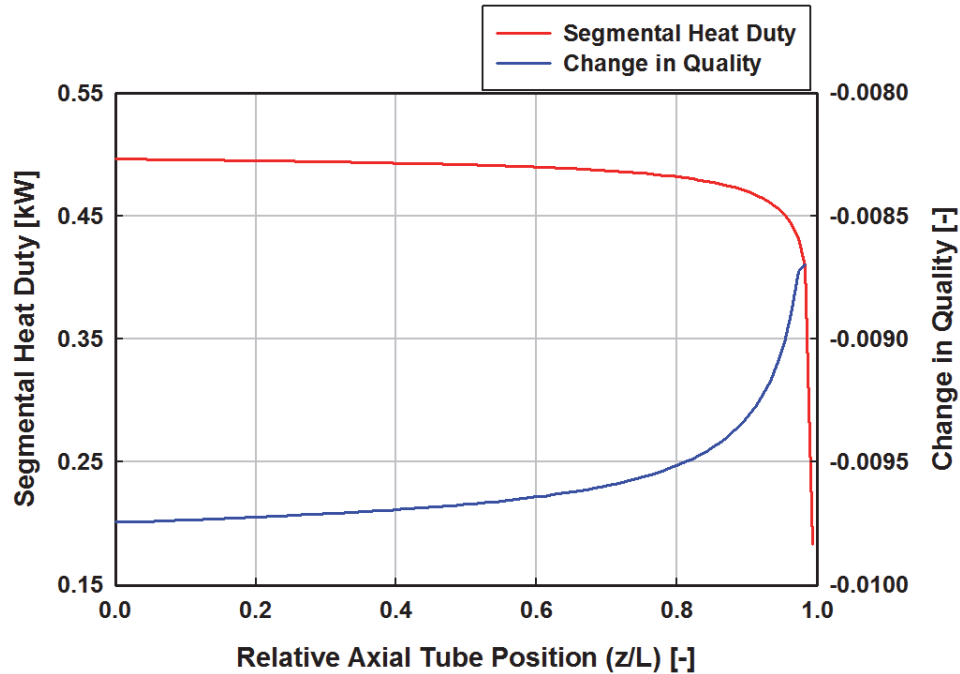


Figure 4.2 Segmental heat duty and corresponding change in quality as a function of relative axial tube position

Condensation of the steam along the tube also results in a decrease in segmental heat duty (Figure 4.2). With the decrease in steam quality, the liquids Reynolds number and the two-phase Martinelli parameter increase. A contributing factor to the decrease in steam-side heat transfer coefficient and therefore segmental heat duty is the decrease in phase velocity. The vapor and liquid velocities decrease from 23.04 m s^{-1} and 0.1029 m s^{-1} , respectively, at the top of the tube to 0.0028 m s^{-1} and 0.0054 m s^{-1} at the bottom. A plot of the steam-side heat transfer coefficient, calculated using the correlation of Akhavan-Behabadi *et al.* (2007), as a function of location along the tube is shown in Figure 4.4. The thermal resistances considered in the model include those due to air convection, tube conduction, and steam convection. Calculation of these thermal resistances was done on a segment by segment basis. These thermal resistances were plotted as a function of tube position and shown in Figure 4.3.

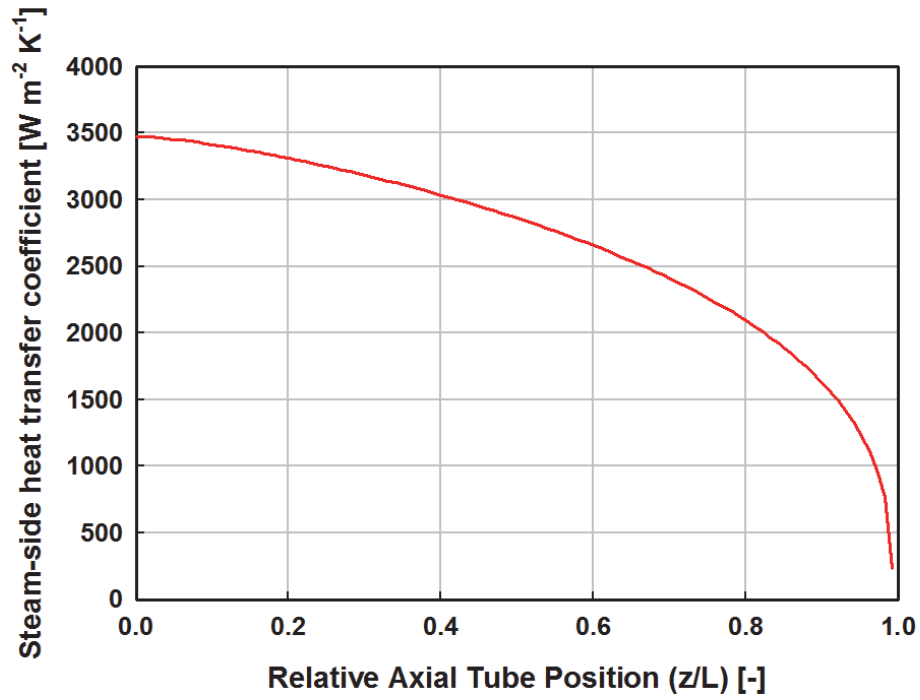


Figure 4.4 Plot of the steam side heat transfer coefficient calculated using the Akhavan-Behabadi *et al.* (2007) correlation as a function of tube position

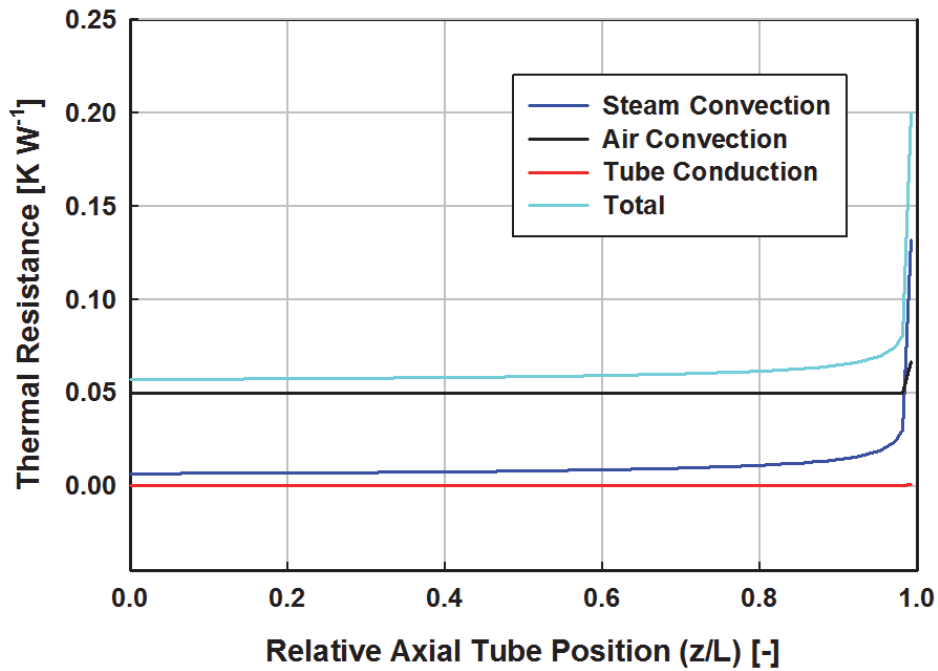


Figure 4.3 Thermal resistances as a function of position along tube

Thermal resistance due to air-side convection was calculated as a function of the air-side heat transfer coefficient, outside surface area, and fin efficiency. With the air-side heat transfer coefficient of $38.36 \text{ W m}^{-2} \text{ K}^{-1}$, outside surface area of 0.684 m^2 per segment length, and overall surface efficiency of 0.7625 , the thermal resistance due to air-side convection remains constant through most of the two-phase portion of the tube. Because the length of the subcooled segment of 0.0800 m is slightly shorter than the length of a two-phase segment (0.1069 m), the outer surface area used in the calculation of thermal resistance is also less (0.5112 m^2 for the subcooled segment compared to 0.6840 m^2 for each two-phase segment). The smaller outer surface area results in a slight increase in the calculated air convection thermal resistance from 0.05 K W^{-1} to 0.0669 K W^{-1} near the end of the tube. Calculation of the thermal resistances due to steam convection and tube conduction also differed between the two-phase segments and the final subcooled section. With a constant thermal conductivity of $60 \text{ W m}^{-1} \text{ K}^{-1}$ and tube thickness of 1.27 mm , the decrease in the internal steam tube area from 0.0430 m^2 to 0.0321 m^2 yielded an increase in the thermal resistance due to the tube conduction from $4.9 \times 10^{-4} \text{ K W}^{-1}$ in the two-phase sections to $6.6 \times 10^{-4} \text{ K W}^{-1}$ in the final subcooled section. The change in the internal tube area is also the reason for the sudden increase in the thermal resistance from steam convection near the end of the tube, even though the decrease in steam-side heat transfer coefficient does contribute slightly. The average two-phase steam-side heat transfer coefficient is $2705.4 \text{ W m}^{-2} \text{ K}^{-1}$, a value at least 70 times the air-side heat transfer coefficient of $38.36 \text{ W m}^{-2} \text{ K}^{-1}$. However, the effective surface area per two-phase segment on the air-side (0.684 m^2) is greater than the surface area per two-phase segment on the steam-side (0.043 m^2). Therefore, the average thermal resistance due to steam convection

per segment is less than the air-side thermal resistance (0.0095 K W^{-1} compared to 0.05 K W^{-1}). From Figure 4.3, convection on the air-side of the tube accounts for the majority of the total thermal resistance. However, toward the end of the tube, single-phase convection on the water side over takes the convection on the air-side to be the dominant source of thermal resistance.

The resulting UA, shown as a function of position along the tube in Figure 4.5, decreases with the increase in thermal resistance.

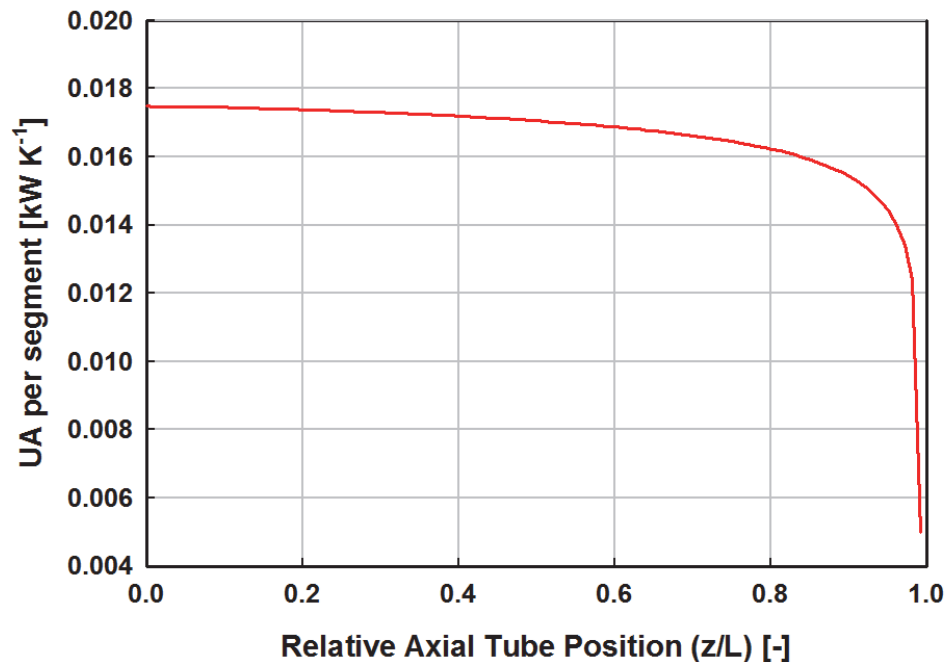


Figure 4.5 UA as a function of location along the tube

Another important variable to track for condenser design is the pressure drop in the inclined tube. As previously mentioned, the total steam-side pressure drop is the sum of three components: frictional, gravitational, and acceleration or deceleration. Frictional pressure drop across each individual segment decreased as the flow condensed along the tube, with a value of 4.04 Pa in the first segment, and decreasing to 0.0041 Pa in the

subcooled section. Even though the friction factor increased from 0.0068 at the beginning of the condensation process to 0.1532 in the subcooled section, the velocity of the fluid flow decreased. At the top of the tube, the vapor phase velocity is 23.04 m s^{-1} , which slows to 0.0028 m s^{-1} as it approaches the subcooled section. Assuming single-phase water in the final segment, the velocity of the fluid is 0.00536 m s^{-1} . The Martinelli parameter, X_{tt} , is dependent on the density, viscosity, and quality of the flow. As the fluid condenses, the Martinelli parameter increases from 0.00152 when the quality is close to one to 3,725 when the quality is almost zero and therefore subcooled. The increase in the Martinelli parameter results in the increase in the vapor two-phase multiplier from 1.011 to 4,282. While the vapor two-phase multiplier increased, the single-phase frictional pressure drop decreased from about 3.98 Pa at the beginning of the condensation to 5.01×10^{-7} Pa. Because the single-phase frictional pressure drop decreased by an even greater order of magnitude than the vapor two-phase multiplier increased, the frictional pressure drop per segment decreased.

Gravitational pressure drop grew increasingly more negative (i.e., a rise in pressure) along the length of tube from -2.675 to -662.5 Pa because of the decrease in void fraction. Pressure drop due to the change of momentum of the flow also increased slightly from -2.304 to 0.062 Pa. Even though the frictional pressure drop across each individual segment decreases, the cumulative total of the frictional pressure losses from the top of the tube continues to increase as the quality decreases; however, this is more than compensated for by the increasingly negative gravitational pressure drop due to the downward inclination of the flow. This results in an overall negative total pressure drop, and therefore an increase in pressure, evident in Figure 4.7, as the flow condenses. As a result, the saturation temperature of the steam in each segment increases as well. A plot of the outlet air temperature with respect to the relative tube position is shown in Figure 4.6.

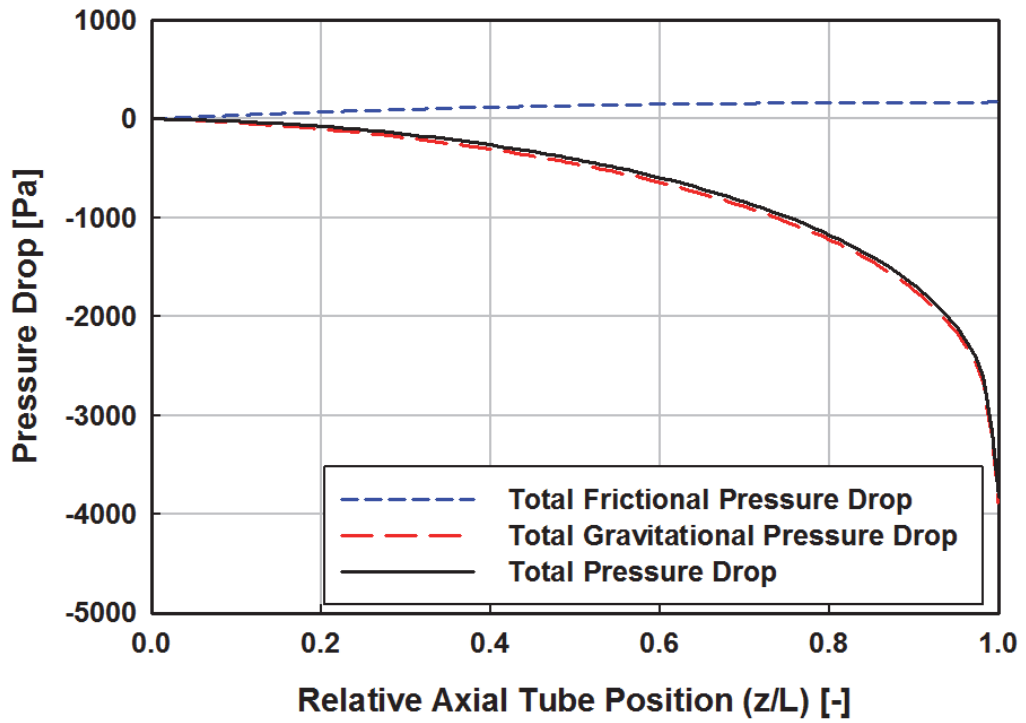


Figure 4.7 Frictional, gravitational, and total steam-side pressure drop

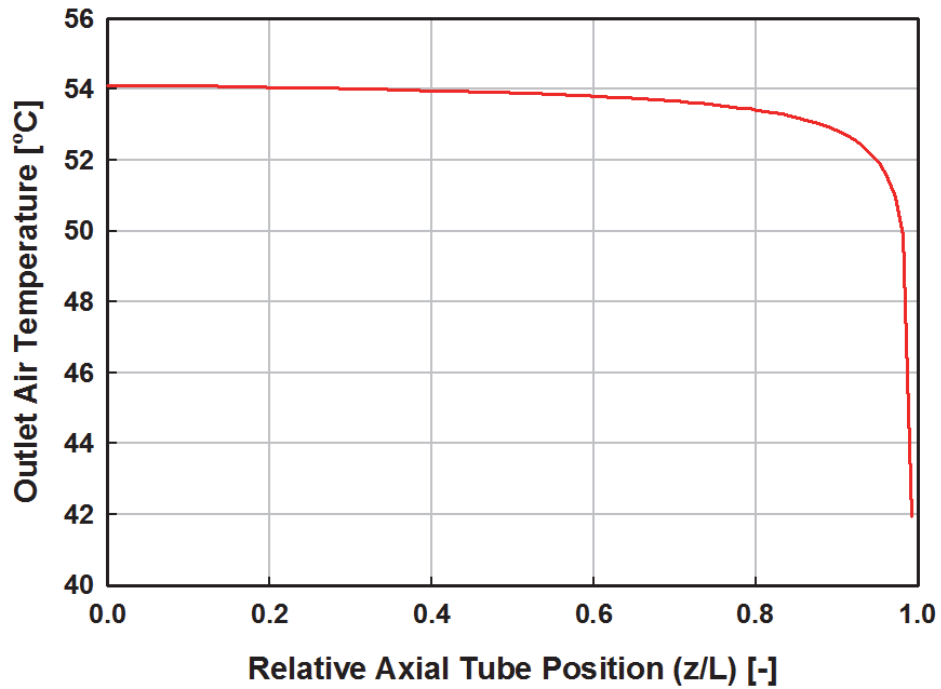


Figure 4.6 Plot of outlet air from the condenser versus location along the tube

For the first approximately 98.25% of the tube where the flow is two-phase, the outlet air temperature changed by only 4.21 K from 54.12°C to 49.91°C. The decrease in outlet air temperature also reflects the fact that the heat transferred from the condenser decreases as the flow condenses, due to the decreasing tube-side heat transfer coefficients shown in Figure 4.4.

Total air-side pressure losses for the baseline conditions, consisting of frictional and minor losses, were calculated and are summarized in Figure 4.8. Minor loss coefficients and the resulting pressure drops were calculated using the method described in Chapter 3.1.2. The outlet loss coefficient was found to be 8.255, upstream and downstream loss coefficients were estimated to be 0.3 and 0.39, and the calculated jetting loss coefficient is 1.75 (Kröger, 1998). Frictional pressure drop accounted for about 20% of the overall air-side pressure drop. Pressure drop associated with the angling of the air as it enters the ACC channels was calculated to be 61.58 Pa, which accounts for 42.9% and is the largest source of the total air-side pressure drop.

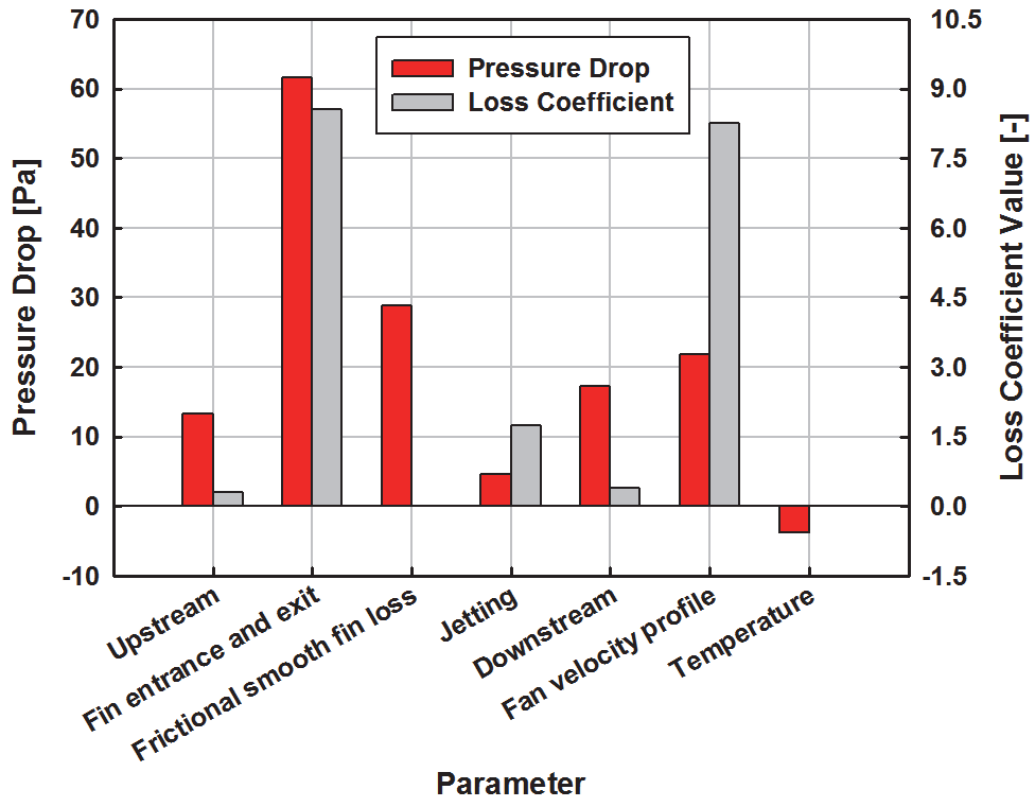


Figure 4.8 Summary of pressure drops at baseline operating conditions

As previously mentioned, the ITD is an important parameter to consider in interpretation of the condenser performance. For the baseline case, an ITD of 42.12 K is required to transfer the design heat duty of 15.32 MW, with an air-side pressure drop of 143.6 Pa. In the following sections, variations in the condenser tube and fin geometry are considered in an attempt to transfer the design heat duty at a lower ITD.

4.1.2 Air-Side Parametric Studies

For the parametric studies discussed here, a 15 K reduction in ITD, corresponding to an ITD of 27 K, was set as the goal. Plain, wavy, and louvered fins were investigated and the results are presented in the following sections.

4.1.2.1 Plain Fins

Plain or smooth fins were considered first, with fin spacing, fin height, and fin thickness varied to see their effect on the required ITD. Air and steam mass flow rates were set at 645 kg s^{-1} and 7 kg s^{-1} , respectively, with an ambient air inlet relative humidity ratio of 0.25 and a temperature and pressure of 30°C and 101.3 kPa , respectively.

A decrease in the fin spacing from 3.81 mm to 1.27 mm results in an increase in the number of fins from 5,248 to 13,998 fins per tube and total outside heat transfer surface area from $15,436 \text{ m}^2$ to $38,838 \text{ m}^2$. However, the air flow cross sectional area is constricted with an increase in the number of fins, leading to an increase in the air flow velocity from 3.417 m s^{-1} to 3.843 m s^{-1} through the fin channels. In this case, the Reynolds number decreases from 1405 to 576.8 because the decrease in the hydraulic diameter from 6.626 mm to 2.419 mm is larger than the increase in the air flow channel velocity. The aspect ratio, defined in this case as the ratio of the fin spacing to the fin height, decreases with the fin spacing as the height is held constant. Both the decrease in the Reynolds number and the aspect ratio contribute to the increase in the friction factor from 0.0938 to 0.1727, and therefore an increase in the air-side pressure drop from 125.45 Pa to 233.14 Pa. The decrease in air-channel hydraulic diameter also contributes to an almost three times greater air-side heat transfer coefficient ($74.16 \text{ W m}^{-2} \text{ K}^{-1}$ versus $27.14 \text{ W m}^{-2} \text{ K}^{-1}$) and therefore a 33.94 K decrease in ITD from 61.91 K to 27.97 K, as shown in Figure 4.9. For the decrease in fin spacing from 3.81 mm to 1.27 mm, the ITD decreased by 54.8% while the pressure drop increased by 85.8%.

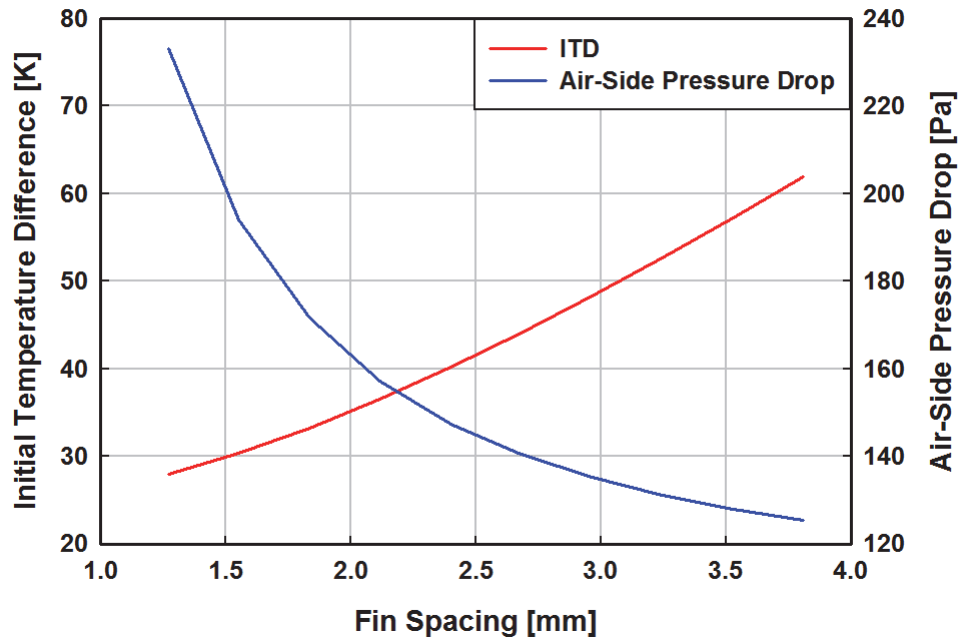


Figure 4.9 Impact of varying fin spacing on the ITD and Air-Side Pressure Drop

Fin thickness, another contributor to the fin pitch, also impacts condenser performance, as shown in Figure 4.10. Calculation of the overall finned tube surface area took into account the fin edge, a product of the fin thickness and the fin height. A decrease in fin thickness from 0.381 mm to 0.127 mm decreases the fin pitch by 0.254 mm, increasing the number of fins from 7,304 to 8,000 per tube. Because the small area perpendicular to the air inlet and outlet was considered in the calculation of the fin area, the area of each individual fin decreased slightly from 8,406 mm² to 8,394 mm². Even though the area of each individual fin decreases, the increase in the number fins resulted in an overall increase in surface area from 20,901 m² to 22,833 m².

Assuming the same overall air mass flow rate of 645 kg s⁻¹ through the ACC, an increase in the number of fins increases the total number of air channels per ACC from 2.337×10^6 to 2.560×10^6 , decreasing the flow velocity from 3.682 m s⁻¹ to 3.362 m s⁻¹

and the Reynolds number from 1,055 to 963.4 through each channel. A decrease in Reynolds number increases the friction factor from 0.1084 to 0.1164, but the decrease in the flow velocity offsets that increase, resulting in a decrease in the air-channel pressure drop from 153.62 Pa to 134.26 Pa. The air channel aspect ratio and hydraulic diameter remain constant while the fin perimeter and fin area decrease with decreasing fin thickness. However, the decrease in fin area is greater than the decrease in fin perimeter, resulting in an overall decrease in fin efficiency from 0.8121 to 0.6125 and surface efficiency from 0.8234 to 0.6353. As the fin thickness decreases from 0.381 mm to 0.127 mm, the fin surface area changes from 8,406 mm² to 8,394 mm², and the air-side heat transfer coefficient decreases from 38.55 W m⁻² K⁻¹ to 38.16 W m⁻² K⁻¹. In this case, the decrease in fin thickness from 0.381 mm to 0.127 mm resulted in an increase in the ITD from 41.25 K to 45.66 K and a 12.6% decrease in pressure drop from 153.62 Pa to 134.26 Pa.

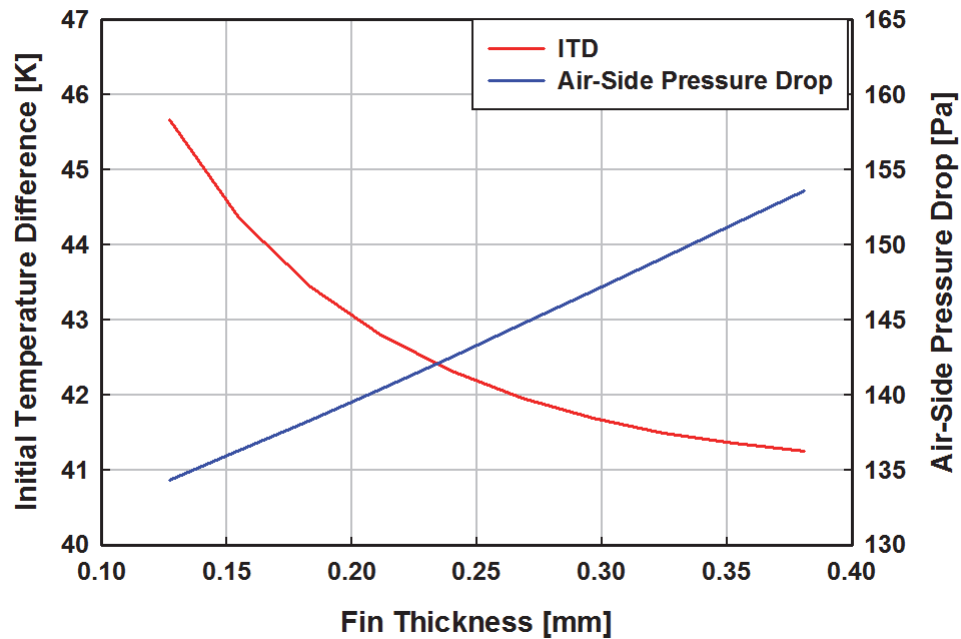


Figure 4.10 Impact of varying fin thickness on the ITD and Air-Side Pressure Drop

The air-side pressure drop curve appears almost linear. The change in fin thickness directly influences the area of the ACC that is blocked, which impacts the air flow velocity. By varying the fin thickness from 0.381 mm to 0.127 mm, the Reynolds number decreases from 1,055 to 963.4 and velocity per channel decreases from 3.682 m s⁻¹ to 3.362 m s⁻¹. The decrease in the fin thickness also decreased the fin efficiency from 0.8121 to 0.6125, therefore decreasing the total effective area of the ACC from 17,209 m² to 14,506 m². The friction factor, which is a function of the Reynolds number, increases from 0.1084 to 0.1164 with the decrease in fin thickness. Because the channel hydraulic diameter is constant, the combination of an increase in friction factor and the decrease in velocity ($\Delta P \propto fV^2$) leads to the decrease in pressure drop seen in Figure 4.10.

Fin height influences the tube pitch and therefore the number of tubes. A decrease in fin height from 38.1 mm to 12.7 mm decreases the tube pitch, doubling the number of tubes in the ACC from 240 to 480 and therefore increasing the overall number of fins and channels from 1.833×10^6 to 3.665×10^6 . Even though the number of fins and channels increases, the channel area available for air flow decreases from 177.35 m² to 118.24 m², increasing the air flow velocity from 3.131 m s⁻¹ to 4.696 m s⁻¹ and the Reynolds number from 925.2 to 1,234. With a decrease in fin height from 38.1 mm to 12.7 mm, the air channel friction factor decreased from 0.1242 to 0.0885. However, the increase in the air flow velocity is greater than the decrease in the friction factor, resulting in an increase from 112.37 Pa to 344.69 Pa in air-side pressure drop, which can be seen in Figure 4.11. The increase in the aspect ratio from 0.067 to 0.200 leads to a decrease in the Nusselt number from 7.215 to 5.955 and a decrease in the channel hydraulic diameter from 4.763 mm to 4.233 mm. The air-side heat transfer coefficient is dependent on the Nusselt number, air

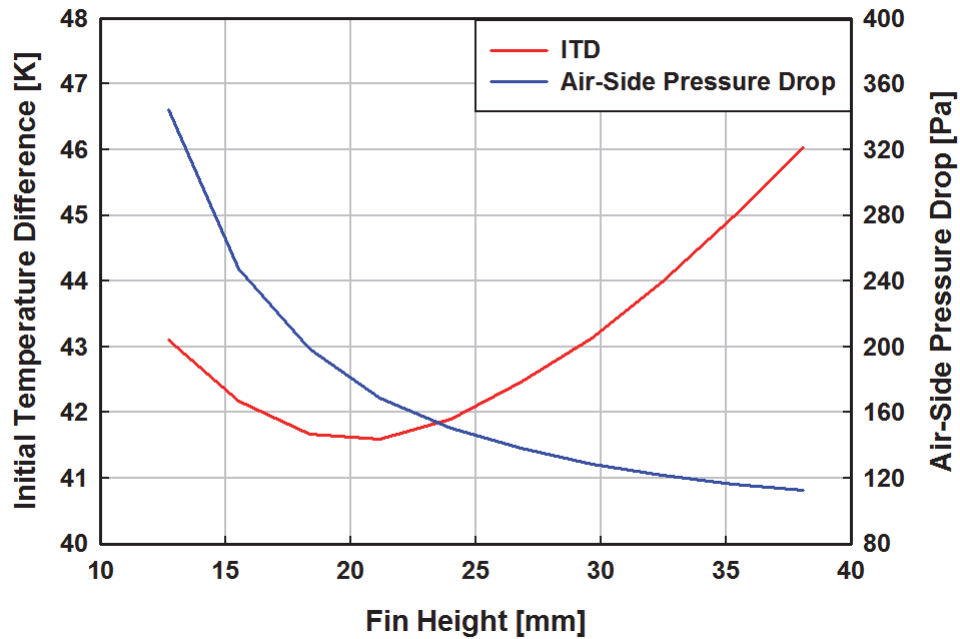


Figure 4.11 Impact of varying fin height on the ITD and Air-Side Pressure Drop

thermal conductivity, and the channel hydraulic diameter. With a constant air thermal conductivity, the 17% decrease in the Nusselt number was greater than the 11% decrease in channel hydraulic diameter. Therefore, even though a decrease in the hydraulic diameter should result in an overall increase in the heat transfer coefficient, the change in Nusselt number overcame the change in the hydraulic diameter and resulted in an overall decrease the heat transfer coefficient from $39.21 \text{ W m}^{-2} \text{ K}^{-1}$ to $36.41 \text{ Wm}^{-2} \text{ K}^{-1}$.

‘The minima in ITD seen in Figure 4.11 is due to the peak in total effective area available for heat transfer. Even though the fin efficiency, and therefore overall fin surface efficiency, increases from 0.5816 to 0.9222 as the fin height decreases, the effective area of a single tube decreases from 60.02 m^2 to 33.63 m^2 because of the reduction in fin area on each tube. A decrease in fin height from 38.1 mm to 12.7 mm increases the total number of tubes in the condenser from 240 to 480. Total effective area of the ACC, the product of

the number of tubes and the effective area of the single tube and shown in Figure 4.12, peaked at 17,026 m² at a fin height of around 21 mm, which corresponds to the minimum ITD of about 41.59 K seen in Figure 4.11.

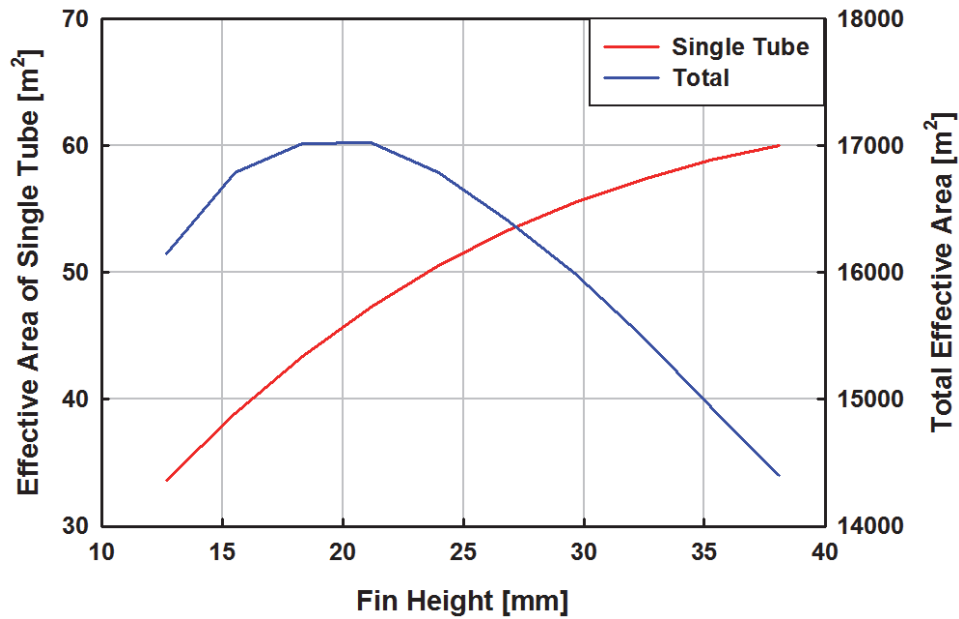


Figure 4.12 Single tube and total effective area versus fin height

The fin spacing, height, and thickness were varied by $\pm 50\%$ with respect to the original baseline conditions. To compare the result of each geometric combination, the air-side pressure drop was plotted against the ITD to allow for visual inspection of combinations that result in poorer condenser performance. An example of a set of results is shown in Figure 4.13 for fins with a fin thickness of 0.254 mm. Each colored line reflects some fin height between 12.7 mm to 33.02 mm, while each data point (filled black circle) in the figure corresponds to the result for some fin spacing between 1.27 mm (leftmost point) to 3.81 mm (rightmost point).

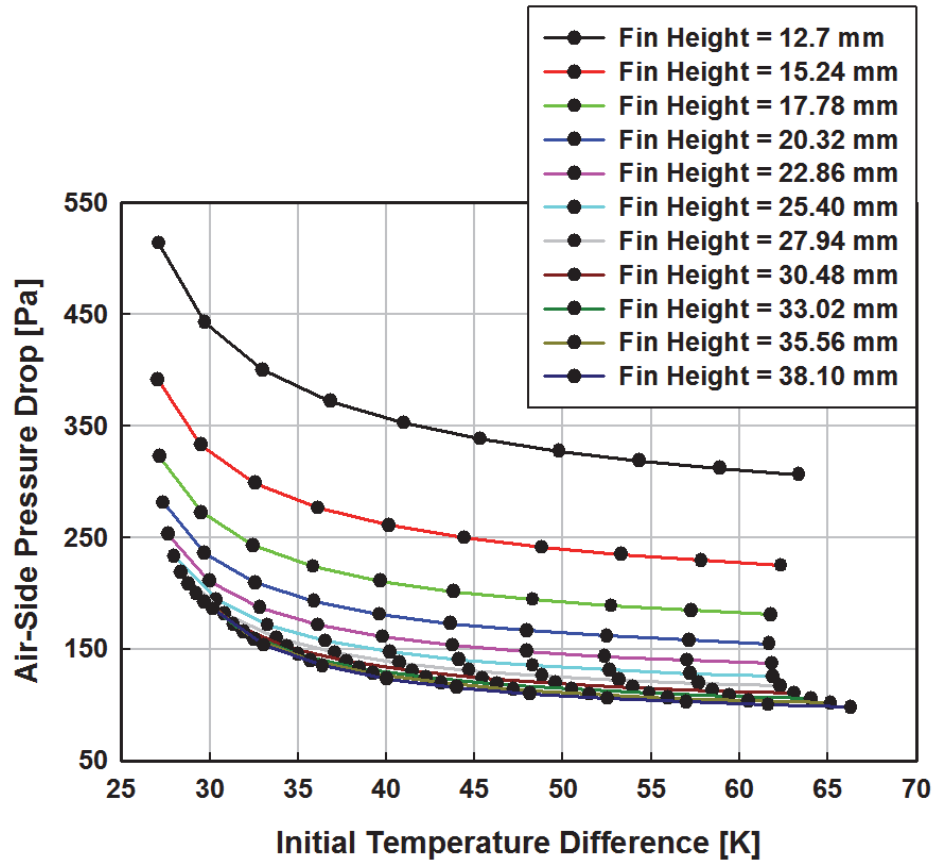


Figure 4.13 Example of plot used to visually eliminate poor performing fin geometry combinations

As previously mentioned, the goal of the parametric studies is to find geometric combinations that result in an ITD of around 27 K with minimal increase in air-side pressure drop. A close up of Figure 4.13 with a focus on an ITD of around 27 K is seen in Figure 4.14. Upon inspection, it is found that none of the predicted ITD values actually reach the goal ITD of 27 K. The cutoff of predicted ITD greater than 27 K corresponds to the fin spacing that is half of the baseline value (2.54 mm).

From a visual inspection of Figure 4.14, lower fin heights result in higher air-side pressure drops for ITDs greater than 28 K. Therefore, fin heights of 12.70 mm and 20.32 mm were eliminated from further consideration. Although the larger fin heights result in

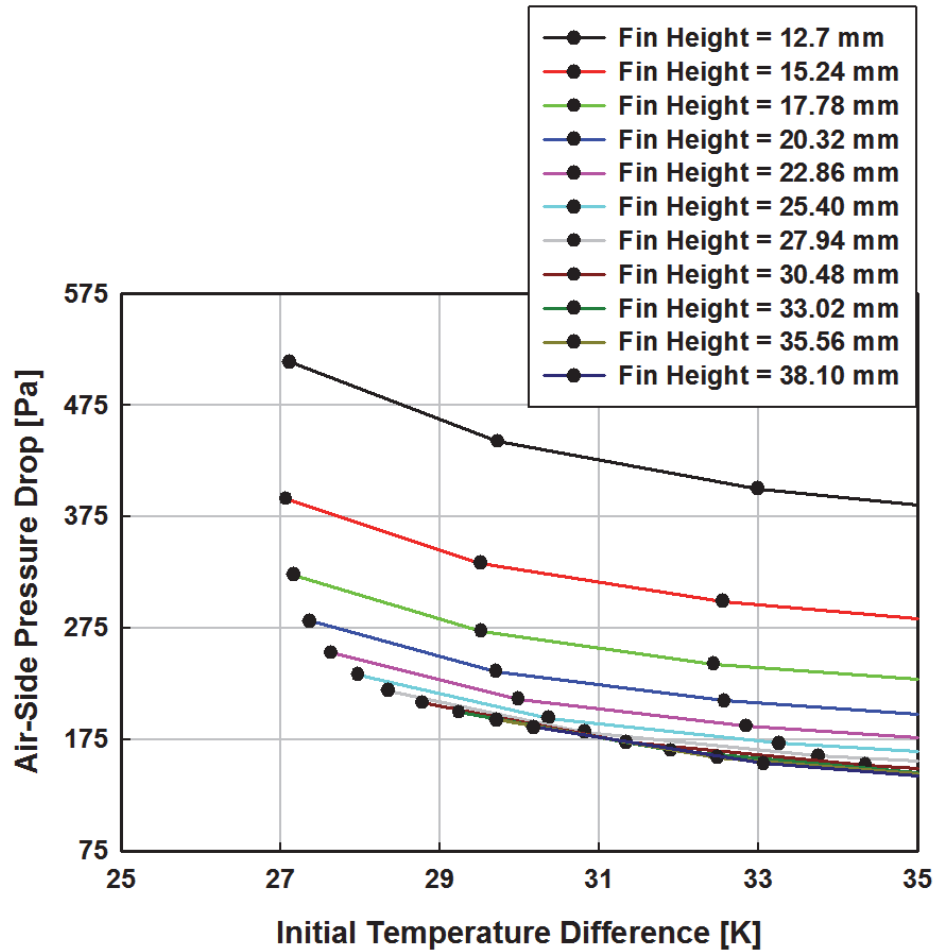


Figure 4.14 Enlargement of plot used to visually eliminate poor performing fin geometry combinations

lower air-side pressure drops for higher values of ITDs, the resulting air-side pressure drop increases more drastically at lower ITD values for each respective fin height. For a fin thickness of 0.254 mm, the lowest air-side pressure drop for an ITD slightly greater than 27 K appears to be somewhere between 180 and 200 Pa. After eliminating the fin heights of 17.78 mm and 20.32 mm, the remaining cases were further refined by increasing the number of analyzed fin spacings to obtain a smoother curve. Predicted performances from the refined studies were plotted in a manner similar to Figure 4.13 and Figure 4.14 to eliminate additional fin heights until an optimal combination of fin dimensions remained.

Results show that the fin spacing had the most influence on condenser performance. Assuming constant fin height and thickness, a 0.282 mm change in fin spacing can reduce the ITD by 2 to 5 K depending on the value of the fin height. For example, with a fin height of 38.1 mm and fin thickness of 0.254 mm, a change in fin spacing from 0.0944 mm to 0.0833 mm resulted in a 3.941 K decrease in ITD (43.98 K to 40.03 K). Another example is when the fin height is 22.86 mm, fin thickness is 0.254 mm, and the fin spacing decreases from 3.81 mm to 3.53 mm. For that 0.282 mm change in fin spacing, the ITD decreases by 4.821 K from 61.828 K to 57.008 K. In comparison, assuming a fin thickness of 0.254 mm and a fin spacing of 2.032 mm, a 2.554 mm change in fin height from 27.94 mm to 25.4 mm results in only a 0.525 K drop in ITD (36.054 K to 35.529 K). After eliminating poor performing cases and comparing the results between different fin thicknesses, the optimum combination of fin geometries to reach an ITD of 27.07 K with a pressure drop of 260.96 Pa was found to be a fin height of 25.4 mm, fin spacing of 1.143 mm, and thickness of 0.254 mm. Even though the 1.143 mm is 0.127 mm less than the minimum fin spacing tested (2.54 mm), it was seen to be a minor enough change to include in the fin dimension combinations used to calculate an ITD of around 27 K and the corresponding pressure drops for the different fin heights in Figure 4.14. A visual comparison of the ITD and air-side pressure drop results from this combination with the baseline combination is shown in Figure 4.15.

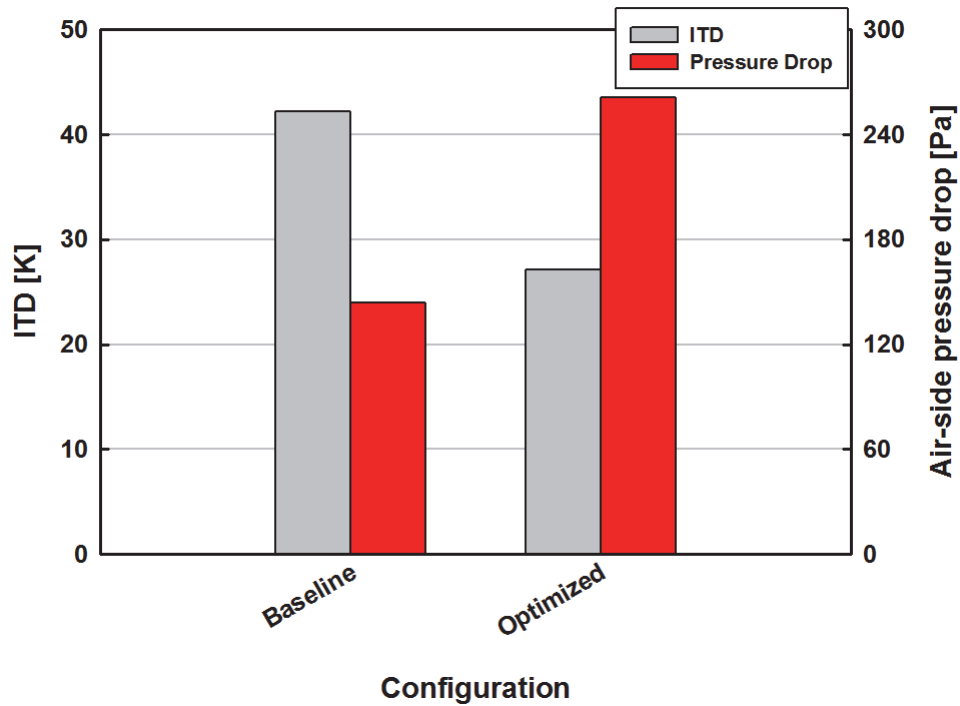


Figure 4.15 Comparison of ITD and air-side pressure drop of the baseline and optimized configurations

When comparing the results of the optimum combination of fin geometries to those from the baseline fin geometry combination (fin height of 25.4 mm, fin thickness of 0.254 mm, and fin spacing of 2.54 mm), the 15.05 K change in ITD corresponds to a pressure drop difference of 117.36 Pa.

4.1.2.2 Wavy Fins

Wavy fins are similar to plain fins, but include oscillations, or waves, in the air-flow direction to induce mixing to improve heat transfer. Geometric parameters that have an impact on the heat transfer and air-side pressure drop characteristics of wavy fins are the fin pitch, fin thickness, fin height, wavelength, and wave amplitude. Both the wavelength, λ , and wave amplitude, M , are labeled in Figure 4.16.

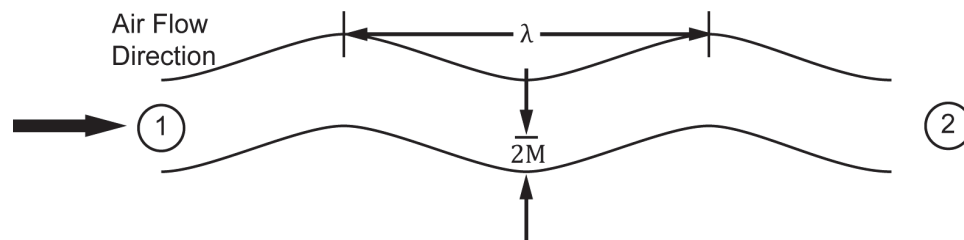


Figure 4.16 Schematic of wavy fin geometry

The straight distance between points one, the air inlet location, and two, air outlet location, is a constant 0.1651 m for all cases. In reality, the addition of the waves increases the fin length between points one and two to some value greater than 0.1651 m. Assuming a constant wavelength, an increase in wave amplitude increases the distance between the highest and lowest points on the fin and, therefore, the overall wavy fin size. If the higher amplitude wavy fin is extended out such that it is flat and compared to a wavy fin with a lower wave amplitude that is also extended to be flat, the wavy fin with the higher amplitude would be longer. Therefore, increasing the wave amplitude of the wavy fin will increase surface area of the fin by extending the actual fin length, leading to a decrease in the bare area of each tube. The greater the wave amplitude, the greater the distance between the peak and valley of each wave, resulting in more turbulence and heat transfer in the flow. However, the larger waves introduce additional flow resistance, leading to a higher

pressure drop. Assuming a fin height of 25.4 mm, fin spacing of 2.54 mm, fin thickness of 0.254 mm, and wavelength of 16.51 mm, the wave amplitude was varied and Colburn j factor and Fanning friction factor were computed using three correlations (Junqi *et al.*, 2007; Ismail *et al.*, 2008; Khoshvaght Aliabadi *et al.*, 2014), as shown in Table 4.4. In general, both the Colburn and Fanning friction factors increased with the increase in wave amplitude. However, the predictions of the three correlations are different from each other.

Table 4.4 Predicted Colburn and friction factors as a function of wave amplitude

M [mm]	Khoshvaght Aliabadi <i>et al.</i> (2014)		Ismail <i>et al.</i> (2008)		Junqi <i>et al.</i> (2007)	
	j	f	j	f	j	f
0.5	0.0046	0.0386	0.0087	0.0169	0.0051	0.0358
0.5625	0.0048	0.0438	0.0089	0.0192	0.0052	0.0369
0.6667	0.0050	0.0528	0.0093	0.0231	0.0054	0.0385
0.75	0.0051	0.0600	0.0096	0.0262	0.0055	0.0397
1.0	0.0055	0.0821	0.0104	0.0358	0.0057	0.0426

Another wavy fin specific parameter investigated is the wavelength, which affects the number of waves along the flow path. Assuming the same fin height, spacing, and thickness as the previous case and a wave amplitude of 0.75 mm, the wavelength was allowed to vary such that there were between two and ten waves along the channel. Results from this analysis are shown in Figure 4.17. An increase in wavelength leads to a decrease in the number of waves, and thus a smoother passage similar to that of a plain fin. This implies less flow resistance and therefore decreases in heat transfer and pressure drop. This trend is reflected in the values predicted by the correlations of Khoshvaght Aliabadi *et al.* (2014) and Ismail *et al.* (2008), where the Colburn j and friction factors monotonically decrease with an increase in wave length. The correlation of Junqi *et al.* (2007), however, predicts an increase in heat transfer and pressure drop as the number of waves decreases.

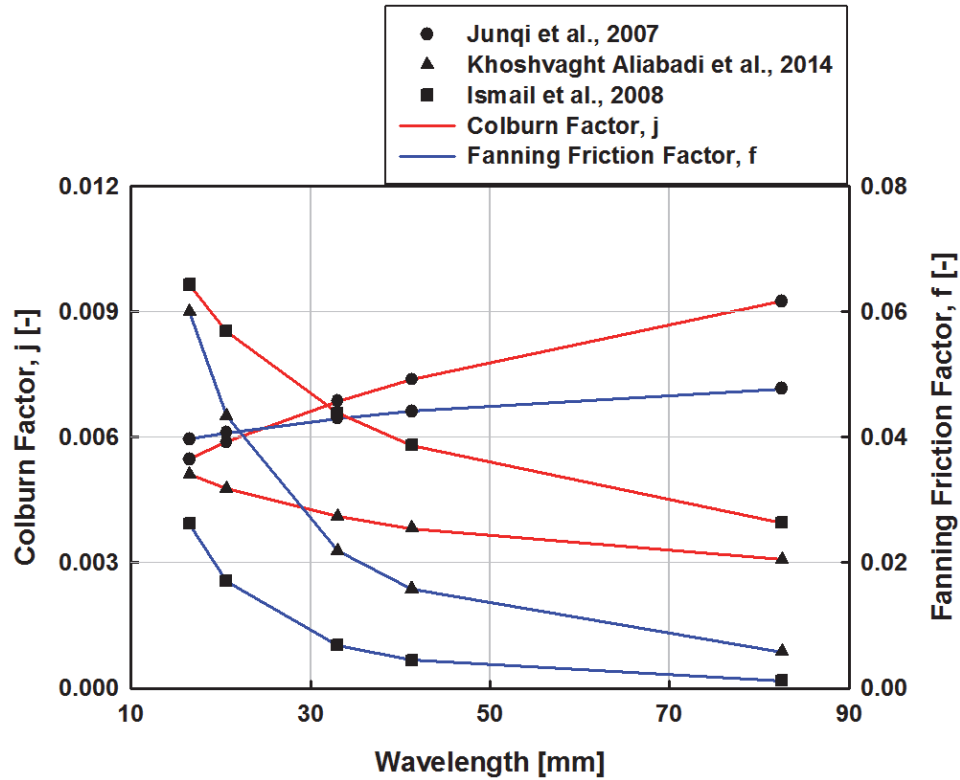


Figure 4.17 Impact of wavelength on Colburn j and friction factors

Because of this questionable trend, the correlation of Junqi *et al.* (2007) was not used for further analyses.

An analysis similar to that conducted for the smooth fins was conducted, in which the parameters were varied and combinations were eliminated based on the predicted performance. Example runs are plotted in Figure 4.18 and Figure 4.19 with an assumed wave amplitude of 0.75 mm and wavelength of 8.255 mm (or 20 waves) to match the average values used by Khoshvagh Aliabadi *et al.* (2014) in the development of their correlation.

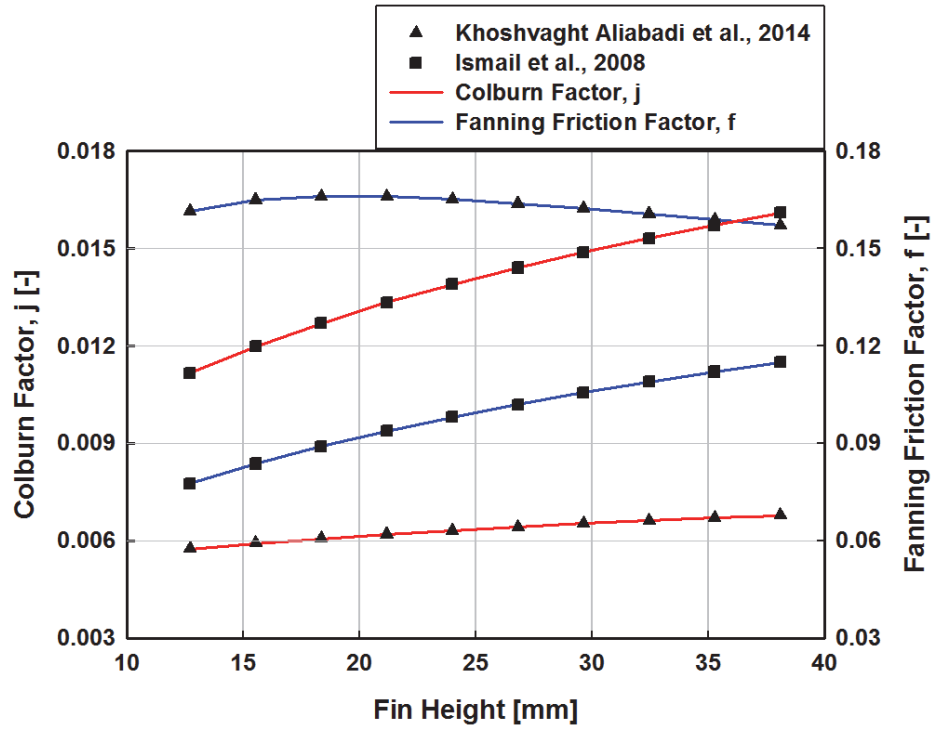


Figure 4.18 Effects of varying fin height on two wavy fin correlations

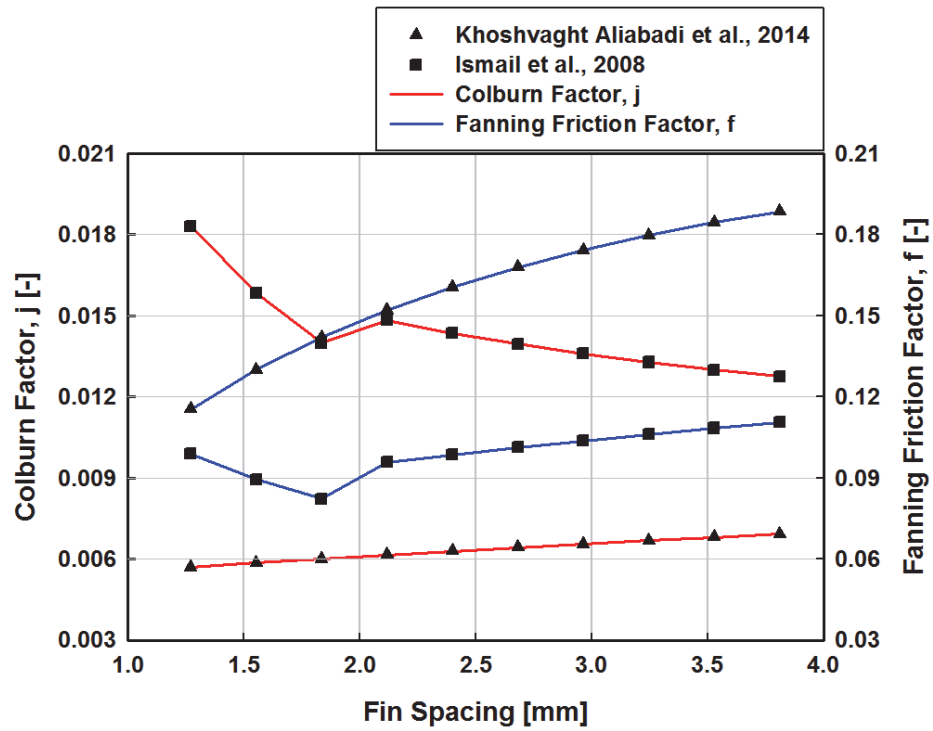


Figure 4.19 Effects of varying fin spacing on two wavy fin correlations

In general, both correlations predicted an increase in heat transfer with an increase in fin height, a trend also evident for the plain fins. There is a slight discrepancy in the friction factor, however, with the friction factor values predicted by the Khoshvaght Aliabadi *et al.* (2014) correlation being fairly constant compared to the increase predicted by the Ismail *et al.* (2008) correlation. Ismail *et al.* (2008) attribute the increase in friction factor to the increase in the aspect ratio and hydraulic diameter that occur as a result of the increase in fin height. The roughly constant predicted friction factors using the Khoshvaght Aliabadi *et al.* (2014) correlation agreed well with the data from Junqi *et al.* (2007), who observed that the fin height had little impact on the friction factor.

The Ismail *et al.* (2008) correlation consists of separate equations for low ($Re < 800$) and high ($Re > 1,000$) Reynolds numbers. The inflection points seen in Figure 4.19 for both the Colburn j and Fanning friction factors at the fin spacing of around 1.8 mm correspond to the jump from the set of equations for the lower Re to those for the higher Re . If the inflection point in the predicted friction factor is neglected, both correlations generally show an increase in friction factor with an increase in fin spacing. However, the predicted Colburn factor trends contradict each other. The Ismail *et al.* (2008) correlation generally predicted a decrease in the Colburn j factor with increasing fin spacing as opposed to the increase predicted by the Khoshvaght Aliabadi *et al.* (2014) correlation.

Predictions of the Ismail *et al.* (2008) correlation are generally more optimistic than those from the Khoshvaght Aliabadi *et al.* (2014) correlation, as can be seen from Table 4.5. Table 4.5 compares ITD versus air-side pressure drop for a wave amplitude of 0.75 mm, wavelength of 8.255 mm, fin spacing between 1.27 and 3.81 mm, fin height of 25.4 mm, and fin thickness of 0.254 mm.

Table 4.5 Comparison between ITD and pressure drop predictions using two sets of wavy fin correlations

F_s [mm]	Khoshvaght Aliabadi <i>et al.</i> (2014)		Ismail <i>et al.</i> (2008)	
	ITD [K]	$\Delta P_{airside}$ [Pa]	ITD [K]	$\Delta P_{airside}$ [Pa]
1.27	33.43	402.52	26.49	363.87
1.91	38.81	326.37	30.27	235.21
2.54	43.75	284.14	32.83	217.73
3.18	48.23	256.57	36.33	197.31
3.81	52.33	236.98	39.92	184.12

At the lowest fin spacing of 1.27 mm, the predicted ITD and pressure drop values differ by 23.16% and 10.09%, respectively, between the two correlations. Both prediction models were validated by their respective authors through comparisons with different experimental results in literature. All but one of the dimensions of the geometric parameters input into the analysis fall within the range of dimensions used in the development of the Khoshvaght Aliabadi *et al.* (2014) correlation. The baseline fin height value of 25.4 mm is at least two times greater than the largest fin height value (10 mm) used in the development of the correlation, leading to potential inaccuracies at the fin heights analyzed here. The Ismail *et al.* (2008) correlation was developed from fin geometric parameters more similar to other baseline geometries. The fin heights used in the development of their correlation ranged from 2 mm to 25 mm, while the fin pitch ranged from 1.0 to 2.18 mm. While these ranges do fall slightly short of the baseline fin height and fin pitch of 25.4 mm and 2.79 mm, respectively, it appears that the Ismail *et al.* (2008) correlation is better suited for this parametric study.

The correlations were used individually to determine if there was a combination that achieved the goal ITD of 27 K with a pressure drop less than the approximately 260 Pa achieved by the plain fins. Using the Khoshvaght Aliabadi *et al.* (2014) correlation, the

lowest ITD for a pressure drop of about 260 Pa is approximately 40 K range. Therefore, according to the predictions of this correlation, while it is possible to reach an ITD of 27 K, it would result in a significantly higher air-side pressure drop than if plain fins were used. For example, for a set of wavy fins with a fin height of 12.7 mm, fin spacing of 1.27 mm, fin thickness of 0.254 mm, wavelength of 16.51 mm, and wave amplitude of 4.00 mm, while the ITD is 27.65 K, the corresponding air-side pressure is 1,578 Pa.

The Ismail *et al.* (2008) correlation predicts different results, showing that air-side pressure drops are comparable to those for plain fins for higher ITD values. For example, an air-side pressure drop of only 124.43 Pa is predicted for one geometric combination (fin height and spacing of 25.4 and 2.54 mm, with a wave amplitude of 2 mm and wavelength of 33.02 mm) that resulted in an ITD of 42.87 K. In general, the pressure drop increases significantly as lower ITDs are achieved. However, there were a few wavy fin geometric combinations, shown in Table 4.6, that rival the pressure drops found for the plain fins. A combination of a wave amplitude of 1 mm, wavelength of 16.51 mm, fin height of 22.86, fin spacing of 1.27 mm, and a fin thickness of 0.254 mm resulted in an ITD of 27.14 K, close to the ITD goal of 27 K, and an air-side pressure drop of 312.84 Pa. While the ITD between this combination and the optimized plain fin combination differs only by 0.07 K (27.14 K versus 27.07 K for the plain fin), the air-side pressure drop of the wavy fin combination is 51.88 Pa greater than the 260.96 Pa that results from the plain fin combination.

Table 4.6 Summary of dimension combinations for wavy fins to reach an ITD of 27 K using the Ismail *et al.* (2008) correlation

		Combination			
		1	2	3	4
M	mm	1	1	1	0.5
λ	mm	16.51	16.51	20.64	8.26
# waves	-	10	10	8	20
F_h	mm	22.86	25.4	20.32	27.94
F_s	mm	1.27	1.27	1.27	1.27
t	mm	0.254	0.254	0.254	0.254
ITD	K	27.14	27.40	27.40	27.23
$\Delta P_{airside}$	Pa	312.84	294.21	319.08	330.62

While the correlations of Ismail *et al.* (2008) resulted in promising results, it is worth remembering that it is difficult to accurately predict wavy fin performance due to the wide number of parameters that have to be taken into consideration.

4.1.2.3 Louvered Fins

The final fin geometry considered is the louvered fin. For this parametric study, variations in the air channel width and height, louver angle, louver length, louver pitch, and number of louver banks were considered. Performance of louvered fins was predicted using the heat transfer and pressure drop correlations of Kim and Bullard (2002), as well as those of Park and Jacobi (2009). Predictions from these models are functions of all but two of the same geometric parameters, fin depth and the number of louver banks. As expected, an increase in the fin depth increases the total fin and outer surface area available for heat transfer, with a corresponding increase in frictional pressure loss. To be consistent

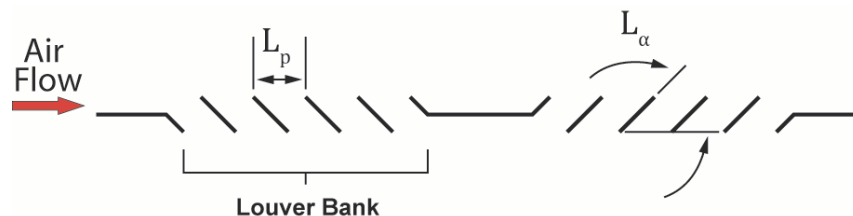


Figure 4.20 Cross-sectional view of louver fin

with the baseline condenser geometry, the fin depth was maintained at the original 0.1651 m. A cross-sectional view of the louvered fin is seen in Figure 4.20.

The database used to develop the generalized correlation for Park and Jacobi (2009) consisted of test sections that had between one and four louver banks, with the majority being two-louver banks. An increase in the number of louver banks decreases both the Colburn j and friction factors.

The heat exchanger data used by Kim and Bullard (2002) consisted of two louver banks, so the number of louver banks for the correlation of Park and Jacobi (2009) was set to two as well to more easily compare the predictions between the models. Similar to the plain and smooth fin runs, a decrease in the air channel height or fin spacing resulted in a decrease in the ITD and an increase in the air-side pressure drop. In a manner similar to the case for the plain fin, a decrease in air channel area results in an increase in the flow velocity through the channel. A decrease in air channel area due to a decrease in the fin spacing results in additional fins per tube, and therefore, an increase in the overall heat transfer area. Decreasing the air channel, or fin height, to decrease the air channel area will increase the number of tubes, and therefore total number of fins, per condenser, resulting in an overall increase in heat transfer area.

Assuming baseline fin dimensions, louver length of 22.86 mm, and louver pitch of 1.5 mm, the Colburn j and Fanning friction factors as a function of louver angle are shown in Figure 4.21.

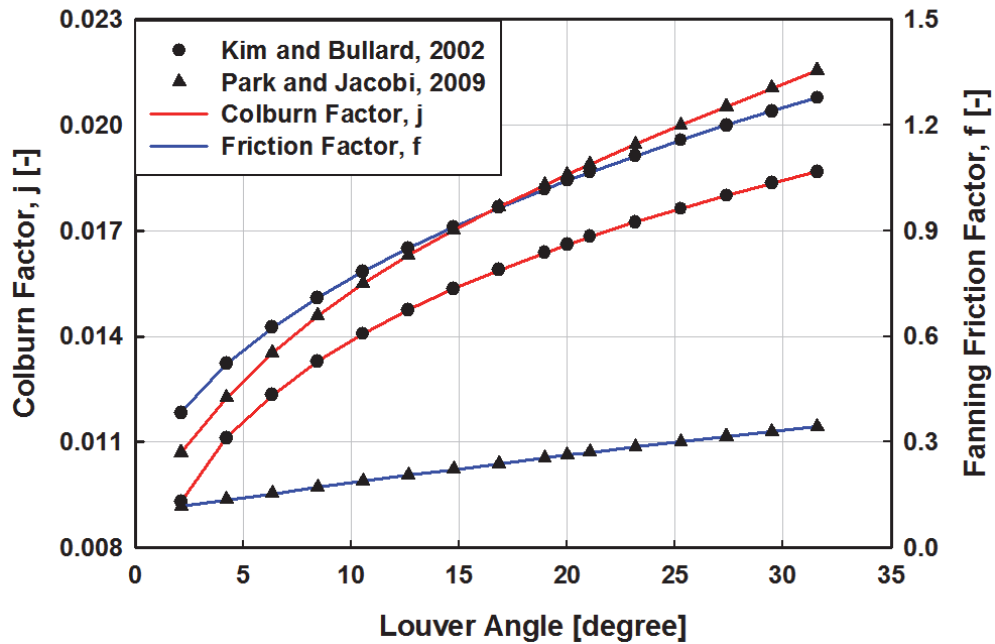


Figure 4.21 Colburn j and friction factors as a function of louver angle

In general, Colburn j and friction factors increase with an increase in louver angle. An increase in louver angle leads to larger flow turning and losses, thereby increasing the Colburn j and friction factors. For this case, the Colburn j factors predicted by the two models differ by an insignificant amount. This is not the case for the friction factor, where the friction factor predicted using the Kim and Bullard (2002) correlation is between three and four times greater than the friction factor predicted using the Park and Jacobi (2009) correlation. Assuming a louver length of 22.86 mm, louver pitch of 6.35 mm, fin height of 25.4 mm, fin spacing of 2.54 mm, and fin thickness of 0.254 mm, ITD values predicted by the correlations of Kim and Bullard (2002) and Park and Jacobi (2009) for a louver angle of 30 degrees were 33.58 and 30.85 K, respectively. While the two models predicted similar ITD values, the corresponding pressure drops are 610.19 Pa and 369.7 Pa, a difference of about 49%.

Table 4.7 Performance predictions as a function of louver pitch

Louver pitch [mm]	Kim and Bullard (2002)		Park and Jacobi (2009)	
	j	f	j	f
1.20	0.0173	1.209	0.0168	0.2758
1.35	0.0169	1.118	0.0179	0.2688
1.50	0.0166	1.042	0.0186	0.2628
1.65	0.0163	0.9778	0.0191	0.2575
1.80	0.0161	0.9227	0.0194	0.2527

Results from varying the louver pitch, the distance between the louvers along the fin, predicted by both correlations, are presented in Table 4.7. For this analysis, the fin height, fin spacing, and fin thickness dimensions are 25.4 mm, 2.54 mm, and 0.254 mm like the baseline configuration, the louver angle is 20°, the louver length is 22.86 mm, and the number of louver banks is two. The louver angle was chosen as the minimum tested angle because some of the databases used in the development of the model of Park and Jacobi (2009) included louvered fins with angles in the 20 to 30 degree range, the louver length was chosen to represent 90% of the fin height of 25.4 mm, and two was the number of louver banks most common in the databank.

As the louver pitch increases, the number of louvers on the fins decrease and the fin essentially becomes more like a smooth, plain fin. Friction factors predicted by both correlations decrease with the increase in louver pitch. However, the predicted heat transfer coefficient decreases according to the model of Kim and Bullard (2002) in contrast to the increase predicted by the model of Park and Jacobi (2009).

Louver length, i.e., the length of each of the louvers along the fin height, was also varied from 50 to 90% of the fin height of 25.4 mm, at a louver angle of 20 degrees. The fin height, fin spacing, and fin thickness were left at the baseline values, and predicted Colburn j and friction factor values as functions of the louver length from both of the

correlations are listed in Table 4.8. An increase in louver length allows for more flow along the louver paths. This causes more mixing, and therefore increases the Colburn j and friction factor values.

Table 4.8 Predicted Colburn j and friction factor values as a function of louver length

L_{louver} [mm]	Kim and Bullard		Park and Jacobi	
	j [-]	f [-]	j [-]	f [-]
12.70	0.0111	0.3273	0.0135	0.1796
15.24	0.0126	0.4688	0.0149	0.2021
17.78	0.0140	0.6351	0.0162	0.2233
20.32	0.0153	0.8262	0.0174	0.2435
22.86	0.0166	1.042	0.01869	0.2628

Five geometric parameters associated with louver fins were varied, as discussed above, and the predicted performances that resulted from each combination were compared amongst themselves and to the baseline, smooth fin result. While it was possible to achieve the goal ITD of about 27 K as predicted by both correlations, air side pressure drops are greater than those for the plain fin cases. For example, a louvered fin with a fin height of 20.32 mm, fin spacing of 1.524 mm, fin thickness of 0.254 mm, louver angle of 30 degrees, louver pitch of 6.5 mm, and a louver length of 13.72 mm would result in an ITD of 27.49 K and an air-side pressure drop of 1884.26 Pa when predicted using the correlation of Kim and Bullard (2002). In contrast, louvered fins with the exact same dimensions yield an ITD of 25.38 K and an air-side pressure drop of 1,030.4 Pa when the predicted by the Park and Jacobi (2009) correlation. If the Park and Jacobi (2009) correlation is used, louvered fins with a louver angle of 30 degrees, louver pitch of 7 mm, fin spacing of 2.54 mm, fin height of 12.7 mm, and fin thickness of 0.254 mm can result in an ITD of 27.03 K and an air-side pressure drop of 623.4 Pa. While this combination does reach the goal ITD of 27 K, the

air-side pressure drop of 623.4 Pa associated with it is over two times the air-side pressure drop (260.96 Pa) that results with the optimized plain fins.

The values predicted by the two correlations, especially the pressure drop, differ significantly, leading to high uncertainties in the prediction of the actual pressure drops for the ACC under consideration. Park and Jacobi (2009) noted that their own correlation performed better than the Kim and Bullard (2002) correlation at predicting the Colburn j factor for the heat exchangers tested by Kim and Bullard (2002). Also, Park and Jacobi (2009) found that the correlation of Kim and Bullard (2002) only worked well at predicting the friction factor in their database, and not results of other data sets.

4.1.2.4 Fins with Auto-Flutter Reeds

Preliminary experimental data were obtained by members of the Fluid Mechanics Research Laboratory at the Georgia Institute of Technology for a 101.6 mm long test section composed of five 1.778 mm thick channels 10 mm high and spaced 2.54 mm apart. A picture of an example test section for the reed experiments is shown in Figure 4.22

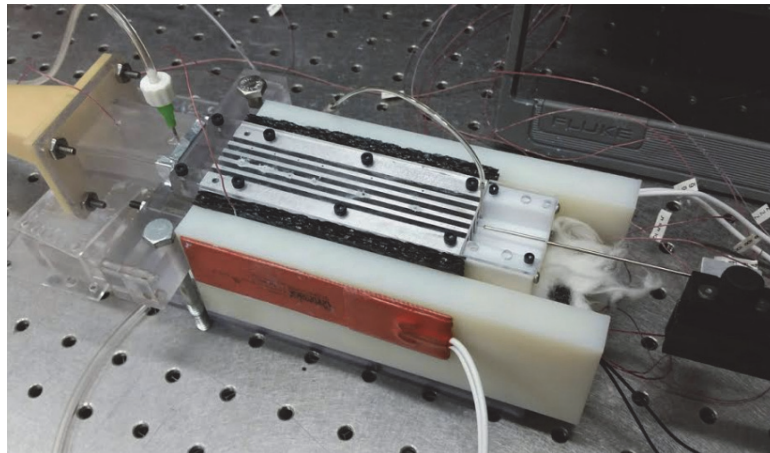


Figure 4.22 Test section used for the reed experiments (Crittenden and Glezer, 2015)

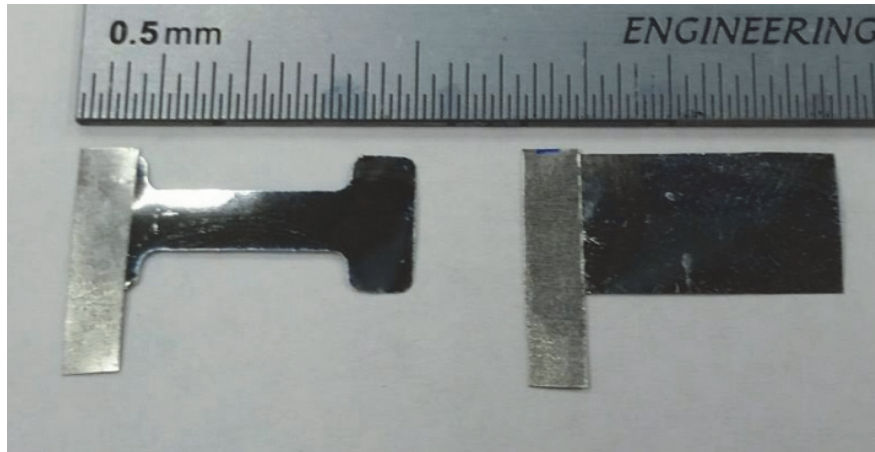


Figure 4.23 A “H” (left) and rectangular (right) that will be inserted into the channels (Crittenden and Glezer, 2015)

Figure 4.23 shows an “H” reed, which will be tested in the future, and a rectangular reed that can be inserted into the test section and enhance the air-side heat transfer.

For air at 22.75°C entering the channels at $0.001 \text{ m}^3 \text{ s}^{-1}$, preliminary data resulted in heat transfer coefficients of 55.98 and $99.59 \text{ W m}^{-2} \text{ K}^{-1}$ for the cases without and with the reeds installed, which corresponded to pressure drops in the channel of 95.62 and 143.7 Pa, respectively. Thus, the reeds have the ability to enhance heat transfer by 1.78 times with only a 1.50 times increase pressure drop. Based on the enhanced heat transfer and pressure drop ratios from this case, the ITD and air-side pressure drop at the baseline dimensions are 34.21 K and 157.98 Pa, respectively. These predictions can be made with greater certainty when more data over a range of geometric parameters and operating conditions are available.

Implementing plain, plain with reeds, wavy, and louvered fins into the design of ACCs can lead to improvements in the ITD. A comparison of the ITD and resulting air-side pressure drop from using each of the different fin combinations is shown in Figure 4.24.

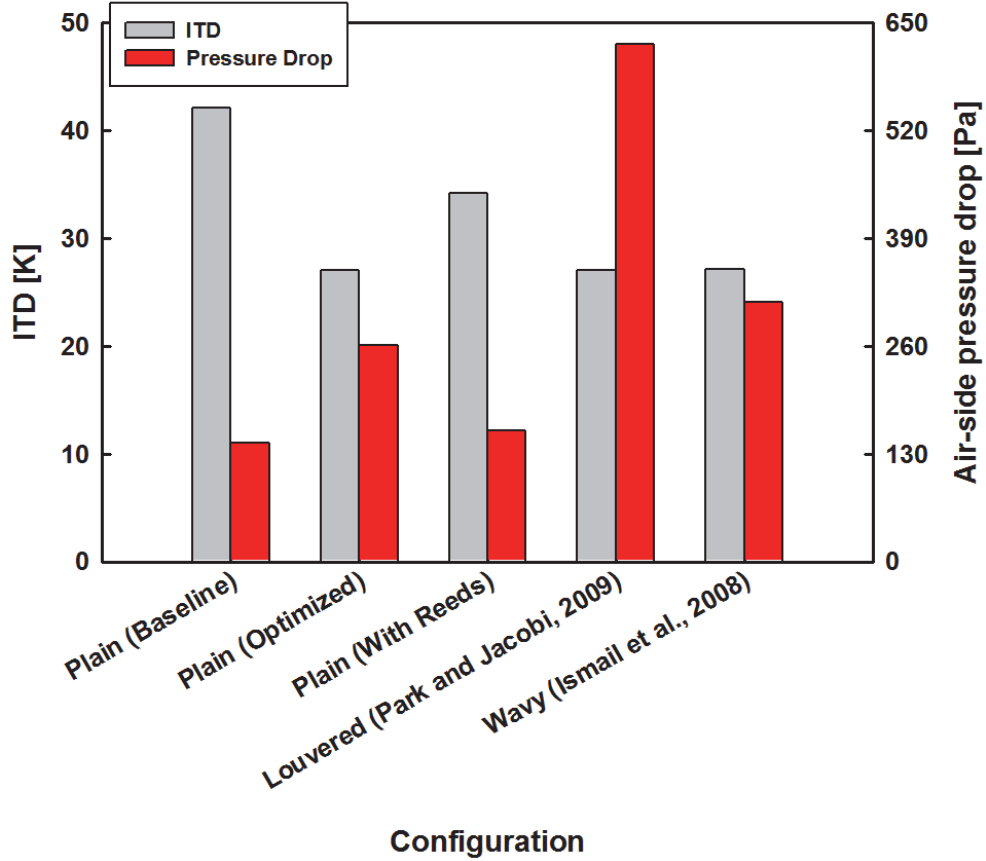


Figure 4.24 ITD and air-side pressure drop comparison for the different fin configurations in the stand-alone condenser

Values of the ITD, air side pressure drop, and amount of heat rejected from each individual ACC for the different fin configurations shown in Figure 4.24 are displayed in Table 4.9.

Table 4.9 Summary of ITD, air side pressure drop, and amount of heat rejected from each individual ACC for different fin types

	Plain (Baseline)	Plain (Optimized)	Plain (Reed)	Louvered (Park and Jacobi, 2009)	Wavy (Ismail <i>et al.</i> , 2008)
ITD [K]	42.12	27.07	34.21	27.03	27.14
$\Delta P_{airside}$ [Pa]	143.59	260.96	157.98	623.41	312.84
$\dot{Q}_{indiv.,condenser}$ (1 ACC) [MW]	15.318	15.537	15.435	15.539	15.536

Changing the plain fin dimensions, adding the AFRs, or switching to other fin types can all result in a decrease in ITD from the original 42.12 K to close to the goal ITD of 27 K. The corresponding air-side pressure drop values, and therefore the resulting detrimental fan power, range significantly from only around 260 kPa for the plain fin case all the way to 623 kPa for the louvered case. Therefore, if choosing the fin configuration for optimal ACC performance was done solely based on the ITD and picking the one with the least air-side pressure drop, the best choice would be to simply change the dimensions of the plain fins. A plain fin dimension change from a fin height of 25.4 mm, fin spacing of 2.54 mm, and a fin thickness of 0.254 mm to 25.4 mm, 1.143 mm, and 0.254 mm, respectively, would result in the an ITD of 27.07 mm and air-side pressure drop of only 260.96 Pa.

4.2 Power Plant Cycle Model

While improving stand-alone condenser performance is important, the main goal is to optimize the condenser to enhance overall cycle performance. Baseline operating conditions and component efficiencies as specified in Chapter 3.2 were used along with the condenser predictions to explore condenser configurations that could lead to better plant level performance.

4.2.1 Rankine Cycle Model

State points of the Rankine cycle are labeled in Figure 4.25, and the resulting values at these points, as well as important values to consider for the baseline geometry smooth fins and smooth fins with a reduction in fin spacing, F_s , are summarized in Table 4.10. For both of the cases shown in Table 4.10, the fin height is 25.4 mm and the fin thickness is 0.254 mm.

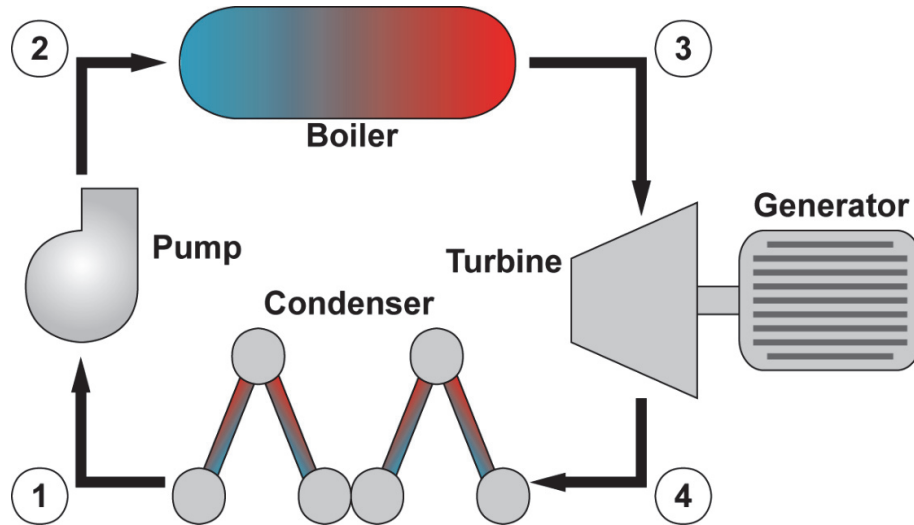


Figure 4.25 State points of the Rankine Cycle

Table 4.10 Summary of property values at the different state points and key values to consider for plain fins with a fin height of 25.4 mm and fin thickness of 0.254 mm

State	Baseline ($F_s = 2.54$ mm)		Reduced F_s ($F_s = 1.27$ mm)	
	T [°C]	P [kPa]	T [°C]	P [kPa]
1	69.78	34.4	56.94	19.92
2	70.79	16,529	57.82	16,529
3	550	16,529	550	16,529
4	67.44	30.46	55.64	16.25

Key Values		Baseline	Reduced F_s
x_4	-	0.8899	0.8738
ITD	K	39.44	25.64
$\Delta P_{\text{pairside}}$ (1 ACC)	Pa	143.9	233.5
$\dot{W}_{\text{fan,condenser}}$ (1 ACC)	kW	145.2	235.7
$\dot{Q}_{\text{condenser,total}}$ (70 ACCs)	MW	1,006.6	1001.1
\dot{Q}_{boiler} (70 ACCs)	MW	1,531	1,557
$\dot{W}_{\text{total,fan}}$ (70 ACCs)	MW	10.17	16.5
\dot{W}_{pump} (70 ACCs)	MW	8.67	8.62
\dot{W}_{turbine} (70 ACCs)	MW	522.3	554.6
$\dot{W}_{\text{net,cycle}}$	MW	503.5	529.4
η_{cycle}	%	32.89	34.00

The difference between the baseline and the optimal smooth, plain fin case compared in Table 4.10 is the width of the air channel, or the fin spacing. The reduction in fin spacing increases the number of fins per condenser, and therefore the overall surface area for heat transfer. However, the increase in the number of fins per condenser leads to a decrease in the available free flow area, thus increasing the air flow velocity. Thus, while the total amount of heat removed from the condenser decreased with a reduction in fin spacing, the required parasitic fan power per condenser increased.

Under the same operating conditions, the condenser inlet temperature (point 4) for the adjusted fin configuration is less than that of the baseline fin configuration, leading to lower turbine backpressures and, therefore, higher turbine work output. Also, the lower condenser and pump outlet temperature requires a higher heat input to the boiler to achieve the set boiler pressure and outlet temperature. This is due to the greater temperature difference between the pump outlet at point 2 to the boiler exit at point 3 for the adjusted case than the baseline case, which had values of 492.18 K and 479.21 K, respectively. Although the sum of the required fan and pump work increases by 6.28 MW (18.84 MW to 25.12 kW) with the reduction in fin spacing, the overall turbine work output, and therefore net base work output from the generator, increases by 25.9 MW (503.5 to 529.4 MW). The overall cycle efficiency for this case is 34.00%, close to the average cycle efficiency of coal-based electricity generating plants installed in the United States of 34% (Beér, 2007). The 1.11% increase in efficiency from 32.89% to 34.00% can lead to significant cost savings for electricity generation. This analysis shows that changes to geometric parameters while retaining the plain fin configuration can yield improvements in plant level performance.

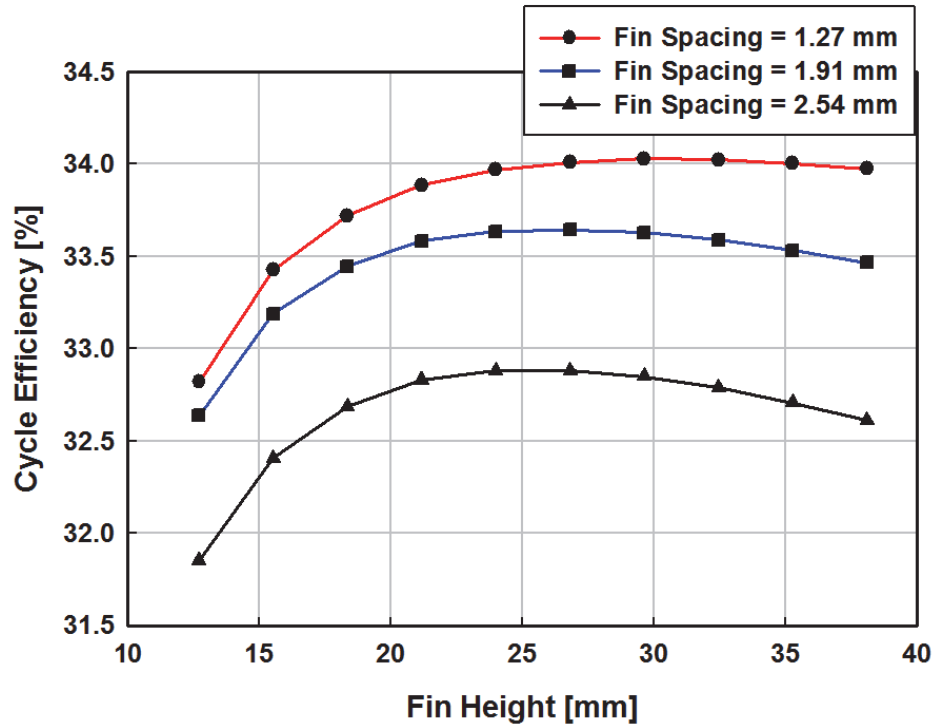


Figure 4.26 Rankine Cycle efficiency as a function of fin height and fin spacing

Simultaneously varying the fin height and fin spacing, shown in Figure 4.26, can also slightly increase the cycle efficiency. As previously discussed, a decrease in fin spacing results in an increase in cycle efficiency. It is interesting to note that as the fin spacing decreases, a larger fin height is needed in combination with it to achieve maximum cycle efficiency. Assuming a fin spacing of 2.54 mm, the maximum cycle efficiency of 32.88% occurred at a fin height of about 24 mm. In contrast, the maximum cycle efficiency of 34.03% at the fin spacing of 1.27 mm occurred at a fin height of about 30.48 mm. The greater fin height resulted in a larger tube pitch and therefore less tubes and air channels.

As discussed in Chapter 4.1.2.1, an increase in fin height decreases the number of tubes and air channels present in the ACC. However, the area of each fin increases because of the longer height, resulting in an increase of the total fin area per tube and a decrease in the fin efficiency. The velocity of the air also decreases with increasing fin height because

of the increasing channel size, resulting in an overall decrease in the required fan power. Like the stand-alone condenser analysis, varying the fin height results in some maximum effective area for the ACC, which corresponds to the lowest temperature and pressure at the condenser inlet at point 4 and, therefore, the point of greatest turbine work output. It is interesting to note, however, that the fin height that results in the highest turbine work does not necessarily correspond to the fin height at which the highest cycle efficiency occurs. Computed values of ITD, and total turbine, pump, and fan work for a fin spacing of 2.54 mm and fin thickness of 0.254 mm are presented in Table 4.11. From this table, even though the maximum turbine work occurs for a fin height of 21.17 mm, the maximum efficiency of the cycle results from a fin height of 24.00 mm.

Table 4.11 Rankine Cycle performance results as a function of fin height

Fin Height [mm]	ITD [K]	$\dot{W}_{turbine}$ [MW]	\dot{W}_{pump} [MW]	$\dot{W}_{total,fan}$ [MW]	\dot{Q}_{boiler} [MW]	$\dot{W}_{net,base}$ [MW]	η_{cycle} [%]
12.7	40.42	520.1	8.675	24.40	1,529.0	487.0	31.85
21.17	38.91	523.6	8.669	11.96	1,531.9	502.9	32.83
24.00	39.23	522.8	8.670	10.67	1,531.3	503.5	32.88
32.46	41.30	518.1	8.678	8.63	1,527.3	500.8	32.79
38.10	43.35	513.4	8.687	7.96	1,523.3	496.8	32.61

From this set of parameters, the lowest ITD of 38.91 K occurs at a fin height of 21.17 mm. However, the maximum cycle efficiency is not at the fin height of 21.17 mm, but at 24.00 mm where the net cycle work is the highest. At the fin height of 21.17 mm, the low ITD corresponds to a condenser saturation pressure (33.66 kPa) less than that of the 24.00 mm fin height case (34.09 kPa), and therefore, the greatest turbine work output. The overall negative work from the fans and the pumps of 20.63 MW for a fin height of 21.17 mm is greater than the 19.34 MW negative work for a fin height of 24.00 mm. While

the turbine work output for the 21.17 mm is greater than the work output for the 24.00 mm case (523.6 MW compared to 522.8 MW), this increase is not great enough to offset the increase in negative work from the fans and pumps, resulting in approximately 0.5 MW less net work. Therefore, while the ITD is a good indicator of the inlet conditions that will result in the greatest turbine output, the maximum cycle efficiency might not occur under the same circumstances. After comparing results of different fin height and fin spacing combinations, it was found that a fin height of 29.21 mm and a fin spacing of 1.27 mm result in a cycle efficiency of 34.03%, the highest cycle efficiency for the given set of operating conditions and assumptions.

For the analysis of wavy fins, two additional parameters were considered: wave amplitude and wavelength. With a constant fin height of 25.4 mm, fin thickness of 0.254 mm, wavelength of 16.51 mm, and fin spacing ranging from 1.27 mm to 2.54 mm, an

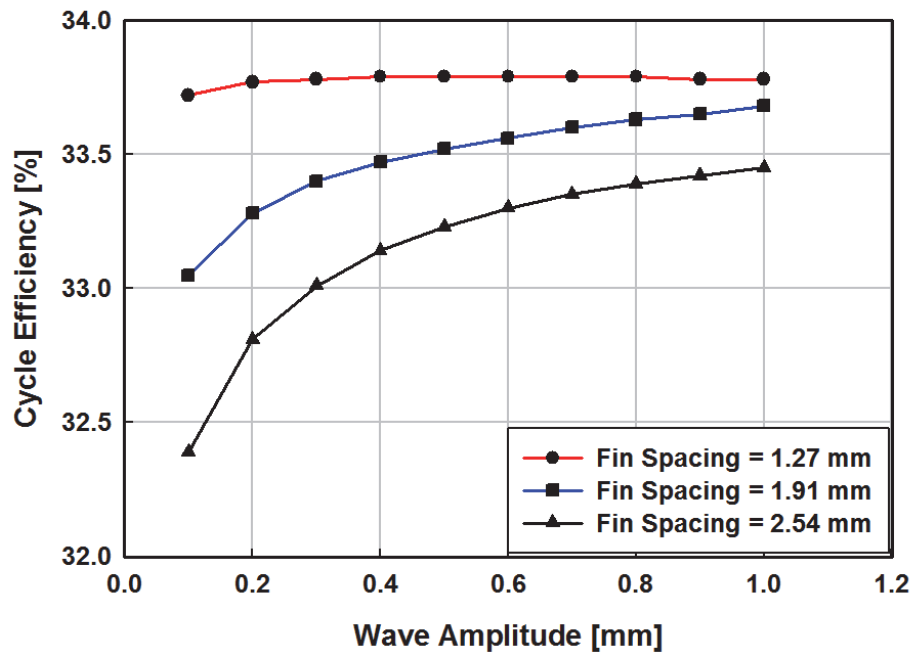


Figure 4.27 Rankine Cycle efficiency as a function of wave amplitude and fin spacing

increase in the wave amplitude corresponds to an increase in the cycle efficiency, as seen in Figure 4.27.

While the fin efficiency and effective areas decrease with the increasing wave amplitude, the air-side heat transfer coefficient increases due to the additional mixing within the channels and, therefore, decreasing the ACC inlet and outlet temperatures and pressure. Although the mixing also induces higher air-side pressure drop and therefore required fan power, the turbine work also increases. The increase in turbine work is enough to offset the increase in negative work from the pump and the fans, yielding an overall net increase in cycle efficiency. Representative values for these effects for a fin with a fin height of 25.4 mm, fin thickness of 0.254 mm, fin spacing of 2.54 mm, and wavelength of 16.51 mm are shown in Table 4.12.

Table 4.12 Representative values for wavy fins in the Rankine Cycle due to a change in wave amplitude

Wave Amplitude [mm]	ITD [K]	$\dot{W}_{turbine}$ [MW]	\dot{W}_{pump} [MW]	$\dot{W}_{total, fan}$ [MW]	\dot{Q}_{boiler} [MW]	$\dot{W}_{net, base}$ [MW]	η_{cycle} [%]
0.1	45.17	509.3	8.694	8.343	1,519.7	492.2	32.39
0.5	36.81	528.4	8.660	9.360	1,536.0	510.4	33.23
1	33.94	535.1	8.649	10.74	1,541.5	515.7	33.45

For a fin height of 25.4 mm, fin thickness of 0.254 mm, and wave amplitude of 1 mm, cycle efficiency as a function of the wavelength and fin spacing is shown in Figure 4.28. The points in the figure correspond to 13, 10, 7, 5, and 2 waves, respectively, where the increase in wavelength corresponds to a decrease in the number of waves. An increase in the wavelength decreases the amount of mixing the air experiences as it flows through the channels, reducing the required fan power and the air-side heat transfer coefficient. The decrease in the air-side heat transfer coefficient results in an increase in the ACC inlet

temperature (point 4 in the cycle model), and therefore a decrease in the turbine work. A longer wavelength also results in a higher ACC steam outlet temperature and pressure. The pump work increases somewhat due to a combination of a higher specific volume and a lower required pressure rise, while the boiler heat input decreases due to the lower heat input required to raise the water temperature back to the set temperature at the turbine inlet.

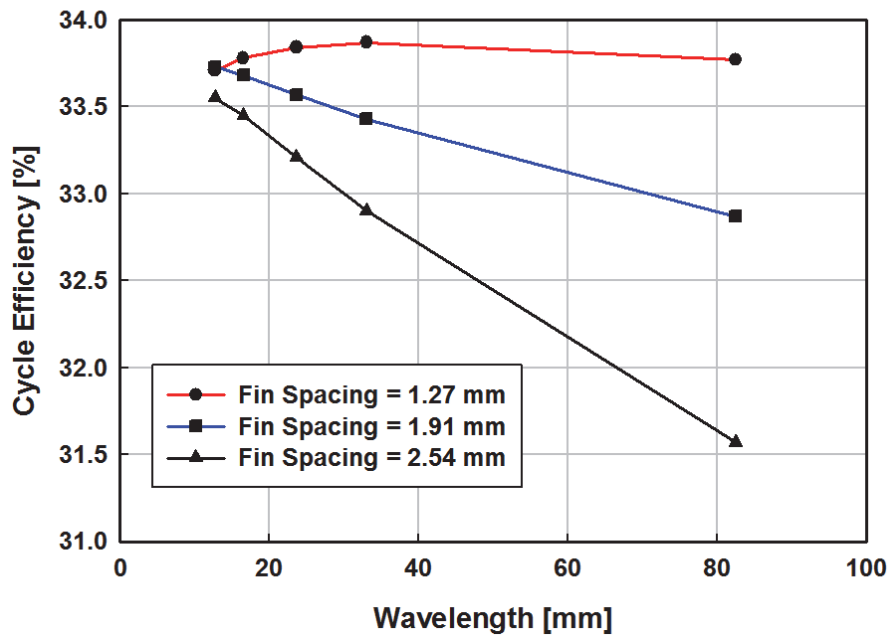


Figure 4.28 Rankine Cycle efficiency as a function of wavelength and fin spacing

Representative values for the turbine, pump, and fan work for a fin with a height of 25.4 mm, thickness of 0.254 mm, fin spacing of 2.54 mm, wave amplitude of 0.5 mm, and various wavelengths are shown in Table 4.13.

Table 4.13 Representative values for wavy fins in the Rankine Cycle due to a change in wavelength

λ [mm]	ITD [K]	$\dot{W}_{turbine}$ [MW]	\dot{W}_{pump} [MW]	$\dot{W}_{total, fan}$ [MW]	\dot{Q}_{boiler} [MW]	$\dot{W}_{net, base}$ [MW]	η_{cycle} [%]
33.02	44.12	511.7	8.690	8.451	1521.8	494.5	32.50
23.59	40.22	520.5	8.674	8.747	1529.4	503.1	32.90
12.70	34.68	533.3	8.652	10.17	1540.1	514.5	33.41

After running the parametric analyses for the wavy fins, it was found that a combination of wavy fins with a fin height of 30.48 mm, fin spacing of 1.27 mm, fin thickness of 0.254 mm, wave amplitude of 1 mm, and wavelength of 33.02 mm resulted in the highest wavy fin cycle efficiency of 33.90%.

The influence of louvered fins in the cycle is dependent on the louver angle, louver length, and louver pitch in addition to the fin height, fin spacing, and fin thickness dimensions common to the plain fin. For a fin height of 25.4 mm, fin thickness of 0.254 mm, louver angle of 30 degrees, and two louver banks, cycle efficiency as a function of the louver pitch with a fin spacing of 1.27, 1.91, and 2.54 mm is plotted in Figure 4.29. An increase in the louver pitch decreases the number of louvers per fin, therefore theoretically decreasing the heat transfer coefficient. The fin efficiency, overall surface efficiency, and effective heat transfer area therefore increase as a result. However, the air-side thermal resistance increases due to the decrease in the heat transfer coefficient, decreasing the UA and heat transfer capability of the condenser and increasing the ITD. Because there are less louvers, the required fan power decreases. Even though the turbine work decreases because of the lower condenser heat transfer ability and higher ITD and condenser inlet temperature, the overall cycle efficiency increases. This trend is most clearly shown for the fin spacing of 1.27 mm. For the fin spacing of 1.91 mm and 2.54 mm, there were some fluctuations in some of the intermediate Colburn factor calculations due to the use of some trigonometric functions in the correlations. These fluctuations in the Colburn factor meant the resulting air-side heat transfer coefficient would not decrease monotonically, ultimately being also reflected in the variation of the cycle efficiency.

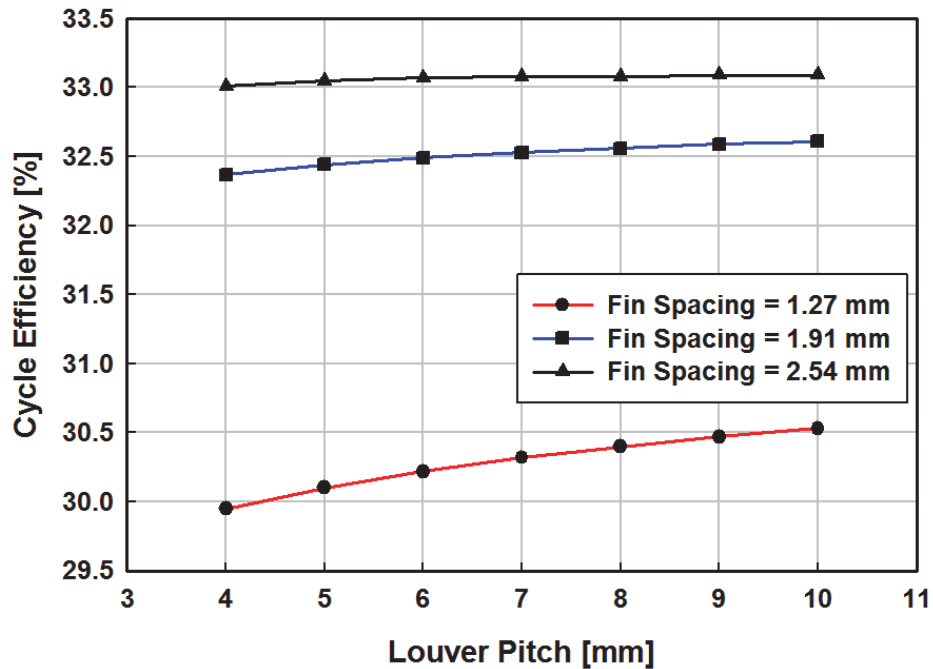


Figure 4.29 Rankine Cycle efficiency as a function of louver pitch for fin spacings of 1.27, 1.91, and 2.54 mm

It is interesting to note that the cycle efficiency increased as the fin spacing increased. This is in contrast to the case of the wavy fins and the plain fins, where the decrease in fin spacing resulted in the higher cycle efficiency. A decrease in fin spacing for the louvered fins increases the air velocity through each channel, as is also the case for the wavy and plain fins, inevitably increasing the corresponding fan power. Even though the decrease in spacing does increase the air-side heat transfer coefficient and, therefore, the turbine work, it was not enough to overcome the increase in fan work. For the fin spacings of 1.27 mm and 2.54 mm with a louver pitch of 5 mm shown in Figure 4.29, the turbine work associated with a fin spacing of 2.54 mm is 548.7 MW in comparison to 558.5 MW for the fin spacing of 1.27 mm case. However, this approximately 10 MW difference is not enough to overcome the large increase in required fan power, with values of 80.11 MW for the 1.27 mm case versus 27.03 MW for the 2.54 mm case. Values for the turbine, fan, and

pump work for three different louver pitches for a fin with a height of 25.4 mm, fin thickness of 0.254 mm, louver angle of 30 degrees, louver length of 22.86 mm, two louver banks, fin spacing of 1.27, 1.91, and 2.54 mm are shown in Table 4.14.

Table 4.14 Representative values for louvered fins in the Rankine Cycle as a function of louver pitch

F_s [mm]	L_{pitch} [mm]	$\dot{W}_{turbine}$ [MW]	\dot{W}_{pump} [MW]	$\dot{W}_{total, fan}$ [MW]	\dot{Q}_{boiler} [MW]	$\dot{W}_{net, base}$ [MW]	η_{cycle} [%]
1.27	4	558.7	8.612	82.7	1,560.6	467.3	29.95
1.27	7	558.0	8.613	76.4	1,560.1	473.0	30.32
1.27	10	557.5	8.614	72.8	1,559.6	476.1	30.53
1.91	4	554.2	8.619	41.7	1,557.0	503.9	32.37
1.91	7	553.1	8.620	38.2	1,556.1	506.2	32.53
1.91	10	552.0	8.622	36.2	1,555.3	507.2	32.61
2.54	4	549.3	8.626	27.94	1,553.1	512.7	33.01
2.54	7	547.7	8.629	25.74	1,551.8	513.3	33.08
2.54	10	546.2	8.631	24.47	1,550.6	513.1	33.09

An increase in louver length increases the friction factor and the air-side heat transfer coefficient. The increase in friction factor yields an increase in pressure drop, and therefore parasitic fan power. On the other hand, the increase in the air-side heat transfer coefficient results in a decrease in fin efficiency and effective heat transfer area. Even though the effective heat transfer area decreases, air-side thermal resistance per segment decreases because of the increase in the product of the heat transfer coefficient and heat transfer area, resulting in an increase in the heat transfer capability and, therefore, a decrease in ITD. The decrease in the ITD, and the corresponding decrease in ACC inlet and outlet temperatures, results in an increase in the turbine work. Because the louver length should not exceed the fin channel height, the louver length values were set to vary between 55 and 95% of the fin channel height. Figure 4.30 shows the cycle efficiency as a

function of louver length for fins with a fin height of 25.4 mm, fin thickness of 0.254 mm, louver angle of 30 degrees, and a louver pitch of 5 mm.

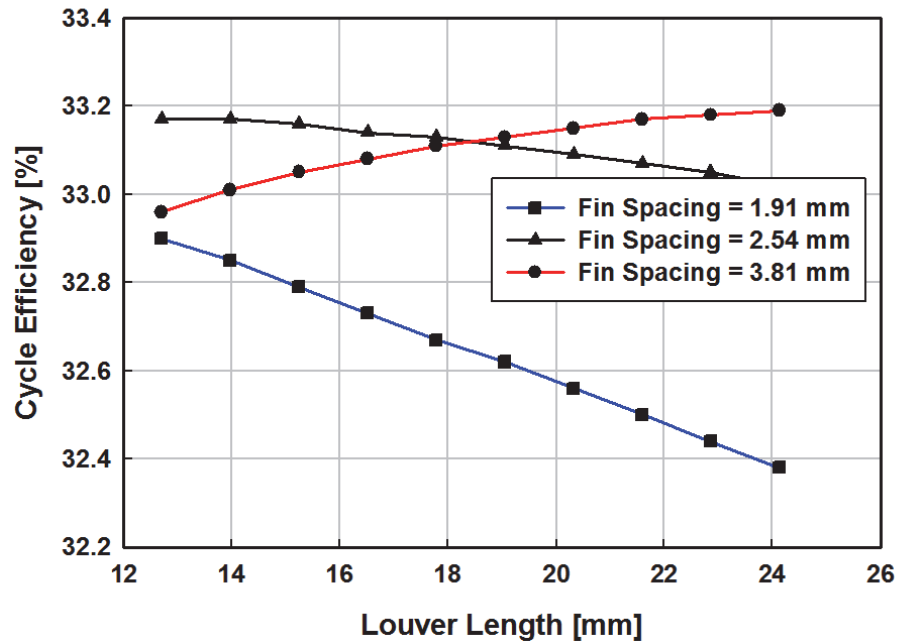


Figure 4.30 Rankine Cycle efficiency as a function of louver length for a fin height of 25.4 mm

As evidenced from Figure 4.30, the pairing of fin spacing to some louver length has a noticeable impact on the cycle efficiency. For fin spacings of 1.91 mm and 2.54 mm, the cycle efficiency decreased with an increase in louver length. In contrast, the cycle efficiency increased for the same increase in louver length when the fin spacing is 3.81 mm. This different dependence is due to the change in turbine, fan, and pump work as well as the heat added by the boiler, for each of the different fin spacing cases.

Table 4.15 Change in turbine, fan, and pump work in the Rankine Cycle for a change in louver length from 12.7 mm to 24.13 mm

Louver length [mm]	$F_s = 1.91$ mm		$F_s = 2.54$ mm		$F_s = 3.81$ mm	
	12.7	24.13	12.7	24.13	12.7	24.13
\dot{Q}_{boiler} [MW]	1,553.7	1,556.9	1,548.2	1,553.0	1,537.0	1,544.8
$\dot{W}_{turbine}$ [MW]	550.0	554.1	543.3	549.2	529.7	539.1
\dot{W}_{fan} [MW]	30.18	41.35	21.05	27.70	14.36	17.74
\dot{W}_{pump} [MW]	8.63	8.62	8.64	8.63	8.66	8.64
\dot{W}_{net} [MW]	511.2	504.1	513.6	512.8	506.7	512.7

As seen from Table 4.15, an increase in louver length resulted in an increase in boiler heat duty, turbine work, and fan power and a decrease in the pump work for the three tested fin spacings. While an increase in louver length does decrease the pump inlet temperature and pressure to yield a greater pressure difference across the pump, the enthalpy and entropy also decreased. This resulted in a lower isentropic enthalpy and less of a difference between the pump inlet enthalpy and outlet isentropic enthalpy, yielding an overall decrease in pump work. However, the proportion of positive to negative work decreases for the fin spacing cases of 1.91 mm and 2.54 mm, which show the decrease in cycle efficiency. The increase in turbine work was greater than the increase in parasitic fan work for a fin spacing of 3.81 mm as the louver length increases from 12.7 mm to 24.13 mm, yielding the increase in cycle efficiency shown in Figure 4.30.

The above parametric studies on louvered fins addressed variations in the fin height, fin spacing, louver angle, louver pitch, and louver length. A louvered fin with a fin height of 20.32 mm, fin spacing of 3.81 mm, fin thickness of 0.254 mm, louver angle of 30 degrees, louver pitch of 4 mm, and louver length of 18.29 mm was found to yield the highest cycle

efficiency of 33.27%. This is an increase of 0.38% from the baseline plain fin efficiency, which had a value of 32.89%.

The AFRs are designed to attach to existing ACCs in power plants with the ultimate goal to increase the overall cycle efficiency. With the heat transfer enhancement of 1.78 times and 1.50 times increase in pressure drop due to the implementation of the reeds, the required fan power for the cycle increased from 10.17 MW in the baseline case to 11.19 MW when the reeds are attached. The increase in heat transfer results in a decrease in the condenser inlet temperature and pressure, yielding an increase in the turbine work from 522.3 MW to 540.4 MW. As a result, the attachment of the reeds to the baseline plain fins increases the overall Rankine Cycle efficiency from 32.89% to 33.67%.

A plot comparing the maximum cycle efficiencies achieved using the different fin geometries and the resulting turbine, pump, and fan work is shown in Figure 4.31.

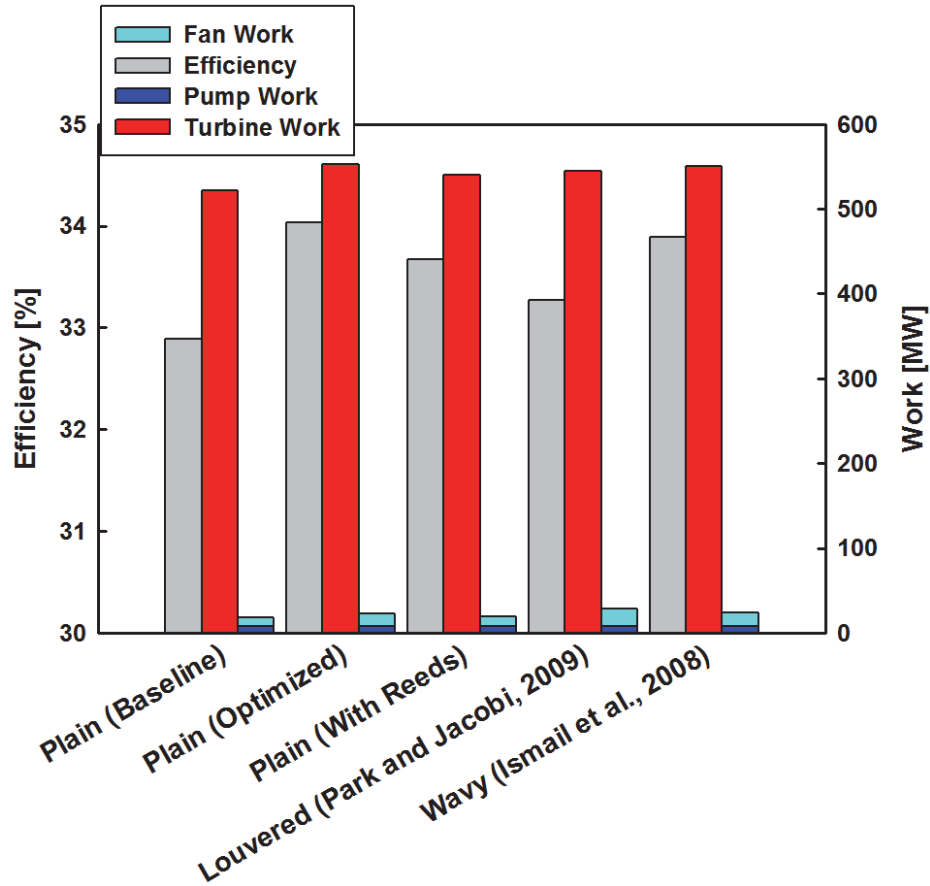


Figure 4.31 Comparison of the highest Rankine cycle efficiency for each fin type and the corresponding compressor, turbine, pump, and fan work

Table 4.16 Dimensions and efficiencies of the optimized plain, louvered, and wavy fins for the Rankine Cycle

Plain	Plain with AFRs	Louvered	Wavy
$F_h = 30.48$ mm	$F_h = 25.4$ mm	$F_h = 20.32$ mm	$F_h = 30.48$ mm
$F_s = 1.27$ mm	$F_s = 2.54$ mm	$F_s = 3.81$ mm	$F_s = 1.27$ mm
$F_t = 0.254$ mm	$F_t = 0.254$ mm	$F_t = 0.254$ mm	$F_t = 0.254$ mm
		$L_\alpha = 30$ degrees	$M = 1$ mm
		$L_p = 4$ mm	$\lambda = 33.02$ mm
		$L_l = 18.29$ mm	
$\eta_{\text{cycle}} = 34.03\%$	$\eta_{\text{cycle}} = 33.67\%$	$\eta_{\text{cycle}} = 33.27\%$	$\eta_{\text{cycle}} = 33.90\%$

As seen in Figure 4.31, the pump work does not vary drastically between the different fin cases. However, even though the louvered fins can result in an increase in cycle efficiency, the fan work required for the louvered fins is higher than that required for

the other fin configurations. Dimensions of the optimized plain, louvered, and wavy fins that yield the efficiencies displayed in Figure 4.31 are shown in Table 4.16. Cycle efficiency for the baseline plain fin is 32.89%.

Cycle efficiencies, work loads, condenser loads, and the ACC inlet quality values associated with the different fin cases shown in Figure 4.31 are shown in Table 4.17.

Table 4.17 Summary of cycle efficiencies and work and heat loads for the different fin types in the Rankine Cycle

		Plain (Baseline)	Plain (Optimized)	Plain (Reed)	Louvered (Park and Jacobi, 2009)	Wavy (Ismail <i>et al.</i> , 2008)
η_{cycle}	[%]	32.89	34.03	33.67	33.27	33.90
$\dot{W}_{net,cycle}$	[MW]	503.51	529.25	520.55	515.44	526.87
$\dot{Q}_{indiv.,condenser}$ (1 ACC)	[MW]	14.383	14.306	14.340	14.329	14.311
$\dot{Q}_{condenser}$ (70 ACCs)	[MW]	1006.81	1001.42	1003.80	1003.03	1001.77
\dot{Q}_{boiler}	[MW]	1530.90	1555.82	1545.85	1549.30	1554.35
x_4	[-]	0.8899	0.8747	0.8808	0.8787	0.8756
ITD	[K]	39.44	26.42	31.66	29.85	27.20

As the fins change from the baseline plain fin to other fin geometries and dimensions, the overall cycle efficiency and cycle work increases. Because the quality at the ACC inlet was allowed to vary, the quality of the steam entering the condenser also decreased, resulting in a decrease in the amount of heat rejected by each individual ACC as well as the total heat rejected from all 70 ACCs in the cycle. The higher cycle efficiencies also correspond to the cases with lower ITDs, resulting in an increase in the required boiler heat input.

From these analyses, it appears that the maximum increase in efficiency due to changes in fin configuration or changes in geometric parameters is just slightly over 1%, from 32.89% for the baseline plain fin to 34.03% for the optimized plain fin case. The next best option would be to use wavy fins which, according to the correlation of Ismail *et al.* (2008), results in an approximately 1% increase in cycle efficiency from the baseline case. Attachment of the AFRs directly to the baseline plain fins would be the number three option, followed by louvered fins as the last choice.

4.2.2 Combined Cycle Model

A similar analysis was conducted on a combined cycle. State points of the cycle used in the calculations are shown in Figure 4.32, while the resulting values at these points, as well as important values to consider for the baseline geometry smooth fins and optimized smooth fins, are summarized in Table 4.18.

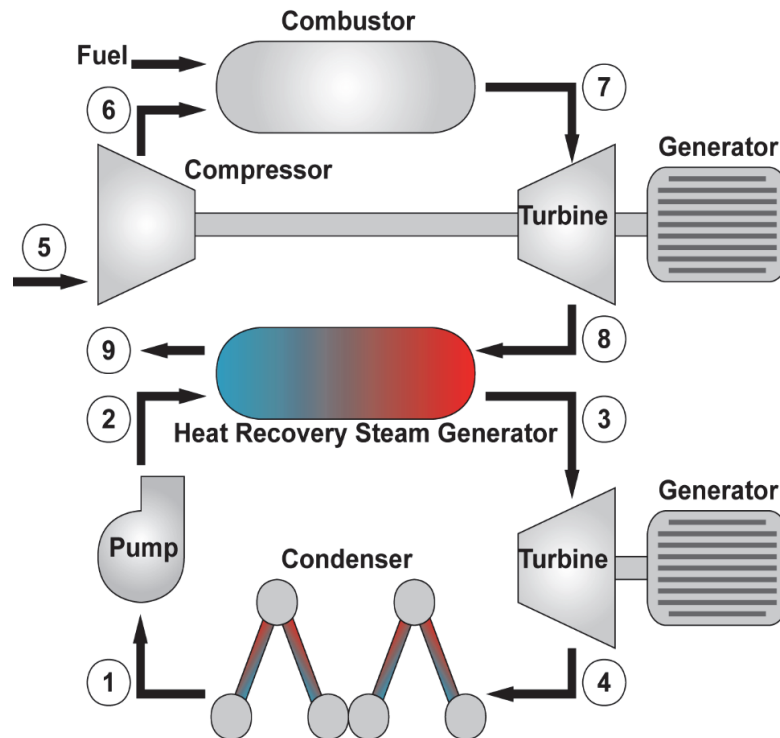


Figure 4.32 Labeled picture of the states in the Combined Cycle

Table 4.18 Summary of property values at the different state points and key parameters and results

State	Baseline ($F_s = 2.54$ mm)		Optimized ($F_s = 1.27$ mm)	
	T [°C]	P [kPa]	T [°C]	P [kPa]
1	69.78	34.4	56.94	19.92
2	70.79	16,529	57.82	16,529
3	550	16,529	550	16,529
4	69.44	30.46	55.64	16.25
5	30	101.3	30	101.3
6	490.6	2,027	490.6	2,027
7	1,244	2,027	1,244	2,027
8	582.1	101.3	582.1	101.3
9	205.3	101.3	198.5	101.3

Key Values		Baseline	Optimized
# ACCs	-	22	22
$\dot{W}_{compressor}$	MW	483.4	483.4
$\dot{Q}_{combustor}$	MW	971.1	971.1
$\dot{W}_{turbine,pri}$	MW	836.7	836.8
$\dot{W}_{net,topping}$	MW	353.3	353.3
$\eta_{topping}$	-	0.3638	0.3638
\dot{Q}_{HRSG}	MW	481.1	489.4
x_4	-	0.8899	0.8738
$\dot{W}_{turbine,bottom}$ (22 ACCs)	MW	164.2	174.3
$\dot{W}_{total,fan}$ (22 ACCs)	MW	3.195	5.19
\dot{W}_{pump} (22 ACCs)	MW	2.725	2.71
$\dot{W}_{net,bottom}$ (22 ACCs)	MW	158.2	166.4
$\dot{Q}_{condenser}$ (22 ACCs)	MW	316.4	314.6
$\eta_{bottoming}$	-	0.3289	0.34
$\dot{W}_{net,cycle}$	MW	511.6	519.7
η_{cycle}	%	52.68	53.52

Temperature and pressure results from the bottoming cycle (points 1 – 4) are the same as those from the Rankine Cycle analysis because most of the input values were the same. The number of condensers was decreased from 70 in the Rankine Cycle analysis to 22 in the Combined Cycle analysis, which decreases the steam flow rate in the bottoming

cycle, turbine work, fan work, and pump work. Reducing the fin spacing from 2.54 mm to 1.27 mm decreased the condenser and pump exit temperatures. Therefore, more heat had to be transferred from the gas exiting the gas turbine to the steam in the heat recovery steam generator to reach the desired 550°C steam turbine inlet temperature. The additional 8.3 MW (481.1 to 489.4 MW) of heat transferred from the topping cycle gas in the heat recovery steam generator is reflected by the 6.8°C decrease in gas exhaust temperature.

Overall combined cycle efficiency as a function of fin spacing and fin height was analyzed in a manner similar to that used for the Rankine cycle, and is presented in Figure 4.33. Again, a decrease in fin spacing increases the overall cycle efficiency and an inflection point in the efficiency occurs with a change in fin height.

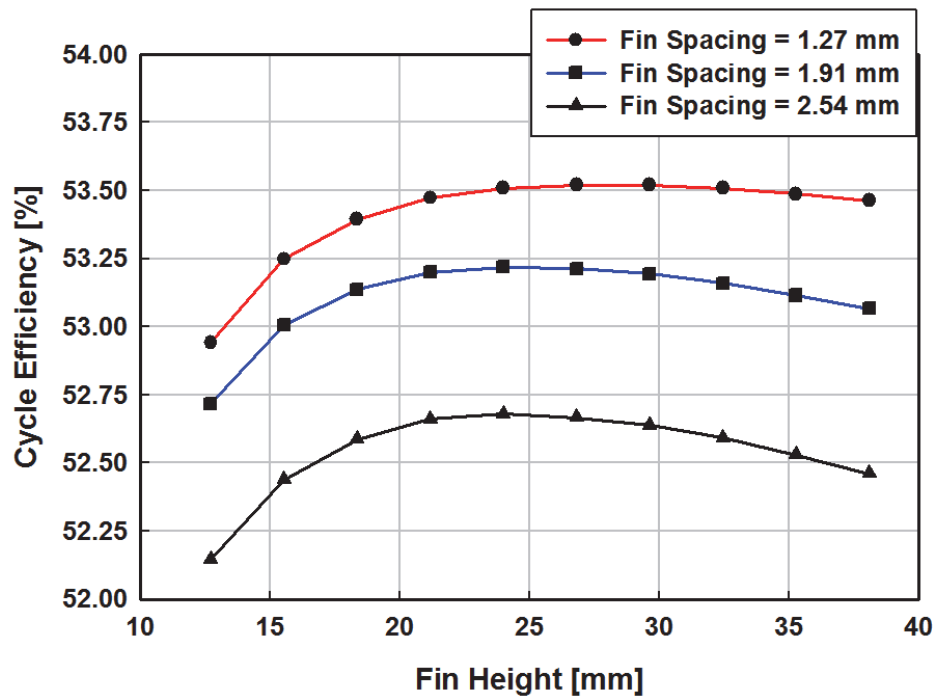


Figure 4.33 Combined Cycle efficiency as a function of fin height and fin spacing

After varying the fin height and fin spacing, the maximum resulting cycle efficiency of about 53.52 % was seen for a combination of a fin height of 27.94 mm and a fin spacing

of 1.27 mm. The predicted overall cycle efficiency falls short of the 60% that is achievable by some combined cycles

Similar to the Rankine Cycle study on wavy fins, the wavy fin amplitude and wavelength were varied in addition to the fin height and fin spacing for the Combined Cycle parametric study. Assuming a fin height of 25.4 mm, fin thickness of 0.254 mm, and wavelength of 16.5 mm, the combined cycle efficiency as a function of wave amplitude and three fin spacings is shown in Figure 4.34.

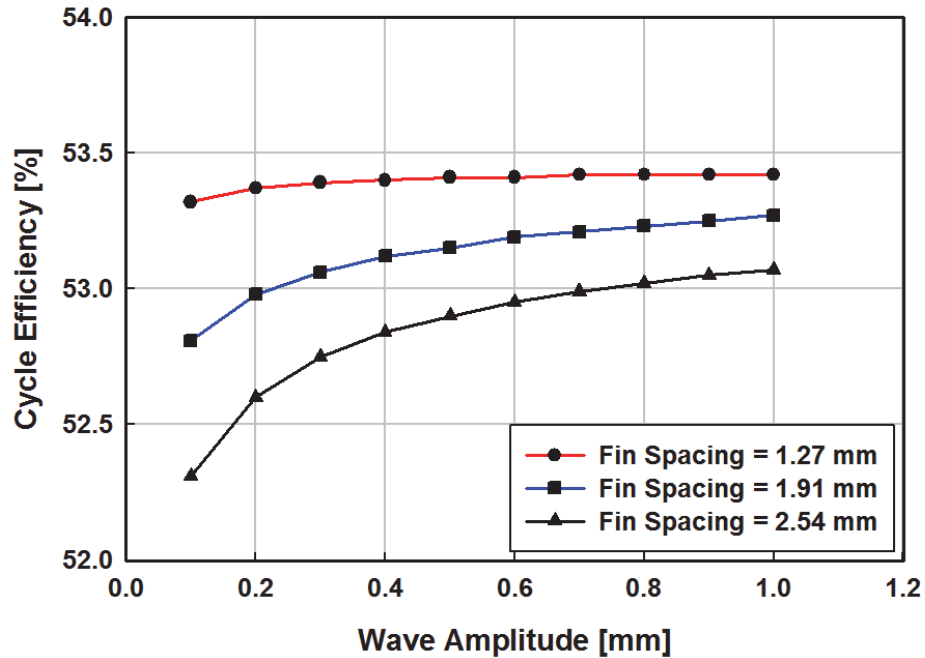


Figure 4.34 Combined Cycle efficiency as a function of wave amplitude and fin spacing assuming a constant fin height, fin thickness, and wavelength

Similar to the case of the Rankine Cycle, an increase in wave amplitude resulted in an increase in overall cycle efficiency. For the case with a fin spacing of 1.27 mm, the increase in wave amplitude from 0.1 mm to 1.0 mm resulted in an increase in the air-side heat transfer coefficient from $47.02 \text{ W m}^{-2} \text{ K}^{-1}$ to $81.71 \text{ W m}^{-2} \text{ K}^{-1}$. This increase in heat

transfer coefficient led to a decrease in ACC inlet temperature (58.2°C to 55.09 °C), and therefore the increase in steam turbine work from 172.4 MW to 174.7 MW. Even though the fan power also increases due to the larger amplitude waves, the increase from 5.17 MW to 6.54 MW is still less than the increase in the steam turbine work. An additional 1.85 MW was transferred from the topping cycle to the bottoming cycle through the heat recovery steam generator (487.91 MW to 489.76 MW), which is reflected in the 1.5°C decrease in the topping gas exhaust air (199.7°C to 198.2°C). With just a 0.9 mm change in amplitude, the overall cycle efficiency increased from 53.32% to 53.42%. Some other representative values for the cycle work changes for a fin with a fin height of 25.4 mm, fin thickness of 0.254 mm, fin spacing of 2.54 mm, and wavelength of 16.51 mm are shown in Table 4.19.

Table 4.19 Representative values for wavy fins in the Combined Cycle due to a change in wave amplitude

Wave Amplitude [mm]	$\dot{W}_{turb,top}$ [MW]	$\dot{W}_{turb,bot}$ [MW]	\dot{W}_{comp} [MW]	\dot{W}_{pump} [MW]	$\dot{W}_{total,fan}$ [MW]	\dot{Q}_{HRSG} [MW]	$\dot{W}_{net,base}$ [MW]	η_{cycle} [%]
0.1	836.7	160.1	483.4	2.732	2.622	477.63	508.0	52.31
0.5	836.7	166.1	483.4	2.722	2.942	482.74	513.7	52.90
1	836.7	168.2	483.4	2.718	3.374	484.47	515.4	53.07

Assuming a fin height of 25.4 mm, fin thickness of 0.254 mm, and wave amplitude of 1 mm, the Combined Cycle efficiency as a function of wavelength and fin spacing is shown in Figure 4.35.

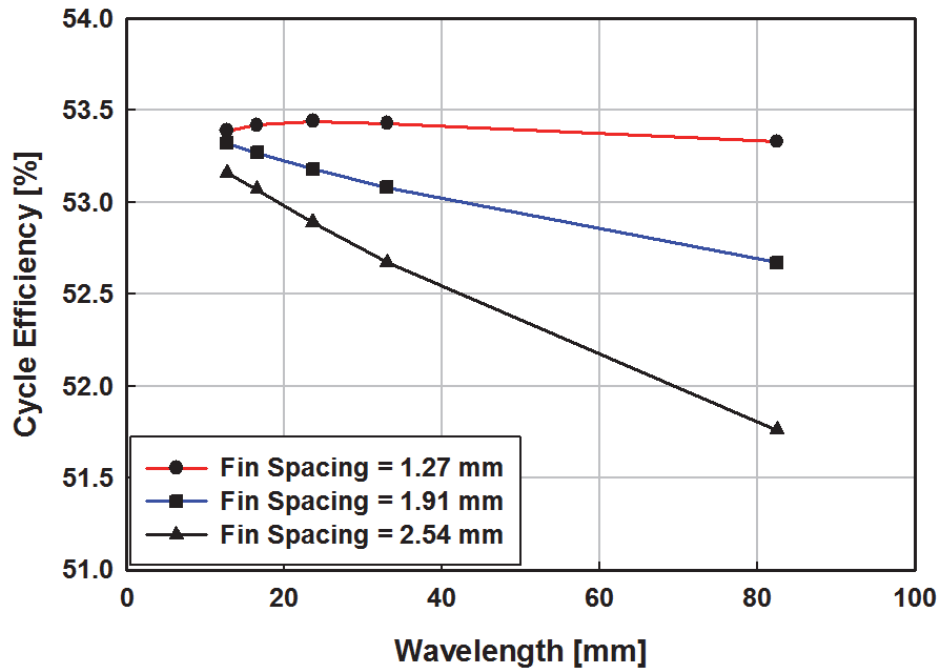


Figure 4.35 Combined cycle efficiency as a function of wavelength and fin spacing

Similar to the case for the Rankine Cycle analysis, the increase in wavelength generally led to a decrease in cycle efficiency because of the fewer number of waves, and therefore mixing of the air in the channels. This led to a decrease in the steam turbine work (175.0 MW to 171.6 MW for a fin spacing of 1.27 mm) and required fan power (7.16 MW to 4.31 MW for a fin spacing of 1.27 mm). The heat transferred from the topping to bottoming cycle also decreases as the wavelength increases (490.04 MW to 487.24 MW) because of the increase in the ACC outlet temperature (56.00°C to 60.33°C). A point of maximum cycle efficiency does occur for the fin spacing of 1.27 mm, showing that it is possible to find some combination of fin spacing and wavelength for the highest cycle efficiency. Representative values for the turbine, pump, and fan work for a fin with a height

of 25.4 mm, thickness of 0.254 mm, fin spacing of 2.54 mm, wave amplitude of 1.0 mm, and various wavelengths are shown in Table 4.20.

Table 4.20 Representative values for wavy fins in the Combined Cycle for a change in wavelength

λ [mm]	$\dot{W}_{turb,top}$ [MW]	$\dot{W}_{turb,bot}$ [MW]	\dot{W}_{comp} [MW]	\dot{W}_{pump} [MW]	$\dot{W}_{total,fan}$ [MW]	\dot{Q}_{HRSG} [MW]	$\dot{W}_{net,base}$ [MW]	η_{cycle} [%]
33.02	836.8	163.6	483.4	2.726	2.770	480.7	511.5	52.67
23.59	836.8	166.0	483.4	2.722	2.966	482.7	513.6	52.89
16.51	836.8	168.2	483.4	2.718	3.374	484.5	515.4	53.07

Based on a parametric study on the different wavy fin dimensions, a combination of a fin height of 27.94 mm, fin spacing of 1.27 mm, fin thickness of 0.254 mm, wave amplitude of 1 mm, and wavelength of 23.586 mm yielded the highest cycle efficiency. With these dimensions, the maximum Combined Cycle efficiency for the operating conditions under consideration here is 53.45%.

The performance of the combined cycle with louvered fins was also investigated. A plot of the Combined Cycle efficiency as a function of louver pitch and fin spacing, for a fin height of 25.4 mm, fin thickness of 0.254, louver angle of 30 degrees, and louver length of 22.86 mm, is shown in Figure 4.36.

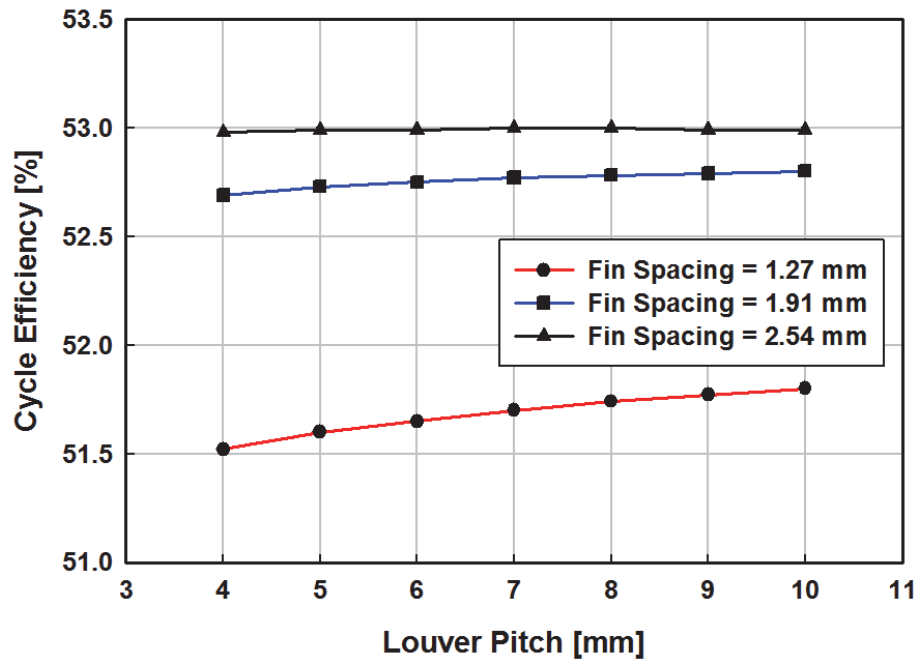


Figure 4.36 Combined Cycle efficiency as a function of louver pitch for fin spacings of 1.27, 1.91, and 2.54 mm

Similar to the case for the Rankine Cycle analysis, the fin spacing of 1.27 mm resulted in lower cycle efficiencies than the cases where the fin spacing is 1.91 mm or 2.54 mm. Values for the turbine, fan, and pump work for three different louver pitches for a fin with a height of 25.4 mm, fin thickness of 0.254 mm, louver angle of 30 degrees, louver length of 22.86 mm, two louver banks, fin spacing of 1.27, 1.91, and 2.54 mm are shown in Table 4.21.

Table 4.21 Representative values for louvered fins in the Combined Cycle due to a change in louver pitch

F_s [mm]	L_{pitch} [mm]	$\dot{W}_{top,turb}$ [MW]	$\dot{W}_{bot,turb}$ [MW]	\dot{W}_{comp} [MW]	\dot{W}_{pump} [MW]	$\dot{W}_{total,fan}$ [MW]	\dot{Q}_{HRSG} [MW]	$\dot{W}_{net,base}$ [MW]	η_{cycle} [%]
1.27	4	836.8	175.7	483.4	2.706	26.00	490.5	500.3	51.52
1.27	7	836.8	174.5	483.4	2.707	24.01	490.4	502.1	51.70
1.27	10	836.8	174.3	483.4	2.707	22.87	490.2	503.0	51.80
1.91	4	836.8	174.2	483.4	2.709	13.09	489.3	511.7	52.69
1.91	7	836.8	173.8	483.4	2.709	12.01	489.1	512.4	52.77
1.91	10	836.8	173.5	483.4	2.710	11.38	488.8	512.7	52.80
2.54	4	836.8	172.6	483.4	2.711	8.782	488.1	514.5	52.98
2.54	7	836.8	172.1	483.4	2.712	8.088	487.7	514.6	53.00
2.54	10	836.8	171.7	483.4	2.713	7.690	487.3	514.6	52.99

While the cycle efficiency continues to increase with the increase in louver pitch for the cases with a fin spacing of 1.27 and 1.91 mm, the cycle efficiency peaks at 53.00% for the 2.54 mm fin spacing and louver pitch of 7 mm. This corresponds to combination at which the maximum cycle work occurs for the fin spacing of 2.54 mm case.

For a fin height of 25.4 mm, fin thickness of 0.254 mm, louver angle of 30 degrees, louver pitch of 5 mm, and two louver banks, the Combined Cycle efficiency as a function of louver length and fin spacing is shown in Figure 4.37.

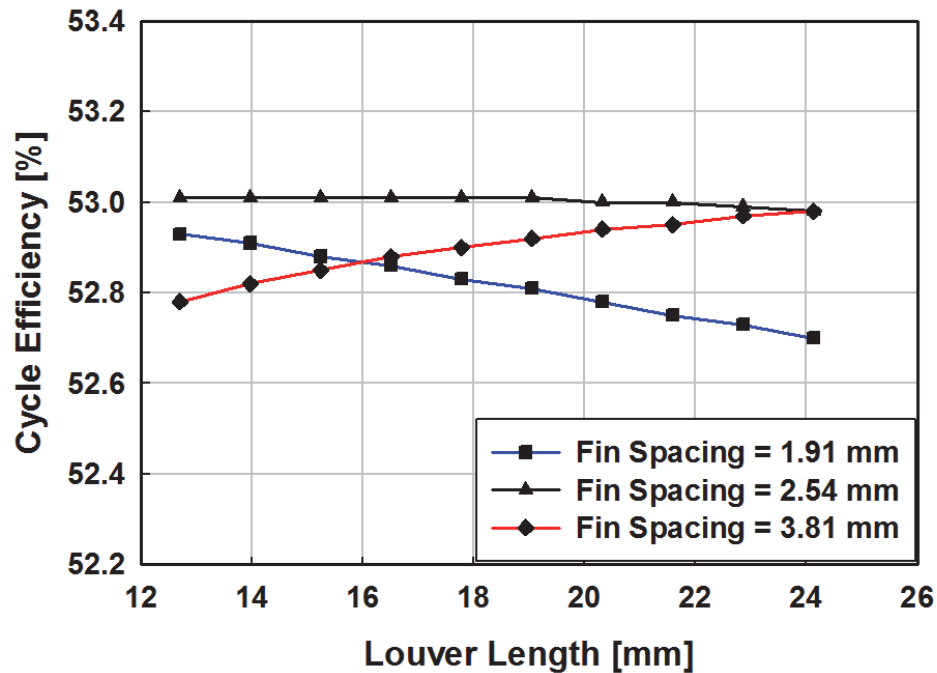


Figure 4.37 Combined Cycle efficiency as a function of louver length and fin spacing

Once again, the pairing of the fin spacing and louver length affects the cycle efficiency. The increase in louver length for all the fin spacings (1.91 mm, 2.54 mm, and 3.81 mm) increases the air-side heat transfer coefficient, which decreases the ACC inlet and outlet temperatures and increases the steam turbine work. Heat transferred from the boiler also increases, decreasing the exhaust air temperature in the gas turbine cycle. Representative values are shown in Table 4.22. The increase in heat transfer coefficient due to the increase in louver length from 12.7 mm to 24.13 mm contributes to 1.2 MW, 1.9 MW, and 2.9 MW increases in the steam turbine work for the fin spacings of 1.91 mm, 2.54 mm, and 3.81 mm, respectively. For the same increase in louver length, the negative work from the fan and pump also increased, with increases of 3.512 MW, 2.086, and 1.059 MW for the fin spacings of 1.91 mm, 2.54 mm, and 3.81 mm, respectively. Even though

the steam turbine work does increase by 1.2 MW for the 1.91 mm and by 1.9 MW for the 2.54 mm cases, the increase in negative work (3.512 MW and 2.086 MW) for these fin spacings is greater, resulting in a decrease in the net cycle work. The 1.059 MW increase in negative work for the fin spacing of 3.81 mm case is less than the 2.9 MW increase in steam turbine work, yielding an increase in the net cycle work. Again, an increase in louver length for the fin spacing of 1.91 mm and 2.54 mm resulted in a decrease in net cycle work while the net work increased for the fin spacing of 3.81 mm case. The decrease in net cycle work for the 1.91 mm and 2.54 mm cases contributes to the decrease in the overall cycle efficiency shown in Figure 4.37 while the increase in net cycle work for the 3.81 mm case leads to the increase in overall cycle efficiency.

Table 4.22 Change in turbine, fan, and pump work in the Combined Cycle for a change in louver length from 12.7 mm to 24.13 mm

		$F_s = 1.91 \text{ mm}$		$F_s = 2.54 \text{ mm}$		$F_s = 3.81 \text{ mm}$	
Louver length	[mm]	12.7	24.13	12.7	24.13	12.7	24.13
h_{air}	[W m ⁻² K ⁻¹]	82.23	116.3	78.13	110.5	73.69	104.2
T_9	[°C]	199.4	198.6	200.8	199.6	203.7	201.7
\dot{Q}_{HRSG}	[MW]	488.3	489.3	486.6	488.1	483.1	485.5
$\dot{W}_{turbine, Rankine}$	[MW]	172.9	174.1	170.7	172.6	166.5	169.4
\dot{W}_{fan}	[MW]	9.486	13.00	6.617	8.706	4.514	5.577
\dot{W}_{pump}	[MW]	2.711	2.709	2.714	2.711	2.721	2.717
\dot{W}_{net}	[MW]	514.0	511.8	514.7	514.5	512.6	514.4
η_{cycle}	[%]	52.93	52.70	53.01	52.98	52.78	52.98

Similar to the case for the Rankine Cycle, inserting the AFRs into the baseline plain fins results in an increase in the ACC heat transfer coefficient, the air-side pressure drop and the required fan power, and the overall cycle efficiency. With the reeds, the ACC outlet

(point 1 in Figure 4.32) temperature and pressure are less than the 69.78°C and 34.4 kPa from the baseline case, with values of 62.5°C and 25.31 kPa, respectively. This resulted in an increase in heat transferred in the heat recovery steam generator, and an overall cycle efficiency increase from 52.68% to 53.23%.

A comparison of the cycle efficiencies, turbine work, fan work, and pump work for each of the optimized cases is shown in Figure 4.38, with the associated dimensions shown in Table 4.23.

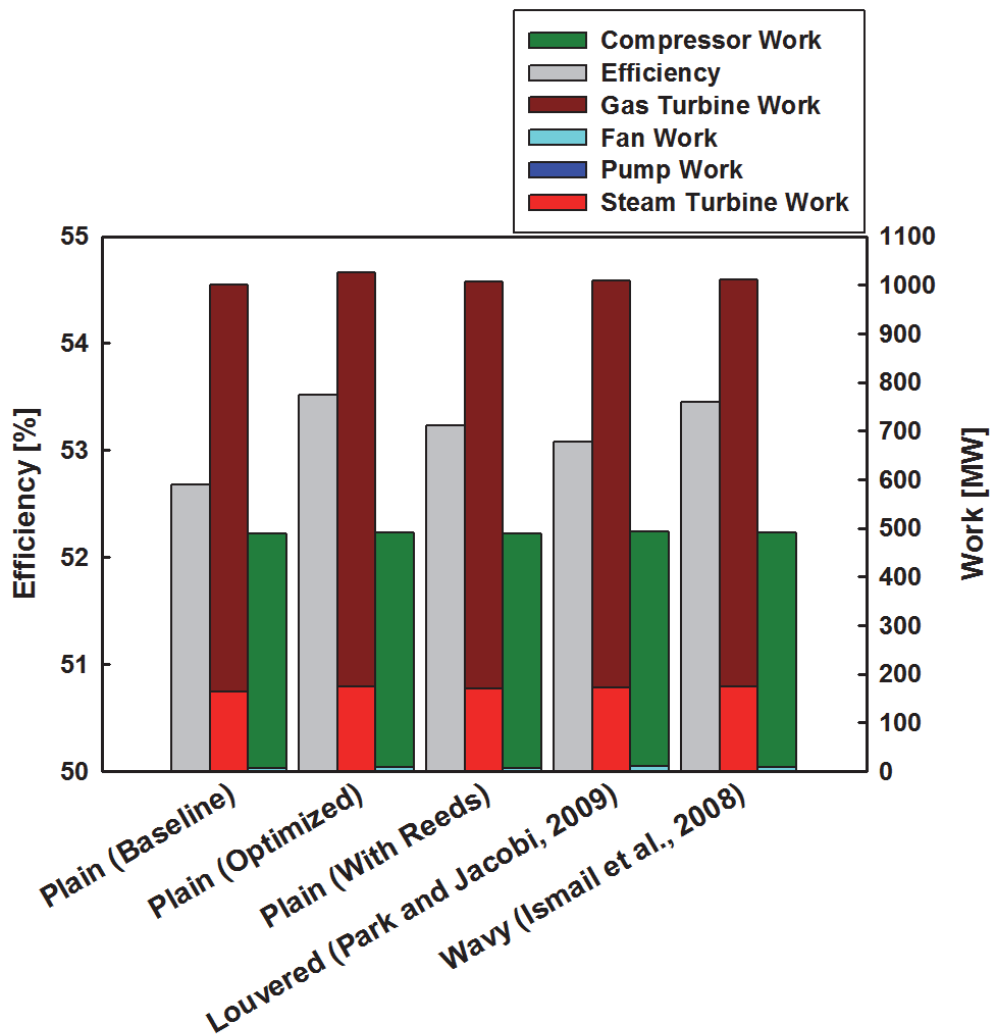


Figure 4.38 Comparison of the highest efficiency for each fin type and the corresponding compressor, turbine, pump, and fan work

Table 4.23 Dimensions of the optimized plain, louvered, and wavy fins for the Combined Cycle

Plain	Plain with AFRs	Louvered	Wavy
$F_h = 27.94$ mm $F_s = 1.27$ mm $F_t = 0.254$ mm	$F_h = 25.4$ mm $F_s = 2.54$ mm $F_t = 0.254$ mm	$F_h = 19.05$ mm $F_s = 3.302$ mm $F_t = 0.254$ mm $L_\alpha = 30$ degrees $L_p = 5$ mm $L_l = 17.15$ mm	$F_h = 27.94$ mm $F_s = 1.27$ mm $F_t = 0.254$ mm $M = 1$ mm $\lambda = 23.586$ mm
$\eta_{\text{cycle}} = 53.52\%$	$\eta_{\text{cycle}} = 53.23\%$	$\eta_{\text{cycle}} = 53.08\%$	$\eta_{\text{cycle}} = 53.45\%$

Because the fan and pump work are an order of magnitude less than the compressor and turbine work, they are shown separately, with the cycle efficiency, in Figure 4.39.

Cycle efficiencies, work loads, condenser loads, and the ACC inlet quality values associated with the different fin cases shown in Figure 4.38 are shown in Table 4.24.

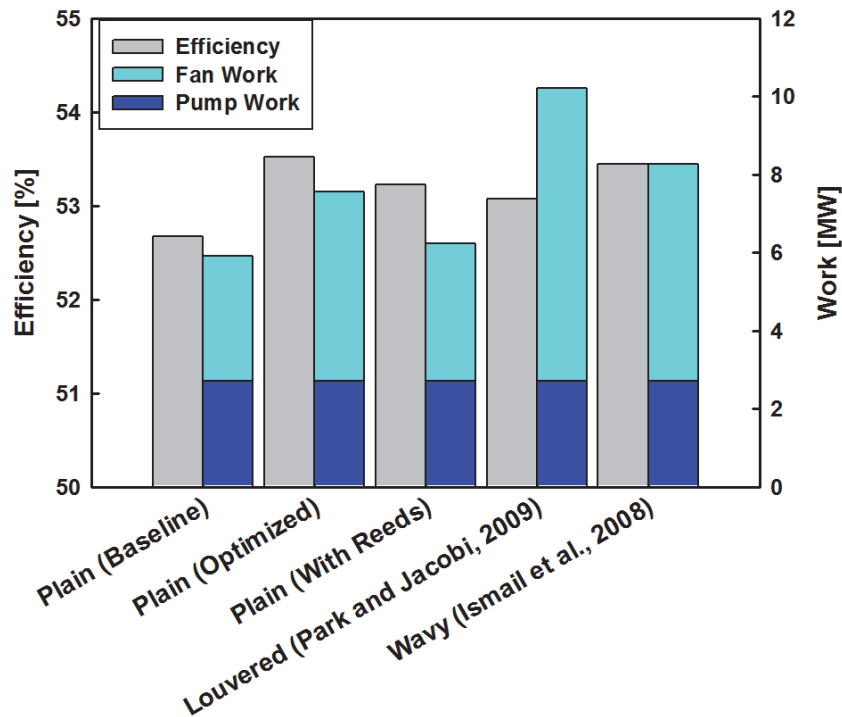


Figure 4.39 Optimal Combined Cycle efficiency and fan and pump work for different fin configurations

Table 4.24 Summary of cycle efficiencies and work and heat loads for the different fin types in the Combined Cycle

		Plain (Baseline)	Plain (Optimized)	Plain (Reed)	Louvered (Park and Jacobi, 2009)	Wavy (Ismail <i>et al.</i> , 2008)
η_{cycle}	[%]	52.68	53.52	53.23	53.08	53.45
$\dot{W}_{net,cycle}$	[MW]	511.57	519.76	516.92	515.48	519.00
$\dot{Q}_{indiv.,condenser}$ (1 ACC)	[MW]	14.383	14.304	14.340	14.319	14.304
$\dot{Q}_{condenser}$ (22 ACCs)	[MW]	316.43	314.69	315.48	315.02	314.69
\dot{Q}_{boiler}	[MW]	481.14	489.22	485.94	487.90	489.16
x_4	[-]	0.8899	0.8742	0.8808	0.8768	0.8743
ITD	[K]	39.44	26.00	31.66	28.21	26.10

Adjusting the plain fin dimensions, adding the AFRs to the plain fins, or using either louvered or wavy fins results in an increase from the 52.68% baseline plain fin cycle efficiency. Adjusting the plain fin dimensions yields the highest overall cycle efficiency of 53.52%, followed closely by the wavy fins with an efficiency of 53.45%. Even though the difference in cycle efficiency between the optimized plain fin and wavy fin only differ by 0.07%, the fan power associated with the wavy fin is 0.693 MW greater than that needed for the optimized plain fins. The third highest efficiency of 53.23% was a result of the AFRs, and finally the louvered fins were the least favorable option with a cycle efficiency of 53.08%. Similar to the Rankine Cycle results, the fin cases with the higher efficiencies correspond to higher net cycle work and boiler heat input, and lower ITD, ACC inlet quality, and heat rejected from each individual ACC and from the total of all 22 ACCs in the cycle.

From these parametric studies for the operating conditions under consideration, changing the plain fin dimensions results in the highest possible cycle efficiencies. As pointed out from previous discussions, the correlations for the wavy and louvered fins

(those developed by Ismail *et al.* (2008) and Park and Jacobi (2009), respectively) might not accurately predict the actual performance of these fins in the ACCs because some of the dimensions are outside the range of applicability for these correlations. The AFRs show promise as a technology that could increase the cycle efficiency, but are currently not as effective as the plain fin dimension change. With further investigations, however, the addition of the reeds to the plain fins could lead to better performance than the optimized plain fin geometry in the future.

CHAPTER 5: CONCLUSIONS AND RECOMMENDATIONS

5.1 Conclusions

A variety of configurations for air-cooled condensers to be used in power plants were investigated in this study. A segmented model to predict the heat transfer and pressure drop performance of a 10.67 m by 12.2 m A-frame Air cooled condenser was developed on the *Engineering Equation Solver* software platform. Condenser performance as a stand-alone unit, and also when installed in a power plant was analyzed. Appropriate two-phase heat transfer and pressure drop models for inclined flows were incorporated into the condenser model, which calculates the progression of the saturation temperature and pressure, and the amount of heat removed, from each segment. Minor losses associated with the path of the air flow from upstream of the fan to a point downstream of the A-frame were accounted for using the methods described by Kröger (1998).

Baseline fin height, fin spacing, and fin thickness for the plain fin case were based on common ACC dimensions and assumed to be 25.4 mm, 2.54 mm, and 0.254 mm, respectively. Assuming an inlet quality of 0.95 and baseline plain fin and tube dimensions, the condenser rejected 15.318 MW of heat and the initial temperature difference (ITD) for the condenser was predicted to be 42.12 K, which corresponds to an air-side pressure drop of 143.59 Pa. The air-side geometry was varied in an effort to reduce the initial temperature difference with a minimal increase in air-side pressure drop. Parametric studies were conducted by varying the fin height, fin spacing, and fin thickness by $\pm 50\%$ of the baseline values. Results from these studies showed that it is possible to decrease the initial temperature difference by 15 K by reducing the fin spacing to 1.143 mm; however, the associated air-side pressure drop rises to 260.96 Pa, which also affects the net power

generation of the cycle. Optimizing the plain fin dimensions to a fin height of 25.4 mm, fin spacing of 1.143 mm, and a fin thickness of 0.254 mm to reach the target ITD of 27 K resulted in 15.537 MW of heat transferred from a single ACC, 0.22 MW more than the baseline ACC.

Wavy and multilouver fins were also investigated as possible alternatives to the plain fins. Heat transfer and pressure drop correlations developed by Junqi *et al.* (2007); Ismail *et al.* (2008), and Khoshvagt Aliabadi *et al.* (2014) for wavy fins were compared by varying the fin height, fin spacing, fin thickness, wave amplitude, and wave amplitude. One out of the three models, Ismail *et al.* (2008) predicted initial temperature difference and air-side pressure drop results that were comparable to those achieved by the smooth fins (ITD between 27 and 28 K with pressure drops between 290 and 320 Pa). For example, a wavy fin with a height of 22.86 mm, spacing of 1.27 mm, thickness of 0.254 mm, wave amplitude of 1 mm, and wavelength of 16.51 mm yielded an ITD of 27.14 K, air-side pressure drop of 312.84 Pa, and 15.536 MW of heat transferred from the single ACC. However, discrepancies in performance predictions from the three different correlations led to a lower level of confidence in the application of these correlations for this analysis.

Similarly, two different multilouver fin correlations (Kim and Bullard, 2002; Park and Jacobi, 2009) were compared. Parameters considered for these fins include the fin height, fin spacing, fin thickness, louver angle, louver length, louver pitch, and the number of louver banks. While the heat transfer coefficients predicted by these two correlations were similar, friction factors predicted by the Kim and Bullard (2002) correlation were potentially four times greater than friction factors predicted by the Park and Jacobi (2009) correlation. The Park and Jacobi (2009) correlation yielded the most optimal ITD versus

air-side pressure drop results for a fin height of 12.7 mm, fin spacing of 2.54 mm, fin thickness of 0.254 mm, louver pitch of 7 mm, louver angle of 30 degrees, and louver length of 11.43 mm. This combination yielded an ITD of 27.03 K, air-side pressure drop of 623.4 Pa, and 15.539 MW of heat transferred from the ACC. Discrepancies in the performance of wavy and louvered fins predicted by different correlations could be due to the many parameters involved.

Auto-flutter reeds, or AFRs, being designed by the Fluid Mechanics Research Laboratory at the Georgia Institute of Technology to attach directly to existing ACCs at power plants and enhance the air-side heat transfer were also considered. Based on preliminary performance data provided by the lab in October 2015, the AFRs can enhance heat transfer by 1.78 times with only a 1.50 times increase in pressure drop. The integration of the AFRs into the model at the operating conditions of interest results in an ACC with an ITD and air-side pressure drop of 34.21 K and 157.98 Pa, respectively, although these findings must be treated as very preliminary in nature. A comparison of the predicted ITDs and the predicted parasitic fan power required for one ACC for the plain, plain with AFRs, louvered, and wavy fins is shown in Figure 5.1.

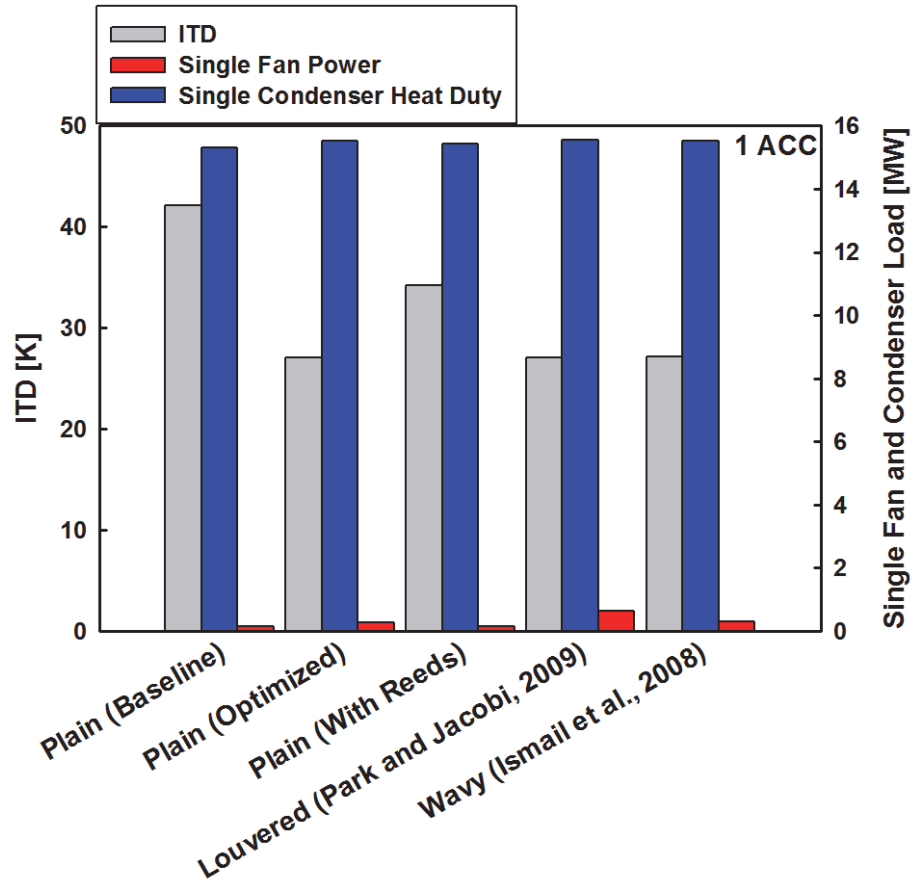


Figure 5.1 ITD and resulting fan power comparison for the standalone ACC with different fin types

From Figure 5.1, changing the plain fin dimensions, attaching the AFRs, or utilizing wavy or louvered fins can all decrease the ITD of the ACC. However, the required fan power differs greatly depending on the fin choice. Performance predictions from the louvered and wavy fin models indicate that the fan power corresponding to an ITD of 27 K are higher than that associated with a change in plain fin dimensions. Plain fins with the AFRs attached failed to reach the goal ITD of 27 K, but show promise in increasing the air-side heat transfer with the promise of not incurring commensurately high increases in the fan power. While changing the fin configuration resulted in a decrease in ITD and

therefore the ACC condensing temperature, the difference between the steam inlet and outlet temperatures increased. For example, at an ITD of 42.12 K, steam enters the baseline plain fin case at 72.12°C and exits at 72.21°C, yielding a temperature rise of about 0.09°C and a single condenser heat duty of 15.32 MW. Adjusting the plain fin dimensions such that the ITD is 27.07 K, the steam enters the ACC at 57.07°C and leaves at 58.06°C, a temperature rise of 0.99°C and single condenser heat duty of 15.54 MW. The larger rise in steam temperature from inlet to outlet in the latter case ultimately yielded an increase in the heat transferred from each ACC.

Finally, the performance of simple 500 MW Rankine and Combined Cycles with an air-cooled condenser was predicted. Similar to the stand-alone condenser analyses, the different fin types were implemented into the pertinent cycle models to determine the fin configurations that yield the highest cycle efficiency.

The Rankine Cycle model assumed there were 70 ACCs to maintain a net cycle work of at least 500 MW. When incorporated into the Rankine Cycle model, the plain fins with the baseline dimensions resulted in a cycle efficiency of 32.89%, 14.383 MW of heat rejected per ACC, and 1006.81 MW total rejected from all 70 ACCs in the cycle, and net cycle work of 503.5 MW. Changing the plain fin height, thickness, and spacing to 30.48 mm, 0.254 mm, and 1.27 mm results in a cycle efficiency of 34.03%, 14.306 MW of heat rejected per ACC, and 1001.42 MW rejected from all 70 ACCs with a net cycle work of 529.4 MW, and baseline plain fins with the AFRs attached would yield a cycle efficiency of 33.67%, 14.34 MW rejected per ACC, and 1003.8 MW rejected from all 70 ACCs with a net cycle work of 520.5 MW. Wavy fins (when fin performance is predicted using the Ismail *et al.* (2008) correlation) with a height of 30.48 mm, thickness of 0.254 mm, spacing

of 1.27 mm, wave amplitude of 1 mm, and wavelength of 33.02 mm yield a cycle efficiency of 33.89%, 14.31 MW rejected per ACC for a total of 1001.8 MW from all 70 ACCs, and net cycle work of 526.8 MW. Using the Park and Jacobi (2009) correlation, louvered fins with a 19.05 mm fin height, 3.81 mm fin spacing, 0.254 mm fin thickness, 30 degree louver angle, 17.15 mm louver length, and 4 mm louver pitch, result in an overall cycle efficiency of 33.27%, 14.329 MW rejected per ACC for a total of 1003.03 MW rejected from all 70 ACCs and net cycle work of 515.7 MW for the same cycle operating conditions. A comparison of the maximum cycle efficiencies and net cycle work found from the Rankine Cycle models using the different fin types is shown in Figure 5.2. Cycle efficiencies and

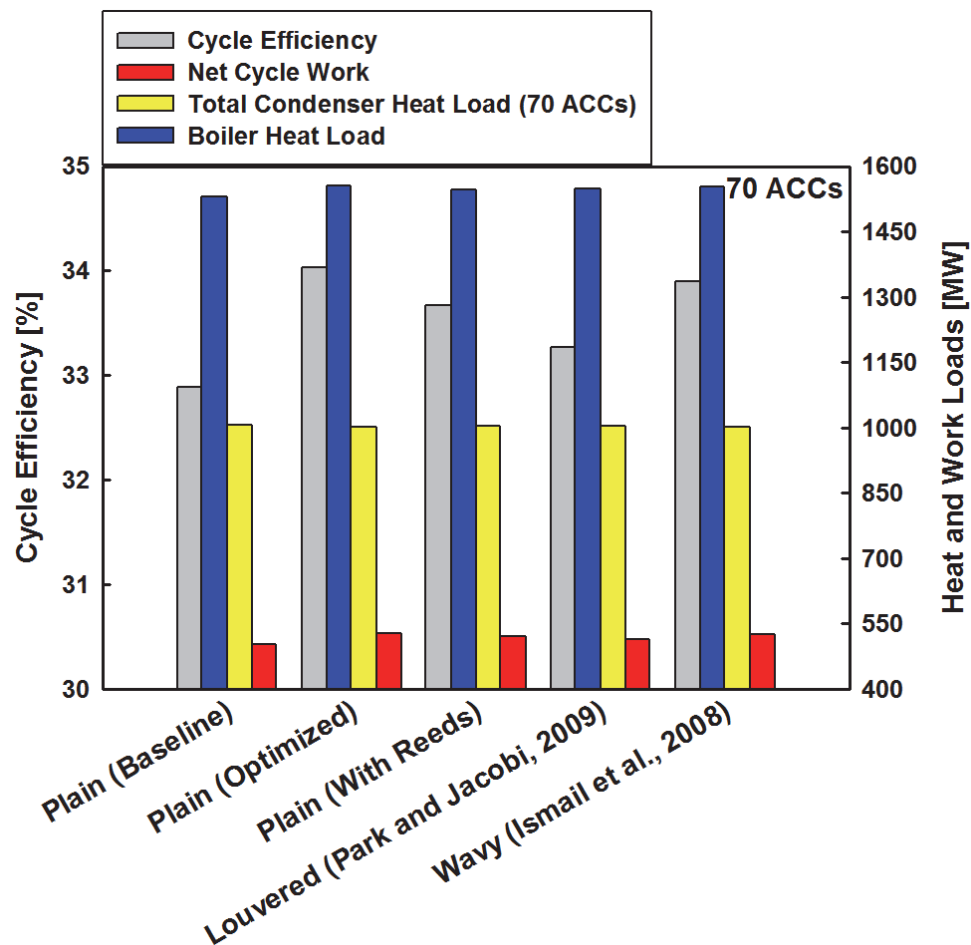


Figure 5.2 Comparison of Rankine Cycle efficiency and net cycle work for the different fin types

Table 5.1 Summary of cycle efficiencies and work and heat loads for the different fin types in the Rankine Cycle

	Plain (Baseline)	Plain (Optimized)	Plain (Reed)	Louvered (Park and Jacobi, 2009)	Wavy (Ismail <i>et al.</i> , 2008)
η_{cycle} [%]	32.89	34.03	33.67	33.27	33.90
$\dot{W}_{net,cycle}$ [MW]	503.51	529.25	520.55	515.44	526.87
$\dot{Q}_{indiv.,condenser}$ (1 ACC) [MW]	14.383	14.306	14.340	14.329	14.311
$\dot{Q}_{condenser}$ (70 ACCs) [MW]	1006.81	1001.42	1003.80	1003.03	1001.77
\dot{Q}_{boiler} [MW]	1530.90	1555.82	1545.85	1549.30	1554.35

the different heat and work loads found for the condensers and the cycle are summarized in Table 5.1. Adjustment of the air-side geometry on the condenser could lead to a 1% increase in cycle efficiency and 25.9 MW increase in net cycle work.

A similar analysis was conducted for the Combined Cycle using the same fin types and fin performance correlations used in the Rankine Cycle analysis. For these studies, each combined cycle consisted of 22 ACCs. ACCs with baseline plain fins in the combined cycle model yield an overall cycle efficiency of 52.68% and net cycle work of 511.6 MW. When the plain fin dimensions were changed to a fin height of 27.94 mm, fin spacing of 1.27 mm, and fin thickness of 0.254 mm, the cycle efficiency increased to 53.52% and the net cycle work increased by 8.2 MW to 519.8 MW. Plain fins with the AFRs resulted in an increase in cycle efficiency to 53.23%, and an increase in net work to 516.9. Wavy fins with a height of 30.48 mm, 0.254 mm thickness, 1.27 mm spacing, 1 mm amplitude, and 23.586 mm wavelength yielded a cycle efficiency of 53.44% and net work of 518.9 MW. Louvered fins with a fin height of 19.05 mm, thickness of 0.254 mm, spacing of 3.175 mm, louver angle of 30 degrees, louver length of 17.15 mm, and louver pitch of 7 mm yielded

a cycle efficiency of 53.07% and net cycle work of 515.3 MW. While louvered fins are used extensively in the automobile industry due to the compactness that they enable, the predictions from the present study developed model do not show them to be an optimal choice for application in power plants due to the large fan and pump work penalties associated with louvered fins. Figure 5.3 shows the cycle efficiencies and net cycle work for each of the fin types.

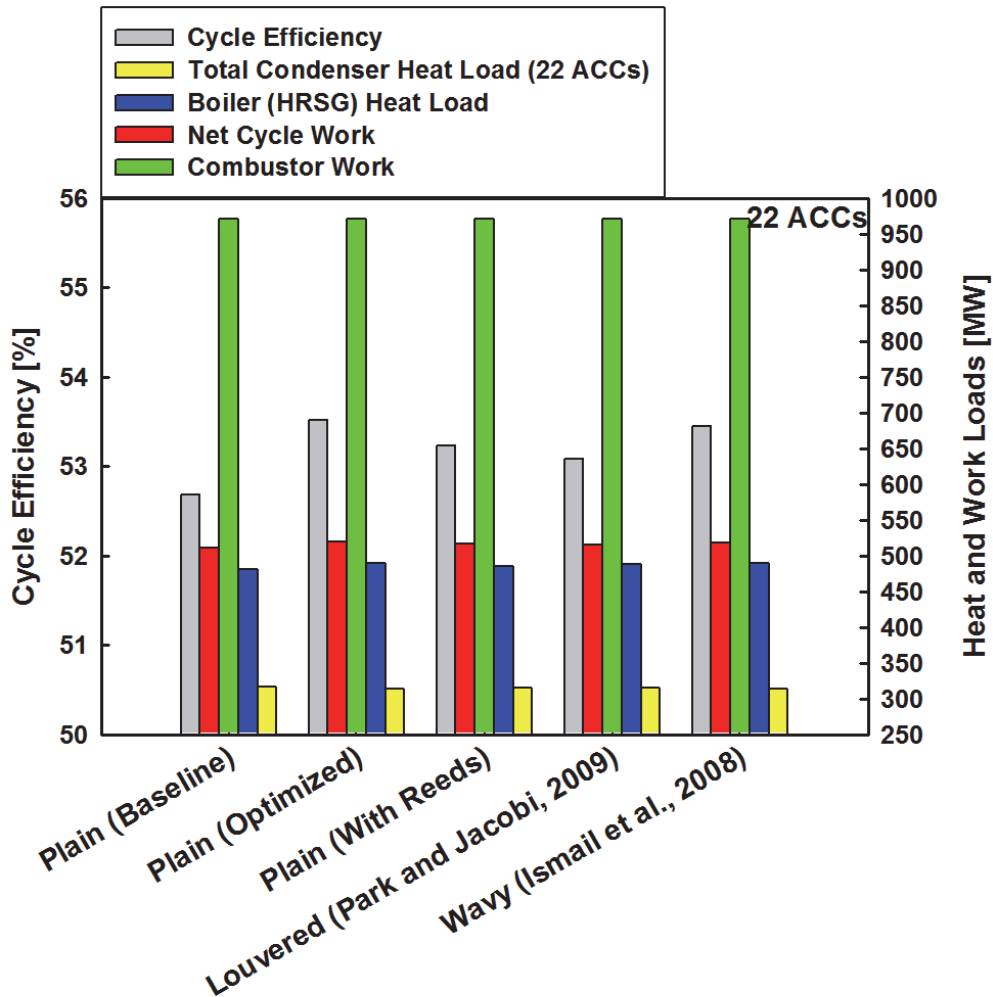


Figure 5.3 Comparison of Combined Cycle efficiency and net cycle work for the different fin types

Cycle efficiencies and the different heat and work loads found for the condensers and in the Combined Cycle are summarized in Table 5.2.

Table 5.2 Summary of cycle efficiencies and work and heat loads for the different fin types in the Combined Cycle

		Plain (Baseline)	Plain (Optimized)	Plain (Reed)	Louvered (Park and Jacobi, 2009)	Wavy (Ismail <i>et al.</i> , 2008)
η_{cycle}	[%]	52.68	53.52	53.23	53.08	53.45
$\dot{W}_{net,cycle}$	[MW]	511.57	519.76	516.92	515.48	519.00
$\dot{Q}_{indiv.,condenser}$ (1 ACC)	[MW]	14.383	14.304	14.340	14.319	14.304
$\dot{Q}_{condenser}$ (22 ACCs)	[MW]	316.43	314.69	315.48	315.02	314.69
\dot{Q}_{boiler}	[MW]	481.14	489.22	485.94	487.90	489.16
$\dot{Q}_{combustor}$	[MW]	971.1	971.1	971.1	971.1	971.1

Varying the plain fin dimensions was once again the most effective way of increasing the cycle efficiency from that of the baseline plain fin case.

5.2 Recommendations for future work

The present study investigated air-cooled condensers in power plants given some constant steam flow rate and ambient conditions. For a globally optimized system with optimal condenser designs, additional ambient conditions and flow rates that represent seasonal variations and load fluctuations should be considered. Mal-distribution of the steam entering the tubes in the condenser, which was not accounted for in this model, will also affect condenser performance. Also, few correlations in the literature address the steam-side geometries for ACCs with the large hydraulic diameters and the inclined orientation, making accurate performance prediction difficult. The impact of wind on the

distribution of air flow in the condenser is also a concern that was not addressed in this analysis, an important parameter that is currently being widely investigated in the literature (Bredell *et al.*, 2006; Gu *et al.*, 2007). Because the performance of the auto-flutter reeds is still under investigation, future data should be incorporated into the condenser model to fully understand the potential of the novel technology.

Data on heat transfer and the pressure drop associated with tubes of this size would be extremely beneficial in the validation of this model. The overall cycle model could be further developed to include reheat and regeneration to more closely represent power plants in operation today. While ACCs do not require water to condense the steam from the turbine, water consumption is still necessary in overall cycle operations for processes such as cleaning and flue gas desulphurization (Macknick *et al.*, 2011). A comparison of the water consumption and withdrawals rates for power plants with the baseline condenser and any optimized condenser from this study to typical cycles with wet-cooled condensing technologies could show the potential water savings from the use of dry-cooling technologies. Finally, the cost of the system should also be studied. One of the main hurdles for the installation of the air-cooled condensers is first cost, which was not considered in this work. Economic analyses should guide the selection of modeling inputs such as the pinch and approach temperature in the HRSG, and the sizing of other components.

The present investigation is a preliminary step in the design and selection of A-frame air-cooled condensers for power plants. With the additional considerations mentioned above, it could serve as a guide for the implementation of air-cooled condensers for thermoelectric power plants under increasingly stringent water consumption constraints.

APPENDIX A: Segmented Heat Transfer Model Sample Calculations

Table A.1 Baseline inputs

<i>Condenser</i>	
ACC_w	12.2 m
ACC_h	10.67 m
β	60°
<i>Tube</i>	
$Tube_d$	190.5 mm
$Tube_w$	25.4 mm
$Tube_t$	1.27 mm
<i>nodes</i>	100
<i>Material</i>	Carbon Steel
k_{tube}	60 W m ⁻¹ K ⁻¹
<i>Fin</i>	
F_h	25.4 mm
F_s	2.54 mm
F_t	0.254 mm
F_d	165.1 mm
ϵ_{fin}	0.005
<i>Material</i>	Aluminum
k_{fin}	180 W m ⁻¹ K ⁻¹

<i>Operating Conditions</i>	
\dot{m}_{steam} (per ACC)	7 kg s ⁻¹
\dot{m}_{air}	645 kg s ⁻¹
$P_{air,in}$	101.3 kPa
$T_{air,in}$	30°C
$\phi_{ambient}$	0.25

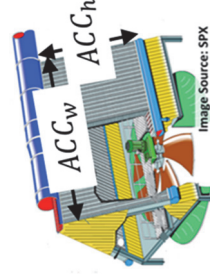
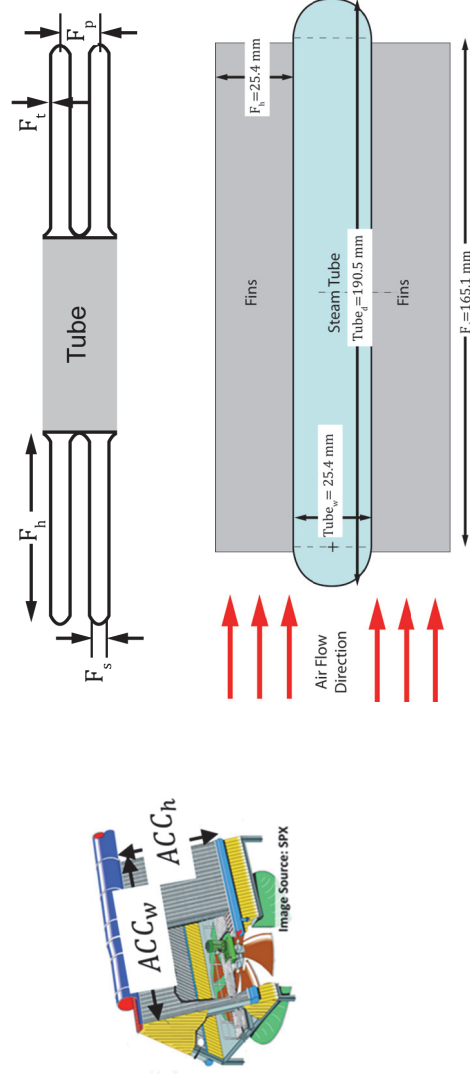


Figure A.1 Condenser, fin, and tube geometry schematic (Source: (SPX, 2015))

Segmented Model Smooth Fin Sample Calculations		Equations	Results
Input			
<i>Number of Fins and Tubes</i>			
$ACC_w = 12.2$ m	Tube pitch	$Tube_p = 2 \times F_h + Tube_w$	$Tube_p = 76.2$ mm
$ACC_h = 10.67$ m	Total number of tubes on ACC	$Num_{tube} = (2 \times ACC_w) / Tube_p$	$Num_{tube} = 320$
$F_h = 25.4$ mm	Number of fins on one side of tube	$Num_{fin} = ACC_h / F_p$	$Num_{fin} = 3,818$
$F_s = 2.54$ mm	Total number of air channels (fins) on ACC		
$F_p = 2.79$ mm	$Num_{channel} = 2 \times \left(\frac{ACC_h}{F_p} \right) \times \left(\frac{2 \times ACC_w}{Tube_p} \right)$		$Num_{channel} = 2.44E + 06$
$Tube_p = 76.2$ mm			
<i>Tube-Side Equations</i>			
$Tube_d = 190.5$ mm	Steam tube cross sectional area		$A_{tube,cs} = 4,185$ mm ²
$Tube_w = 25.4$ mm	$A_{tube,cs} = \frac{\pi}{4} (Tube_w - 2Tube_t)^2 + (Tube_d - Tube_w)(Tube_w - 2Tube_t)$		
$Tube_t = 1.27$ mm	Steam tube internal surface area		$A_{tube,in} = 4.29$ m ²
$ACC_h = 10.67$ m	$A_{tube,in} = ACC_h \times [2 \times (Tube_d - Tube_w) + \pi(Tube_w - 2Tube_t)]$		
	Steam tube hydraulic diameter		$D_{hy,tube} = 41.64$ mm
	$D_{hy,tube} = \frac{4 \times A_{tube,cs}}{2 \times (Tube_d - Tube_w) + \pi(Tube_w - 2Tube_t)}$		

Segmented Model Smooth Fin Sample Calculations		
Input	Equations	Results
<i>Air-Side Equations</i>		
$F_s = 2.54$ mm	$F_p = 2 \times F_t + F_s$	$F_p = 2.79$ mm
$F_t = 0.254$ mm	$F_d = Tube_d - Tube_w$	$F_d = 0.1651$ m
$F_d = 165.1$ mm	$A_{fin} = (2 \times F_h \times F_d) + (2 \times F_h \times F_t)$	$A_{fin} = 0.0084$ m ²
$Tube_d = 190.5$ mm	$A_{fin,cs} = F_d \times F_t$	$A_{fin,cs} = 41.94$ mm ²
$Tube_w = 25.4$ mm	$A_{fin,base,tube} = 2 \times Num_{fin} \times A_{fin,cs}$	$A_{fin,base,tube} = 0.32$ m ²
$Tube_t = 1.27$ mm	$A_{fin,tube} = 2 \times Num_{fin} \times A_{fin}$	$A_{fin,tube} = 64.14$ m ²
$ACC_h = 10.67$ m	$Per_{fin} = F_d \cdot 2 + F_t \cdot 2$	$Per_{fin} = 0.33$ m
$Num_{fin} = 3,818$		
	$D_{hy,channel} = \frac{4 \times F_s \times F_h}{F_d \cdot 2 + F_t \cdot 2}$	$D_{hy,channel} = 4.61$ mm
<i>Area calculations continued</i>		
$ACC_w = 12.2$ m	$A_{fr} = 2 \times ACC_h \times ACC_w$	$A_{fr} = 260.3$ m ²
$ACC_h = 10.67$ m	Area of a single tube not covered by fins (bare tube area)	$A_{tube,bare} = 4.05$ m ²
$Tube_d = 190.5$ mm	$A_{tube,bare} = ACC_h \times [2 \times (Tube_d - Tube_w) + \pi(Tube_w)] - A_{fin,base,tube}$	
$Tube_w = 25.4$ mm	Total air-side surface area	$A_{os,total} = 21,823$ m ²
$A_{fin,tube} = 64.14$ m ²	$A_{os,total} = (A_{tube,bare} + A_{fin,tube}) \times Num_{tube}$	
$Num_{tube} = 320$	Air minimum free-flow area	$A_{ff} = 157.65$ m ²
$Num_{channel} = 2.44E + 06$	$A_{ff} = Num_{channel} \times F_s \times F_h$	

Segmented Model Smooth Fin Sample Calculations		
Input	Equations	Results
<i>Fin-specific equations – used to calculate fin efficiency and effective area</i>		
$h_{air} = 38.36 \text{ W m}^{-2} \text{ K}^{-1}$	$m_{fin} = \sqrt{Per \cdot h_{air} / k_{fin} \cdot A_{fin,cs}}$	$m_{fin} = 40.99 \text{ m}^{-1}$
$Per_{fin} = 0.33 \text{ m}$		
$A_{fin,cs} = 41.94 \text{ mm}^2$		
$F_h = 25.4 \text{ mm}$	$\eta_{fin} = \tanh(m_{fin} F_h) / (m_{fin} F_h)$	$\eta_{fin} = 0.75$
$k_{fin} = 180 \text{ W m}^{-1} \text{ K}^{-1}$		
$Tube_d = 190.5 \text{ mm}$		
$Tube_w = 25.4 \text{ mm}$		
$A_{fin,tube} = 64.14 \text{ m}^2$		
$Num_{tube} = 320$		
$Num_{channel} = 2.44\text{E}+06$		
$Num_{fin} = 3,818$		
<i>Flow rates and mass fluxes</i>		
$\dot{m}_{steam} = 7 \text{ kg s}^{-1}$		
$\dot{m}_{air} = 645 \text{ kg s}^{-1}$		
$Num_{tube} = 320$		
$Num_{channel} = 2.44\text{E}+06$		
$A_{tube,cs} = 4,185 \text{ mm}^2$		
Density of air is based on ambient temperature, pressure, and relative humidity		
$\rho_{air} = 1.162 \text{ kg m}^{-3}$		
Mass flow rate of air per channel	$\dot{m}_{air,channel} = \dot{m}_{air} / Num_{channel}$	$\dot{m}_{air,channel} = 2.64\text{E}-04 \text{ kg s}^{-1}$
Fan volumetric flow rate	$\dot{V}_{fan} = \dot{m}_{air} / \rho_{air}$	$\dot{V}_{fan} = 555.3 \text{ m}^3 \text{ s}^{-1}$
Air frontal velocity	$V_{channel} = \frac{\dot{m}_{air,channel}}{\rho_{air} \times (F_s \times F_h)}$	$V_{channel} = 3.522 \text{ m s}^{-1}$
Mass flow rate of steam per tube	$\dot{m}_{steam,tube} = \dot{m}_{steam} / Num_{tube}$	$\dot{m}_{steam,tube} = 0.022 \text{ kg s}^{-1}$
Mass flux of steam	$G = \left(\frac{\dot{m}_{steam}}{Num_{tube}} \right) \left(\frac{1}{A_{tube,cs}} \right)$	$G = 5.227 \text{ kg m}^{-2} \text{ s}^{-1}$
Overall fin surface efficiency	$\eta_{overall} = 1 - (2 \cdot Num_{fin}) \cdot \frac{A_{fin}}{A_{bare,onetube} + A_{fin,onetube}} \cdot (1 - \eta_{fin})$	$\eta_{overall} = 0.7625$
Effective area of a single tube	$A_{eff} = A_{tube,bare} + \eta_{fin} \times A_{fin,tube}$	$A_{eff} = 52 \text{ m}^2$

Segmented Model Smooth Fin Sample Calculations	
Inlet air properties - calculated in Engineering Equation Solver	
$P_{air,in} = 101.3 \text{ kPa}$ $T_{air,in} = 30^\circ\text{C}$ $\phi_{ambient} = 0.25$	$\rho_{air} = 1.162 \text{ kg m}^{-3}$ $\mu_{air} = 1.871\text{E-}05 \text{ kg m}^{-1}\text{s}^{-1}$ $k_{air} = 0.02591 \text{ W m}^{-1}\text{K}^{-1}$
	$Cp_{air} = 1.017 \text{ kJ kg}^{-1}\text{K}^{-3}$ $Pr_{air} = 0.7268$
	$\omega_{air} = 6.585\text{E-}03$ $H_{air} = 46.96 \text{ kJ kg}^{-1}$
Input	
Air-side heat transfer and pressure drop calculations	
$F_h = 25.4 \text{ mm}$ $F_s = 2.54 \text{ mm}$ $F_d = 165.1 \text{ mm}$ $V_{channel} = 3.522 \text{ m s}^{-1}$ $D_{hy,channel} = 4.61 \text{ mm}$	$\alpha^* = F_s / F_h$ $Re_{channel} = \frac{\rho_{air} V_{channel} D_{hy,channel}}{\mu_{air}}$ $Nusselt \text{ number calculation (Shah and London, 1978a)}$ $Nu_{channel} = 7.541(1 - 2.61\alpha^* + 4.97\alpha^{*2} - 5.119\alpha^{*3} + 2.702\alpha^{*4} - 0.548\alpha^{*5})$ $h_{air} = \frac{Nu_{channel} k_{air}}{D_{hy,channel}}$ $Friction \text{ factor calculation (Shah and London, 1978a)}$ $f_{air,darcy} = \frac{96}{Re_{channel}} (1 - 1.3553\alpha^* + 1.9467\alpha^{*2} - 1.7012\alpha^{*3} + 0.9564\alpha^{*4} - 0.2537\alpha^{*5})$ $\Delta P_{channel} = \frac{1}{2} \frac{f_{air,darcy} \rho_{air} V_{channel}^2 F_d}{D_{hy,channel}}$
	$\alpha^* = 0.1$ $Re_{channel} = 1009$ $Nu_{channel} = 6.845$ $h_{air} = 38.36 \text{ W m}^{-2}\text{K}^{-1}$ $f_{air,darcy} = 0.1122$ $\Delta P_{channel} = 28.84 \text{ Pa}$
Results	
The two phase percentage, TPP, was calculated using the iterative solving ability of EES.	
$ACC_h = 10.67 \text{ m}$ $TPP = 0.9925$ $nodes = 100$ $Num_{tube} = 320$	$L_{section} = (ACC_H \cdot TPP) / nodes - 1$ $SP = L_{section} / ACC_h$ $\dot{m}_{air,seg} = \frac{\dot{m}_{air}}{Num_{tube}} \cdot \frac{TPP}{nodes - 1}$
	$L_{section} = 0.107 \text{ m}$ $SP = 0.01003$ $\dot{m}_{air,seg} = 0.020 \text{ kg s}^{-1}$

Segmented Model Smooth Fin Sample Calculations

The following calculations show calculations done on a segment at about the halfway point of the tube. Inlet properties are taken for the steam entering node 49. Outlet property values, which were calculated using the iterative properties of Engineering Equation Solver, correspond to node number 50. Unless otherwise stated, all values presented are for node 49.

Steam properties for segment 49 - calculated in Engineering Equation Solver

$x = 0.4739$ $T = 72.387^\circ\text{C}$ $P = 34.568 \text{ kPa}$	<u>Liquid only properties (x = 0) at node 49</u> $\mu_l = 3.91\text{E-}04 \text{ kg m}^{-1}\text{s}^{-1}$ $\rho_l = 976.4 \text{ kg m}^{-3}$ $C_{p_l} = 4.192 \text{ kJ kg}^{-1}\text{K}^{-1}$ $\text{Pr}_l = 2.465$ $k_l = 0.6649 \text{ W m}^{-1}\text{K}^{-1}$ $H_l = 303.1 \text{ kJ kg}^{-1}$	<u>Vapor only properties (x = 1) at node 49</u> $\rho_v = 0.2184 \text{ kg m}^{-3}$ $\mu_v = 1.134\text{E-}05 \text{ kg m}^{-1}\text{s}^{-1}$ $H_v = 2,630 \text{ kJ kg}^{-1}$
--	---	---

Input		Equations		Results
$G = 5.227 \text{ kg m}^{-2}\text{s}^{-1}$ $D_{hy,tube} = 41.64 \text{ mm}$ $\beta = 60^\circ$	Liquid only Reynolds number	$Re_{lo} = \frac{GD_{hy,tube}}{\mu_l}$		$Re_{lo} = 556.6$
	Vapor only Reynolds number	$Re_{vo} = \frac{GD_{hy,tube}}{\mu_v}$		$Re_{vo} = 19,195$
	Liquid Reynolds number	$Re_l = \frac{G(1-x)D_{hy,tube}}{\mu_l}$		$Re_l = 292.8$
	Vapor Reynolds number	$Re_v = \frac{GxD_{hy,tube}}{\mu_v}$		$Re_v = 9,097$
	Two-Phase Homogeneous Density	$\rho_{TP} = \left(\left(\frac{x}{\rho_v} \right) + \left(\frac{1-x}{\rho_l} \right) \right)^{-1}$		$\rho_{TP} = 0.461 \text{ kg m}^{-3}$
	Martinelli Parameter	$X_{tt} = \left(\frac{1-x}{x} \right)^{0.90} \left(\frac{\rho_v}{\rho_l} \right)^{0.5} \left(\frac{\mu_v}{\mu_l} \right)^{0.1}$		$X_{tt} = 0.02341$

Segmented Model Smooth Fin Sample Calculations		
The following calculations show calculations done on a segment at about the halfway point of the tube. Inlet properties are taken for the steam entering node 49. Outlet property values, which were calculated using the iterative properties of Engineering Equation Solver, correspond to node number 50. Unless otherwise stated, all values presented are for node 49.		
Steam properties for segment 49 - calculated in Engineering Equation Solver		
$x = 0.4739$ $T = 72.387^\circ\text{C}$ $P = 34.568 \text{ kPa}$	Liquid only properties ($x = 0$) at node 49 $\mu_l = 3.91\text{E-}04 \text{ kg m}^{-1}\text{s}^{-1}$ $\rho_l = 976.4 \text{ kg m}^{-3}$ $Cp_l = 4.192 \text{ kJ kg}^{-1}\text{K}^{-1}$ $Pr_l = 2.465$ $k_l = 0.6649 \text{ W m}^{-1}\text{K}^{-1}$ $H_l = 303.1 \text{ kJ kg}^{-1}$	Vapor only properties ($x = 1$) at node 49 $\rho_v = 0.2184 \text{ kg m}^{-3}$ $\mu_v = 1.134\text{E-}05 \text{ kg m}^{-1}\text{s}^{-1}$ $H_v = 2,630 \text{ kJ kg}^{-1}$
Input		
Akhtavan-Behabadi <i>et al.</i> (2007) correlation		
$D_{hy,tube} = 41.64 \text{ mm}$ $\beta = 60^\circ$ $X_{tt} = 0.02341$	Correction factor in the correlation $F_\beta = \frac{1 + (1-x)^{0.2} \cos(\beta - 10^\circ)}{x^{0.4}}$	$F_\beta = 2.11$
	Heat transfer coefficient prediction $h_{steam} = 1.09 \left(\frac{k_l}{D_{hy,tube}} \right) Re_l^{0.45} F_\beta^{0.3} \sqrt{\frac{Pr_l}{X_{tt}}}$	$h_{steam} = 2,879 \text{ W m}^{-2}\text{K}^{-1}$
$h_{air} = 38.36 \text{ W m}^{-2}\text{K}^{-1}$ $A_{os,total} = 21,823 \text{ m}^2$ $A_{os,total,tube} = 68.2 \text{ m}^2$ $\eta_{overall} = 0.7625$ $SP = 0.01003$ $Tube_i = 1.27 \text{ mm}$ $A_{tube,in} = 4.29 \text{ m}^2$ $k_{tube} = 60 \text{ W m}^{-1}\text{K}^{-1}$	Thermal resistance due to air convection per segment $R_{air} = \frac{1}{h_{air} A_{os,total,tube} \eta_{overall} SP}$	$R_{air} = 0.05 \text{ K W}^{-1}$
	Thermal resistance due to tube conduction per segment $R_{wall} = \frac{Tube_i}{k_{tube} A_{tube,in} SP}$	$R_{wall} = 4.92\text{E-}04 \text{ K W}^{-1}$

Segmented Model Smooth Fin Sample Calculations

Input		Equations		Results
$h_{steam} = 2,879 \text{ W m}^{-2} \text{ K}^{-1}$ $A_{tube,in} = 4.29 \text{ m}^2$ $SP = 0.01003$ $R_{air} = 0.05 \text{ K W}^{-1}$ $R_{wall} = 4.92\text{E-}04 \text{ K W}^{-1}$	<p>Thermal resistance due to steam convection per segment</p> $R_{steam,convection} = \frac{1}{h_{steam} A_{tube,in} SP}$	$R_{steam,convection} = 8.08\text{E-}03 \text{ K W}^{-1}$		
$H_{steam,in} = 1405.93 \text{ kJ kg}^{-1}$ $H_{air,in} = 46.96 \text{ kJ kg}^{-1}$ $\dot{m}_{air,seg} = 0.020 \text{ kg s}^{-1}$ $\dot{m}_{steam,tube} = 0.022 \text{ kg s}^{-1}$		$UA_{seg} = \left(\frac{1}{R_{steam,convection} + R_{wall} + R_{air}} \right)$ $LMTD = \frac{(T_{steam,in} - T_{air,out}) - (T_{steam,out} - T_{air,in})}{\ln \left(\frac{T_{steam,in} - T_{air,out}}{T_{steam,out} - T_{air,in}} \right)}$	$UA_{seg} = 0.0171 \text{ kW K}^{-1}$ $LMTD = 28.8 \text{ K}$	
<p><u>Inlet (node 49)</u></p> $\rho_v = 0.2184 \text{ kg m}^{-3}$ $\rho_l = 976.4 \text{ kg m}^{-3}$ $\mu_l = 3.91\text{E-}04 \text{ kg m}^{-1} \text{ s}^{-1}$ $\mu_v = 1.13\text{E-}05 \text{ kg m}^{-1} \text{ s}^{-1}$ $x = 0.4739$	<p><u>Outlet (node 50)</u></p> $\rho_v = 0.2185 \text{ kg m}^{-3}$ $\rho_l = 976.3 \text{ kg m}^{-3}$ $\mu_l = 3.91\text{E-}04 \text{ kg m}^{-1} \text{ s}^{-1}$ $\mu_v = 1.13\text{E-}05 \text{ kg m}^{-1} \text{ s}^{-1}$ $x = 0.4642$	<p>Energy Balance</p> $\dot{Q} = UA_{seg} \cdot LMTD$ $H_{steam,in} \cdot \dot{m}_{water,tube} = H_{steam,out} \cdot \dot{m}_{water,tube} + \dot{Q}$ $H_{air,in} \cdot \dot{m}_{air,seg} = H_{air,out} \cdot \dot{m}_{air,seg} - \dot{Q}$	$\dot{Q} = 0.4917 \text{ kW}$ $H_{steam,out} = 1,383.45 \text{ kJ kg}^{-1}$ $H_{air,out} = 71.3 \text{ kJ kg}^{-1}$	
	<p>Martinelli Parameter</p> $X_{tt} = \left(\frac{\rho_v}{\rho_l} \right)^{0.5} \left(\frac{\mu_l}{\mu_v} \right)^{0.125} \left(\frac{1-x}{x} \right)^{0.875}$		$X_{t,in} = 0.02551$ $X_{t,out} = 0.0264$	

Segmented Model Smooth Fin Sample Calculations		
<i>Equations required for segmental pressure drop calculations- values needed for both the inlet and outlet of the segment</i>		
Input	Equations	
Results		
$L_{section} = 0.107 \text{ m}$ $G = 5.227 \text{ kg m}^{-2} \text{ s}^{-1}$	Void Fraction (Lockhart and Martinelli, 1949) $\alpha = \left(1 + 0.28 \left(\frac{1-x}{x} \right)^{0.64} \left(\frac{\rho_v}{\rho_l} \right)^{0.36} \left(\frac{\mu_l}{\mu_v} \right)^{-1} \right)^{-1}$	$\alpha_{in} = 0.9817$ $\alpha_{out} = 0.9813$
<u>Inlet (node 49)</u> $\rho_v = 0.2184 \text{ kg m}^{-3}$ $\rho_l = 976.4 \text{ kg m}^{-3}$ $\mu_l = 3.91\text{E-}04 \text{ kg m}^{-1} \text{ s}^{-1}$ $\mu_v = 1.13\text{E-}05 \text{ kg m}^{-1} \text{ s}^{-1}$ $x = 0.4739$ $Re_l = 292.8$ $Re_v = 9,097$	Single Phase Friction Factor (Blasius) (if $Re_v < 2,000$, $B = 16$ and $n = 1$ else $B = 0.079$ and $n = 0.25$) $f_v = B \cdot Re_v^{-n}$ Two-Phase Multiplier (Chisholm, 1967) $\phi_{v,CL} = (1 + CX_t + X_t^2)^{1/2}$ Multipliers used in the trapezoidal rule $I_z = 0.5 \left((f_{v,out} x_{out}^2 \phi_{v,CL,out}^2) + (f_{v,in} x_{in}^2 \phi_{v,CL,in}^2) \right) L_{section}$ $J_z = 0.5 \left(((1 - \alpha_{out}) \rho_l + \alpha_{out} \rho_v) + ((1 - \alpha_{in}) \rho_l + \alpha_{in} \rho_v) \right) L_{section}$	$f_{v,in} = 0.008089$ $f_{v,out} = 0.008131$ $\phi_{v,CL,in} = 1.143$ $\phi_{v,CL,out} = 1.148$ $I_z = 2.504\text{E-}04$ $J_z = 1.954$
<u>Outlet (node 50)</u> $\rho_v = 0.2185 \text{ kg m}^{-3}$ $\rho_l = 976.3 \text{ kg m}^{-3}$ $\mu_l = 3.91\text{E-}04 \text{ kg m}^{-1} \text{ s}^{-1}$ $\mu_v = 1.13\text{E-}05 \text{ kg m}^{-1} \text{ s}^{-1}$ $x = 0.4642$ $Re_l = 298.3$ $Re_v = 8,911$	Frictional Pressure Drop $\Delta P_{TP,Fric} = \left(\frac{2G^2}{\rho_v D} \right) I_z$ Gravitational Pressure Drop $\Delta P_{TP,Grav} = 9.81 \cdot \sin(-\beta) J_z$ Momentum Pressure Drop $\Delta P_{TP,Dec} = G^2 \left(\left(\frac{x_{out}^2}{\rho_v \alpha_{out}} \right) - \left(\frac{1-x_{out}}{\rho_l (1-\alpha_{out})} \right) \right) - G^2 \left(\left(\frac{x_{in}^2}{\rho_v \alpha_{in}} \right) - \left(\frac{1-x_{in}}{\rho_l (1-\alpha_{in})} \right) \right)$	$\Delta P_{TP,Fric} = 1.505 \text{ Pa}$ $\Delta P_{TP,Grav} = -16.6 \text{ Pa}$ $\Delta P_{TP,Dec} = -1.149 \text{ Pa}$
	Total pressure drop in the segment $\Delta P_{TP} = \Delta P_{TP,Fric} + \Delta P_{TP,Dec} + \Delta P_{TP,Grav}$ Outlet pressure $P_{out} = P_{in} - \Delta P_{TP}$	$\Delta P_{TP} = -16.24 \text{ Pa}$ $P_{out} = 34.584 \text{ kPa}$

Segmented Model Smooth Fin Sample Calculations		
<i>Equations required for calculations in the final, subcooled section (final segment). Two degrees of subcooling were allowed.</i>		
Steam properties for segment 99 - calculated in Engineering Equation Solver		
$x \approx 0$ $T = 74.207^\circ\text{C}$ $P = 37.334 \text{ kPa}$	Single phase (sp) properties entering the final segment: $\rho_{sp} = 975.3 \text{ kg m}^{-3}$ $Cp_{\text{steam,sp}} = 4.193 \text{ kJ kg}^{-1}\text{K}^{-1}$ $Pr_{sp} = 2.402$ $\mu_{sp} = 3.817\text{E-}04 \text{ kg m}^{-1}\text{s}^{-1}$ $k_{sp} = 0.6662 \text{ W m}^{-1}\text{K}^{-1}$	
Input	Equations	Results
$\dot{m}_{\text{steam,tube}} = 0.022 \text{ kg s}^{-1}$ $A_{\text{tube,cs}} = 4,185 \text{ mm}^2$ $D_{\text{hy,tube}} = 41.64 \text{ mm}$ $TP = 0.9925$ $ACC_h = 10.67 \text{ m}$ $Tube_d = 190.5 \text{ mm}$ $Tube_w = 25.4 \text{ mm}$ $Tube_l = 1.27 \text{ mm}$	Velocity of water in final segment $V_{\text{tube}} = \frac{\dot{m}_{\text{steam,tube}}}{\rho_{sp} A_{\text{tube,cs}}}$ Reynolds number in final segment $Re_{\text{tube,sp}} = \frac{\rho_{sp} V_{\text{tube}} D_{\text{hy,tube}}}{\mu_{sp}}$ Tube aspect ratio $\alpha_{\text{tube}}^* = \frac{Tube_l - 2Tube_w}{Tube_w - 2Tube_l}$ Nusselt number for final segment $Nu_{sp} = 3.66 + \frac{0.065 Re_{\text{tube,sp}} Pr_{sp} \frac{D_{\text{hy,tube}}}{ACC_h (1-TPP)}}{1 + 0.04 \left(Re_{\text{tube,sp}} Pr_{sp} \frac{D_{\text{hy,tube}}}{ACC_h (1-TPP)} \right)^{2/3}}$	$V_{\text{tube}} = 0.0054 \text{ m s}^{-1}$ $Re_{\text{tube,sp}} = 570.3$ $\alpha_{\text{tube}}^* = 0.1216$ $Nu_{sp} = 14.72$
	Heat transfer coefficient for final segment $h_{sp} = \frac{Nu_{sp} k_{sp}}{D_{\text{hy,tube}}}$	$h_{sp} = 235.4 \text{ W m}^{-2}\text{K}^{-1}$
	Friction factor calculation (Shah and London, 1978a) $f_{sp,darcy} = \frac{96}{Re_{\text{tube,sp}}} \left(1 - 1.3553 \alpha_{\text{tube}}^* + 1.9467 \alpha_{\text{tube}}^{*2} - 1.7012 \alpha_{\text{tube}}^{*3} + 0.9564 \alpha_{\text{tube}}^{*4} - 0.2537 \alpha_{\text{tube}}^{*5} \right)$	$f_{sp,darcy} = 0.1532$
	Frictional component of pressure drop $\Delta P_{sp,fric} = \frac{1}{2} \frac{f_{sp,darcy} \rho_{sp} V_{\text{tube}}^2 ACC_h (1-TPP)}{D_{\text{hy,tube}}}$	$\Delta P_{sp,fric} = 4.12\text{E-}03 \text{ Pa}$
	Gravitational component of pressure drop $\Delta P_{sp,grav} = \rho_{sp} 9.81 (H_{ACC,CELL} (1-TPP) \sin(-\beta))$	$\Delta P_{sp,grav} = -662.5 \text{ Pa}$

Segmented Model Smooth Fin Sample Calculations		
<i>Equations required for calculations in the final, subcooled section (final segment). Two degrees of subcooling were allowed.</i>		
Input	Equations	Results
$TP = 0.9925$ $ACC_h = 10.67 \text{ m}$ $A_{os, total, tube} = 68.2 \text{ m}^2$ $A_{tube, in} = 4.29 \text{ m}^2$ $h_{air} = 38.36 \text{ W m}^{-2} \text{ K}^{-1}$ $h_{sp} = 235.4 \text{ W m}^{-2} \text{ K}^{-1}$ $\dot{m}_{steam, tube} = 0.022 \text{ kg s}^{-1}$	Length of the final, single phase segment $L_{subcool} = ACC_h (1 - TPP)$ Percentage of the tube that is subcooled $SSP = L_{subcool} / ACC_h$ Thermal resistance due to air convection per segment $R_{air, sp} = \frac{1}{h_{air} A_{os, total, onetube} \eta_{overall} SSP}$ Thermal resistance due to tube conduction per segment $R_{wall, sp} = \frac{Tube_i}{k_{tube} A_{tube, in} SSP}$ Thermal resistance due to steam convection per segment $R_{steam, convection, sp} = \frac{1}{h_{sp} A_{tube, in} SSP}$	$L_{subcool} = 0.08 \text{ m}$ $SSP = 0.0075$ $R_{air, sp} = 0.06686 \text{ K W}^{-1}$ $R_{wall, sp} = 6.583-04 \text{ K W}^{-1}$ $R_{steam, convection, sp} = 0.1321 \text{ K W}^{-1}$
Properties Air properties taken at ambient temperature, pressure, and relative humidity $Cp_{air} = 1.017 \text{ kJ kg}^{-1} \text{ K}^{-1}$ $Cp_{steam, sp} = 4.19 \text{ kJ kg}^{-1} \text{ K}^{-1}$	$UA_{seg, sp} = \left(\frac{1}{R_{steam, convection, sp} + R_{wall, sp} + R_{air, sp}} \right)$ Capacity rate of air $C_{air, sp} = \dot{m}_{air, sp} Cp_{air}$ Capacity rate of steam $C_{steam, sp} = \dot{m}_{steam, tube} Cp_{steam}$ Capacity rate ratio $C_{rat, sp} = \frac{\min(C_{air, sp}, C_{steam})}{\max(C_{air, sp}, C_{steam})}$	$UA_{seg, sp} = 0.00501 \text{ kW K}^{-1}$ $C_{air, sp} = 0.01537 \text{ kW K}^{-1}$ $C_{steam, sp} = 0.09172 \text{ kW K}^{-1}$ $C_{rat, sp} = 0.1676$
	$NTU_{sp} = \frac{UA_{seg, sp}}{C_{min, sp}}$ $C_{min, sp}$ is the minimum heat capacity rate between the air and steam	$NTU_{sp} = 0.3259$

Segmented Model Smooth Fin Sample Calculations		
<i>Equations required for calculations in the final, subcooled section (final segment). Two degrees of subcooling were allowed.</i>		
Input	Equations	Results
(minimum between air and steam) $C_{min,sp} = 0.01537 \text{ kW K}^{-1}$ Temperature of steam entering subcooled section was calculated in EES $T_{steam,sp} = 74.207^\circ\text{C}$ $\dot{m}_{air,seg} = 0.020 \text{ kg s}^{-1}$ $Num_{tube} = 320$ $TPP = 0.9925$	Assuming both fluids unmixed $\varepsilon_{sp} = 1 - \exp\left[\left(\frac{NTU_{sp}^{0.22}}{C_{rat,sp}}\right) \left(\exp\left[-C_{rat,sp} NTU_{sp}^{0.78}\right] - 1\right)\right]$ Heat transfer in the final segment $Q_{sp} = \varepsilon_{sp} C_{min,sp} (T_{steam,sp} - T_{air,ambient})$ Mass flow rate of air entering the final segment (calculated by determining the mass flow rate of air per tube and subtracting the mass flow rate across the two phase section) $\dot{m}_{air,sp} = \frac{\dot{m}_{air}}{Num_{tube}} - \left(\frac{\dot{m}_{air}}{Num_{tube}}\right) TPP$	$\varepsilon_{sp} = 0.2701$ $Q_{sp} = 0.1835 \text{ kW}$ $\dot{m}_{air,sp} = 0.015 \text{ kg s}^{-1}$
$\dot{m}_{steam,tube} = 0.022 \text{ kg s}^{-1}$ $H_{steam,in} = 2513.34 \text{ kJ kg}^{-1}$ $H_{steam,out} = 302.32 \text{ kJ kg}^{-1}$ $\dot{m}_{air,seg} = 0.02021 \text{ kg s}^{-1}$ $\dot{m}_{air,sp} = 0.01511 \text{ kg s}^{-1}$ $H_{air,in} = 46.96 \text{ kJ kg}^{-1}$ $H_{air,out,sp} = 59.11 \text{ kJ kg}^{-1}$ $H_{air,out,seg} = 71.51$ to 67.23 kJ kg^{-1}	Overall energy balance check on a single tube for steam side and air side Steam side: $\dot{m}_{steam,tube} (H_{steam,in} - H_{steam,out})$ Air side: $\dot{m}_{air,sp} (H_{air,out,sp} - H_{air,in}) + \sum \dot{m}_{air,seg} (H_{air,out,seg} - H_{air,in})$ $H_{air,in}$ = enthalpy of ambient air $H_{air,out,seg}$ = enthalpy of the air exiting each segment	Steam side: 48.38 kW Air side: 48.38 kW
	Final results from the analysis: $T_{steam} = 72.207^\circ\text{C}$ $P_{steam} = 37.997 \text{ kPa}$ ITD = 42.12 K $\Delta P_{air,total} = 143.59 \text{ kPa}$	

APPENDIX B: Air-Side Minor Loss Calculations

Relevant Dimensions from Kröger (1998)					
Term	Definition	Upstream		Downstream	
		si	bi	so	bo
d_c	Fan casing diameter [m]	9.17	9.17	9.17	9.17
x	Obstacle distance from fan [m]	1.30	1.34	1.00	0.53
x/d_c	Ratio of obstacle distance to fan diameter [-]	0.14	0.15	0.11	0.06
A/A_c	Ratio of obstacle obstruction area to fan cross sectional area [-]	0.13	0.15	0.11	0.04
K	Loss coefficient	0.13	0.17	0.23	0.16

Inputs	
ρ_{in}	1.162 kg m ⁻³
\dot{m}_{air}	645 kg s ⁻¹
A_{fan}	63.62 m ²

- Relevant obstacle dimensions for upstream and downstream obstacles taken from Kröger (1998)
- x/d_c and A/A_c ratios for the obstacles si and bi used in plot for upstream losses
- x/d_c and A/A_c ratios for the obstacles so and bo used in plot

Upstream Loss coefficient: K_{up}

Source: (Figure 6.4.1 in Kröger (1998))

$$K_{up} = K_{si} + K_{bi} = 0.30$$

$$\Delta P_{K,up} = K_{up} \frac{1}{2} \rho_{in} \left(\frac{\dot{m}_{air}}{A_{fan} \rho_{in}} \right)^2 = 13.27 \text{ Pa}$$

Downstream Loss coefficient: K_{do}

Source: (Figure 6.4.2 in Kröger (1998))

$$K_{do} = K_{so} + K_{bo} = 0.39$$

$$\Delta P_{K,do} = K_{do} \frac{1}{2} \rho_{in} \left(\frac{\dot{m}_{air}}{A_{fan} \rho_{in}} \right)^2 = 17.25 \text{ Pa}$$

Inputs	
θ	30°
ρ_{in}	1.162 kg m ⁻³
ρ_{out}	1.078 kg m ⁻³
\dot{m}_{air}	645 kg s ⁻¹
A_{ff}	157.6 m ²
A_{fr}	260.3 m ²
A_{fan}	63.62 m ²
$Tube_w$	25.4 mm
$Tube_p$	0.0762 m

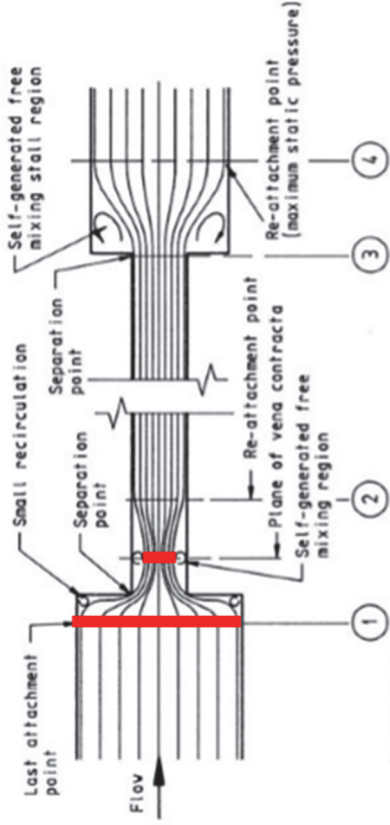


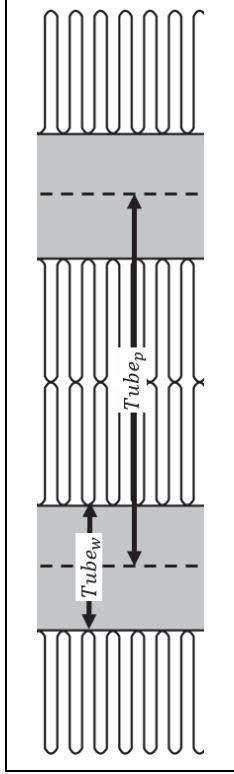
(Figure 2.3.2 in Kröger (1998))

Contraction Ratio

$$\sigma = \frac{A_{ff}}{A_{fr}} = 0.606$$

Jetting Contraction Ratio (Equation 2.3.10 in Kröger (1998)):

$$\sigma_c = 0.614 + 0.046\sigma - 0.337\sigma^2 + 0.408\sigma^3 + 2.672\sigma^4 - 5.963\sigma^5 + 3.559\sigma^6 = 0.659$$



Inlet Contraction Loss, K_{ci} (Equation

5.6.13 in Kröger (1998)):

$$K_{ci} = \left(1 - \frac{1/\sigma_c}{\sigma}\right)^2 = 0.733$$

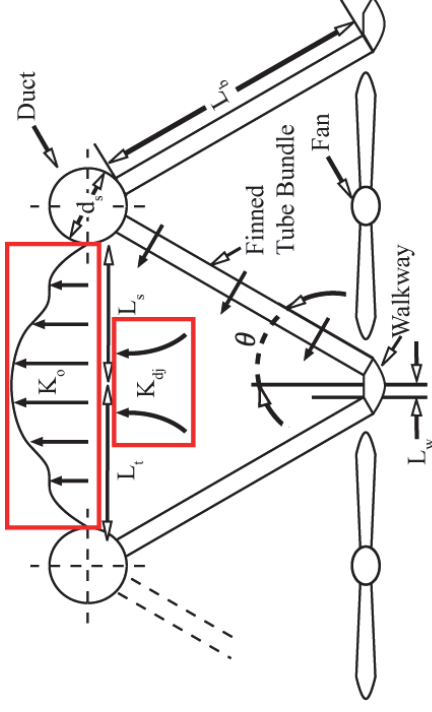
Mean Incidence Angle: $\theta_m = 0.0019\theta^2 + 0.9133\theta - 3.1558 = 29.95^\circ$

Angled Inlet and Outlet Loss Coefficient: $K_{i,\theta,e}$ (Equation 5.6.19 in Kröger (1998))

$$K_{i,\theta,e} = \frac{2}{\sigma^2} \left(\frac{\rho_{in} - \rho_{out}}{\rho_{in} + \rho_{out}} \right) + 2 \frac{\rho_{out}}{\rho_{in} + \rho_{out}} \left(\frac{1}{\sin(\theta_m)} - 1 \right) \left(\left(\frac{1}{\sin(\theta_m)} - 1 \right) + 2K_{ci}^{0.5} \right) \left(\frac{Tube_p}{Tube_p - Tube_w} \right)^2 = 8.55$$

$$\Delta P_{K,i,\theta,e} = K_{i,\theta,e} \frac{1}{2} \rho_{in} \left(\frac{\dot{m}_{air}}{A D} \right)^2 = 61.58 \text{ Pa}$$

Inputs		
Term	Definition	Value
L_w	Walkway Width	0.6096 m
L_b	Steam Tube Length	10.67 m
L_s	Half distance between condensate removal tube edges	5.004 m
L_t	Half distance between condensate tube edges	5.334 m
L_r	Length of tube and walkway bend	10.67 m
d_s	Inlet steam tube diameter	0.1524 m
θ	Steam tube angle	30°



Jetting Loss coefficient: K_{dj} (Equation 5.6.21 in Kröger (1998))

$$K_{dj} = \left[\left(\left[-2.892 \left(\frac{L_w}{L_b} \right) + 2.933 \left(\frac{L_w}{L_b} \right) \left(\frac{L_t}{L_s} \right) \left(\frac{L_r}{L_s} \right) \left(\frac{28^\circ}{\theta} \right)^{0.4} + \left(e^{2.370+0.059\theta-0.003797\theta^2} \left(\frac{L_s}{L_t} \right) \right)^{0.5} \left(\frac{L_b}{L_r} \right) \right]^2 \right) \right] = 1.75$$

$$\Delta P_{K,dj} = K_{dj} \frac{1}{2} \rho_{in} \left(\frac{\dot{m}_{air}}{A_{fr} \rho_{in}} \right)^2 = 4.626$$

Outlet Loss coefficient: K_o (Equation 5.6.22 in Kröger (1998))

$$K_o = \left[\left(\left[-2.891 \frac{L_w}{L_b} + 2.933 \left(\frac{L_w}{L_b} \right) \left(\frac{L_s}{L_t} \right) \left(\frac{L_r}{L_s} \right) \right]^3 + 1.987 - 3.028 \frac{d_s}{2L_t} + 2.018 \cdot \left(\frac{d_s}{2L_t} \right)^2 \right) \left(\frac{L_b}{L_s} \right)^2 \right] = 8.255$$

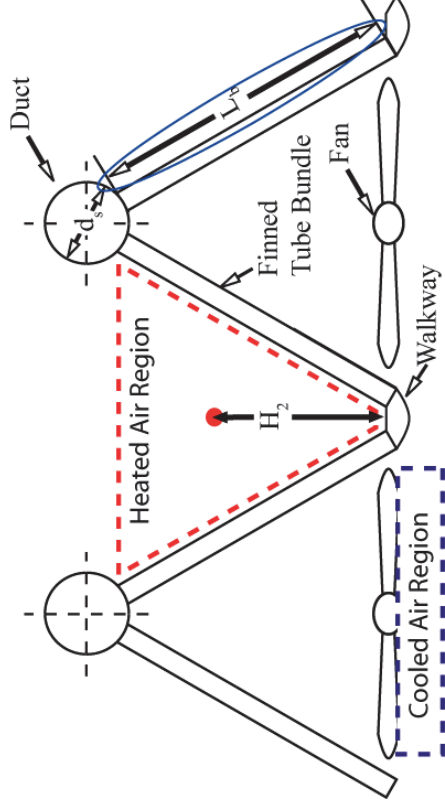
$$\Delta P_{K,o} = K_o \frac{1}{2} \rho_{in} \left(\frac{\dot{m}_{air}}{A_{fr} \rho_{in}} \right)^2 = 21.82 \text{ Pa}$$

Minor loss due to temperature change

Inputs		
Term	Definition	Value
H_2	Average height of heated air	4.619 m
θ	Inclination Angle	28°
L_b	Steam Tube Length	10.668 m
ρ_{out}	Air outlet density	1.078 kg m ⁻³
ρ_{in}	Air inlet density	1.162 kg m ⁻³

$$H_2 = \cos(\theta) \frac{L_b}{2} = 4.619 \text{ m}$$

$$\Delta P_{temp} = g \cdot H_2 (\rho_{out} - \rho_{in}) = -3.79 \text{ Pa}$$



Air-side Minor Losses Summary

Source of Minor Loss	Loss Coefficient, K [-]	Pressure Drop [Pa]
K_{up}	0.3	13.27
K_{do}	0.39	17.26
$K_{i,\theta,e}$	8.545	61.58
K_{dj}	1.75	4.63
K_o	8.255	21.82
ΔT	N/A	-3.79
		114.8

$$\Delta P_{MinorLosses} = \Delta P_{K,o} + \Delta P_{K,dj} + \Delta P_{K,up} + \Delta P_{K,do} + \Delta P_{K,i,\theta,e} + \Delta P_{temp} = 114.8 \text{ Pa}$$

APPENDIX C: Louvered and Wavy Fin Sample Calculations

C.1 Wavy fin calculations

Table C.1 Wavy Fin Inputs

<i>Tube</i>	
$Tube_d$	190.5 mm
$Tube_w$	25.4 mm
$Tube_t$	1.27 mm
<i>nodes</i>	100
<i>Material</i>	Carbon Steel
k_{tube}	$60 \text{ W m}^{-1} \text{ K}^{-1}$
<i>Fin</i>	
F_h	25.4 mm
F_s	2.54 mm
F_t	0.254 mm
F_d	165.1 mm
M	0.5 mm
λ	16.51 mm
ϵ_{fin}	0.005
<i>Material</i>	Aluminum
k_{fin}	$180 \text{ W m}^{-1} \text{ K}^{-1}$

<i>Operating Conditions</i>	
\dot{m}_{steam} (per ACC)	7 kg s^{-1}
\dot{m}_{air}	645 kg s^{-1}
$P_{air,in}$	101.3 kPa
$T_{air,in}$	30°C
$\phi_{ambient}$	0.25

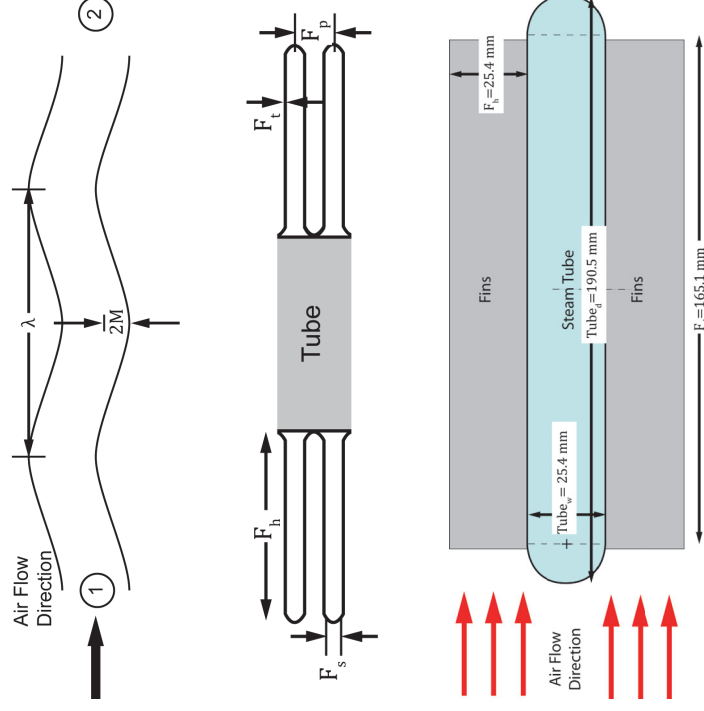
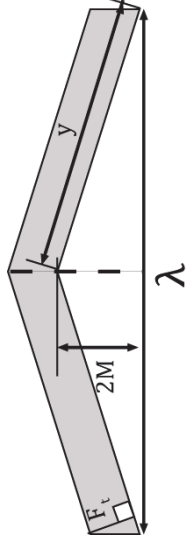


Figure C.1 Wavy fin and tube schematic

Wavy Fin Sample Calculations		Equations	Results
Input		Equations	
<i>Geometry dependent calculations</i>			
$M = 0.5$ mm $\lambda = 16.51$ mm $F_h = 25.4$ mm $F_d = 165.1$ mm $F_t = 0.254$ mm	 <p>Number of waves</p> $num_{waves} = F_d / \lambda$ <p>Picture of a single wave on a fin to calculate total wavy fin area (Figure not drawn to scale)</p> $y = \sqrt{(\lambda/2)^2 + (2M)^2}$ <p>Solving for the length, y</p> <p>Fin perimeter</p> $Per_{fin} = (y \cdot num_{waves}) \cdot 2 + F_t \cdot 2$ <p>Single fin surface area</p> $A_{fin} = 2 \cdot (2 \cdot y \cdot num_{waves}) + (2 \cdot F_h \cdot F_t)$ <p>Fin cross sectional area</p> $A_{fin,cs} = (2 \cdot y \cdot num_{waves}) \cdot F_t$	$num_{waves} = 10$ $y = 8.315$ mm $Per_{fin} = 0.3331$ mm $A_{fin} = 8,461$ mm ² $A_{fin,cs} = 42.24$ mm ²	
<i>Junqi et al. (2007) correlation</i>			
$Re = 1,009$ $F_h = 25.4$ mm $F_d = 165.1$ mm $F_p = 2.79$ mm $Tube_p = 76.2$ mm $M = 0.5$ mm $\lambda = 16.51$ mm	$j = 0.0836 Re^{-0.2309} \left(\frac{F_p}{F_h} \right)^{0.1284} \left(\frac{F_p}{2M} \right)^{-0.153} \left(\frac{F_d}{\lambda} \right)^{-0.326}$	$j = 0.0051$	
	$f = 1.16 Re^{-0.309} \left(\frac{F_p}{F_h} \right)^{0.3703} \left(\frac{F_p}{2M} \right)^{-0.25} \left(\frac{F_d}{\lambda} \right)^{-0.1152}$	$f = 0.0358$	

Wavy Fin Sample Calculations		Equations	Results
Input			
<i>Ismail et al. (2008) correlation</i>			
Re = 1,009			
$F_h = 25.4$ mm			
$F_s = 2.54$ mm			
$F_d = 165.1$ mm			
$F_p = 2.79$ mm			
M = 0.5 mm			
$\lambda = 16.51$ mm			
	Laminar Range ($100 \leq Re \leq 800$)	$j = 2.348Re^{-0.786} \left(\frac{F_h}{F_s}\right)^{0.312} \left(\frac{2M}{F_s}\right)^{-0.192} \left(\frac{\lambda}{2M}\right)^{-0.432}$ $f = 9.827Re^{-0.705} \left(\frac{F_h}{F_s}\right)^{0.322} \left(\frac{2M}{F_s}\right)^{-0.394} \left(\frac{\lambda}{2M}\right)^{-0.603}$	Air is in the turbulent range, so turbulent equations were used $j = 0.0087$ $f = 0.0169$
	Turbulent Range ($1000 \leq Re \leq 15000$)	$j = 0.242Re^{-0.375} \left(\frac{F_h}{F_s}\right)^{0.235} \left(\frac{2M}{F_s}\right)^{-0.288} \left(\frac{\lambda}{2M}\right)^{-0.553}$ $f = 10.628Re^{-0.359} \left(\frac{F_h}{F_s}\right)^{0.264} \left(\frac{2M}{F_s}\right)^{-0.848} \left(\frac{\lambda}{2M}\right)^{-0.1931}$	
<i>Khoshvaght Aliabadi et al. (2014) correlation</i>			
Re = 1,009			
$F_h = 25.4$ mm			
$F_d = 165.1$ mm			
$F_p = 2.79$ mm			
Tube _p = 76.2 mm			
M = 0.5 mm			
$\lambda = 16.51$ mm			
	Laminar Range ($Re < 1,900$)	$j = 0.295Re^{-0.191} \left(\frac{F_p}{D_h}\right)^{0.736} \left(\frac{F_h}{D_h}\right)^{0.138} \left(\frac{\lambda}{D_h}\right)^{-0.317} \left(\frac{F_t}{D_h}\right)^{0.049} \left(\frac{2M}{D_h}\right)^{0.247} \left(\frac{L_d}{D_h}\right)^{-0.498}$ $f = 38.8Re^{-0.384} \left(\frac{F_p}{D_h}\right)^{-1.48} \left(\frac{F_h}{D_h}\right)^{-0.370} \left(\frac{\lambda}{D_h}\right)^{-1.45} \left(\frac{F_t}{D_h}\right)^{0.102} \left(\frac{2M}{D_h}\right)^{1.09} \left(\frac{L_d}{D_h}\right)^{-0.155}$	Air is in the laminar range, so laminar equations used $j = 0.0046$ $f = 0.0386$
	Turbulent Range ($1,900 \leq Re$)	$j = 0.729Re^{-0.364} \left(\frac{F_p}{D_h}\right)^{0.797} \left(\frac{F_h}{D_h}\right)^{0.240} \left(\frac{\lambda}{D_h}\right)^{-0.498} \left(\frac{F_t}{D_h}\right)^{0.040} \left(\frac{2M}{D_h}\right)^{0.201} \left(\frac{L_d}{D_h}\right)^{-0.303}$ $f = 52.2Re^{-0.352} \left(\frac{F_p}{D_h}\right)^{-1.63} \left(\frac{F_h}{D_h}\right)^{-0.353} \left(\frac{\lambda}{D_h}\right)^{-1.75} \left(\frac{F_t}{D_h}\right)^{0.103} \left(\frac{2M}{D_h}\right)^{1.23} \left(\frac{L_d}{D_h}\right)^{-0.237}$	

Louvered Fin Sample Calculations		Equations		Results
Input		Equations		Results
$U = 3.522 \text{ m s}^{-1}$	$L_p = 6.35 \text{ mm}$	Louver pitch dependent Reynolds number	$Re_p = U \cdot L_p / \nu$	$Re_p = 1,389$
$\nu = 1.61 \times 10^{-4} \text{ m}^2 \text{ s}^{-1}$				
<i>Kim and Bullard (2002) correlation</i>				
$Re = 1,389$	$L_p = 6.35 \text{ mm}$	$j = Re^{-0.487} \left(\frac{L_\alpha}{90} \right)^{0.257} \left(\frac{F_p}{L_p} \right)^{-0.13} \left(\frac{F_h}{L_p} \right)^{-0.29} \left(\frac{F_d}{L_p} \right)^{-0.235} \left(\frac{L_l}{L_p} \right)^{0.68} \left(\frac{Tube_p}{L_p} \right)^{-0.279} \left(\frac{F_l}{L_p} \right)^{-0.05}$		$j = 0.0142$
$F_h = 25.4 \text{ mm}$	$L_l = 22.86 \text{ mm}$			
$F_d = 165.1 \text{ mm}$	$F_p = 2.79 \text{ mm}$	$f = Re^{-0.781} \left(\frac{L_\alpha}{90} \right)^{0.444} \left(\frac{F_p}{L_p} \right)^{-1.682} \left(\frac{F_h}{L_p} \right)^{-1.22} \left(\frac{F_d}{L_p} \right)^{-0.818} \left(\frac{L_l}{L_p} \right)^{1.97}$		$f = 0.4765$
$Tube_p = 76.2 \text{ mm}$	$L_\alpha = 30^\circ$			
<i>Park and Jacobi (2009) correlation</i>				
$C_1 = 0.872$	$C_8 = 2.62$	$j = C_1 j_{Re} j_{low} j_{louver} \alpha^{C_3} N_{LB}^{C_5} \left(\frac{F_l}{L_p} \right)^{C_4} \left(\frac{F_d}{F_p} \right)^{C_5} \left(\frac{L_l}{F_l} \right)^{C_6} \left(\frac{F_l}{T_p} \right)^{C_7} \left(1 - \frac{F_l}{L_p} \right)^{C_8} \left(\frac{L_p}{F_p} \right)^{C_9}$		$j = 0.0198$
$C_2 = 0.219$	$C_9 = 0.301$	$j_{Re} = Re^{\left[C_{10} + C_{11} \cosh \left(\frac{F_p}{L_p} - 1 \right) \right]}$		$j_{Re} = 0.0338$
$C_3 = -0.0881$	$C_{10} = -0.458$	$j_{low} = 1 - \sin \left(\frac{L_p}{F_p} \alpha \right) \left[\cosh \left(C_{12} Re - C_{13} \frac{F_d}{N_{LB} F_p} \right) \right]^{-1}$		$j_{low} = 1$
$C_4 = 0.149$	$C_{11} = -0.00874$	$j_{louver} = 1 - C_{14} \tan(\alpha) \left[\frac{F_d}{N_{LB} F_p} \right] \cos \left[2\pi \left(\frac{F_p}{L_p \tan(\alpha)} - 1.8 \right) \right]$		$j_{louver} = 1.11$
$C_5 = -0.259$	$C_{12} = 0.049$			
$C_6 = 0.540$	$C_{13} = 0.142$			
$C_7 = -0.902$	$C_{14} = -0.0065$			
$D_1 = 3.69$	$D_7 = -0.647$	$f = D_1 f_{Re} N_{LB}^{D_2} \left(\frac{F_p}{L_p} \right)^{D_3} \sin(\alpha + D_4) \left(1 - \frac{F_l}{T_p} \right)^{D_5} \left(\frac{L_l}{F_l} \right)^{D_6} \left(\frac{F_l}{L_p} \right)^{D_7} \left(\frac{F_l}{F_p} \right)^{D_8}$		$f = 0.2451$
$D_2 = -0.256$	$D_8 = 0.799$	$f_{Re} = \left(Re \frac{F_p}{L_p} \right)^{D_9} + D_{10} Re^{\left[D_{11} \left(\frac{F_p}{F_l} \right) \right]}$		$f_{Re} = 0.0074$
$D_3 = 0.904$	$D_9 = -0.845$			
$D_4 = 0.200$	$D_{10} = 0.00130$			
$D_5 = 0.733$	$D_{11} = 1.26$			
$D_6 = 0.648$				

APPENDIX D: Cycle Model Sample Calculations

D.1 Rankine cycle sample calculations

Condenser, tube, and fin	
ACC_w	12.2 m
ACC_h	10.67 m
β	60°
$Tube_d$	190.5 mm
$Tube_w$	25.4 mm
$Tube_t$	1.27 mm
$nodes$	100
Material	Carbon Steel
k_{tube}	60 W m ⁻¹ K ⁻¹
F_h	25.4 mm
F_s	2.54 mm
F_t	0.254 mm
F_d	165.1 mm
ϵ_{fin}	0.005
Material	Aluminum
k_{fin}	180 W m ⁻¹ K ⁻¹

\dot{m}_{steam} (per ACC)	7 kg s ⁻¹
\dot{m}_{air}	645 kg s ⁻¹
$P_{air,in}$	101.3 kPa
$T_{air,in}$	30°C
$\phi_{ambient}$	0.25

Number of ACCs (N_{ACC})	70
$\eta_{turbine}$	0.85
η_{fan}	0.55
η_{pump}	0.95
\dot{m}_{cycle}	490 kg s ⁻¹
$T_{boiler,sat}$	350°C
Maximum boiler T: T_3	550°C

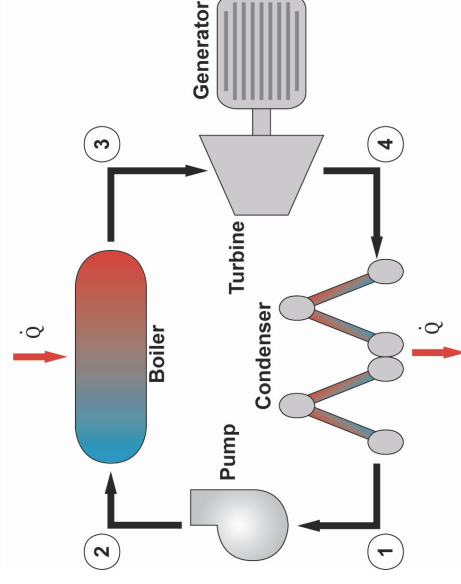


Figure D.1 Rankine cycle schematic

Rankine Cycle Sample Calculations		
Input	Equations	Results
Turbine $T_3 = 550^\circ\text{C}$ $P_3 = 16,529 \text{ kPa}$ (from boiler saturation T) $H_3 = 3,434 \text{ kJ kg}^{-1}$ $x_3 = \text{Superheated}$ $\eta_{\text{turbine}} = 0.85$ $\dot{m}_{\text{cycle}} = 490 \text{ kg s}^{-1}$	Used energy balance to calculate turbine work and outlet enthalpy $\dot{W}_{\text{turbine}} = \dot{m}_{\text{cycle}} (H_3 - H_{s,4}) \eta_{\text{turbine}} = \dot{m}_{\text{cycle}} (H_3 - H_4)$	$T_4 = 69.44^\circ\text{C}$ $P_4 = 30.46 \text{ kPa}$ $H_4 = 2,368 \text{ kJ kg}^{-1}$ $x_4 = 0.89$ $\dot{W}_{\text{turbine}} = 522.3 \text{ MW}$
Condenser – Calculated using segmented model as seen in Appendix A		
$T_4 = 69.44^\circ\text{C}$ $P_4 = 30.46 \text{ kPa}$ $H_4 = 2,368 \text{ kJ kg}^{-1}$ $x_4 = 0.89$ $\eta_{\text{fan}} = 0.55$ $\dot{m}_{\text{fan}} = 645 \text{ kg s}^{-1}$ $\Delta P_{\text{air}} = 143.9 \text{ Pa}$ $\rho_{\text{air}} = 1.162 \text{ kg m}^{-3}$ $N_{\text{ACC}} = 70$	Fan volumetric flow rate $\dot{V}_{\text{fan}} = \frac{\dot{m}_{\text{fan}}}{\rho_{\text{air}}}$ Fan power for one condenser $\dot{W}_{\text{fan, single}} = \frac{\dot{V}_{\text{fan}} \Delta P_{\text{air}}}{\eta_{\text{fan}}}$ Total cycle fan power $\dot{W}_{\text{fan, total}} = N_{\text{ACC}} \dot{W}_{\text{fan, single}}$	$T_1 = 69.78^\circ\text{C}$ $P_1 = 34.4 \text{ kPa}$ $H_1 = 292.1 \text{ kJ kg}^{-1}$ $x_1 = \text{Subcooled}$ $\dot{V}_{\text{fan}} = 555.3 \text{ m}^3 \text{ s}^{-1}$ $\dot{W}_{\text{fan, single}} = 145.2 \text{ kW}$ $\dot{W}_{\text{fan, total}} = 10.17 \text{ MW}$ $\dot{Q}_{\text{condenser, total}} = 1,006.6 \text{ MW}$
Pump $\eta_{\text{pump}} = 0.95$ $T_1 = 69.78^\circ\text{C}$ $P_1 = 34.4 \text{ kPa}$ $H_1 = 292.1 \text{ kJ kg}^{-1}$ $P_3 = 16,529 \text{ kPa}$	Used energy balance to calculate pump work and outlet enthalpy $\dot{W}_{\text{pump}} = \dot{m}_{\text{cycle}} \frac{H_{s,2} - H_1}{\eta_{\text{pump}}} = \dot{m}_{\text{cycle}} (H_2 - H_1)$	$T_2 = 70.79^\circ\text{C}$ $P_2 = 16,529 \text{ kPa}$ $H_2 = 309.8 \text{ kJ kg}^{-1}$ $x_2 = \text{Subcooled}$ $\dot{W}_{\text{pump}} = 8.67 \text{ MW}$

Rankine Cycle Sample Calculations

Input	Equations	Results																									
<i>Boiler</i>																											
$T_2 = 70.79^\circ\text{C}$	Heat input to boiler $\dot{Q}_{boiler} = \dot{m}_{cycle} (H_3 - H_2)$	$\dot{Q}_{boiler} = 1,531 \text{ MW}$ $\dot{Q}_{boiler, heating} = 667.1 \text{ MW}$ $\dot{Q}_{boiler, boiling} = 437.4 \text{ MW}$ $\dot{Q}_{boiler, superheating} = 426.4 \text{ MW}$																									
$P_2 = 16,529 \text{ kPa}$	Heating (from boiler inlet temperature to T_{sat}) $\dot{Q}_{boiler, heating} = \dot{m}_{cycle} (H_{b,2} - H_2)$																										
$H_2 = 309.8 \text{ kJ kg}^{-1}$	Boiling (from sat. liquid to vapor at sat. temperature and pressure) $\dot{Q}_{boiler, boiling} = \dot{m}_{cycle} (H_{b,3} - H_{b,2})$																										
$T_{sat} = 350^\circ\text{C}$	Superheating (from saturation temperature to exit temperature, T_3) $\dot{Q}_{boiler, superheating} = \dot{m}_{cycle} (H_3 - H_{b,3})$																										
$T_3 = 550^\circ\text{C}$																											
$H_3 = 3,434 \text{ kJ kg}^{-1}$																											
<u>Enthalpies in boiler</u>																											
$H_{b,2} (T_{sat}, x = 0) = 1,671 \text{ kJ kg}^{-1}$																											
$H_{b,3} (T_{sat}, x = 1) = 2,564 \text{ kJ kg}^{-1}$																											
<i>Overall</i>																											
$\dot{W}_{turbine} = 522.3 \text{ MW}$	Overall cycle work $\dot{W}_{net, Base} = \dot{W}_{turbine} - \dot{W}_{pump} - \dot{W}_{fan, total}$	$\dot{W}_{net, Base} = 503.5 \text{ MW}$ $\eta_{cycle} = 0.3289$																									
$\dot{W}_{pump} = 8.67 \text{ MW}$	Overall cycle efficiency $\eta_{cycle} = \frac{\dot{W}_{net, Base}}{\dot{Q}_{boiler}}$																										
$\dot{W}_{fan, total} = 10.17 \text{ MW}$																											
$\dot{Q}_{boiler} = 1,531 \text{ MW}$																											
<div style="display: flex; justify-content: space-between; align-items: center;"> <div style="width: 45%;"> <p>Table D.3 Summary of cycle properties</p> <table border="1" style="width: 100%; border-collapse: collapse; text-align: center;"> <thead> <tr> <th>State</th> <th>T [°C]</th> <th>P [kPa]</th> <th>H [kJ kg⁻¹]</th> <th>x</th> </tr> </thead> <tbody> <tr> <td>1</td> <td>69.78</td> <td>34.4</td> <td>292.1</td> <td>Subcooled</td> </tr> <tr> <td>2</td> <td>70.79</td> <td>16,529</td> <td>309.8</td> <td>Subcooled</td> </tr> <tr> <td>3</td> <td>550</td> <td>16,529</td> <td>3,434</td> <td>Superheated</td> </tr> <tr> <td>4</td> <td>69.44</td> <td>30.46</td> <td>2,368</td> <td>0.89</td> </tr> </tbody> </table> </div> <div style="width: 45%; text-align: center;"> </div> </div>			State	T [°C]	P [kPa]	H [kJ kg ⁻¹]	x	1	69.78	34.4	292.1	Subcooled	2	70.79	16,529	309.8	Subcooled	3	550	16,529	3,434	Superheated	4	69.44	30.46	2,368	0.89
State	T [°C]	P [kPa]	H [kJ kg ⁻¹]	x																							
1	69.78	34.4	292.1	Subcooled																							
2	70.79	16,529	309.8	Subcooled																							
3	550	16,529	3,434	Superheated																							
4	69.44	30.46	2,368	0.89																							

D.2 Combined cycle sample calculations

Table D.4 Baseline inputs	
<i>Condenser</i>	
ACC_w	12.2 m
ACC_h	10.67 m
β	60°
<i>Tube</i>	
$Tube_d$	190.5 mm
$Tube_w$	25.4 mm
$Tube_t$	1.27 mm
<i>nodes</i>	100
<i>Material</i>	Carbon Steel
k_{tube}	60 W m ⁻¹ K ⁻¹
<i>Fin</i>	
F_h	25.4 mm
F_s	2.54 mm
F_t	0.254 mm
F_d	165.1 mm
ϵ_{fin}	0.005
<i>Material</i>	Aluminum
k_{fin}	180 W m ⁻¹ K ⁻¹

Table D.5 Cycle inputs	
<i>Topping Gas Turbine Cycle</i>	
Assume intake air consists of 21% oxygen and 79% nitrogen	
$\eta_{compressor}$	0.85
<i>Pressure ratio</i>	20
<i>Fuel</i>	Methane
<i>% Excess Air</i>	200%
T_{fuel}	30°C
$\eta_{turbine}$	0.85
<i>Heat Recovery Steam Generator (HRSG)</i>	
<i>Approach T</i> $\Delta T_{approach}$	8°C
<i>Pinch point T</i> $\Delta T_{pinchpoint}$	15°C
ΔP_{HRSG}	0 kPa
<i>Bottoming Rankine Cycle</i>	
<i>Number of ACCs</i>	22
$\eta_{turbine}$	0.85
η_{fan}	0.55
η_{pump}	0.95
\dot{m}_{cycle}	154 kg s ⁻¹

Operating Conditions	
\dot{m}_{steam} (per ACC)	7 kg s ⁻¹
\dot{m}_{air}	645 kg s ⁻¹
$P_{air,in}$	101.3 kPa
$T_{air,in}$	30°C
$\phi_{ambient}$	0.25

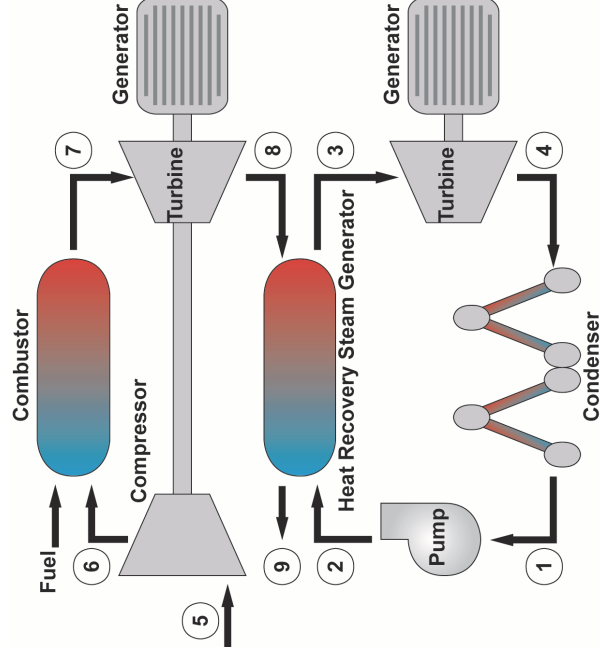


Figure D.2 Combined cycle schematic

Combined Cycle Sample Calculations	
<i>General, assuming EA = 2</i>	
$MM_{O_2} = 32 \text{ kg kmol}^{-1}$ $MM_{N_2} = 28.01 \text{ kg kmol}^{-1}$ $MM_{fuel} = 16.04 \text{ kg kmol}^{-1}$	$MM_{CO_2} = 44.01 \text{ kg kmol}^{-1}$ $MM_{H_2O} = 18.02 \text{ kg kmol}^{-1}$ $MM_{air} = 2(1 + EA)(MM_{O_2} + 3.76MM_{N_2}) = 824 \text{ kg kmol}^{-1}$ $MM_{comb,out} = MM_{CO_2} + 2MM_{H_2O} + 7.52MM_{N_2} + 2EA \cdot MM_{O_2} = 840 \text{ kg kmol}^{-1}$ Combustion equilibrium equation $CH_4 + 2(1 + EA)(O_2 + 3.76N_2) \rightarrow CO_2 + 2H_2O + 7.52N_2 + 2EA \cdot O_2$
Equations	
Input Calculation of air fuel ratio assuming 200% excess air - used to calculate mass flow rates of the fuel and air later	Results Stoichiometric combustion: $CH_4 + 2(O_2 + 3.76N_2) \rightarrow CO_2 + 2H_2O + 7.52N_2$ Air: $2(4.76 \text{ kmol})(28.98 \text{ kg kmole}^{-1}) = 275.79 \text{ kg}$ Methane: $(1 \text{ kmol})(16.04 \text{ kg kmole}^{-1}) = 16.04 \text{ kg}$ Calculate the actual air to fuel ratio $\%EA = \frac{AF_{actual} - AF_{stoich}}{AF_{stoich}} = 51.57$ Use the air fuel ratio to relate the mass flow rate of intake air to the mass flow rate of fuel $AF_{actual} = \frac{\dot{m}_{GT}}{\dot{m}_{fuel}} \quad \dot{m}_{GT} = 1,001 \text{ kg s}^{-1}$ $AF_{actual} = \frac{\dot{m}_{GT}}{\dot{m}_{fuel}} \quad \dot{m}_{fuel} = 19.41 \text{ kg s}^{-1}$
Compressor	
$T_5 = 30^\circ\text{C}$ $P_5 = 101.3 \text{ kPa}$ $\eta_{compressor} = 0.85$ Pressure ratio (PR) = 20 Mass flow rate found in subsequent calculation $\dot{m}_{GT} = 1,001 \text{ kg s}^{-1}$	Compressor outlet pressure $P_6 = PR \cdot P_5$ Enthalpy of air (can be used to determine temperature) $H_5 = \frac{2MM_{N_2}(1 + EA)3.76H_{N_2}(T_5) + 2MM_{O_2}(1 + EA)H_{O_2}(T_5)}{MM_{air}}$ Entropy of air $S_5 = \frac{2MM_{N_2}(1 + EA)3.76S_{N_2}(T_5, 0.79P_5) + 2MM_{O_2}(1 + EA)S_{O_2}(T_5, 0.21P_5)}{MM_{air}}$ Used energy balance to calculate outlet enthalpy and compressor work $\dot{W}_{comp} = \frac{\dot{m}_{GT}(H_{s,6} - H_5)}{\eta_{compressor}} = \dot{m}_{GT}(H_{6,air} - H_5)$ $T_6 = 490.6^\circ\text{C}$ $P_6 = 2,027 \text{ kPa}$ $H_{6,air} = 487.9 \text{ kJ kg}^{-1}$ $\dot{W}_{comp} = 483.4 \text{ MW}$

Combined Cycle Sample Calculations	
<i>General</i>	
$MM_{O_2} = 32 \text{ kg kmol}^{-1}$	$MM_{CO_2} = 44.01 \text{ kg kmol}^{-1}$
$MM_{N_2} = 28.01 \text{ kg kmol}^{-1}$	$MM_{H_2O} = 18.02 \text{ kg kmol}^{-1}$
$MM_{fuel} = 16.04 \text{ kg kmol}^{-1}$	
Equations	
<i>Combustor – assuming no pressure drop and no heat loss in combustion</i>	
$T_{fuel} = 30^\circ\text{C}$	Assume combustor outlet temperature is adiabatic flame temperature
$P_{fuel} = 101.3 \text{ kPa}$	$H_{react} = H(CH_4, T_{fuel})MM_{CH_4} + 2(1+EA)H(O_2, T_6)MM_{O_2}$
$T_6 = 490.6^\circ\text{C}$	$+3.76(2+2EA)H(O_2, T_6)MM_{N_2}$
$P_6 = 2,027 \text{ kPa}$	$H_{prod} = H(CO_2, T_7)MM_{CO_2} + 2H(H_2O, T_7)MM_{H_2O}$
$H_6 = 487.9 \text{ kJ kg}^{-1}$	$+2(1+EA)3.76H(N_2, T_7)MM_{N_2} + 2EA \cdot H(O_2, T_7)MM_{O_2}$
	$H_{react} = H_{prod} \text{ [kJ kmol}^{-1}\text{]}$
	$H_7 = H_{prod} / MM_{comb,out}$
	$H_{6,LHV} = H(CH_4, T_{fuel})MM_{CH_4} + 2(1+EA)H(O_2, T_{fuel})MM_{O_2}$
	$+3.76(2+2 \cdot EA)H(O_2, T_{fuel})MM_{N_2}$
	$H_{7,LHV} = H(CO_2, T_{fuel})MM_{CO_2} + 2H(H_2O, T_{fuel})MM_{H_2O}$
	$+2(1+EA)3.76H(N_2, T_{fuel})MM_{N_2} + 2EA \cdot H(O_2, T_{fuel})MM_{O_2}$
Used lower heating value of reactants and products to calculate heat input	Lower heating value $LHV = \frac{H_{6,LHV} - H_{7,LHV}}{MM_{fuel}}$
	Combustor heat input $\dot{Q}_{combustor} = \dot{m}_{fuel} LHV$
	Results
	$T_7 = 1,244^\circ\text{C}$
	$P_7 = 2,027 \text{ kPa}$
	$H_7 = 390 \text{ kJ kg}^{-1}$
	$H_{react} = H_{prod}$
	$= 327,619 \text{ kJ kmol}^{-1}$
	$H_{6,LHV} = -70,258 \text{ kJ kmol}^{-1}$
	$H_{7,LHV} = -872,722 \text{ kJ kmol}^{-1}$
	$LHV = 50,020 \text{ kJ kg}^{-1}$
	$\dot{Q}_{combustor} = 971.1 \text{ MW}$

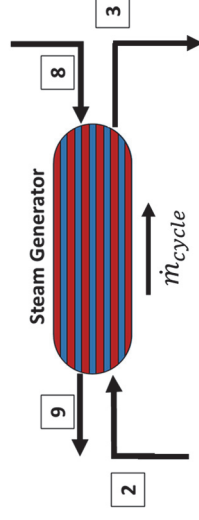
Combined Cycle Sample Calculations		Equations	Results
Input			
Mole fractions of each product were calculated assuming one kmole of fuel (CH ₄) was used		Kmoles of products $N_{CO_2} = 1$ $N_{H_2O} = 2$ $N_{N_2} = 2(1 + EA)3.76 = 22.56$ $N_{O_2} = 2EA = 4$ $N_{total} = 29.56$	Mole fraction (N/N_{total}) $y_{CO_2} = 0.03383$ $y_{H_2O} = 0.06766$ $y_{N_2} = 0.7632$ $y_{O_2} = 0.1353$ $y_{total} = 1$
Turbine			
$T_7 = 1,244^\circ\text{C}$ $P_7 = 2,027 \text{ kPa}$ $H_7 = 390 \text{ kJ kg}^{-1}$ $\eta_{turbine} = 0.85$ Found in subsequent analysis $\dot{m}_{GT} = 1,001 \text{ kg s}^{-1}$ $\dot{m}_{fuel} = 19.41 \text{ kg s}^{-1}$	Entropy of products after expansion $S_p = \frac{S(CO_2, T_p, y_{CO_2} P_p) MM_{CO_2} + 2S(H_2O, T_p, y_{H_2O} P_p) MM_{H_2O} + 7.52(1 + EA)S(N_2, T_p, y_{N_2} P_p) MM_{N_2} + 2EA \cdot S(O_2, T_p, y_{O_2} P_p) MM_{O_2}}{MM_{products}}$ Enthalpy of products after expansion $H_8 = \frac{H(CO_2, T_8) \cdot MM_{CO_2} + 2 \cdot H(H_2O, T_8) \cdot MM_{H_2O} + 7.52 \cdot (1 + EA) \cdot H(N_2, T_8) \cdot MM_{N_2} + 2 \cdot EA \cdot H(O_2, T_8) \cdot MM_{O_2}}{MM_{products}}$ Used energy balance to calculate turbine work and outlet enthalpy $\dot{W}_{turb, top} = (\dot{m}_{GT} + \dot{m}_{fuel}) \cdot (H_7 - H_{s,8}) \cdot \eta_{turbine} = (\dot{m}_{GT} + \dot{m}_{fuel}) \cdot (H_7 - H_8)$	$T_8 = 582.1^\circ\text{C}$ $P_8 = 101.3 \text{ kPa}$ $H_8 = -429.9 \text{ kJ kg}^{-1}$ $\dot{W}_{turb, top} = 836.7 \text{ MW}$	

Combined Cycle Sample Calculations

Heat Recovery Steam Generator (HRSG) Calculations

Unknown Values

$$\begin{array}{ll}
 T_2 = 70.79^\circ\text{C} & P_2 = 16,529 \text{ kPa} \\
 T_3 = 550^\circ\text{C} & P_3 = 16,529 \text{ kPa} \\
 T_8 = 582.1^\circ\text{C} & P_8 = 101.3 \text{ kPa} \\
 \dot{m}_{\text{cycle}} = 154 \text{ kg s}^{-1} & P_9 = 101.3 \text{ kPa}
 \end{array}$$



Rankine cycle: Assumed turbine inlet temperature (T_3), pressure (P_3), flow rate (\dot{m}_{cycle}), calculated the pump outlet temperature (T_2)

Gas turbine cycle: Assumed ambient pressure at exhaust (P_9) and no pressure drop across HRSG, calculated T_8 using gas turbine analysis

Input

$$\begin{array}{l}
 \Delta T_{\text{approach}} = 8^\circ\text{C} \\
 \Delta T_{\text{pinchpoint}} = 15^\circ\text{C}
 \end{array}$$

Steam saturation temperature

$$T_{\text{sat}} = 350^\circ\text{C}$$

$$MM_{\text{O}_2} = 32 \text{ kg kmol}^{-1}$$

$$MM_{\text{N}_2} = 28.01 \text{ kg kmol}^{-1}$$

$$MM_{\text{fuel}} = 16.04 \text{ kg kmol}^{-1}$$

$$MM_{\text{CO}_2} = 44.01 \text{ kg kmol}^{-1}$$

$$MM_{\text{H}_2\text{O}} = 18.02 \text{ kg kmol}^{-1}$$

$$MM_{\text{products}} = 840 \text{ kg kmol}^{-1}$$

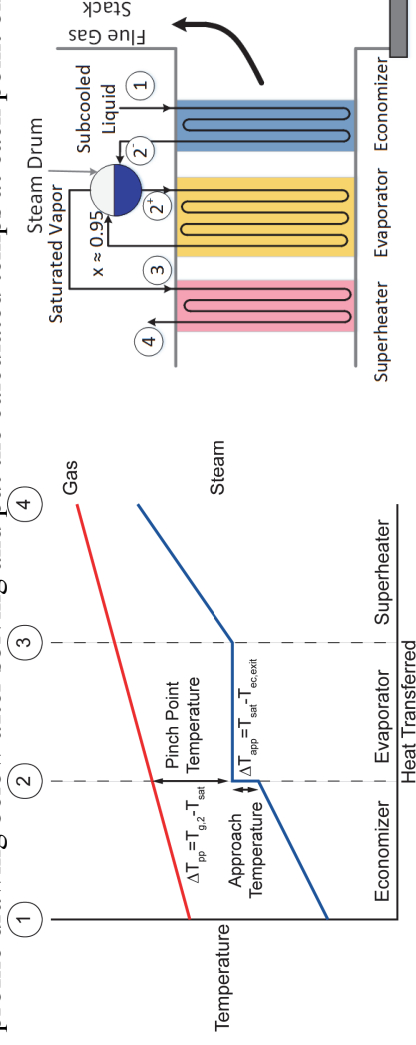
Equations

Equation used to calculate specific heat of gas in the HRSG, where x,y refers to the average temperature between points x and y

$$Cp(CO_2, T_{x,y}) \cdot MM_{CO_2} + 2 \cdot Cp(H_2O, T_{x,y}) \cdot MM_{H_2O}$$

$$Cp_{x,y} = \frac{+7.52 \cdot (1 + EA) \cdot Cp(N_2, T_{x,y}) \cdot MM_{N_2} + 2 \cdot EA \cdot Cp(O_2, T_{x,y}) \cdot MM_{O_2}}{MM_{\text{products}}} \text{ reproduce the temp}$$

profile drawing below after solving and put the calculated temps at each point on it

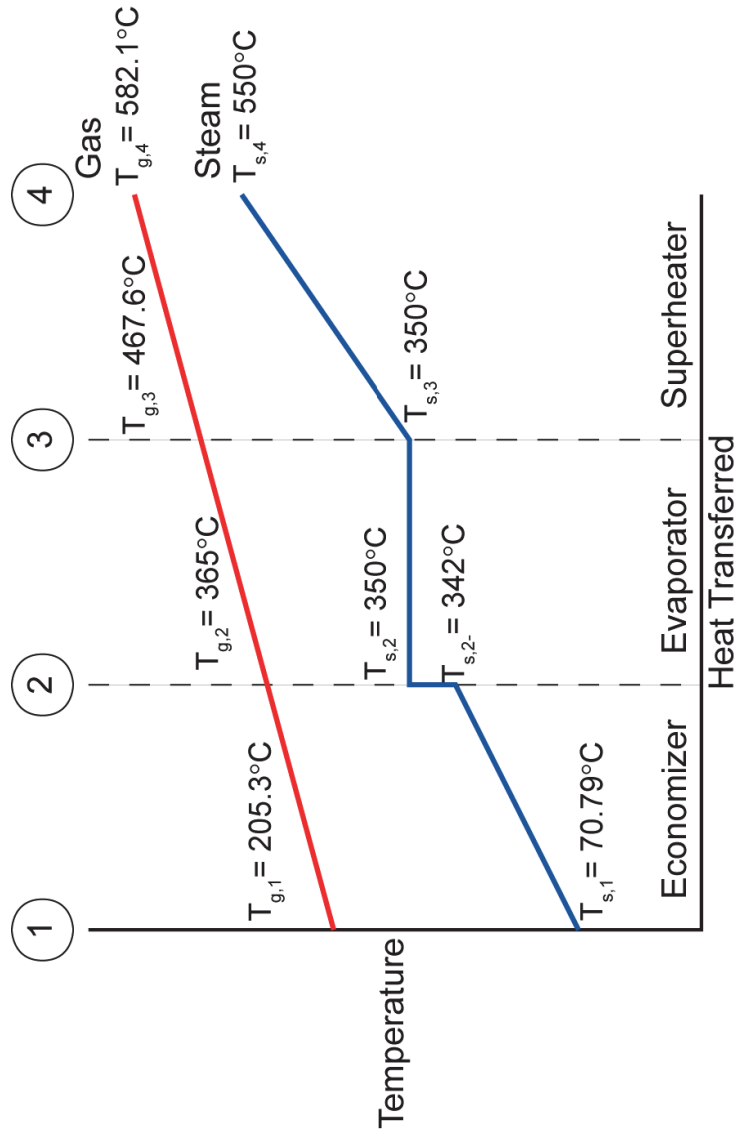


Combined Cycle Sample Calculations												
Heat Recovery Steam Generator (HRSG) Calculations continued												
Input	Equations	Results										
<p>Approach temp. $\Delta T_{\text{approach}} = 8^{\circ}\text{C}$</p> <p>Pinch point temp. $\Delta T_{\text{pinchpoint}} = 15^{\circ}\text{C}$</p> <p>Steam saturation temperature $T_{\text{sat}} = 350^{\circ}\text{C}$</p> <table border="1"> <thead> <tr> <th>Cycle State Point</th> <th>HRSG State Point</th> </tr> </thead> <tbody> <tr> <td>2</td> <td>s,1</td> </tr> <tr> <td>3</td> <td>s,4</td> </tr> <tr> <td>8</td> <td>g,4</td> </tr> <tr> <td>9</td> <td>g,1</td> </tr> </tbody> </table> <p> $H_{s,1} = 309.8 \text{ kJ kg}^{-1}$ $H_{s,4} = 3,434 \text{ kJ kg}^{-1}$ $T_{g,4} = 582.1^{\circ}\text{C}$ $\dot{m}_{\text{cycle}} = 490 \text{ kg s}^{-1}$ </p>	Cycle State Point	HRSG State Point	2	s,1	3	s,4	8	g,4	9	g,1	<p><i>Subscript "g" refers to gas, "s" refers to steam. All number subscripts in the following equations refers to the HRSG state point</i></p> <p>Solve for steam economizer exit temperature $\Delta T_{\text{app}} = T_{\text{sat}} - T_{s,2-}$</p> <p>Solve for gas temperature at point 2 $\Delta T_{\text{pp}} = T_{g,2} - T_{\text{sat}}$</p> <p><u>Economizer (Point 1: Steam inlet, gas outlet; Point 2: gas inlet, steam outlet)</u> Heat transferred from gas to steam in the economizer</p> $\dot{Q}_{\text{ec}} = \dot{m}_{\text{GT}} Cp_{1,2} (T_{g,2} - T_{g,1}) \left(1 + \frac{1}{AF_{\text{actual}}} \right) = \dot{m}_{\text{cycle}} (H_{s,2-} - H_{s,1})$ <p><u>Evaporator (Point 2: Steam inlet, gas outlet; Point 3: gas inlet, steam outlet)</u> Heat transferred from gas to steam in the evaporator</p> $\dot{Q}_{\text{ev}} = \dot{m}_{\text{GT}} Cp_{2,3} (T_{g,3} - T_{g,2}) \left(1 + \frac{1}{AF_{\text{actual}}} \right) = \dot{m}_{\text{cycle}} (H_{s,2+} - H_{s,2-})$ <p><u>Superheater (Point 3: Steam inlet, gas outlet; Point 4: gas inlet, steam outlet)</u></p> $\dot{Q}_{\text{sh}} = \dot{m}_{\text{GT}} Cp_{3,4} (T_{g,4} - T_{g,3}) \left(1 + \frac{1}{AF_{\text{actual}}} \right) = \dot{m}_{\text{cycle}} (H_{s,4} - H_{s,3})$	<p><u>Economizer</u> $T_{s,2-} = 342^{\circ}\text{C}$ $H_{s,2-} = 1,600 \text{ kJ kg}^{-1}$ $x_{s,2-} = \text{subcooled}$ $T_{g,1} = 205.3^{\circ}\text{C}$ $T_{g,2} = 365^{\circ}\text{C}$ $Cp_{1,2} = 1.219 \text{ kJ kg}^{-1}\text{K}^{-1}$ $\dot{Q}_{\text{ec}} = 198.7 \text{ MW}$</p> <p><u>Evaporator</u> $T_{s,2} = 350^{\circ}\text{C}$ $H_{s,2} = 1,671 \text{ kJ kg}^{-1}$ $x_{s,2} = 0$ $H_{s,2+} = 2,527 \text{ kJ kg}^{-1}$ $x_{s,2+} = 0.9582$ $T_{g,3} = 467.6^{\circ}\text{C}$ $Cp_{2,3} = 1.258 \text{ kJ kg}^{-1}\text{K}^{-1}$ $\dot{Q}_{\text{ev}} = 131.7 \text{ MW}$</p> <p><u>Superheater</u> $T_{s,3} = 350^{\circ}\text{C}$ $H_{s,3} = 2,456 \text{ kJ kg}^{-1}$ $x_{s,3} = 0.879$ $Cp_{3,4} = 1.29 \text{ kJ kg}^{-1}\text{K}^{-1}$ $\dot{Q}_{\text{sh}} = 150.7 \text{ MW}$</p>
Cycle State Point	HRSG State Point											
2	s,1											
3	s,4											
8	g,4											
9	g,1											
<p><u>Adiabatic mixing in the steam drum</u> (to increase economizer outlet temperature so steam can enter evaporator saturated)</p> $\dot{Q}_{\text{drum}} = \dot{m}_{\text{cycle}} (H_{s,2+} - H_{s,3})$ $\dot{Q}_{\text{drum}} = \dot{m}_{\text{cycle}} (H_{s,2} - H_{s,2-})$	<p><u>Steam drum</u> $\dot{Q}_{\text{drum}} = 10.9 \text{ MW}$</p>											

Combined Cycle Sample Calculations

Heat Recovery Steam Generator (HRSG) Calculations continued

Temperature profile of the HRSG with calculated values (note: figure not drawn to scale)



Combined Cycle Sample Calculations (Rankine Cycle)			Results
Input	Equations		
Turbine $T_3 = 550^\circ\text{C}$ $P_3 = 16,529 \text{ kPa}$ (from boiler saturation T) $H_3 = 3,434 \text{ kJ kg}^{-1}$ $x_3 = \textit{Superheated}$ $\eta_{\text{turbine}} = 0.85$ $\dot{m}_{\text{cycle}} = 154 \text{ kg s}^{-1}$	Used energy balance to calculate turbine work and outlet enthalpy $\dot{W}_{\text{turbine}} = \dot{m}_{\text{cycle}} (H_3 - H_{s,4}) \eta_{\text{turbine}} = \dot{m}_{\text{cycle}} (H_3 - H_4)$	$T_4 = 69.44^\circ\text{C}$ $P_4 = 30.46 \text{ kPa}$ $H_4 = 2,368 \text{ kJ kg}^{-1}$ $x_4 = 0.89$ $\dot{W}_{\text{turbine}} = 164.2 \text{ MW}$	
Condenser – Calculated using segmented model as seen in Appendix A			
$T_4 = 69.44^\circ\text{C}$ $P_4 = 30.46 \text{ kPa}$ $H_4 = 2,368 \text{ kJ kg}^{-1}$ $x_4 = 0.89$ $\eta_{\text{fan}} = 0.55$ $\dot{m}_{\text{fan}} = 645 \text{ kg s}^{-1}$ $\Delta P_{\text{air}} = 143.9 \text{ Pa}$ $\rho_{\text{air}} = 1.162 \text{ kg m}^{-3}$ $N_{\text{ACC}} = 22$	Fan volumetric flow rate $\dot{V}_{\text{fan}} = \frac{\dot{m}_{\text{fan}}}{\rho_{\text{air}}}$ Fan power for one condenser $\dot{W}_{\text{fan, single}} = \frac{\dot{V}_{\text{fan}} \Delta P_{\text{air}}}{\eta_{\text{fan}}}$ Total cycle fan power $\dot{W}_{\text{fan, total}} = N_{\text{ACC}} \dot{W}_{\text{fan, single}}$	$T_1 = 69.78^\circ\text{C}$ $P_1 = 34.4 \text{ kPa}$ $H_1 = 292.1 \text{ kJ kg}^{-1}$ $x_1 = \textit{Subcooled}$ $\dot{V}_{\text{fan}} = 555.3 \text{ m}^3 \text{ s}^{-1}$ $\dot{W}_{\text{fan, single}} = 145.2 \text{ kW}$ $\dot{W}_{\text{fan, total}} = 3.195 \text{ MW}$ $\dot{Q}_{\text{condenser, total}} = 316.36 \text{ MW}$	
Pump $\eta_{\text{pump}} = 0.95$ $T_1 = 69.78^\circ\text{C}$ $P_1 = 34.4 \text{ kPa}$ $H_1 = 292.1 \text{ kJ kg}^{-1}$ $P_3 = 16,529 \text{ kPa}$	Used energy balance to calculate pump work and outlet enthalpy $\dot{W}_{\text{pump}} = \dot{m}_{\text{cycle}} \frac{H_{s,2} - H_1}{\eta_{\text{pump}}} = \dot{m}_{\text{cycle}} (H_2 - H_1)$	$T_2 = 70.79^\circ\text{C}$ $P_2 = 16,529 \text{ kPa}$ $H_2 = 309.8 \text{ kJ kg}^{-1}$ $x_2 = \textit{Subcooled}$ $\dot{W}_{\text{pump}} = 2.73 \text{ MW}$	

Combined Cycle Sample Calculations

Input	Equations	Results
<p><u>Rankine (Bottoming)</u></p> $\dot{W}_{turbine} = 164.2 \text{ MW}$ $\dot{W}_{pump} = 2.73 \text{ MW}$ $\dot{W}_{fan,total} = 3.20 \text{ MW}$ $\dot{Q}_{HRSG} = 481.1 \text{ MW}$	$\dot{Q}_{HRSG} = \dot{Q}_{ec} + \dot{Q}_{ev} + \dot{Q}_{sh}$ <p><u>Rankine</u></p> $\dot{W}_{net, Rankine} = \dot{W}_{turbine} - \dot{W}_{pump} - \dot{W}_{fan,total}$ <p><u>Gas Turbine</u></p> $\dot{W}_{net, GT} = \dot{W}_{turb, top} - \dot{W}_{compressor}$	$\dot{Q}_{HRSG} = 481.1 \text{ MW}$ $\dot{W}_{net, Rankine} = 158.2 \text{ MW}$ $\eta_{R, cycle} = 0.3289$ $\dot{W}_{net, GT} = 353.3 \text{ MW}$ $\eta_{GT, cycle} = 0.3638$
<p><u>Overall</u></p> $\dot{W}_{net} = \dot{W}_{net, Rankine} + \dot{W}_{net, GT}$ $\dot{Q}_{combustor} = 971.1 \text{ MW}$	$\eta_{cycle} = \frac{\dot{W}_{net}}{\dot{Q}_{combustor}}$	$\dot{W}_{net} = 511.6 \text{ MW}$ $\eta_{cycle} = 0.5268$

Table D.6 Summary of cycle properties

State	T [°C]	P [kPa]	H [kJ kg ⁻¹]	x [-]	
Rankine (Bottoming)	1	69.78	34.4	292.1	Subcooled
	2	70.79	16,529	309.8	Subcooled
	3	550	16,529	3,434	Superheated
	4	69.44	30.46	2,368	0.89
Gas Turbine (Topping)	5	30	101.3	5,045	-
	6	490.6	2,027	487.9	-
	7	1,244	2,027	390	-
	8	582.1	101.3	-429.9	-
	9	205.3	101.	-853.3	-

REFERENCES

- Accessories, C. T. (-). *Air-Cooled Condensers*.
- Achaichia, A. and T. Cowell (1988), "Heat Transfer and Pressure Drop Characteristics of Flat Tube and Louvered Plate Fin Surfaces," *Experimental Thermal and Fluid Science* Vol. 1(2) pp. 147-157
- Acharya, S., S. Bushart and J. Shi (2013). NSF/EPRI Joint Solicitation Informational Webcast.
- Akers, W., H. Deans and O. Crosser (1958), "Condensing Heat Transfer within Horizontal Tubes," *Chem. Eng. Progr.* Vol. 54
- Akhavan-Behabadi, M., R. Kumar and S. Mohseni (2007), "Condensation Heat Transfer of R-134a inside a Microfin Tube with Different Tube Inclinations," *International Journal of Heat and Mass Transfer* Vol. 50(23) pp. 4864-4871
- Aljundi, I. H. (2009), "Energy and Exergy Analysis of a Steam Power Plant in Jordan," *Applied Thermal Engineering* Vol. 29(2) pp. 324-328
- Andrews, D. E., C. Knowles, B. Eaton, I. Silberberg and K. Brown (1967), "The Prediction of Pressure Loss During Two-Phase Horizontal Flow in Two-Inch Pipe," *Journal of Engineering for Industry* Vol. 89(1) pp. 44-51
- Aoki, H., T. Shinagawa and K. Suga (1989), "An Experimental Study of the Local Heat Transfer Characteristics in Automotive Louvered Fins," *Experimental Thermal and Fluid Science* Vol. 2(3) pp. 293-300
- Bahaidarah, H. M., N. Anand and H. Chen (2005), "Numerical Study of Heat and Momentum Transfer in Channels with Wavy Walls," *Numerical Heat Transfer, Part A* Vol. 47(5) pp. 417-439
- Bandel, J. (1973). *Druckverlust Und Wärmeübergang Bei Der Verdampfung Siedender Kältemittel Im Durchströmten Waagerechten Rohr*, na.
- Beecher, D. and T. Fagan (1987). Effects of Fin Pattern on the Air Side Heat Transfer Coefficient in Plate Finned Tube Heat Exchangers. Westinghouse Research and Development Center, Pittsburgh, PA (USA).
- Beér, J. M. (2007), "High Efficiency Electric Power Generation: The Environmental Role," *Progress in Energy and Combustion Science* Vol. 33(2) pp. 107-134
- Beggs, H. D. (1972). *An Experimental Study of Two-Phase Flow in Inclined Pipes*, University of Tulsa.
- Bergles, A. E. (2002), "ExHFT for Fourth Generation Heat Transfer Technology," *Experimental Thermal and Fluid Science* Vol. 26(2) pp. 335-344
- Boyce, M. P. (2002). *Handbook for Cogeneration and Combined Cycle Power Plants*, ASME Press.
- Bredell, J. R., D. Kröger and G. Thiart (2006), "Numerical Investigation of Fan Performance in a Forced Draft Air-Cooled Steam Condenser," *Applied Thermal Engineering* Vol. 26(8) pp. 846-852
- Brown, R., G. Sullivan and G. Govier (1960), "The Upward Vertical Flow of Air - Water Mixtures: III. Effect of Gas Phase Density on Flow Pattern, Holdup and Pressure Drop," *The Canadian Journal of Chemical Engineering* Vol. 38(2) pp. 62-66
- Cavallini, A., G. Censi, D. Del Col, L. Doretti, G. Longo and L. Rossetto (2001), "Experimental Investigation on Condensation Heat Transfer and Pressure Drop of

- New HFC Refrigerants (R134a, R125, R32, R410a, R236ea) in a Horizontal Smooth Tube," *International Journal of Refrigeration* Vol. 24(1) pp. 73-87
- Cavallini, A., G. Censi, D. Del Col, L. Doretti, G. A. Longo and L. Rossetto (2002), "Condensation of Halogenated Refrigerants inside Smooth Tubes," *HVAC&R Research* Vol. 8(4) pp. 429-451
- Cavallini, A., L. Doretti, N. Klammsteiner, G. Longo and L. Rossetto (1995), "Condensation of New Refrigerants inside Smooth and Enhanced Tubes," *Proceedings of the International Congress of Refrigeration*, pp. 105-114.
- Chang, Y.-J., K.-C. Hsu, Y.-T. Lin and C.-C. Wang (2000), "A Generalized Friction Correlation for Louver Fin Geometry," *International Journal of Heat and Mass Transfer* Vol. 43(12) pp. 2237-2243
- Chang, Y.-J. and C.-C. Wang (1997), "A Generalized Heat Transfer Correlation for Louver Fin Geometry," *International Journal of heat and mass transfer* Vol. 40(3) pp. 533-544
- Chen, Y., K.-S. Yang and C.-C. Wang (2002), "An Empirical Correlation for Two-Phase Frictional Performance in Small Diameter Tubes," *International Journal of Heat and Mass Transfer* Vol. 45(17) pp. 3667-3671
- Chisholm, D. (1967), "A Theoretical Basis for the Lockhart-Martinelli Correlation for Two-Phase Flow," *International Journal of Heat and Mass Transfer* Vol. 10(12) pp. 1767-1778
- Cicchitti, A., C. Lombardi, M. Silvestri, G. Soldaini and R. Zavattarelli (1959). Two-Phase Cooling Experiments: Pressure Drop, Heat Transfer and Burnout Measurements. Centro Informazioni Studi Esperienze, Milan.
- Comini, G., C. Nonino and S. Savino (2003), "Effect of Space Ratio and Corrugation Angle on Convection Enhancement in Wavy Channels," *International Journal of Numerical Methods for Heat & Fluid Flow* Vol. 13(4) pp. 500-519
- Crittenden, T. and A. Glezer (2015). *Reed Test Section*. Private Communications.
- Davenport, C. (1983), "Correlation for Heat Transfer and Flow Friction Characteristics of Louvered Fin," *AIChE Symp. Ser.*, pp. 19-27.
- Davies, E. G., P. Kyle and J. A. Edmonds (2013), "An Integrated Assessment of Global and Regional Water Demands for Electricity Generation to 2095," *Advances in Water Resources* Vol. 52 pp. 296-313
- Dewan, A., P. Mahanta, K. S. Raju and P. S. Kumar (2004), "Review of Passive Heat Transfer Augmentation Techniques," *Proceedings of the Institution of Mechanical Engineers, Part A: Journal of Power and Energy* Vol. 218(7) pp. 509-527
- Dillen, E. R. and R. L. Webb (1994). Rationally Based Heat Transfer and Friction Correlations for the Louver Fin Geometry. SAE Technical Paper, 0148-7191.
- Dobson, M. and J. Chato (1998), "Condensation in Smooth Horizontal Tubes," *Journal of Heat Transfer* Vol. 120(1) pp. 193-213
- DOE and NETL (2010). Estimating Freshwater Needs to Meet Future Thermoelectric Generation Requirements. DOE/NETL.
- Dong, J., J. Chen, Z. Chen, W. Zhang and Y. Zhou (2007), "Heat Transfer and Pressure Drop Correlations for the Multi-Louvered Fin Compact Heat Exchangers," *Energy Conversion and Management* Vol. 48(5) pp. 1506-1515

- Dong, J., J. Chen, W. Zhang and J. Hu (2010), "Experimental and Numerical Investigation of Thermal-Hydraulic Performance in Wavy Fin-and-Flat Tube Heat Exchangers," *Applied Thermal Engineering* Vol. 30(11) pp. 1377-1386
- Dukler, A. (1962), "Two-Phase Flow, Data Analysis and Correlation, Studies at University of Houston,"
- Dukler, A., M. Wicks and R. Cleveland (1964), "Frictional Pressure Drop in Two - Phase Flow: B. An Approach through Similarity Analysis," *AIChE Journal* Vol. 10(1) pp. 44-51
- Duvenhage, K. and D. Kröger (1996), "The Influence of Wind on the Performance of Forced Draught Air-Cooled Heat Exchangers," *Journal of Wind Engineering and Industrial Aerodynamics* Vol. 62(2) pp. 259-277
- Eaton, B. A. (1966). *The Prediction of Flow Patterns, Liquid Holdup and Pressure Losses Occurring During Continuous Two-Phase in Horizontal Pipelines*, University of Texas.
- El-Wakil, M. (1984). *Powerplant Technology*, McGraw-Hill International. ISBN 0-07-066274-6.
- El Hajal, J., J. R. Thome and A. Cavallini (2003), "Condensation in Horizontal Tubes, Part 1: Two-Phase Flow Pattern Map," *International Journal of Heat and Mass Transfer* Vol. 46(18) pp. 3349-3363
- EPRI (2004). Comparison of Alternate Cooling Technologies for U. S. Power Plants: Economic, Environmental, and Other Tradeoffs. EPRI. Palo Alto, CA, 1005358.
- EPRI (2005). Air-Cooled Condenser Design, Specification, and Operation Guidelines. EPRI. Palo Alto, CA, 1007688.
- EPRI (2013). Power Plant Cooling System Overview for Researchers and Technology Developers. EPRI, 3002001915.
- Fiebig, M., P. Kallweit, N. Mitra and S. Tiggelbeck (1991), "Heat Transfer Enhancement and Drag by Longitudinal Vortex Generators in Channel Flow," *Experimental Thermal and Fluid Science* Vol. 4(1) pp. 103-114
- Friedel, L. (1979), "Improved Friction Pressure Drop Correlations for Horizontal and Vertical Two-Phase Pipe Flow," *European two-phase flow group meeting, Paper E*, p. 1979.
- GEA (2012). *Air Cooled Condensers (ACC)*. G. H. E. GmbH.
- Gerty, D. R. (2008), "Fluidic Driven Cooling of Electronic Hardware Part I: Channel Integrated Vibrating Reed Part II: Active Heat Sink,"
- Ghiaasiaan, S. M. (2007). *Two-Phase Flow, Boiling, and Condensation: In Conventional and Miniature Systems*, Cambridge University Press.
- Ghosh, I. (2004). *Experimental and Computational Studies on Plate Fin Heat Exchangers*, Ph. D. thesis, Indian Institute of Technology, Kharagpur.
- Govier, G. and M. Omer (1962), "The Horizontal Pipeline Flow of Air - Water Mixtures," *The Canadian Journal of Chemical Engineering* Vol. 40(3) pp. 93-104
- Gu, Z., X. Chen, W. Lubitz, Y. Li and W. Luo (2007), "Wind Tunnel Simulation of Exhaust Recirculation in an Air-Cooling System at a Large Power Plant," *International Journal of Thermal Sciences* Vol. 46(3) pp. 308-317

- Guo, Z., D. Li and B. Wang (1998), "A Novel Concept for Convective Heat Transfer Enhancement," *International Journal of Heat and Mass Transfer* Vol. 41(14) pp. 2221-2225
- Harrison, R. F. (1975). *Methods for the Analysis of Geothermal Two-Phase Flow*.
- Herrault, F., P. Hidalgo, C.-H. Ji, A. Glezer and M. Allen (2012), "Cooling Performance of Micromachined Self-Oscillating Reed Actuators in Heat Transfer Channels with Integrated Diagnostics," *Micro Electro Mechanical Systems (MEMS), 2012 IEEE 25th International Conference on*, IEEE, pp. 1217-1220.
- Hewitt, G. F., S. King and P. Lonergore (1961). *Holdup and Pressure Drop Measurement in the Two-Phase Annular Flow of Air-Water Mixtures*, UKAEA Atomic Energy Research Establishment, Harwell Research Group.
- Hidalgo, P. and A. Glezer (2015), "Small-Scale Vorticity Induced by a Self-Oscillating Fluttering Reed for Heat Transfer Augmentation in Air Cooled Heat Sinks," *ASME 2015 International Technical Conference and Exhibition on Packaging and Integration of Electronic and Photonic Microsystems collocated with the ASME 2015 13th International Conference on Nanochannels, Microchannels, and Minichannels*, American Society of Mechanical Engineers, pp. V001T009A004-V001T009A004.
- Hidalgo, P., F. Herrault, A. Glezer, M. Allen, S. Kaslusky and B. S. Rock (2010), "Heat Transfer Enhancement in High-Power Heat Sinks Using Active Reed Technology," *Thermal Investigations of ICs and Systems (THERMINIC), 2010 16th International Workshop on*, IEEE, pp. 1-6.
- Hidalgo, P., S. Jha and A. Glezer (2015), "Enhanced Heat Transfer in Air Cooled Heat Sinks Using Aeroelastically Fluttering Reeds," *Thermal Investigations of ICs and Systems (THERMINIC), 2015 21st International Workshop on*, IEEE, pp. 1-6.
- Institute, E. P. R., G. Ramachandran, E. P. R. I. Technology and F. A. Department (1993). *TAG Technical Assessment Guide: Electricity Supply, 1993 (Revision 7)*, Electric Power Research Institute.
- Isbin, H., N. C. Sher and K. Eddy (1957), "Void Fractions in Two - Phase Steam - Water Flow," *AIChE Journal* Vol. 3(1) pp. 136-142
- Ismail, L. S., C. Ranganayakulu, P. S. Reddy, D. Jyotsna and V. V. Rao (2008), "Heat Transfer and Flow Friction Correlations for Compact Wavy Plate Fin Heat Exchangers," *19th National 8th ISHMT ASME HMT Conference*, JNTU, Hyderabad, India
- Jacobi, A. and R. Shah (1995), "Heat Transfer Surface Enhancement through the Use of Longitudinal Vortices: A Review of Recent Progress," *Experimental Thermal and Fluid Science* Vol. 11(3) pp. 295-309
- Jung, D., K.-h. Song, Y. Cho and S.-j. Kim (2003), "Flow Condensation Heat Transfer Coefficients of Pure Refrigerants," *International Journal of Refrigeration* Vol. 26(1) pp. 4-11
- Junqi, D., C. Jiangping, C. Zhijiu, Z. Yimin and Z. Wenfeng (2007), "Heat Transfer and Pressure Drop Correlations for the Wavy Fin and Flat Tube Heat Exchangers," *Applied Thermal Engineering* Vol. 27(11) pp. 2066-2073
- Kakaç, S., R. K. Shah and W. Aung (1987). *Handbook of Single-Phase Convective Heat Transfer*, Wiley New York et al.
- Kays, W. M. and A. L. London (1984), "Compact Heat Exchangers,"

- Kedzierski, M. A. and J. Goncalves (1999), "Horizontal Convective Condensation of Alternative Refrigerants within a Micro-Fin Tube," *Journal of Enhanced Heat Transfer* Vol. 6(2-4)
- Kehlhofer, R., F. Hannemann, B. Rukes and F. Stirnimann (2009). *Combined-Cycle Gas & Steam Turbine Power Plants*, Pennwell Books.
- Khoshvaght Aliabadi, M., F. Hormozi and E. Hosseini Rad (2014), "New Correlations for Wavy Plate-Fin Heat Exchangers: Different Working Fluids," *International Journal of Numerical Methods for Heat & Fluid Flow* Vol. 24(5) pp. 1086-1108
- Kim, D. and A. J. Ghajar (2002), "Heat Transfer Measurements and Correlations for Air-Water Flow of Different Flow Patterns in a Horizontal Pipe," *Experimental Thermal and Fluid Science* Vol. 25(8) pp. 659-676
- Kim, M.-H. and C. W. Bullard (2002), "Air-Side Thermal Hydraulic Performance of Multi-Louvered Fin Aluminum Heat Exchangers," *International Journal of Refrigeration* Vol. 25(3) pp. 390-400
- Kim, N.-H., J.-H. Yun and R. Webb (1997), "Heat Transfer and Friction Correlations for Wavy Plate Fin-and-Tube Heat Exchangers," *Journal of heat transfer* Vol. 119(3) pp. 560-567
- Kim, S. J. and H. C. No (2000), "Turbulent Film Condensation of High Pressure Steam in a Vertical Tube," *International Journal of Heat and Mass Transfer* Vol. 43(21) pp. 4031-4042
- Klein, S. (2015), "Engineering Equation Solver," *F-Chart Software, Madison, WI*
- Klein, S. N., G. (2012). *Thermodynamics*. New York, Cambridge.
- Kröger, D. (1998). *Air-Cooled Heat Exchangers and Cooling Tower: Thermal-Flow Performance and Design*. Matieland, South Africa, Dept. of Mechanical Engineering, University of Stellenbosch.
- Kröger, D. G. (2004). *Air-Cooled Heat Exchangers and Cooling Towers*, PennWell Books.
- Larinoff, M., W. Moles and R. Reichhelm (1978), "Design and Specification of Air-Cooled Steam Condensers," *Chem. Engng* Vol. 22
- Li, K. W. and A. Pridov (1985), "Power Plant System Design,"
- Lips, S. and J. P. Meyer (2012), "Experimental Study of Convective Condensation in an Inclined Smooth Tube. Part II: Inclination Effect on Pressure Drops and Void Fractions," *International Journal of Heat and Mass Transfer* Vol. 55(1-3) pp. 405-412 DOI: <http://dx.doi.org/10.1016/j.ijheatmasstransfer.2011.09.034>.
- Lips, S. and J. P. Meyer (2012a), "Experimental Study of Convective Condensation in an Inclined Smooth Tube. Part I: Inclination Effect on Flow Pattern and Heat Transfer Coefficient," *International journal of heat and mass transfer* Vol. 55(1) pp. 395-404
- Lockhart, R. and R. Martinelli (1949), "Proposed Correlation of Data for Isothermal Two-Phase, Two-Component Flow in Pipes," *Chem. Eng. Prog* Vol. 45(1) pp. 39-48
- Macknick, J., R. Newmark, G. Heath and K. Hallett (2011), "A Review of Operational Water Consumption and Withdrawal Factors for Electricity Generating Technologies," *Contract* Vol. 303 pp. 275-3000

- Mahalingam, R. and A. Glezer (2005), "Design and Thermal Characteristics of a Synthetic Jet Ejector Heat Sink," *Journal of Electronic Packaging* Vol. 127(2) pp. 172-177
- Mahto, D. and S. Pal (2013), "Thermodynamics and Thermo-Economic Analysis of Simple Combined Cycle with Inlet Fogging," *Applied Thermal Engineering* Vol. 51(1) pp. 413-424
- Masuyama, F. (2001), "History of Power Plants and Progress in Heat Resistant Steels," *ISIJ international* Vol. 41(6) pp. 612-625
- Maupin, M. A., J. F. Kenny, S. S. Hutson, J. K. Lovelace, N. L. Barber and K. S. Linsey (2014). Estimated Use of Water in the United States in 2010. US Geological Survey, 2330-5703.
- McAdams, W., W. Woods and L. Heroman (1942), "Vaporization inside Horizontal Tubes-II-Benzene-Oil Mixtures," *Trans. ASME* Vol. 64(3) pp. 193-200
- Miles, J. and J. Shih (1967), "Reconsideration of Nusselt Number for Laminar Fully Developed Flow in Rectangular Ducts," *Mechanical Engineering Department, University of Missouri, Columbia*
- Miliaras, E. S. (1974), "Power Plants with Air-Cooled Condensing Systems,"
- Mitra, N. and M. Fiebig (1994), "Comparison of Wing-Type Vortex Generators for Heat Transfer Enhancement in Channel Flows," *Journal of heat transfer* Vol. 116(4) pp. 880-885
- Mohseni, S., M. Akhavan-Behabadi and M. Saeedinia (2013), "Flow Pattern Visualization and Heat Transfer Characteristics of R-134a During Condensation inside a Smooth Tube with Different Tube Inclinations," *International Journal of Heat and Mass Transfer* Vol. 60 pp. 598-602
- Moser, K., R. Webb and B. Na (1998), "A New Equivalent Reynolds Number Model for Condensation in Smooth Tubes," *Journal of Heat Transfer* Vol. 120(2) pp. 410-417
- Mukherjee, H. and J. Brill (1985), "Pressure Drop Correlations for Inclined Two-Phase Flow," *Journal of energy resources technology* Vol. 107(4) pp. 549-554
- Müller-Steinhagen, H. and K. Heck (1986), "A Simple Friction Pressure Drop Correlation for Two-Phase Flow in Pipes," *Chemical Engineering and Processing: Process Intensification* Vol. 20(6) pp. 297-308
- Nagel, P. (1994), "New Developments in Aircooled Steam Condensers and Dry Cooling Towers," *9th IAHR Cooling Tower and Spraying Pond Symposium, von Karman Institute, Brussels, Belgium*
- Ničeno, B. and E. Nobile (2001), "Numerical Analysis of Fluid Flow and Heat Transfer in Periodic Wavy Channels," *International Journal of Heat and Fluid Flow* Vol. 22(2) pp. 156-167
- Park, I., S.-M. Kim and I. Mudawar (2013), "Experimental Measurement and Modeling of Downflow Condensation in a Circular Tube," *International Journal of Heat and Mass Transfer* Vol. 57(2) pp. 567-581
- Park, Y.-G. and A. M. Jacobi (2009), "Air-Side Heat Transfer and Friction Correlations for Flat-Tube Louver-Fin Heat Exchangers," *Journal of Heat Transfer* Vol. 131(2) p. 021801

- Pesteei, S., P. Subbarao and R. Agarwal (2005), "Experimental Study of the Effect of Winglet Location on Heat Transfer Enhancement and Pressure Drop in Fin-Tube Heat Exchangers," *Applied Thermal Engineering* Vol. 25(11) pp. 1684-1696
- Polyzakis, A., C. Koroneos and G. Xydis (2008), "Optimum Gas Turbine Cycle for Combined Cycle Power Plant," *Energy conversion and management* Vol. 49(4) pp. 551-563
- Putman, R. E., J. W. Harpster, P. Verona and O. Westerville (2000), "The Economic Effects of Condenser Backpressure on Heat Rate, Condensate Subcooling and Feedwater Dissolved Oxygen," *Proceedings on CD, of 2000 International Joint Power Generation Conference*
- Putman, R. E. and D. Jaresch (2002), "The Cleaning of Air Cooled Condensers to Improve Performance," *2002 International Joint Power Generation Conference*, American Society of Mechanical Engineers, pp. 139-146.
- Quiben, J. M. and J. R. Thome (2007), "Flow Pattern Based Two-Phase Frictional Pressure Drop Model for Horizontal Tubes, Part II: New Phenomenological Model," *International Journal of Heat and Fluid Flow* Vol. 28(5) pp. 1060-1072
- Rathje, U. and H.-J. Pflaumbaum (1996), "Die Generation 2000 Luftgekühlter Abdampfkondensatoren," *VGB Kraftwerkstechnik* Vol. 76(1) pp. 31-36
- Sahnoun, A. and R. Webb (1992), "Prediction of Heat Transfer and Friction for the Louver Fin Geometry," *Journal of heat transfer* Vol. 114(4) pp. 893-900
- Salta, C. and D. Kröger (1995), "Effect of Inlet Flow Distortions on Fan Performance in Forced Draught Air-Cooled Heat Exchangers," *Heat Recovery Systems and CHP* Vol. 15(6) pp. 555-561
- Schulenberg, F. J. (1966), "Finned Elliptical Tubes and Their Application in Air-Cooled Heat Exchangers," *Journal of Manufacturing Science and Engineering* Vol. 88(2) pp. 179-186
- Shah, M. (1979), "A General Correlation for Heat Transfer During Film Condensation inside Pipes," *International Journal of heat and mass transfer* Vol. 22(4) pp. 547-556
- Shah, M. M. (2009), "An Improved and Extended General Correlation for Heat Transfer During Condensation in Plain Tubes," *HVAC&R Research* Vol. 15(5) pp. 889-913
- Shah, R. and A. London (1978a), "Laminar Flow Forced Convection in Ducts: A Source Book for Compact Heat Exchanger Analytical Data, Supl. 1," *Adv. Heat Transfer*
- Shah, R. and A. London (1978b). *Laminar Flow Forced Convection in Ducts: A Sourcebook for Compact Heat Transfer Exchange Analytical Data*, Academic Press.
- Shah, R. K. and A. L. London (1971). *Laminar Flow Forced Convection Heat Transfer and Flow Friction in Straight and Curved Ducts-a Summary of Analytical Solutions*. DTIC Document.
- Shikazono, N., M. Itoh, M. Uchida, T. Fukushima and T. Hatada (1998), "Predictive Equation Proposal for Condensation Heat Transfer Coefficient of Pure Refrigerants in Horizontal Micro-Fin Tubes," *JSME Int. J., Ser. B* Vol. 64 pp. 196-203
- Smith, B. L. and A. Glezer (1998), "The Formation and Evolution of Synthetic Jets," *Physics of Fluids (1994-present)* Vol. 10(9) pp. 2281-2297

- Sohal, M. and J. O'Brien (2001), "Improving Air-Cooled Condenser Performance Using Winglets and Oval Tubes in a Geothermal Power Plant," *Geothermal resources council transactions* Vol. 25(26-29) pp. 1-7
- Spedding, P., J. Chen and V. T. Nguyen (1982), "Pressure Drop in Two Phase Gas-Liquid Flow in Inclined Pipes," *International Journal of Multiphase Flow* Vol. 8(4) pp. 407-431
- Spedding, P. and V. T. Nguyen (1980), "Regime Maps for Air Water Two Phase Flow," *Chemical Engineering Science* Vol. 35(4) pp. 779-793
- SPX (2015). *Air Cooled Condensers*, SPX Corporation.
- Srinivas, T., A. V. S. S. K. Gupta and B. V. Reddy (2008), "Thermodynamic Modeling and Optimization of Multi-Pressure Heat Recovery Steam Generator in Combined Power Cycle," *Journal of Scientific and Industrial Research* Vol. 67(10) pp. 827-834
- Stewart, D. (2014). *Inside the Medupi Power Station*. The Citizen. Gauteng.
- Storek, H. and H. Brauer (1980), "Pressure Drop in Adiabatic Gas/Liquid-Flow in Horizontal and Vertical Tubes
Reibungsdruckverlust Der Adiabaten Gas/Fluessigkeit-Stroemung in Horizontalen Und Vertikalen Rohren," *VDI Forschungsheft*(599)
- Taitel, Y. and A. Dukler (1976), "A Model for Predicting Flow Regime Transitions in Horizontal and near Horizontal Gas - Liquid Flow," *AIChE Journal* Vol. 22(1) pp. 47-55
- Thome, J. R., J. El Hajal and A. Cavallini (2003), "Condensation in Horizontal Tubes, Part 2: New Heat Transfer Model Based on Flow Regimes," *International Journal of Heat and Mass Transfer* Vol. 46(18) pp. 3365-3387
- Torii, K., K. Kwak and K. Nishino (2002), "Heat Transfer Enhancement Accompanying Pressure-Loss Reduction with Winglet-Type Vortex Generators for Fin-Tube Heat Exchangers," *International Journal of Heat and Mass Transfer* Vol. 45(18) pp. 3795-3801
- Traviss, D., W. Rohsenow and A. Baron (1973), "Forced-Convection Condensation inside Tubes: A Heat Transfer Equation for Condenser Design," *ASHRAE Trans* Vol. 79(1) pp. 157-165
- Valdés, M., M. D. Duran and A. Rovira (2003), "Thermoeconomic Optimization of Combined Cycle Gas Turbine Power Plants Using Genetic Algorithms," *Applied Thermal Engineering* Vol. 23(17) pp. 2169-2182
- Webb, R. L. and P. Trauger (1991), "Flow Structure in the Louvered Fin Heat Exchanger Geometry," *Experimental Thermal and Fluid Science* Vol. 4(2) pp. 205-217
- Wheeler, K. R., A. B. J. Johnson and R. P. May (1982), "Aluminum Alloy Performance in Industrial Air-Cooled Applications," *Atmospheric Corrosion of Metals: A Symposium*, ASTM International, p. 116.
- Yang, L., Y. Asako, Y. Yamaguchi and M. Faghri (1997), "Numerical Prediction of Transitional Characteristics of Flow and Heat Transfer in a Corrugated Duct," *Journal of heat transfer* Vol. 119(1) pp. 62-69
- Yu, J. and S. Koyama (1998), "Condensation Heat Transfer of Pure Refrigerants in Microfin Tubes,"

Zhai, H. and E. S. Rubin (2010), "Performance and Cost of Wet and Dry Cooling Systems for Pulverized Coal Power Plants with and without Carbon Capture and Storage," *Energy Policy* Vol. 38(10) pp. 5653-5660